Physics of Atomic Nuclei, Vol. 68, No. 6, 2005, pp. 1007–1015. From Yadernaya Fizika, Vol. 68, No. 6, 2005, pp. 1045–1053.
Original English Text Copyright © 2005 by Bakker, Veselov, Zubkov.

ELEMENTARY PARTICLES AND FIELDS
Theory

An Additional Symmetry in the Weinberg–Salam Model*

B. L. G. Bakker[1)], A. I. Veselov, and M. A. Zubkov

Institute of Theoretical and Experimental Physics,
Bol'shaya Cheremushkinskaya ul. 25, Moscow, 117259 Russia

Received February 10, 2004; in final form, July 2, 2004

Abstract—An additional Z_6 symmetry hidden in the fermion and Higgs sectors of the Standard Model has been found recently. It has a singular nature and is connected to the centers of the $SU(3)$ and $SU(2)$ subgroups of the gauge group. A lattice regularization of the Standard Model was constructed that possesses this symmetry. In this paper, we report our results on the numerical simulation of its electroweak sector. © *2005 Pleiades Publishing, Inc.*

1. INTRODUCTION

It is the conventional point of view that all the symmetries of the Standard Model (SM), which must be used when dealing with its discretization, are known. Recently, it was found that there exists an additional $Z_6 = Z_2 \otimes Z_3$ symmetry in the fermion and Higgs sectors of the SM [1]. It has a singular nature and is connected to the centers Z_3 and Z_2 of the $SU(3)$ and $SU(2)$ subgroups.[2)] The gauge sector of the SM (in its discretized form) was redefined in such a way that it has the same perturbation expansion as the original one, while keeping the aforementioned symmetry. The resulting model differs from the conventional SM via its symmetry properties. Therefore, we expect that it would describe nature better than the conventional discretized SM if the additional symmetry did take place.

It is worth mentioning that the present status of the SM on the lattice implies that it must be considered as a finite cutoff theory [3]. This is in agreement with the understanding that the SM does not describe physics at extremely small distances. Hence, it is sufficient to consider a cutoff Λ that is finite but much larger than all observed energies. The consideration of the infinite cutoff limit would be an attempt to continue the SM to infinitesimal distances. Now it is believed that this attempt leads to a trivial continuum theory [4]. Nevertheless, at energies much less than the cutoff, we can calculate any physical variable.

Thus, we can examine our model in order to understand whether the considered additional symmetry is important for the discretization of the SM or not. As a first step in this direction, we investigate numerically the quenched electroweak sector of the constructed discretized SM.

2. A HIDDEN SYMMETRY

In this section, we repeat our construction reported in [1] in continuum notation. This is done in order to demonstrate the universal (regularization-independent) nature of the additional symmetry found.

2.1. The Standard Model

The SM contains the following variables:

(i) The gauge fields associated with the symmetry group $SU(3) \times SU(2) \times U(1)$, which are the elements of the corresponding algebras:

$$Z_i = Z_i^a \lambda_a \in su(3), \qquad (1)$$
$$A_i = A_i^b \sigma_b \in su(2),$$
$$B_i \in u(1) = (-\infty, \infty).$$

(Here, λ_a are the Gell-Mann matrices, and σ_b are the Pauli matrices.) The corresponding $SU(3)$, $SU(2)$, and $U(1)$ field strengths are

$$H_{ij} = \partial_{[i} Z_{j]} + i[Z_i, Z_j], \qquad (2)$$
$$G_{ij} = \partial_{[i} A_{j]} + i[A_i, A_j],$$
$$F_{ij} = \partial_{[i} B_{j]}.$$

(ii) Anticommuting spinor variables, representing leptons and quarks:

$$\begin{pmatrix} e & \mu & \tau \\ \nu_e & \nu_\mu & \nu_\tau, \end{pmatrix}, \qquad \begin{pmatrix} u & c & t \\ d & s & b \end{pmatrix}. \qquad (3)$$

*This article was submitted by the authors in English.

[1)]Department of Physics and Astronomy, Vrije Universiteit, Amsterdam, The Netherlands.

[2)]The emergence of Z_6 symmetry in the SM and its supersymmetric extension was considered in a different context in [2].

1063-7788/05/6806-1007$26.00 © 2005 Pleiades Publishing, Inc.

(iii) A scalar doublet

$$\Phi^\alpha, \qquad \alpha = 1, 2. \tag{4}$$

The action has the form

$$S = S_g + S_H + S_f, \tag{5}$$

where we denote the fermion part of the action by S_f, the pure gauge part by S_g, and the scalar part of the action by S_H.

As usual, we consider S_g in the form

$$S_g = \frac{1}{4}\int d^4x \Big[\frac{1}{3g^2_{SU(3)}}\mathrm{Tr}H^2 + \frac{1}{2g^2_{SU(2)}}\mathrm{Tr}G^2 + \frac{1}{g^2_{U(1)}}F^2\Big], \tag{6}$$

where we introduced the gauge couplings $g_{SU(3)}$, $g_{SU(2)}$, and $g_{U(1)}$.

The scalar part of the action is

$$S_H = \int d^4x|(\partial_\mu + iA_\mu + iB_\mu)\Phi|^2 + \int d^4x V(|\Phi|), \tag{7}$$

where $V(|\Phi|)$ is the potential, which has a minimum at a nonzero value of $\Phi = v$, causing spontaneous symmetry breaking.

We express S_f through left-handed doublets L and right-handed singlets R of fermions:

$$L^\ell_1 = \frac{1-\gamma_5}{2}\begin{pmatrix} e \\ \nu_e \end{pmatrix}, \quad L^\ell_2 = \frac{1-\gamma_5}{2}\begin{pmatrix} \mu \\ \nu_\mu \end{pmatrix}, \tag{8}$$

$$L^\ell_3 = \frac{1-\gamma_5}{2}\begin{pmatrix} \tau \\ \nu_\tau \end{pmatrix}, \quad L^q_1 = \frac{1-\gamma_5}{2}\begin{pmatrix} u \\ d \end{pmatrix},$$

$$L^q_2 = \frac{1-\gamma_5}{2}\begin{pmatrix} c \\ s \end{pmatrix}, \quad L^q_3 = \frac{1-\gamma_5}{2}\begin{pmatrix} t \\ b \end{pmatrix},$$

$$R^\ell_1 = \frac{1+\gamma_5}{2}e, \quad R^\ell_2 = \frac{1+\gamma_5}{2}\mu,$$

$$R^\ell_3 = \frac{1+\gamma_5}{2}\tau, \quad R^q_{1,1} = \frac{1+\gamma_5}{2}u,$$

$$R^q_{1,2} = \frac{1+\gamma_5}{2}c, \quad R^q_{1,3} = \frac{1+\gamma_5}{2}t,$$

$$R^q_{2,1} = \frac{1+\gamma_5}{2}d, \quad R^q_{2,2} = \frac{1+\gamma_5}{2}s,$$

$$R^q_{2,3} = \frac{1+\gamma_5}{2}b.$$

The fermion part of the action is

$$S_f = \int d^4x\{\mathcal{L}^L_\ell + \mathcal{L}^R_\ell + \mathcal{L}^L_q + \mathcal{L}^{R,1}_q + \mathcal{L}^{R,2}_q + \mathcal{L}^\ell_{\mathrm{mass}} + \mathcal{L}^q_{\mathrm{mass}}\}. \tag{9}$$

Here,

$$\mathcal{L}^L_\ell = i\bar{L}^\ell_i(\partial_\mu + iA_\mu - iB_\mu)\gamma_\mu L^\ell_i, \tag{10}$$

$$\mathcal{L}^R_\ell = i\bar{R}^\ell_i(\partial_\mu - 2iB_\mu)\gamma_\mu R^\ell_i,$$

$$\mathcal{L}^L_q = i\bar{L}^q_i(\partial_\mu + iZ_\mu + iA_\mu + (i/3)B_\mu)\gamma_\mu L^q_i,$$

$$\mathcal{L}^{R,1}_q = i\bar{R}^q_{1,i}(\partial_\mu + iZ_\mu + (4i/3)B_\mu)\gamma_\mu R^q_{1,i},$$

$$\mathcal{L}^{R,2}_q = i\bar{R}^q_{2,i}(\partial_\mu + iZ_\mu - (2i/3)B_\mu)\gamma_\mu R^q_{2,i},$$

$$\mathcal{L}^q_{\mathrm{mass}} = \frac{1}{v}\sum_i m^q_i(\bar{L}^q_i)^\alpha\Phi^\alpha R^q_{1,i} + \frac{1}{v}\sum_{ij} M_{ij}(\bar{L}^q_i)^\alpha\Omega^\alpha R^q_{2,j} + \mathrm{h.c.},$$

$$\mathcal{L}^\ell_{\mathrm{mass}} = \frac{1}{v}\sum_i m^\ell_i(\bar{L}^\ell_i)^\alpha\Phi^\alpha R^\ell_i + \mathrm{h.c.}$$

In these expressions, $\Omega = i\sigma_2\Phi$ ($i\sigma_2$ is the charge conjugation operator), $\bar{\psi} = \psi^\dagger\gamma_0$, and

$$m^\ell_1 = m_e, \quad m^\ell_2 = m_\mu, \quad m^\ell_3 = m_\tau, \qquad m^q_1 = m_u, \quad m^q_2 = m_c, \quad m^q_3 = m_t. \tag{11}$$

M is the mass matrix, whose eigenvalues represent the masses of the d, s, and b quarks. The nondiagonality of this matrix gives rise to the phenomenon of quark mixing.

All necessary information about the Euclidean dynamics of the SM is contained in the gauge invariant correlators:

$$\langle O(\mathrm{fields})\rangle = \int DZDADBDeD\bar{e}D\nu_eD\bar{\nu_e}\ldots D\Phi \times \exp(-S(\mathrm{fields}))O(\mathrm{fields}). \tag{12}$$

2.2. Representation of the Standard Model in Loop Space

The hidden symmetry we are talking about may be seen after reformulation of the SM through loop variables. (For the definition of the notation connected with loop space dynamics, see [5].) The derivation is as follows.

First, we note that, in Eq. (10), L and R can be treated as independent two-component Weil spinors. In the Weil basis of the γ matrices, the Euclidean fermion Lagrangian contains quadratic terms like $L^\dagger(\nabla_0 - i\nabla_i\sigma_i)L$ and $R^\dagger(\nabla_0 + i\nabla_i\sigma_i)R$ [where ∇_μ

is a covariant derivative and σ_i ($i = 1, 2, 3$) are Pauli matrices] and an interaction term like $(L^\dagger\Phi)R$.

For an arbitrary gauge invariant correlator, we have

$$\langle O(\text{fields})\rangle = \int DZDADB \exp(-S_g)\langle O(\text{fields})\rangle_{f,s}. \tag{13}$$

Here, $\langle O(\text{fields})\rangle_{f,s}$ is an integral over fermions and over the scalar field. It is calculated in the model with an external gauge field. First, we perform an integration over the Grassmann variables. We can do it using simple Feynman rules. The diagrams contain propagators of Weil spinors, correlation functions of the scalar field, and interaction vertices that come from the term $L^{\dagger\alpha}\Phi^\alpha R$. The loops coming from the fermion determinant should also be taken into account. We use the path-integral representation of the propagators and of the fermion determinant (see, for example, [5, 6]). In order to calculate the scalar field correlators, we use lattice regularization. It is well known that the bosonic path integral for any field correlators in the external gauge field on the lattice has a representation as a sum over all possible closed loops. (For the details of the calculation, see, for example, [7].) After returning to the continuum representation, we arrive at a path-integral representation of the scalar field correlators.

Finally, we represent any correlator Eq. (12) in the form

$$\langle O(\text{fields})\rangle = \int D\mathcal{C}_\alpha \mathcal{O}(\mathcal{C}) \int DZDADB \tag{14}$$
$$\times \exp(-S_g)\mathcal{W}(\mathcal{C}) = \int D\mathcal{C}_\alpha \mathcal{O}(\mathcal{C})\langle \mathcal{W}(\mathcal{C})\rangle.$$

Here, $\mathcal{C}_\alpha$ stands for the set of paths. Each path corresponds to one of the fermions (left- or right-handed) or to the scalar. It may either be closed or end in a vertex. Each vertex corresponds to the transformation of left-handed fermions into right-handed ones and emission or absorption of a scalar. The definition of the measure $D\mathcal{C}_\alpha$ comes from the path-integral representations of the bosonic correlator mentioned above, the fermion determinant, and the fermion propagator. It includes all possible paths described above. The index α enumerates all fermions and the scalar. The functionals $\mathcal{O}$ do not depend upon the gauge fields and are, hence, not of interest to us. The full dependence on the gauge fields is now concentrated in the loop variable $\mathcal{W}$ that is simply a product of parallel transporters $W(\mathcal{C}_\alpha)$ corresponding to the fermions and to the scalar:

$$\mathcal{W}(\mathcal{C}) = \text{Tr}\prod W(\mathcal{C}_\alpha). \tag{15}$$

In Eq. (15), we encounter six different parallel transporters:

$$W_{L_\ell}(\mathcal{C}) = P\exp\left(i\int\limits_{\mathcal{C}}(A_\mu - B_\mu)dx_\mu\right) \tag{16}$$
$$= \omega_{SU(2)}\omega_{U(1)}^{-1},$$
$$W_{R_\ell}(\mathcal{C}) = \exp\left(i\int\limits_{\mathcal{C}}(-2B_\mu)dx_\mu\right) = \omega_{U(1)}^{-2},$$
$$W_{L_q}(\mathcal{C}) = P\exp\left(i\int\limits_{\mathcal{C}}\left(Z_\mu + A_\mu + \frac{1}{3}B_\mu\right)dx_\mu\right)$$
$$= \omega_{SU(3)}\omega_{SU(2)}\omega_{U(1)}^{1/3},$$
$$W_{R_q^1}(\mathcal{C}) = P\exp\left(i\int\limits_{\mathcal{C}}\left(Z_\mu + \frac{4}{3}B_\mu\right)dx_\mu\right)$$
$$= \omega_{SU(3)}\omega_{U(1)}^{4/3},$$
$$W_{R_q^2}(\mathcal{C}) = P\exp\left(i\int\limits_{\mathcal{C}}\left(Z_\mu - \frac{2}{3}B_\mu\right)dx_\mu\right)$$
$$= \omega_{SU(3)}\omega_{U(1)}^{-2/3},$$
$$W_H(\mathcal{C}) = P\exp\left(i\int\limits_{\mathcal{C}}(A_\mu + B_\mu)dx_\mu\right)$$
$$= \omega_{SU(2)}\omega_{U(1)},$$

where we introduced Wilson loops corresponding to $SU(3)$, $SU(2)$, and $U(1)$ gauge fields, respectively:

$$\omega_{U(1)} = \exp\left(i\int\limits_{\mathcal{C}}B_\mu dx_\mu\right), \tag{17}$$
$$\omega_{SU(2)} = P\exp\left(i\int\limits_{\mathcal{C}}A_\mu dx_\mu\right),$$
$$\omega_{SU(3)} = P\exp\left(i\int\limits_{\mathcal{C}}Z_\mu dx_\mu\right).$$

In Eq. (16), each ω corresponds to a path connecting different points. However, in Eq. (15), these parallel transporters are arranged in such a way that $\mathcal{W}(\mathcal{C})$ depends only upon ω corresponding to closed loops constructed of $\mathcal{C}_\alpha$.

Thus, any correlator can be represented through vacuum averages of products of those loop variables. The vacuum average is considered in the pure gauge

theory with the action S_g. Using loop calculus, we can express $\langle \mathcal{W}(\mathcal{C})\rangle$ as follows:

$$\langle \mathcal{W}(\mathcal{C})\rangle = \int D\omega_{U(1)} D\omega_{SU(2)} D\omega_{SU(3)} \qquad (18)$$
$$\times \exp\left(\frac{1}{4}\int\left\{\frac{1}{3g^2_{SU(3)}}\mathrm{Tr}\frac{\delta\omega_{SU(3)}}{\delta\sigma_{\mu\nu}(x)}\Big|_0\frac{\delta\omega_{SU(3)}}{\delta\sigma_{\mu\nu}(x)}\Big|_0\right.\right.$$
$$+\frac{1}{2g^2_{SU(2)}}\mathrm{Tr}\frac{\delta\omega_{SU(2)}}{\delta\sigma_{\mu\nu}(x)}\Big|_0\frac{\delta\omega_{SU(2)}}{\delta\sigma_{\mu\nu}(x)}\Big|_0$$
$$\left.\left.+\frac{1}{g^2_{U(1)}}\frac{\delta\omega_{U(1)}}{\delta\sigma_{\mu\nu}(x)}\Big|_0\frac{\delta\omega_{U(1)}}{\delta\sigma_{\mu\nu}(x)}\Big|_0\right\}d^4x\right)\mathcal{W}(\mathcal{C}),$$

where $\sigma_{\mu\nu}$ is the infinitesimal area, $\delta/\delta\sigma_{\mu\nu}$ is the area derivative, and $\ldots|_0$ means that the area derivatives are calculated for infinitesimal contours. The measure over the gauge variables is denoted now as $D\omega$.

2.3. The Symmetry

Now we are in a position to point out the mentioned symmetry. It turns out that $\mathcal{W}(\mathcal{C})$, being expressed through ω corresponding to closed loops, is invariant under the following transformation:

$$\omega_{U(1)}(\mathcal{C}) \to \exp(-i\pi\mathbf{L}(\mathcal{C},\Sigma))\omega_{U(1)}(\mathcal{C}), \qquad (19)$$
$$\omega_{SU(2)}(\mathcal{C}) \to \exp(i\pi\mathbf{L}(\mathcal{C},\Sigma))\omega_{SU(2)}(\mathcal{C}),$$
$$\omega_{SU(3)}(\mathcal{C}) \to \exp(i\,\tfrac{2}{3}\pi\mathbf{L}(\mathcal{C},\Sigma))\omega_{SU(3)}(\mathcal{C}).$$

Here, Σ is an arbitrary closed surface and $\mathbf{L}(\mathcal{C},\Sigma)$ is the integer linking number of this surface and the closed contour $\mathcal{C}$. From Eq. (19), it is clear that this transformation belongs to the Z_6 group.

This transformation corresponds to the centers of the $SU(3)$ and $SU(2)$ subgroups of the gauge group. It is finite, being applied to the gauge invariant loop variables ω. However, it becomes singular in terms of gauge potentials:

$$B_\mu \to B_\mu - \pi\mathcal{V}_\mu, \qquad (20)$$
$$A_\mu \to A_\mu + \pi\mathcal{V}_\mu\frac{A_\nu t_\nu}{(\mathrm{Tr}A_\tau t_\tau)^{1/2}},$$
$$Z_\mu \to Z_\mu + \frac{2\pi}{3}\mathcal{V}_\mu\frac{Z_\nu t_\nu}{(\mathrm{Tr}Z_\tau t_\tau)^{1/2}},$$

where $\mathcal{V}_\mu(x) = \int_V t_\mu\delta(x - y(a,b,c))da\,db\,dc$ is an integral over the three-dimensional hypersurface $y(a,b,c)$, the boundary of which is Σ. The normal vector to V is denoted by $t_\mu = \frac{1}{2}\epsilon_{\mu\nu\rho\sigma}\frac{\partial y_\nu}{\partial a}\frac{\partial y_\rho}{\partial b}\frac{\partial y_\sigma}{\partial c}$.

The invariance of Eq. (15) under the transformations (19) can be easily proven via direct substitution of Eq. (20) into Eq. (16).

2.4. Redefinition of the Gauge Action

The whole SM can be represented (at least, formally) in such a way that it possesses the symmetry with respect to transformation Eq. (19). This can be done by the following redefinition of the pure gauge part:

$$\langle \mathcal{W}(\mathcal{C})\rangle = \int D\omega_{U(1)} D\omega_{SU(2)} D\omega_{SU(3)} \qquad (21)$$
$$\times \exp\left(\sum_k \beta_k \int \mathrm{Tr}\,\frac{\delta W_k}{\delta\sigma_{\mu\nu}(x)}\Big|_0\frac{\delta W_k}{\delta\sigma_{\mu\nu}(x)}\Big|_0\right)\mathcal{W}(\mathcal{C}).$$

Here, the sum is over the six parallel transporters mentioned above. For an appropriate choice of couplings β_k, the action in Eq. (21) is equal to the action in Eq. (18) defined in terms of smooth gauge fields. However, in loop calculus, we are not forced to consider smooth gauge fields. We are allowed to consider *piecewise smooth loop variables* ω instead. The main difference is that the action in Eq. (18) suppresses steplike ω, while Eq. (21) allows the appearance of loop variables with discontinuities like Eq. (19).

Instead, Eq. (21) suppresses the discontinuities in W_k. Therefore, we may apply a transformation like Eq. (19) to all ω in order to make them smooth. After that Eq. (21) becomes identical to Eq. (18). So, these two formulations would define the same theory.

Here, we implied that if the action suppresses some physical quantity, the latter indeed vanishes. However, there is another point of view. Namely, there are some indications that the naively suppressed quantities may survive due to the entropy factor [8]. We do not discuss here this possibility, but we must mention that, if this picture emerges in the SM, Eqs. (18) and (21) may define different models and correspond to different physics. We also notice here that, in this case, say, the topological theta term with $\theta = 2\pi$ being added to the action could, in principle, change the nonperturbative behavior of the theory while keeping the same perturbation expansion [9].

2.5. The Standard Model as a Finite Cutoff Theory

It was mentioned in the introduction that the SM should be regarded as a finite cutoff theory. So, the correct continuum model must contain a short-distance part (related to the unification of the electroweak and strong interactions), which makes the corresponding lattice model cutoff independent.

The unified model could be the origin of our additional symmetry. If so, Eq. (19) emerges in it without any singular transformation of gauge potentials. Actually, in the corresponding examples considered in [1], the realization of Eq. (19) written in terms of the continuum fields is not singular.

Strictly speaking, the only thing we are able to consider is the regularized model. The regularization can be constructed in such a way that it either admits or does not admit Eq. (19). Each choice of regularization is, in essence, the low-energy limit of a regularized unified model. After the discretization is removed, the full continuum theory appears. The finite cutoff SM is an approximation to this hypothetical theory. Our assumption is that, if we construct the Finite Cutoff Standard Model (FCSM) either keeping or not keeping the additional symmetry, the degree to which the resulting model approximates the correct unified model could be different.

We expect that this difference might manifest itself at high enough energies. Probably, this could happen in the intermediate region between the usual SM scale and the GUT scale. Strictly speaking, in this region, neither realizations of the FCSM can describe the physics properly. However, if the symmetry with respect to Eq. (19) is indeed a fundamental symmetry, the corresponding model may give results that are closer to the experimental ones (and vice versa). If so, we would catch the echo of the unified model already at intermediate energies and draw certain conclusions about its structure.

However, we expect that the most important role of the symmetry with respect to (19) is rather technical. The convergence of the lattice methods to physical results could become considerably faster for the models that respect invariance under Eq. (19). This can be crucial for consideration of certain processes. Probably, the same situation takes place, say, for the $SU(2)$ and $SO(3)$ gauge models [10]. They are generally believed to belong to the same universality class. However, physical results are practically unachievable via $SO(3)$ lattice theory. The reason is that the Z_2 symmetry is lost.

In general, it is thought that the convergence of a lattice model to the continuum results is faster if it keeps as many symmetries of the continuum model as possible. It even might occur that models that keep or do not keep a certain symmetry may lead to different continuum theories. Therefore, we also do not exclude that FCSMs that respect or do not respect Eq. (19) would give essentially different results. In any case, nothing definite could be said until the corresponding numerical research is performed.

3. THE LATTICE MODEL

3.1. Discretization of the Continuum Model

In the remaining part of this article, we shall not be interested in a discretization of the fermion sector. We would only notice that there are some difficulties concerning the problem of keeping the chiral symmetry while avoiding doubling. There are many different papers on this subject. For a review, see [11] and references therein.

Now our aim is to recall the construction of [1]. We construct a lattice $SU(3) \times SU(2) \times U(1)$ gauge model coupled to the scalar field in such a way that it reflects all the required properties of the Weinberg–Salam model and, in addition, preserves the symmetry considered above.

The model contains the following variables:

(i) Lattice gauge fields (which live on the links of the lattice):

$$\Gamma \in SU(3), \quad U \in SU(2), \quad e^{i\theta} \in U(1).$$

(ii) A scalar doublet $\Phi^\alpha, \alpha = 1, 2$ (which lives on the lattice sites). The action of the model must have the form

$$S = S_g + S_H, \tag{22}$$

where we denote the pure gauge part by S_g and the scalar part of the action by S_H.

A possible choice of S_H is

$$S_H = \sum_{xy} |U_{xy} e^{-i\theta_{xy}} \Phi_y - \Phi_x|^2 + \sum_x V(|\Phi_x|), \tag{23}$$

where $V(r)$ is the potential, which has a minimum at a nonzero value of $r = \sqrt{\gamma}$.

To construct the pure gauge part of the action, we use the following correspondence between the lattice and the continuum notation:

$$\begin{aligned} \omega_{U(1)}(\mathcal{C}) &\to \prod_{\text{link}\in l} e^{-i\theta_{\text{link}}}, \\ \omega_{SU(2)}(\mathcal{C}) &\to \prod_{\text{link}\in l} U_{\text{link}}, \\ \omega_{SU(3)}(\mathcal{C}) &\to \prod_{\text{link}\in l} \Gamma_{\text{link}}, \end{aligned} \tag{24}$$

where l is a closed contour on the lattice corresponding to the continuum contour $\mathcal{C}$.

The analog of the continuum transformation is the lattice transformation:

$$\begin{aligned} U &\to U e^{-i\pi N}, \\ \theta &\to \theta + \pi N, \\ \Gamma &\to \Gamma e^{(2\pi i/3)N}, \end{aligned} \tag{25}$$

where N is an arbitrary integer link variable. It represents a three-dimensional hypersurface on a dual lattice, the boundary of which corresponds to Σ in Eq. (19). This symmetry reveals the correspondence between the centers of the $SU(2)$ and $SU(3)$ subgroups of the gauge group.

The choice $\beta = \beta_{L_\ell} = \beta_{R_\ell} = \beta_{L_q} = \beta_{R_q^1} = \beta_{R_q^2}$ and $\beta_H = 0$ corresponds to a certain class of unified models [1]. Hence, we choose

$$S_g = \beta \sum_{\text{plaquettes}} \left(2\left(1 - \frac{1}{2}\mathrm{Tr}U_p \cos\theta_p\right) \right. \quad (26)$$
$$+ (1 - \cos 2\theta_p) + 6\Big(1 - \frac{1}{6}\mathrm{Re\ Tr}\Gamma_p \mathrm{Tr}U_p$$
$$\times \exp\Big(\frac{i\theta_p}{3}\Big)\Big) + 3\Big(1 - \frac{1}{3}\mathrm{Re\ Tr}\Gamma_p \exp\Big(\frac{-2i\theta_p}{3}\Big)\Big)$$
$$\left. + 3\Big(1 - \frac{1}{3}\mathrm{Re\ Tr}\Gamma_p \exp\Big(\frac{4i\theta_p}{3}\Big)\Big)\Big),$$

where the sum runs over the elementary plaquettes of the lattice. Each term of the action Eq. (26) corresponds to a parallel transporter along the boundary ∂p of plaquette p. The correspondent plaquette variables constructed of lattice gauge fields are $U_p = \omega_{SU(2)}(\partial p), \Gamma_p = \omega_{SU(3)}(\partial p)$, and $\theta_p = \mathrm{Arg}\omega_{U(1)}(\partial p)$.

3.2. The Simplified Model

In this paper, we report our results on the numerical simulation of the model, in which we omit the dynamical fermions, as well as the color subgroup $SU(3)$. It will be seen below that, even on this level, certain qualitative differences between this model and the conventional one exist.

The potential for the scalar field is considered in the London limit, i.e., in the limit of infinite bare Higgs mass. The action of the model reduces to

$$S = S^L + S^R + S_H \quad (27)$$
$$= \beta \sum_{\text{plaquettes}} \left(\left(1 - \frac{1}{2}\mathrm{Tr}U_p \cos\theta_p\right) \right.$$
$$\left. + \frac{1}{2}(1 - \cos 2\theta_p)\right)$$
$$+ \sum_{xy} |U_{xy} e^{-i\theta_{xy}} \Phi_y - \Phi_x|^2 + V(|\Phi|).$$

(Here, β is rescaled as $\beta \to \beta/2$ for the convenience of comparing the results with those of the $SU(2)$ fundamental Higgs model.) S^L corresponds to the doublet of left-handed fermions and S^R corresponds to the right-handed singlet. Φ is the Higgs doublet and V is an infinitely deep potential, giving rise to the vacuum average $\langle|\Phi|\rangle = \sqrt{\gamma}$. It is worth mentioning that the naive continuum limit of Eq. (27) gives the value of the Weinberg angle $\theta_\mathrm{W} = \pi/6$, which is surprisingly close to the experimental value.

After fixing the unitary gauge, we obtain

$$S = \beta \sum_{\text{plaquettes}} \left(\left(1 - \frac{1}{2}\mathrm{Tr}U_p \cos\theta_p\right) \right. \quad (28)$$
$$\left. + \frac{1}{2}(1 - \cos 2\theta_p) + \gamma \sum_{xy} (1 - \mathrm{Re}(U_{xy}^{11} e^{-i\theta_{xy}}))\right).$$

Of course, we keep in mind that this simplification of the model may lead to some qualitative changes in the description of the dynamics. Thus, the conclusions that we draw after performing the numerical investigation of the simplified model must be justified by the study of the full model, including the color subgroup, dynamical fermions, and a finite Higgs mass.

Below, we briefly describe some of the quantities which we investigate in this work.

The following variables are considered as creating a photon, Z boson, and W boson, respectively:

$$A_{xy} = A_x^\mu = [\mathrm{Arg}U_{xy}^{11} + \theta_{xy}]\mathrm{mod}2\pi, \quad (29)$$
$$Z_{xy} = Z_x^\mu = [\mathrm{Arg}U_{xy}^{11} - \theta_{xy}]\mathrm{mod}2\pi,$$
$$W_{xy} = W_x^\mu = U_{xy}^{12} e^{i\theta_{xy}}.$$

Here, μ represents the direction (xy). After fixing the unitary gauge, the electromagnetic $U(1)$ symmetry remains:

$$U_{xy} \to g_x^\dagger U_{xy} g_y, \quad (30)$$
$$\theta_{xy} \to \theta_{xy} + \alpha_y/2 - \alpha_x/2,$$

where $g_x = \mathrm{diag}(e^{i\alpha_x/2}, e^{-i\alpha_x/2})$. The fields A, Z, and W transform as follows:

$$A_{xy} \to A_{xy} + \alpha_y - \alpha_x, \quad (31)$$
$$Z_{xy} \to Z_{xy},$$
$$W_{xy} \to W_{xy} e^{-i\alpha_x}.$$

As any other compact gauge theory, our model contains monopoles. As in other compact gauge models, their behavior is connected with the possible confinement of charges. On the other hand, the continuum Weinberg–Salam model is believed not to confine any charges and not to be affected by monopoles.

We investigated two types of monopoles. $U(1)$ monopoles extracted from 2θ are defined as

$$j_{2\theta} = \frac{1}{2\pi}{}^* d([d2\theta]\mathrm{mod}2\pi). \quad (32)$$

The electromagnetic monopoles are

$$j_A = \frac{1}{2\pi}{}^* d([dA]\mathrm{mod}2\pi). \quad (33)$$

(Here, we used the notation of differential forms on the lattice. For the definition of that notation, see, for example, [12].)

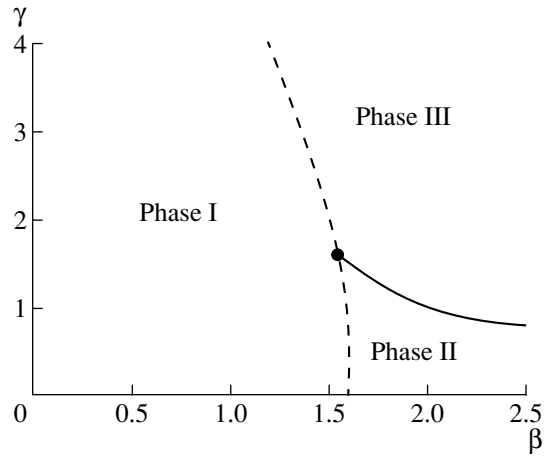

Fig. 1. The phase diagram of the model in the (β, γ) plane.

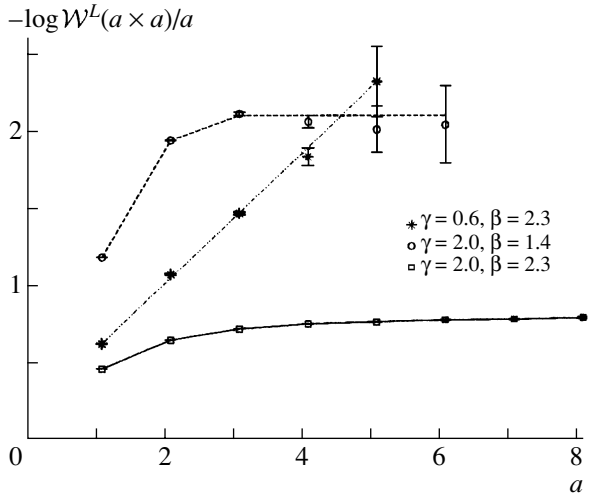

Fig. 2. $\mathcal{V}_L(a)$ calculated at three points that belong to different phases of the model.

The density of the monopoles is defined as follows:

$$\rho = \left\langle \frac{\sum_{\text{links}} |j_{\text{link}}|}{4L^4} \right\rangle, \qquad (34)$$

where L is the lattice size. To understand the dynamics of external charged particles, we consider the Wilson loops defined in the representations of left-handed and right-handed leptons:

$$\mathcal{W}^L(l) = \left\langle \text{ReTr} \prod_{(xy)\in l} U_{xy} e^{-i\theta_{xy}} \right\rangle, \qquad (35)$$

$$\mathcal{W}^R(l) = \left\langle \text{Re} \prod_{(xy)\in l} e^{-2i\theta_{xy}} \right\rangle.$$

Here, l denotes a closed contour on the lattice. We consider the following quantity constructed from the rectangular Wilson loop of size $a \times a$:

$$\mathcal{V}_{R,L}(a) = -\log \mathcal{W}^{R,L}(a \times a)/a. \qquad (36)$$

A linear behavior of $\mathcal{V}(a)$ would indicate the existence of a charge–anticharge string with nonzero tension.

3.3. Numerical Results

In our calculations, we investigated lattices L^4 for $L = 6$, $L = 12$, and $L = 16$ with symmetric boundary conditions.

We summarize our qualitative results in the phase diagram represented in Fig. 1. The model contains three phases. The first one (I) is a confinement-like phase, in which the dynamics of external charged particles is similar to that of QCD with dynamical fermions. In the second phase (II), only the behavior of left-handed particles is confinement-like, while for right-handed ones it is not. The last one (III) is the Higgs phase, in which no confining forces are observed at all. This is illustrated by Figs. 2 and 3, in which we represent $\mathcal{V}_L(a)$ and $\mathcal{V}_R(a)$ at three typical points that belong to different phases of the model. One can see that, in the Higgs phase, the shape of $\mathcal{V}(a)$ excludes the possibility of a linear potential to exist. The same behavior is found in phase II for $\mathcal{V}_R(a)$. On the other hand, in phase II, the shape of $\mathcal{V}_L(a)$ signals the appearance of a linear potential at sufficiently small distances (up to five lattice units). However, as for QCD with dynamical fermions or the $SU(2)$ fundamental Higgs model [13, 14], these results do not mean that confinement occurs. The charge–anticharge string must be torn by virtual charged scalar particles, which are present in the vacuum due to the Higgs field. Thus, $\mathcal{V}(a)$ may be linear only at sufficiently small distances, while starting from some distance it must not increase, indicating the breaking of the string. Unfortunately, the accuracy of our measurements does not allow us to observe this phenomenon in detail. However, it may be partially illustrated by the shapes of $\mathcal{V}_L(a)$ and $\mathcal{V}_R(a)$ in phase I shown in Fig. 2 and Fig. 3.

The phase structure of the model may also be seen through the data for the mean action over the whole lattice $\bar{S} = \langle S \rangle/(6\beta L^4)$ (Fig. 4). It appears to be inhomogeneous in a small vicinity of the phase transition line.

The connection between the properties of monopoles and the phase structure of the model is illustrated by Figs. 5 and 6, which show the monopole density versus the coupling constants. The electromagnetic monopole density drops in the Higgs phase, while the $U(1)$ monopole density falls sharply in both phase II and phase III. We can see that the behavior of the

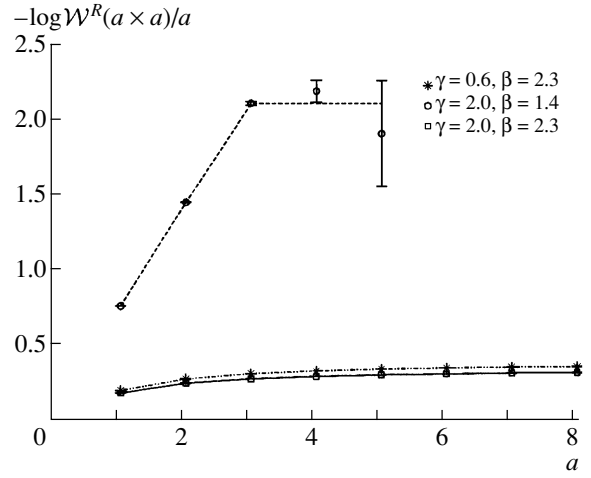

Fig. 3. $\mathcal{V}_R(a)$ calculated at three points that belong to different phases of the model.

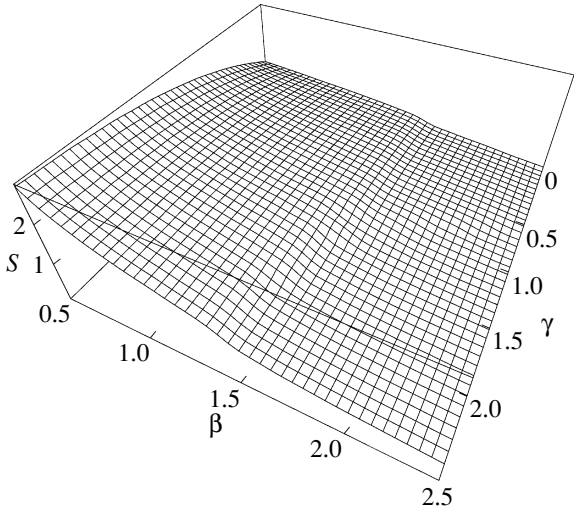

Fig. 4. The action $\bar{S} = \langle S \rangle / (6\beta L^4)$ of the model.

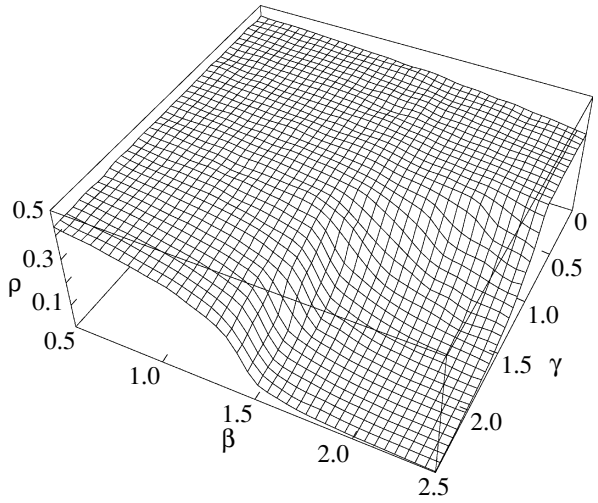

Fig. 5. The density of electromagnetic monopoles. It decreases in the Higgs phase.

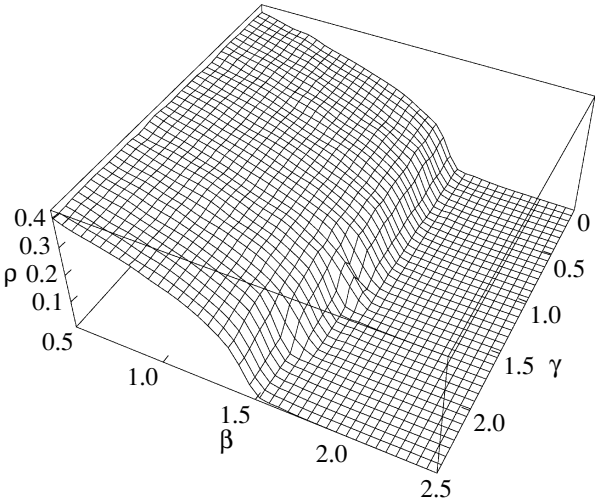

Fig. 6. The density of $U(1)$ monopoles. It decreases when the behavior of right-handed external particles is not confinement-like.

$U(1)$ monopoles is connected with the dynamics of the right-handed particles, while the behavior of electromagnetic monopoles reflects the dynamics of the left-handed particles.

It is worth mentioning that the cousin of our model, the $SU(2)$ fundamental Higgs model, has a similar phase structure as our model, except for the absence of the phase transition line between phases I and II. In the latter model, it was shown that different phases are actually not different. This means that the phase transition line ends at some point and the transition between two states of the model becomes continuous. Thus, one may expect that, in our model, the phase transition line between phases I and III ends at some point. However, we do not observe this for the considered values of couplings.

In our model, both phase transition lines join at a triple point, forming the common line. This is, evidently, the consequence of the aforementioned additional symmetry that relates $SU(2)$ and $U(1)$ excitations. The same picture, of course, does not emerge in the conventional $SU(2) \otimes U(1)$ gauge–Higgs model [15].

We must also note here that the phase diagram may also contain an unphysical region, corresponding to the unphysical region of the pure $SU(2)$ model (which is observed at $\beta < \beta_c$, where β_c is the crossover point). Our investigation shows that, if this region of couplings exists in our model, it must be far from the Higgs phase, which is of main interest

to us. Indeed, this unphysical region might appear for $\beta < 2.25$ and $\gamma < 0.5$.

4. CONCLUSIONS

We summarize our results as follows:

(i) We illustrated an additional symmetry found in the fermion and the Higgs sectors of the Standard Model by the consideration of the SM in loop space.

(ii) We performed a numerical investigation of the quenched electroweak sector of the lattice model, which respects the additional symmetry.

(iii) The lattice model contains three phases. The first one is a confinement-like phase. In the second phase, the confining forces are observed, at sufficiently small distances, only between the left-handed particles. The last one is the Higgs phase.

(iv) The main consequence of the emergence of the additional symmetry is that the phase transition lines corresponding to the $SU(2)$ and $U(1)$ degrees of freedom join at a triple point forming the common line. This reflects the fact that the $SU(2)$ and $U(1)$ excitations are related due to the aforementioned symmetry. The same situation does not take place in the conventional $SU(2) \otimes U(1)$ gauge–Higgs model [15].

Thus, even on this simplified level, we found a qualitative difference between the conventional discretization and the discretization that respects the invariance under Eq. (19).

ACKNOWLEDGMENTS

We are grateful to M.I. Polikarpov and F.V. Gubarev for useful discussions. A.I.V. and M.A.Z. kindly acknowledge the hospitality of the Department of Physics and Astronomy of the Vrije Universiteit, where part of this work was done. We also appreciate R. Shrock and I. Gogoladze, who have brought to our attention references [15] and [2], respectively.

This work was partly supported by the Russian Foundation for Basic Research (project nos. 03-02-16941, 04-02-16079, and 02-02-17308); by INTAS grant no. 00-00111, CRDF award RP1-2364-MO-02, DFG grant no. 436 RUS 113/739/0, and RFBR–DFG grant no. 03-02-04016; and by Federal Program of the Russian Ministry of Industry, Science, and Technology no. 40.052.1.1.1112.

REFERENCES

1. B. L. G. Bakker, A. I. Veselov, and M. A. Zubkov, Phys. Lett. B **583**, 379 (2004).
2. K. S. Babu, I. Gogoladze, and K. Wang, Phys. Lett. B **570**, 32 (2003); Nucl. Phys. B **660**, 322 (2003).
3. U. M. Heller, Nucl. Phys. B (Proc. Suppl.) **34**, 101 (1994); I. Montvay, hep-lat/9703001; I. Montvay, W. Langguth, and P. Weisz, Nucl. Phys. B **277**, 11 (1986); A. Hasenfratz and T. Neuhaus, Nucl. Phys. B **297**, 205 (1988); U. M. Heller, M. Klomfass, H. Neuberger, and P. Vranas, Nucl. Phys. B **405**, 555 (1993).
4. M. Lüscher and P. Weisz, Nucl. Phys. B **318**, 705 (1989); I. Montvay, Nucl. Phys. B **293**, 479 (1987); M. Klomfass, Nucl. Phys. B **412**, 621 (1994).
5. Y. M. Makeenko and A. A. Migdal, Nucl. Phys. B **188**, 269 (1981); A. A. Migdal, Phys. Rep. **102**, 199 (1983).
6. R. A. Brandt, F. Neri, and D. Zwanziger, Phys. Rev. D **19**, 1153 (1979).
7. M. A. Zubkov, Phys. Rev. D **68**, 054503 (2003).
8. B. L. G. Bakker, A. I. Veselov, and M. A. Zubkov, Phys. Lett. B **544**, 374 (2002); F. V. Gubarev and V. I. Zakharov, hep-lat/0211033.
9. M. A. Zubkov, Pis'ma Zh. Éksp. Teor. Fiz. **76**, 691 (2002) [JETP Lett. **76**, 591 (2002)].
10. P. de Forcrand and O. Jahn, Nucl. Phys. B **651**, 125 (2003).
11. N. B. Nielsen and M. Ninomiya, Nucl. Phys. B **185**, 20, 173 (1981); M. Lüscher, Phys. Lett. B **428**, 342 (1998); hep-th/0102028; H. Neuberger, Phys. Lett. B **417**, 141 (1998).
12. M. I. Polikarpov, U. J. Wiese, and M. A. Zubkov, Phys. Lett. B **309**, 133 (1993).
13. I. Montvay, Nucl. Phys. B **269**, 170 (1986).
14. M. Gurtler, E. M. Ilgenfritz, and A. Schiller, Phys. Rev. D **56**, 3888 (1997); B. Bunk, E. M. Ilgenfritz, J. Kripfganz, and A. Schiller, Nucl. Phys. B **403**, 453 (1993); M. N. Chernodub, F. V. Gubarev, E. M. Ilgenfritz, and A. Schiller, Phys. Lett. B **434**, 83 (1998); **443**, 244 (1998).
15. R. Shrock, Phys. Lett. B **162B**, 165 (1985); Nucl. Phys. B **267**, 301 (1986).

Physics of Atomic Nuclei, Vol. 68, No. 6, 2005, pp. 1016–1024. Translated from Yadernaya Fizika, Vol. 68, No. 6, 2005, pp. 1054–1063.
Original Russian Text Copyright © 2005 by Byakov, Kulikov, Perfil'ev, Stepanov.

PROCEEDINGS OF THE CONFERENCE "PHYSICS OF FUNDAMENTAL INTERACTIONS" DEDICATED TO THE 100th ANNIVERSARY OF A.I. ALIKHANOV'S BIRTH, SECTION OF NUCLEAR PHYSICS, DIVISION OF PHYSICAL SCIENCES, RUSSIAN ACADEMY OF SCIENCES; INSTITUTE OF THEORETICAL AND EXPERIMENTAL PHYSICS, MOSCOW, MARCH 1–5, 2004

Primary Chemical Reactions Induced by Radioactive Nuclear Transformations

V. M. Byakov*, L. A. Kulikov[1)], Yu. D. Perfil'ev[1)], and S. V. Stepanov**

Institute of Theoretical and Experimental Physics, Bol'shaya Cheremushkinskaya ul. 25, Moscow, 117259 Russia

Received February 4, 2004; in final form, June 4, 2004

Abstract—A series of chemical reactions is suggested to describe primary chemical transformations induced by Auger electrons from radioactive nuclear decay in glassy and crystalline frozen aqueous media. The mechanism is based on Mössbauer emission spectroscopy data supplemented by data on reactions in the tracks of fast positrons and electrons in an aqueous medium. It is shown that variation of temperature, the degree of crystallinity, the concentration of electron acceptors, etc., results in correlated changes in the yields of the final reaction products—Fe^{2+}, Fe^{3+} or Sn^{2+}, Sn^{4+} ions, positronium atoms, and molecular radiolytic hydrogen. These correlations indicate the similarity of chemical processes in the nanometer vicinity of decayed ^{57}Co and ^{119m}Sn nuclei and in the tracks of fast positrons and electrons. This similarity is caused by the same behavior of secondary intratrack electrons produced due to ionization losses of fast positrons, electrons, and Auger electrons. © *2005 Pleiades Publishing, Inc.*

INTRODUCTION

In this work, we use Mössbauer spectroscopy to study the mechanism of chemical reactions induced by radioactive nuclear transformations such as electron capture and conversion isomeric transition [1]. The general result of these transformations is the atomic emission of Auger electrons whose total energy is about several keV. Ionizing the medium in the vicinity of the radioactive nucleus, Auger electrons initiate radiolysis, i.e., any chemical or physicochemical transformation of the substance subjected to ionizing radiation. Knowledge of these reaction mechanisms is important not only for understanding of the physicochemical transformations occurring in media with radioactive isotopes, but also for a correct interpretation of Mössbauer spectroscopy results.

At the initial stage of radiolysis, chemical reactions occur in Auger-electron tracks. Spurs, blobs, and cylindrical ionization columns are generally picked out as structural elements of ionizing particle tracks in radiation chemistry [2, 3]. A nanometer aggregate of several ion–electron pairs (up to five or six) is called a spur. Spurs arise as a result of energy transfer from an ionizing particle to a molecular electron. This energy ranges from the ionizing potential to 100 eV. A blob is a large spur, a pearlike aggregate of 30–40 ion–electron pairs. A blob arises when energy from 100 to 500 eV is transferred to the molecular electron. Electrons with energy above ~10 keV form isolated (spaced far apart from each other) spurs and blobs. However, spurs begin to overlap, forming a cylindrical ionization column, when the fast-electron energy decreases to several keV. The final sections of the tracks of a fast electron and positron are cylindrical ionization columns with adjacent blobs.

The method of picosecond pulse radiolysis [2] is the most informative and popular method for studying the intratrack reactions. However, the information gained by this method mainly concerns the processes occurring in spurs. The point is that the energy fraction spent on blob formation by γ rays and fast electrons with energies ~1 MeV passing through the condensed medium is not large (about 15%). At the same time, a great number of closely located ion–electron pairs in a blob results in some differences of the intrablob processes from those in spurs. These peculiarities were mentioned previously in the studies of low-energy positron annihilation [3, 4].

The objective of this article is to discuss the potentialities of emission Mössbauer spectroscopy (EMS) together with radiation-chemistry data and positron annihilation spectroscopy for revealing the mechanism of radiation-chemical transformation in blobs. Though reactions in frozen aqueous solutions (77 K) are primarily considered, the results shed some light

[1)]Moscow State University, Vorob'evy gory, Moscow, 119899 Russia.

*e-mail: vsevolod.byakov@itep.ru

**e-mail: sergey.stepanov@itep.ru

on the processes occurring in ionizing particle tracks under normal conditions.

PRIMARY CHEMICAL REACTIONS INDUCED BY AUGER IONIZATION AND IN TRACKS OF FAST POSITRONS AND ELECTRONS: MODEL DESCRIPTION

In the emission version of Mössbauer spectroscopy, radioactive nuclei (e.g., ^{57}Co) are introduced into the medium under investigation in a negligibly low concentration. After E capture, they produce excited ^{57}Fe nuclei, which are sources of Mössbauer radiation. It is the measured spectrum of this radiation that provides information on the physicochemical state of the daughter atom [1, 5, 6].

The E capture results in an appearance of a vacancy in the inner electron shell of the produced Fe atom. The vacancy is rapidly occupied and moves to a higher energy level due to an electron transition from the outer shell. This process is accompanied by the emission of an x-ray photon or an Auger electron. In the latter case, two vacancies appear in the higher shells, and they are occupied by electrons from the outer shells. The probability of the Auger process increases with the shell number. On the one hand, this Auger cascade produces a $^{57}Fe^{n+}$ multiply charged ion with n up to 8 [7]. On the other hand, the emission of a considerable number of soft x-ray photons and Auger electrons with energies of hundreds of electronvolts gives rise to the ionization of a great number of molecules in the nearest ion environment. A cluster of many tens of or even several hundred ion–electron pairs appears around the $^{57}Fe^{n+}$ ion 10^{-14} s after the E-capture event. Such aggregate is called large blob in terms of radiation chemistry. We will call it an Auger blob.

Approximately 10^{-7} s after the production of the Fe nucleus, it emits a Mössbauer photon, which is detected by a detector. The emission time of a λ-wavelength photon can be estimated as $\lambda/c \approx 10^{-18}$ s. It is essential that the photon energy depends on the number of electrons that exist in the $^{57}Fe^{n+}$ shell at that time and thereby it provides information on the ion charge n at the moment of photon emission [1]. Since the electron affinity[2)] is much higher than the first ionization potential of the molecules of a medium (e.g., water), a decrease in the charge of the $^{57}Fe^{n+}$ ion (ion reduction) occurs first via stripping off the outer-shell electrons of the neighboring molecules and then via chemical reactions with Auger blob electrons [8]. By the instant of photon emission, the electron shell of the Fe ion has been mostly restored, and the ion appears to be in one of its chemically stable states, that is, either the Fe^{3+} or Fe^{2+} ion. The ratio between the Fe^{3+} and Fe^{2+} ions is determined by the behavior of Auger electrons and numerous secondary electrons produced in the Auger process, by their chemical reactions with the radiolysis products in an Auger blob, and by their interaction with the medium [8].

It is natural to suppose that the physicochemical transformations in the Auger blob must be similar to the processes both in the final blob of the positron track, which result in the production of the positronium atom (Ps), and in the blobs formed due to ionization losses of fast electrons e^{-**}.[3)]

Radiolytic hydrogen (H_2) is a product of intrablob reactions in the aqueous medium [2, 3]. The following chemical processes presumably proceed in the frozen aqueous medium near the ^{57}Co nucleus after its transformation into an iron nucleus.

(a) Ionization of water molecules by fast Auger electrons e^{-**}:

$$e^{-**} + H_2O \rightarrow e^{-*} + H_2O^+ + e^{-*}. \qquad (1)$$

(b) Thermalization of the above "hot" electrons e^{-*}:

$$e^{-*} + H_2O \rightarrow e^- + H_2O^*. \qquad (2)$$

(c) Capture of thermal electrons e^- into traps, which are created previously or formed by electrons themselves that restructure the medium:

$$e^- + \text{trap} \rightarrow e^-_{tr}. \qquad (3)$$

Electrons localized in the traps of the latter type are called solvated (e^-_s) or hydrated (e^-_{aq}) for the aqueous medium,[4)] in contrast to electrons (e^-_{tr}) captured in the traps of the former type.

(d) Chemical reactions

$$e^- + H_2O^{+\cdot} + H_2O \rightarrow \begin{cases} H_2 + 2\dot{O}H, \\ \dot{H} + \dot{O}H + H_2O, \\ H_2O^* + H_2O \rightarrow 2H_2O, \end{cases} \qquad (4)$$

[2)] The electron affinity is defined as the energy released in the process of electron coupling to an atom, a molecule, or an ion.

[3)] Traditionally, one or more asterisks used as a superscript of a chemical reagent symbol means that the reagent has considerable kinetic energy compared to the heat energy (for instance, e^*), or that it is in the electron-excited state (H_2O^*).

[4)] The first term originates from the English word *solvent*, while the second one from the Greek word *hydro* (water).

$$H_2O^{+\bullet} + H_2O \rightarrow H_3O^+ + \dot{O}H, \quad (5)$$

$$e^- + \dot{O}H \rightarrow OH^-, \quad (6)$$

$$H_3O^+ + OH^- \rightarrow 2H_2O, \quad (7)$$

$$e^- + H_3O^+ \rightarrow \dot{H} + H_2O, \quad (8)$$

$$e^- + S_i \rightarrow S_i^-, \quad (9)$$

$$H_2O^{+\bullet} + S_i \rightarrow \begin{cases} \dot{O}H + S_iH^+, \\ H_2O + S_i^{+\bullet}, \end{cases} \quad (10)$$

$$Fe^{3+} + e^- \rightarrow Fe^{2+}. \quad (11)$$

Here, e^- and e_{tr}^- are thermalized (quasifree or presolvated) and captured (solvated) electrons, respectively; S_i is the chemically active dissolved substance of the ith type. These reactions are written by analogy with the primary reactions proceeding in spurs, blobs, and cylindrical ionization columns of fast-electron tracks [3]. Only one reaction (11) is added, which yields the stable final product from the two stable products in the Mössbauer experiment. It is evident that the same processes must take place in the vicinity of the ^{119m}Sn nuclide after the conversion isomeric transition [9] forming an electron vacancy predominantly (62%) in the L shell of the tin atom.

The only possible way to determine the nature of chemical reactions induced by Auger electrons is probably measurement of the production probabilities of the stable products—$R(Fe^{3+})$ and $R(Fe^{2+}) = 1 - R(Fe^{3+})$—for various chemically active additives, various medium temperatures, and different aggregate states of the medium (crystalline, glassy), etc. According to the above discussion, we should expect similar effects of these factors on the production probabilities (yields) of Fe^{2+}, orthopositronium (o-Ps), and H_2. Indeed, primary chemical transformations that are induced in blobs and spurs by fast positrons and electrons are described by a series of reactions similar to those presented in [2, 3], except for reaction (11). Instead of the last reaction, the following reaction should be included in the final section of the positron track:

$$e^+ + e^- \rightarrow \begin{cases} o\text{-Ps}, \\ p\text{-Ps}. \end{cases} \quad (12)$$

This reaction involving a positron (e^+) yields two kinds of positronium atom—long-lived orthopositronium and short-lived parapositronium—produced in a 3 : 1 ratio, respectively [3, 4]. Orthopositronium is detected most often.

We were mainly interested in three-component systems as objects of Mössbauer emission experiments. These systems are composed of a solvent (water), a minor additive of some chemical compound (salt) containing radioactive nuclei (^{57}Co, ^{119m}Sn), and a specially incorporated substance capable of reacting with ions and radicals produced by Auger electrons in the vicinity of Mössbauer nuclei. Hereafter, indicating a certain substance introduced into the sample under investigation, we will not mention specially the presence of a radioactive additive in it, because it is self-evident.

As is seen from reactions (1)–(11), we suppose that the low-temperature reactions initiated by Auger electrons in a Mössbauer blob involve a quasifree electron e^- rather than a solvated (captured) electron as was assumed by Bondarevskii and Ablesimov [10]. This supposition is based on the fact that the electron solvation times in glassy ethanol and n-propanol at 77–130 K are much longer than the mean lifetimes of the ^{57}Fe (10^{-7} s) and ^{119}Sn (10^{-8} s) Mössbauer nuclei [11, 12].

QUANTITATIVE RESULTS FOLLOWING FROM THE MODEL

A number of quantitative results follow from the above reactions. These results primarily concern the effect of the electron acceptors S_i distributed in the medium on the production yields of positronium, radiolytic hydrogen, hydrated electron (e_{aq}^-), and electron captured by the frozen aqueous medium (e_{tr}^-). If the concentration c_S of the dissolved acceptor is not too low, the inhibition of these yields—$I_{o\text{-Ps}}$, G_{H_2}, $R(Fe^{2+})$, and $G(e_{aq}^-)$—can be approximated by the expressions [3, 13–15]

$$I_{o\text{-Ps}} = I_{o\text{-Ps}}^0/(1 + pc_S), \quad (13)$$

$$G_{H_2} = G_{H_2}^0/(1 + hc_S), \quad (14)$$

$$R(Fe^{2+}) = R^0(Fe^{2+})\exp(-fc_S), \quad (15)$$

$$G(e_{aq}^-) = G^0(e_{aq}^-)\exp(-qc_S). \quad (16)$$

Here, p, h, f, and q are the inhibition factors for the yields of o-Ps, H_2, Fe^{2+}, and $e_{aq}^-(e_{tr}^-)$. They characterize the capability of the substance S_i to interact with nonionizing quasifree electrons e^-, which have yet to be hydrated, that is, appear in a localized state because of either aqueous–medium polarization or capture in the preexisting traps. We treat these electrons as predecessors of o-Ps, H_2, Fe^{2+}, and

$e^-_{aq}(e^-_{tr})$. The quantities with the superscript "0" are extrapolated to zero concentration c_S. Each inhibition factor is proportional to $k(e^- + S_i)$, which is the rate constant of quasifree-electron capture by the substance S_i:

$$p \propto h \propto f \propto q \propto k(e^- + S_i). \qquad (17)$$

They can serve as a measure of the electron reactivity of the substance S_i. If the above assumptions are correct, then, for example, the f_1/f_2 ratio of the experimental inhibition factors for Fe^{2+} yields by electron acceptors S_1 and S_2 determined experimentally must be close to similar ratios p_1/p_2, h_1/h_2, and q_1/q_2. Below, we demonstrate that temperature variation similarly affects the yields of H_2, o-Ps, Fe^{2+}, and $e^-_{aq}(e^-_{tr})$. Our further aim is to provide experimental data in support of these results following from this model. Unfortunately, it is impossible to carry out this comparison under identical conditions at present, because radiation chemical and positronium data that have been obtained in frozen solutions and can be directly compared with the Fe^{2+} yields in the Auger blob are very scarce. Nevertheless, even a correlation between the yields that are obtained under nonidentical conditions indicates the similarity of the intratrack chemical processes under discussion.

COMPARISON WITH EXPERIMENTS

1. Let us start with considering the Fe^{2+} yields obtained in [14] for the frozen aqueous solutions of salt ($NaClO_4$) and acids (H_2SO_4, $HClO_4$, and HNO_3) at 77 K (Fig. 1). At room temperature, these substances dissociate within the concentration range of interest: $NaClO_4 \rightarrow Na^+ + ClO_4^-$, $H_2SO_4 + H_2O \leftrightarrow H_3O^+ + HSO_4^-$, $HClO_4 + H_2O \rightarrow H_3O^+ + HClO_4^-$, and $HNO_3 + H_2O \rightarrow H_3O^+ + NO_3^-$. In the solutions frozen at 77 K, dissociation also likely proceeds with hydrogen ions H^+ appearing in hydroxonium ions H_3O^+ [17]. Then, using the data presented in Fig. 1 and the relation similar to (15)

$$R(Fe^{2+}) = \exp\left(-\sum_i f_i c_{S_i}\right)$$

with $R^0(Fe^{2+}) = 1$, we can determine the f_i inhibition factors for the Fe^{2+} production yields by various ions existing in the medium. The ratios of these values appeared to be the following:

$$f(H_3O^+) : f(ClO_4^-) : f(NO_3^-) \approx 0.04 : 0.05 : 0.1. \qquad (18)$$

The accuracy of these values and other inhibition factors presented below is about 10%.

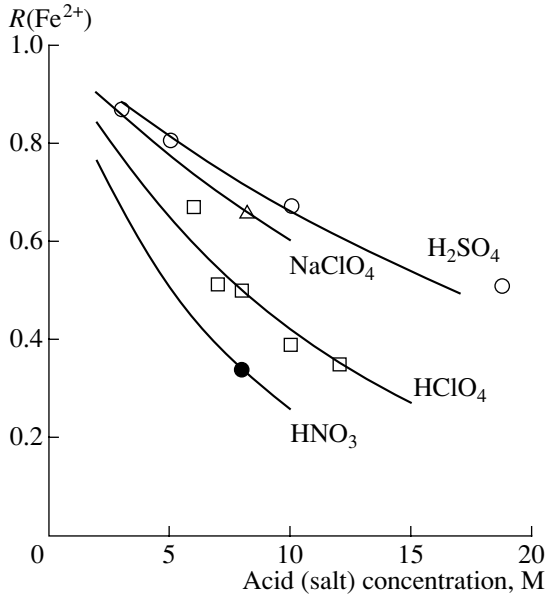

Fig. 1. Fe^{2+} yields in the frozen aqueous solutions of (○) sulfuric, (□) perchloric, and (●) nitric acids and (△) in the frozen solution of $NaClO_4$ at 77 K [16]. The curves are the approximations of these dependences by the formula similar to (15): $R(Fe^{2+}) = \exp(-\sum_i f_i c_{S_i})$ with $R^0(Fe^{2+}) = 1$, where $f_i = 0.005$, 0.04, 0.05, and 0.1 M^{-1} for HSO_4^-, H_3O^+, ClO_4^-, and NO_3^-, respectively. The f_i coefficient for the Na^+ ion is set to zero. Hereafter, the concentration M is presented in terms of the number of solute moles per liter of solution.

It is natural to compare ratios (18) with the ratios of the coefficients q_i characterizing the reactivity of the same ions with respect to the quasifree electron at room temperature [15]:

$$q(H_3O^+) : q(ClO_4^-) : q(NO_3^-) \approx (\leq 0.1) : (\leq 0.1) : 2.4. \qquad (19)$$

The latter ratios were determined by the method of picosecond pulse radiolysis with the use of relation (16).

In positron spectroscopy, the inhibition factor p_i for Ps production from relation (13) is used as a measure of the reactivity of the acceptor S_i of the quasifree electrons [3, 13]. Experiments at room temperature in the solutions of different acids yield [18]

$$p(H_3O^+) : p(ClO_4^-) : p(NO_3^-) \approx (\leq 0.1) : 0.1 : 3.1. \qquad (20)$$

As is seen, pulse radiolysis and positron spectroscopy yield close values of q and p. A monotonic increase in the f values when passing from H_3O^+ to NO_3^- is in agreement with a similar increase in the q and p values. The closeness of q and p in the liquid medium at room temperature and their slight difference from the f values obtained by means of EMS in the frozen media are quite natural. It is important that ratios

(18)–(20) differ considerably from the ratio of the rate constants $k(e^-_{aq} + S_i)$ of the corresponding reactions between S_i and the solvated electron [15]:

$$k(e^-_{aq} + H_2O^+) : k(e^-_{aq} + ClO^-_4) : k(e^-_{aq} + NO^-_3) = 1 : 0.1 : 1. \quad (21)$$

Thus, the suggestion made in [10] that solvated electrons are involved in the chemical reactions in an Auger blob contradicts the experimental data. Moreover, it is inconsistent with the above-mentioned considerable solvation times of quasifree electrons at low temperatures. Only glassy methanol could be an exception, because its solvation time is about 10 ns [11], which is an order of magnitude lower than the time of Mössbauer photon emission.

2. Let us compare the effect of electron acceptors Cu^{2+} and Cr^{2+} on the yield $R(Sn^{2+})$ of double-charged tin in the frozen aqueous solutions of salts $CrCl_2$ and $CuCl_2$ at 77 K to their effect on the yield G_{H_2} of radiolytic hydrogen in these solutions gamma-irradiated at room temperature. Figure 2 (left panel) illustrates the same efficiency of G_{H_2} inhibition by the Cr^{2+} and Cu^{2+} ions due to their capture of quasifree electrons, which are the main predecessors of radiolytic hydrogen [3, 13]. The right panel in Fig. 2 demonstrates a similar effect of these ions on the Sn^{2+} yield. This fact is in favor of the above supposition that the electrons responsible for H_2 and Sn^{2+} production via reactions (4) and (11) in the Compton-electron track and Auger blob, respectively, are of the same origin in spite of a considerable difference in temperature and in the aggregate state of the solvent.

3. The presence of molecular iodine I_2 provides an atypical effect on the Fe^{2+} yield in glassy ethanol frozen at 77 K (Fig. 3). An increase in the I_2 concentration from zero to 0.43 M leads to a more than twofold increase in the Fe^{2+} yield, that is, from 0.28 to 0.72. When the iodine concentration increases further, the Fe^{2+} yield decreases slightly to 0.53 at an iodine concentration of 1.5 M (Fig. 3, left panel). Mil'grom *et al.* [19] supposed that an increase in the Fe^{2+} yield with increasing the I_2 content up to 0.43 M occurred because electron structural traps disappeared in the glass under the effect of iodine molecules.

Here, we present a different explanation based on the following peculiarities of the I_2-involving reactions. The reaction of I_2 with a quasifree electron is a dissociative capture of e^-, which proceeds with the formation of an excited anion radical I^{-*}_2 in the intermediate state [21]:

$$e^- + I_2 \leftrightarrow I^{-*}_2 \rightarrow I^-_2 \rightarrow I + I^-. \quad (22)$$

In spite of a high electron affinity of I_2 (2.6 eV) [22], the electron binding energy in excited I_2 is most likely low [21]. The transition into the ground state, as well as subsequent dissociation, is hindered in the solid phase because of the lack of available volume. Under these conditions, electron migration along I_2 molecules is possible if their concentration is sufficient:

$$I^{-*}_2 + I_2 \rightarrow I_2 + I^{-*}_2. \quad (23)$$

In this case, the electron will drift towards Fe^{3+} under the action of the Coulomb field. As a consequence, the Fe^{2+} yield must increase with the I_2 concentration, and this is the case up to its concentration of 0.5 M.

In addition to increasing the fraction of captured quasifree electrons, a further increase in the I_2 concentration results in the replacement of alcohol cation radicals $C_2H_5OH^{+\bullet}$ with cation radicals $I^{+\bullet}_2$. This process is due both to the direct action of Auger electrons, $e^{-**} + I_2 = I^{+\cdot}_2 + 2e^{-*}$, and to indirect ionization, $C_2H_5OH^{+\bullet} + I_2 = C_2H_5OH + I^{+\bullet}_2$, which is possible because the ionization potential of iodine molecules (9.4 eV) is lower than that of ethanol molecules (10.5 eV) [22]. The dissociation of cation radicals via $I^{+\bullet}_2 \rightarrow I + I^{+\bullet}$ is also hardly possible because of the lack of available volume at 77 K. Therefore, their interaction with electrons and anions ($I^{+\bullet}_2 + e^- = I_2$, $I^{+\bullet}_2 + I^-_2 = 2I_2$) is longer and thus more efficient than that for short-lived ethanol cation radicals. It is this effect that causes a decrease in $R(Fe^{2+})$. It should be borne in mind that the fast ion–molecular reaction $C_2H_5OH^{+\bullet} + C_2H_5OH = C_2H_5OH^+_2 + C_2H_5O^\bullet$ results in products that are much less reactive than $C_2H_5OH^{+\bullet}$. This reaction is not limited by the lack of available volume at 77 K, because the proton leaving the C_2H_5OH molecule simply binds to an unshared orbital of a neighboring molecule.

The addition of I_2 similarly affects the probability of *o*-Ps production in liquid cyclohexane [20] (Fig. 3, right panel). In this case, the *o*-Ps yield also first increases (although not so markedly as the Fe^{2+} yield in frozen ethanol) and then decreases. Such an unpronounced increase in the Ps yield is apparently caused by the absence of obstacles for fast reaction (22) of the dissociative electron capture in the liquid phase.

4. Now, let us consider the correlation of changes in the yields of Fe^{2+}, radiolytic hydrogen, and positronium with the medium temperature (Fig. 4). We begin with the cause for the difference between the Fe^{2+} yields in the solutions of sulfuric and perchloric acids, which is especially noticeable at low temperatures. This difference arises because electron capture by

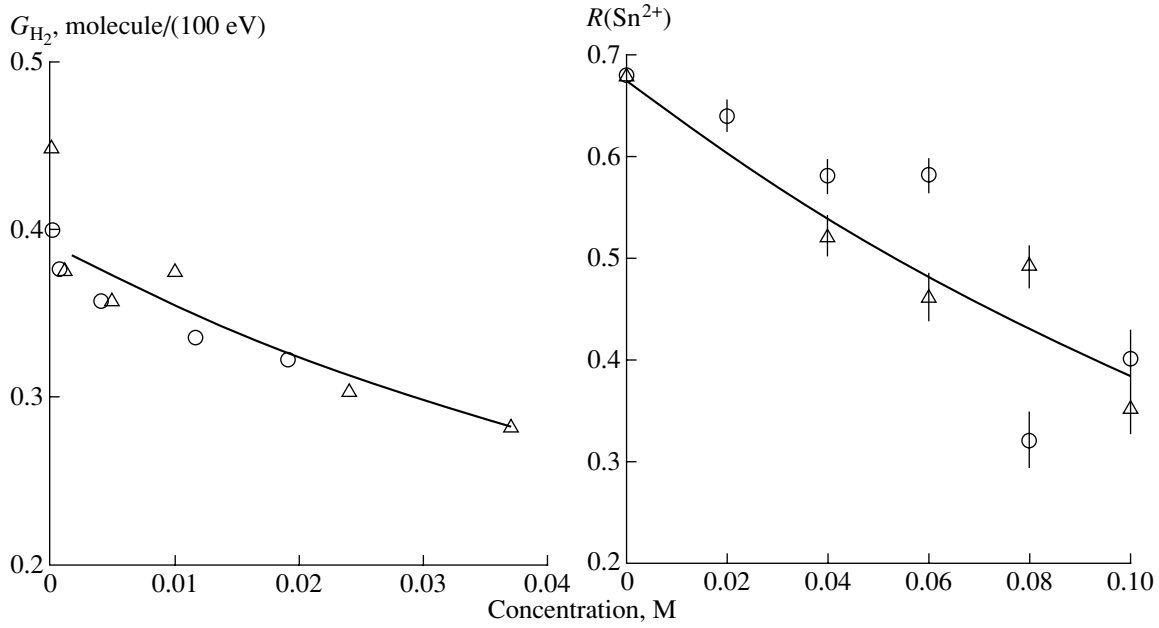

Fig. 2. (Left panel) Radiolytic hydrogen yield vs. the (○) Cu^{2+} and (△) Cr^{2+} ion concentration in aqueous solutions at room temperature [18]. The curve is the approximation by Eq. (14). (Right panel) The concentration of the (△) $CrCl_2$ and (○) $CuCl_2$ salts in ethanol frozen at 77 K on the reverse yield of Sn^{2+} [9]. The curve is the approximation by Eq. (16).

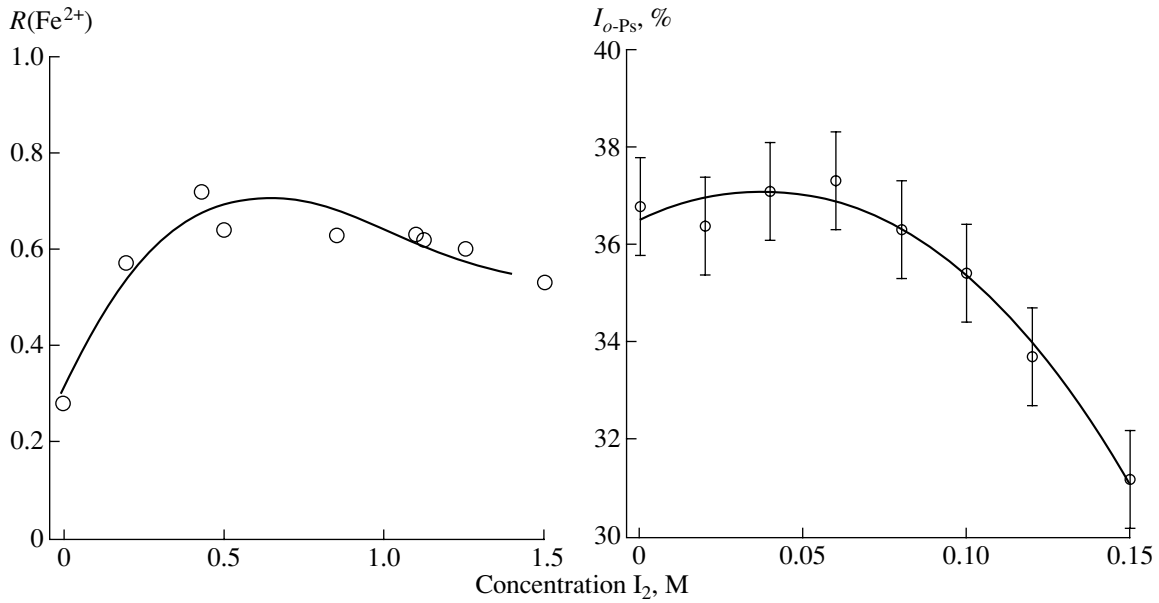

Fig. 3. (Left panel) Fe^{2+} yield in ethanol frozen at 77 K vs. the concentration of molecular iodine [19]. (Right panel) The *o*-Ps yield in liquid cyclohexane at room temperature vs. the concentration of molecular iodine [20].

the products of the dissociation of perchloric acid molecules is more efficient (Fig. 1) and the efficiency of this capture increases when temperature decreases. This difference persists at room temperature as well. Figure 5 shows the yields of radiolytic hydrogen and *o*-Ps in the solutions of sulfuric and perchloric acids. Both yields in the $HClO_4$ solutions are noticeably lower than the respective yields in the H_2SO_4 solutions.

We propose an explanation of the similarity of the $R(Fe^{2+})$ temperature dependences in the glassy solid solutions of sulfuric and perchloric acids (Fig. 4) to analogous dependences of $I_{o\text{-Ps}}$ and G_{H_2} in liquid water. This explanation is based on the fact that the tem-

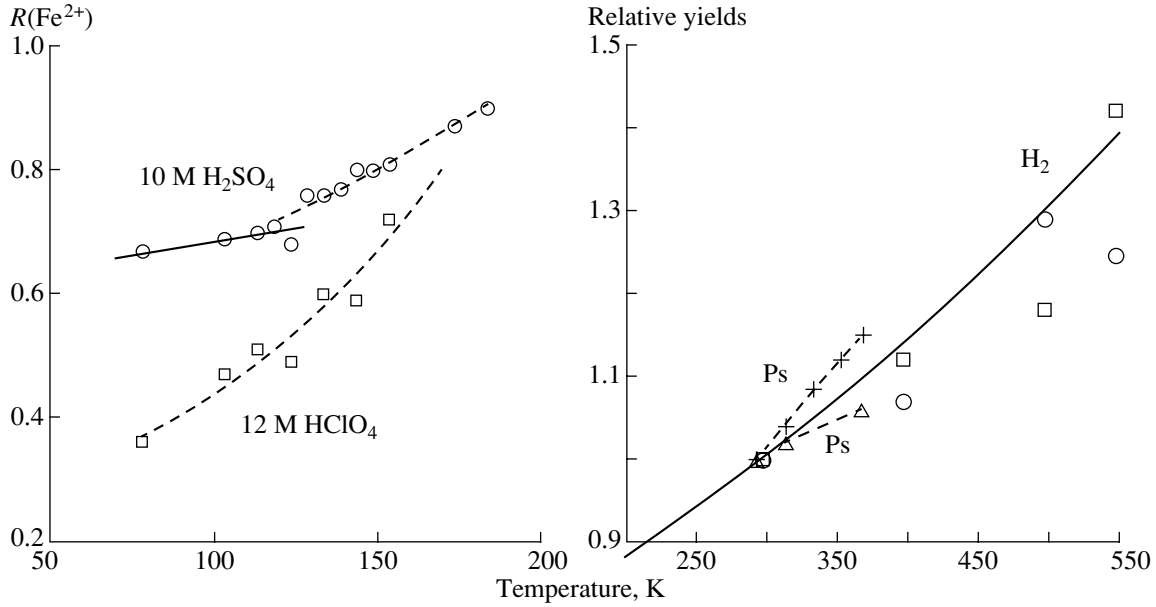

Fig. 4. (left panel) Temperature dependences of the Fe^{2+} yields in frozen glassy solutions of sulfuric (10 M H_2SO_4, ○) and perchloric (12 M $HClO_4$, □) acids [23]. The solid curve is the approximation $0.67\exp[(T-77)/770]$ (see text). The dashed curves show the tendency of data variation. (Right panel) The temperature dependence of the relative yields of (+, △) positronium and (○, □) radiolytic hydrogen production in water [24]. The solid curve is the approximation $\exp[(T-295)/770]$ (see text).

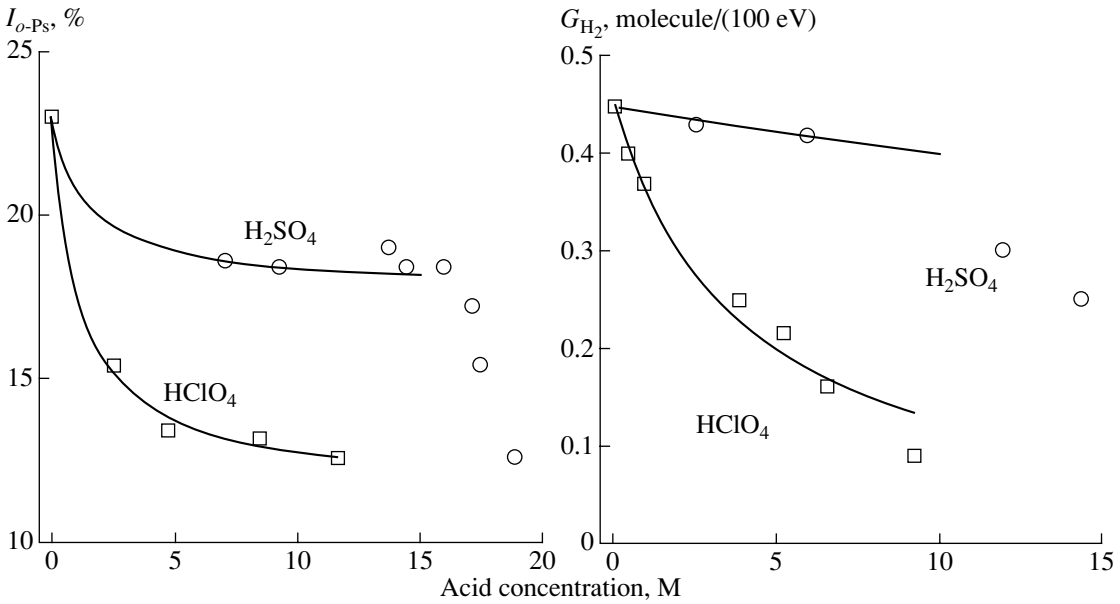

Fig. 5. (Left panel) *o*-Ps yields in the concentrated solutions of (○) sulfuric and (□) perchloric acids [25]. (Right panel) The H_2 yields in the concentrated solutions of (○ [26]) sulfuric and (□ [27]) perchloric acids.

perature coefficients $\left(\frac{1}{G_{H_2}}\frac{dG_{H_2}}{dT}\right.$ and $\left.\frac{1}{I_{o\text{-Ps}}}\frac{dI_{o\text{-Ps}}}{dT}\right)$ of the relative yields of radiolytic hydrogen and *o*-Ps in liquid water under pressure in a temperature range of 300–500 K are close to the temperature coefficient $\frac{1}{R(Fe^{2+})}\frac{dR(Fe^{2+})}{dT}$ in the 10 M frozen H_2SO_4 solution, especially in a temperature range of 78–130 K. All three coefficients are about $1/770\ K^{-1}$. This closeness indicates that the quasifree electron is

a common predecessor of all the products—H_2, Fe^{2+}, and Ps—of reactions (4), (11), and (12).

The temperature coefficient in the 12 M frozen $HClO_4$ solution is higher than that in sulfuric acid, and $R(Fe^{2+})$ in this solution is lower than the value in sulfuric acid, because quasifree electrons are involved in the reaction with the ClO_4^- anion, which is the product of perchloric acid dissociation.

If, following [24], we assume that the G_{H_2} and $I_{o\text{-Ps}}$ yields increase with temperature due to an increase in the initial yield of the ion–electron pairs in medium ionization, then the $e^-_{aq}(e^-_{tr})$ yield must have the same temperature dependence:

$$G \propto \exp[T/770(\mathrm{K})]. \qquad (24)$$

To verify relation (24), we estimate the e^-_{tr} yield for the case of low-temperature radiolysis using this relation. Assuming $G^0(e^-_{aq}) = 4.8$ electron/(100 eV) at $T = 300$ K [2], we obtain a $G^0(e^-_{tr})$ value close to 3.5 electron/(100 eV) at $T = 77$ K.

To test the applicability of this estimate to low-temperature glasses, we consider the data from [17] where the gamma radiolysis of glassy acidic solutions frozen at 77 K was studied. Hydroxonium ions arising in acid dissociation (see Subsection **1**) recapture thermalized electrons e^- formed via radiolysis and thus produce H atoms stable at liquid nitrogen temperature:

$$e^- + H_3O^+ \rightarrow \dot{H} + H_2O. \qquad (25)$$

As a result, the yield of electrons captured by the medium (e^-_{tr}), which are analogs of hydrated electrons (e^-_{aq}), decreases, and the yield of hydrogen atoms must increase.

In the aqueous solutions of perchloric acid that are exposed to a picosecond pulse of ionizing radiation, the $G(e^-_{aq})$ yield decreases with increasing concentration c_S of the acid in accordance with Eq. (16), in which the coefficient $q \leq 0.1$ M^{-1} [15] at room temperature. It means that the yield of H atoms produced in reaction (25) must increase accordingly. The mentioned yield should be supplemented by the yield G_H of H atoms in intratrack reaction (4). Taking into account that the contribution of intratrack reaction (6) is small [28], we obtain the relation

$$G(\mathrm{H}) = G_H + G^0(e^-_{tr}) - G(e^-_{tr}) \qquad (26)$$
$$= G_H + G^0(e^-_{tr})[1 - \exp(-qc_S)].$$

Here, $G^0(e^-_{tr})$ is the initial yield of captured electrons prior to their participation in the chemical reactions. This yield coincides with the yield of ion–electron pairs, which has been estimated at $G^0(e^-_{tr}) = 3.5$ electron/(100 eV).

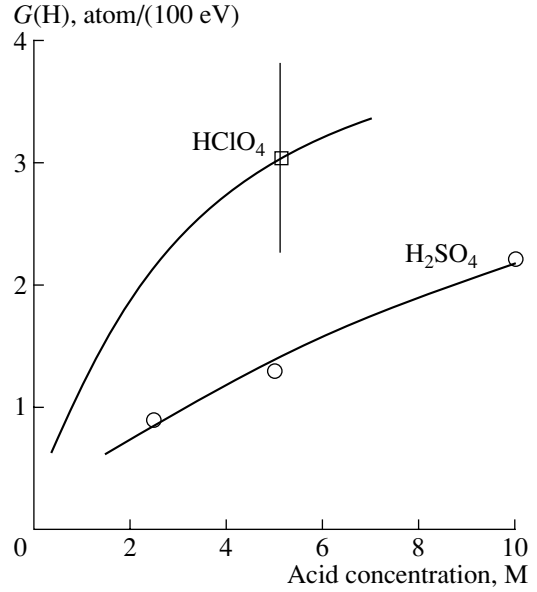

Fig. 6. Radiation-chemical yields $G(H)$ of atomic hydrogen in the frozen solutions of (○) sulfuric and (□) perchloric acids at 77 K [17]. The curves are the approximations by Eq. (26), which has the form $G(H) = 0.23 + 3.5[1 - \exp(-0.08c_S)]$ for the H_2SO_4 solution and $G(H) = 0.23 + 3.5[1 - \exp(-0.3c_S)]$ for the $HClO_4$ solution.

Figure 6 shows the yields of stabilized hydrogen atoms for various concentrations of sulfuric and perchloric acids. The curves in the figure are approximations of the yields by Eq. (26). The presented description of the experimental data was obtained with the following parameters: $G_H \approx 0.23$ atom/(100 eV), $q = q(H_3O^+) + q(HSO_4^-) \approx 0.08$ M^{-1} for H_2SO_4 and $q = q(H_3O^+) + q(ClO_4^-) \approx 0.3 \pm 0.1$ M^{-1} for $HClO_4$. The coefficients q, which characterize the reactivity of quasifree electrons under the conditions of low-temperature radiolysis, are in semiquantitative agreement with the inhibition factors f for the Fe^{2+} yield in Auger blobs that were obtained earlier in the same media (Fig. 1) and that have the same sense as the q coefficients: $f = f(H_3O^+) + f(HSO_4^-) \approx 0.04$ M^{-1} for H_2SO_4 and $f = f(H_3O^+) + f(HClO_4^-) \approx 0.09$ M^{-1} for $HClO_4$. The difference between the ratios $q/f \approx 2$ for H_2SO_4 and $q/f \approx (0.3 \pm 0.1)/0.09 \approx 3 \pm 1$ for $HClO_4$ cannot be treated as significant, because there is only one experimental point for perchloric acid (Fig. 6).

We should note that the intratrack yields of $G^0(e^-_{tr}) = 3.5$ electron/(100 eV) and $G_H \approx 0.23$ atom/(100 eV) also do not contradict the radiation-chemistry data [2]. All these facts indicate that the radiation-chemical reactions proceeding in the nanometer vicinity of the ^{57}Co nucleus after it

captures an electron involve electrons of the same kind as those involved in gamma radiolysis of low-temperature solutions.

CONCLUSIONS

The same type of inhibition of the Fe^{2+}, Sn^{2+}, H_2, *o*-Ps, and e_s^- yields by dissolved substances, as well as the close values of their temperature coefficients obtained by the methods of EMS, positronium spectroscopy, and pulse radiolysis, supports our statements concerning the similarity of the primary processes in all track structures—spurs, blobs, and ionization columns. Differences in their shapes and dimensions in tracks of different ionizing particles slightly affect the ratios of the inhibition factors. The values of these factors indicate that quasifree electrons are involved in the intratrack reactions prior to their capture by the polar medium.

ACKNOWLEDGMENTS

This work was supported by the Russian Foundation for Basic Research (project nos. 01-03-32407 and 01-03-32786) and by the Council of the President of the Russian Federation for Support of Young Russian Scientists and Leading Scientific Schools (project no. NSh-1907.2003.2).

REFERENCES

1. *Mössbauer Spectroscopy of Frozen Solutions*, Ed. by A. Vértes and D. L. Nady (Akadémiai Kiadó, Budapest, 1990; Mir, Moscow, 1998).
2. A. K. Pikaev, *Modern Radiation Chemistry. Basic Principles. Experimental Technique and Methods* (Nauka, Moscow, 1985) [in Russian].
3. V. M. Byakov and F. G. Nichiporov, *Intratrack Chemical Processes* (Énergoatomizdat, Moscow, 1985) [in Russian].
4. *Principles and Applications of Positron and Positronium Chemistry*, Ed. by Y. C. Jean, P. E. Mallone, and D. M. Schrader (World Sci., Singapore, 2003).
5. J. M. Friedt and J. Danon, At. Energy Rev. **184**, 893 (1980).
6. Yu. D. Perfil'ev, Izv. Ross. Akad. Nauk, Ser. Fiz. **63**, 1383 (1999).
7. H. Pollak, Phys. Status Solidi **2**, 720 (1961).
8. L. A. Kulikov, L. T. Bugaenko, Yu. D. Perfil'ev, and A. M. Babeshkin, Vestn. Mosk. Univ., Ser. 2: Khim., No. 3, 347 (1972).
9. Yu. D. Perfil'ev, L. A. Kulikov, V. M. Byakov, *et al.*, Khim. Vys. Energ. **37**, 390 (2003) [High Energy Chem. **37**, 345 (2003)].
10. S. I. Bondarevskiĭ and N. E. Ablesimov, Khim. Vys. Energ. **11**, 285 (1977) [High Energy Chem. **11**, 239 (1977)].
11. A. Namiki, M. Noda, and T. Higashimura, J. Phys. Chem. **79**, 2975 (1975).
12. J. H. Baxendale and P. Wardman, J. Chem. Soc., Faraday Trans. 1 **3**, 584 (1973).
13. V. M. Byakov, J. Phys. IV, Colloq. C4, Suppl. II **3**, 85 (1993).
14. Yu. D. Perfiliev, L. A. Kulikov, L. T. Bugaenko, *et al.*, J. Inorg. Nucl. Chem. **36**, 2115 (1976).
15. K. Y. Lam and J. W. Hunt, Int. J. Radiat. Phys. Chem. **7**, 317 (1975).
16. V. M. Byakov, V. I. Grafutin, O. V. Koldaeva, *et al.*, Preprint ITÉF-37 (Institute of Theoretical and Experimental Physics, Moscow, 1984).
17. G. P. Chernova, B. G. Ershov, and A. K. Pikaev, Izv. Akad. Nauk SSSR, Ser. Khim., No. 1, 43 (1970).
18. M. Faraggi, Int. J. Radiat. Phys. Chem. **5**, 197 (1973).
19. Ya. M. Mil'grom, Yu. D. Perfil'ev, and A. M. Babeshkin, Khim. Vys. Energ. **12**, 272 (1978).
20. B. Levay and P. Hautojarvi, J. Phys. Chem. **76**, 1951 (1972).
21. E. Hart and M. Anbar, *The Hydrated Electron* (Wiley, New York, 1970; Atomizdat, Moscow, 1973).
22. *CRC Handbook of Chemistry and Physics*, 78th ed., Ed. by D. R. Lide (CRC Press, Boca Raton; New York, 1998).
23. Yu. D. Perfil'ev, L. A. Kulikov, and A. M. Babeshkin, Zh. Fiz. Khim. **52**, 1631 (1978) [Russ. J. Phys. Chem. **82**, 1045 (1978)].
24. V. M. Byakov and S. V. Stepanov, Nukleonika **42**, 45 (1997).
25. S. J. Tao and J. H. Green, J. Phys. Chem. **73**, 882 (1969).
26. J. W. Boyle, Radiat. Res. **17**, 427 (1962).
27. D. Katakis and A. O. Allen, J. Phys. Chem. **68**, 3107 (1964).
28. M. Domae, Y. Katsumura, K. Ishigure, and V. M. Byakov, Radiat. Phys. Chem. **48**, 487 (1996).

Translated by E. Kozlovsky

Physics of Atomic Nuclei, Vol. 68, No. 6, 2005, pp. 1025–1033. Translated from Yadernaya Fizika, Vol. 68, No. 6, 2005, pp. 1064–1073.
Original Russian Text Copyright © 2005 by Kotov, Afonin, Baranov, Biryukov, Ivanov, Kardash, Maisheev, Terekhov, Troyanov, Fedotov, Chepegin, Chesnokov.

PROCEEDINGS OF THE CONFERENCE "PHYSICS OF FUNDAMENTAL INTERACTIONS" DEDICATED TO THE 100th ANNIVERSARY OF A.I. ALIKHANOV'S BIRTH, SECTION OF NUCLEAR PHYSICS, DIVISION OF PHYSICAL SCIENCES, RUSSIAN ACADEMY OF SCIENCES; INSTITUTE OF THEORETICAL AND EXPERIMENTAL PHYSICS, MOSCOW, MARCH 1–5, 2004

Use of Oriented Crystals at High-Energy Accelerators

V. I. Kotov, A. G. Afonin, V. T. Baranov, V. M. Biryukov, Yu. M. Ivanov, A. A. Kardash, V. A. Maisheev, V. I. Terekhov, E. F. Troyanov, Yu. S. Fedotov, V. N. Chepegin, and Yu. A. Chesnokov

Institute for High Energy Physics, Protvino, Moscow oblast, 142284 Russia

Received May 24, 2004; in final form, September 13, 2004

Abstract—The application of bent crystals for extracting accelerated beams from high-energy accelerators is reviewed. The results of realizing highly efficient extraction of protons from the IHEP accelerator are presented. Proposals on using oriented crystals for designing efficient positron sources at linear colliders and on developing new undulators are discussed. © *2005 Pleiades Publishing, Inc.*

1. INTRODUCTION

It seems very inviting to use oriented crystals with strong intracrystalline electric fields ($\geq 10^9$ V/cm) to control charged-particle beams. Atoms in crystals are concentrated in their crystallographic planes and along axes. The fields of atomic planes and axes form potential wells in the interplanar space and near the axes. The motion of charged particles in these wells becomes steady, and they can penetrate very deeply into the crystal (the so-called channeling effect). The motion of particles in oriented crystals is considered in detail, for example, in [1–4].

To realize the channeling mode for positively charged particles, crystals oriented along crystallographic planes are used. At the output of such a crystal, channeled and scattered particles (not involved in channeling) move in the same direction. For their spatial separation and controlling the channeled beam, Tsyganov [5] proposed in 1976 to use a bent crystal and theoretically showed that channeled particles passing the entire crystal deviate at a bend angle if crystal bend radii are larger than the critical value.

For the first time, this idea was corroborated in the experiment performed in 1979 by the joint JINR–FNAL group on the 8.4-GeV proton beam extracted from the JINR (HEL) synchrophasotron [6]. In these measurements, a silicon crystal that was oriented along the (111) direction, had a length of 20 mm, and was bent by an angle of 25.7 mrad was used. About 1% of particles falling on the end face of the crystal were deviated at this angle. In the subsequent experiments executed at CERN on a nearly parallel 450-GeV proton beam, a record efficiency of the deviation of beams (~50%) for crystal-bend angles ~2 mrad [7] was achieved using (110) bent silicon crystals.

The emerging possibility of controlling particle beams using bent crystals became a stimulus for the development and investigation of various applications of such crystals at high-energy accelerators [2, 3]. The most advanced works concern the efficient extraction of particle beams from cyclic high-energy accelerators using bent crystals.

2. EXTRACTION OF PROTON BEAMS FROM HIGH-ENERGY ACCELERATORS USING BENT SILICON CRYSTALS

In 1977, Koshkarev [8] proposed to use a bent crystal for extracting accelerated proton beams. The first such experiment was performed in 1984 by Tsyganov's group at the JINR (HEL) synchrophasotron with 8.4-GeV protons [9]. For extraction, they used an $11 \times 10 \times 0.4$-mm (length × height × thickness) (111) silicon crystal bent by an angle of 35 mrad. The accelerated beam was directed to the crystal by reducing the equilibrium-orbit radius. The obtained extraction efficiency (the ratio of the extracted-beam intensity to that of the beam directed to the crystal) was equal to $\sim 10^{-4}$.

In 1989, 50- and 70-GeV proton beams were extracted from the U-70 IHEP accelerator into one of the existing secondary-particle channels [10]. To direct the extracted beam into this channel, it was necessary to bend the $65 \times 15 \times 0.6$-mm (111) silicon crystal by a large angle of ~85 mrad. The accelerated beam was directed to the crystal by the local distortion of the orbit. The efficiency of this extraction was equal to several units of 10^{-4}, and it was later increased to 10^{-3} by using thin carbon films for the preliminary small-angle scattering of the proton beam.

In 1993, extraction of a 120-GeV proton beam with an intensity of 5×10^{11} protons per cycle from

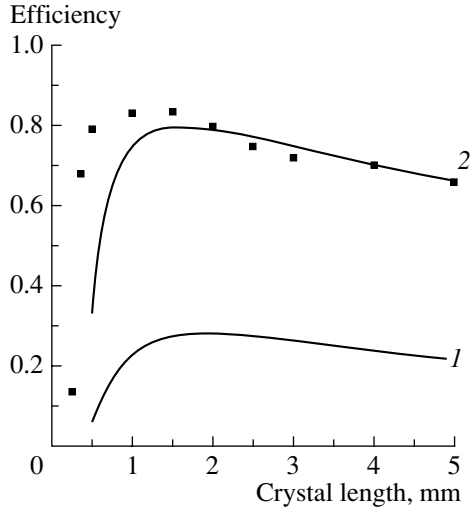

Fig. 1. Efficiency of (*1*) single-turn and (*2*) multiturn extraction vs. the crystal length. The points are the results of direct computer simulation.

the SPS accelerator using $30 \times 18 \times 1.5$-mm (110) bent silicon crystals [11] was investigated at CERN. For directing to the crystal, the accelerated beam was perturbed in the horizontal plane by the electric field of capacitor plates. The field between the capacitor plates had a white-noise spectrum and provided a standard deviation of ~ 0.001 μrad for particles in each passage. The extraction efficiency was equal to $\sim 10\%$, and it reached $\sim 20\%$ at an energy of 270 GeV.

Interesting investigations on the extraction of a 900-GeV proton beam were also performed at the FNAL superconducting accelerator [12]. In those experiments, a $40 \times 10 \times 3$-mm (110) silicon crystal bent by an angle of 0.64 mrad was used. The beam was deviated by the crystal in the vertical plane and it was directed to the crystal in the horizontal plane. The beam was directed to the crystal either by its deviation by a deflector or by exciting the particle diffusion. It was shown in experiments that there is the unique possibility of combining extraction of particles from the beam halo and the operation of the accelerator in the collider mode. The beam extraction efficiency reached $\sim 30\%$. The extraction efficiency that was obtained in those experiments was much lower than that of the classical slow extraction, which reached $\sim 98\%$. The extraction efficiencies were low because, when the lengths and bend angles of crystals are large, the capture of particles to the channeling mode occurs predominantly in the first passage through the crystal. Particles that are not captured in the channeling mode are strongly scattered and finally lost. To realize efficient multiturn extraction, it is necessary to provide the conditions under which particles that are not captured in the channeling mode in the first passage through the crystal can be captured in the subsequent passages. Short crystals with small bend angles are required for this aim according to the calculations performed in [13, 14] with the software packages described in [15, 16]. Figure 1 shows the results of calculations and computer simulation for the extraction efficiency at the IHEP accelerator using (110) silicon crystals of various lengths deflecting the 70-GeV proton beam at a fixed angle of 2 mrad.

As is seen in Fig. 1, multiturn extraction can be threefold more efficient than single-turn extraction. Moreover, the maximum efficiency ($\sim 80\%$) is provided by short crystals $\sim 1-2$ mm in length. Such an extraction was performed at the IHEP accelerator. In this case, one crystal with small (~ 1 mrad) bend angles was insufficient (due to relatively short straight sections). It was necessary to additionally use several septum magnets of the existing extraction system and to guide the beam in the extraction direction.

In various places of the accelerator, we installed three identical crystal stations: Si_{19}, Si_{22}, and Si_{106} (see Fig. 2). Here, the subscripts denote the ordinal numbers of straight sections or magnetic units in which the crystal was installed. The arrangement scale for the magnetic units (MUs) in the accelerator and the straight sections (SSs) preceding each of them is shown in Fig. 3 (at the top).

In addition to the indicated stations, we also arranged the stations Si_{30}, Si_{84}, and Si_{86} at the accelerator. The crystal station Si_{30} serves for selecting a small ($\sim 10^7$) fraction of particles from the extracted beam and for deviating them (at an angle of ~ 9 mrad) into the 22nd channel. The crystal stations Si_{84} and Si_{86} are located in the test area both to test the crystals before their installation in the workstations Si_{19}, Si_{22}, and Si_{106} and to perform a number of investigations, in particular, the study of beam-collimation modes using bent crystals.

We discuss the chosen schemes of extracting an accelerated beam in more detail. Figure 3 shows two of these extraction schemes.

In the first scheme, the station Si_{19} with two crystals (one is in reserve) was installed in the 19th straight section of the U-70 accelerator outside the beam region. It provided independent displacement of each crystal along the radius and a change in its angular orientation with respect to the beam. The beam was directed to the crystal due to local orbit distortion by two pairs of magnetic units (15/21 and 16/22). The particles that are directed to the crystal and captured in the channeling mode are deviated by the crystal at an angle of $\sim 1.7-2.5$ mrad and fall within the aperture of the septum magnet SM_{20}, bypassing the septum ~ 7 mm thick. Then, being deviated by the septum magnets SM_{22} and SM_{26} (curve *2* in Fig. 3), the particles were extracted from

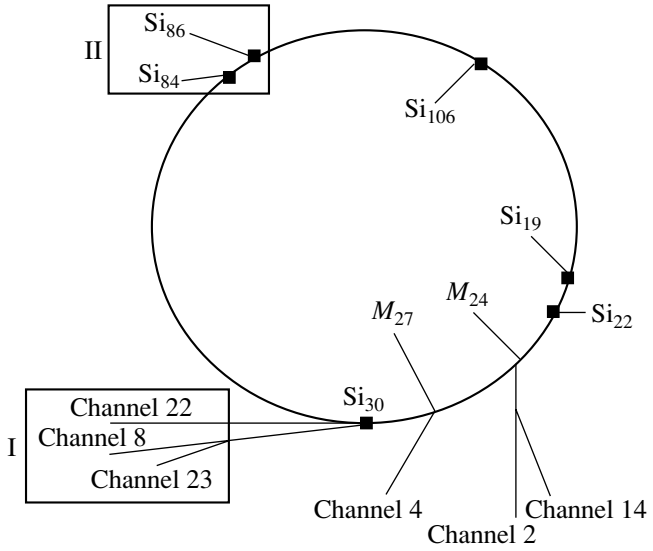

Fig. 2. Schematic diagram of extraction of beams from the U-70 accelerator: Si_{19}, Si_{22}, Si_{30}, Si_{84}, Si_{86}, and Si_{106} are the bent crystals; M_{24} and M_{27} are the internal targets providing beams of secondary particles in channels 2, 4 and 14; I is the area of experimental equipment; and II is the area of investigation of crystals.

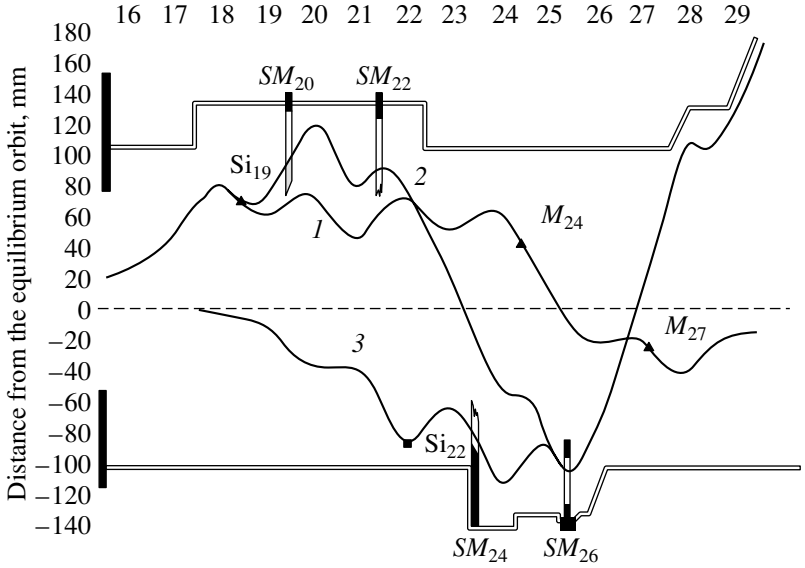

Fig. 3. Schematic diagram of proton-beam extraction using bent crystals: *1* is the trajectory of a circulating beam, which is simultaneously directed to the crystal in straight section 19 (Si_{19}) and to internal targets M_{24} and M_{27}; *2* is the line of extraction of the beam from the Si_{19} crystal; and *3* is the line of extraction of the beam from the Si_{22} crystal.

the vacuum chamber of the accelerator in the 30th straight section. This scheme is promising because it can be used as the basis for organizing simultaneous extraction of a beam by the crystal and two internal targets M_{24} and M_{27} (curve *1* in Fig. 3).

When using the other crystal station Si_{22} placed in the middle of the 22nd magnetic unit, protons can be extracted through the septum magnets SM_{24} and SM_{26} (curve *3* in Fig. 3). In this case, also two pairs of magnetic units are used to direct the beam: 20/26 and 18/30.

When working with the third station Si_{106} installed in the 106th straight section (it is not shown in Fig. 3), two pairs of magnetic units (103/109 in the feedback mode and 104/110 in the dc mode) are also used to direct the beam to the crystal. The beam can be extracted either through the septum magnets SM_{20}, SM_{22}, and SM_{26} or through the septum magnets SM_{24} and SM_{26}. Thus, the third scheme can

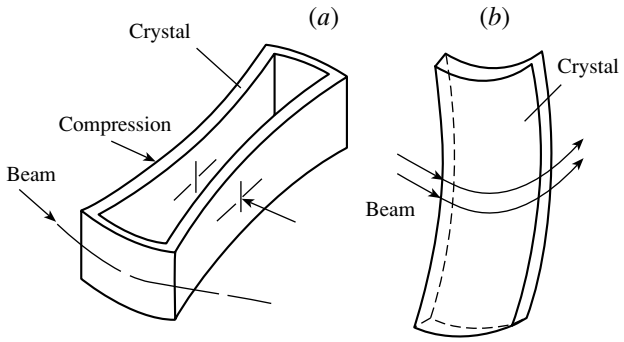

Fig. 4. Schematic representation of the bending of (*a*) O and (*b*) Π crystals.

replace any of the first two schemes in the case of their malfunction.

To realize the above beam-extraction schemes, it was necessary to solve a very complicated problem of bending short silicon crystals by small angles. We succeeded in solving this problem by using two nonconventional approaches. In the first of them, the crystal was manufactured from a monolithic silicon piece of the shape of the letter O (O crystals), and the necessary bend was achieved by compressing the crystal in its middle section (Fig. 4*a*). This crystal provided a high extraction efficiency of ~65% if its working-part sizes were $5.0 \times 5.0 \times 0.7$ mm and the lateral walls were ~1 mm thick. A decrease in the length of the working section of the crystal to 3.5 mm reduced the extraction efficiency due to increasing negative action of lateral walls.

The second method is as follows. A narrow strip ~2 mm in length and 30–40 mm in height is bent in the vertical direction by an angle of ~100 mrad. In this case, it is bent by an angle of ~1 mrad in the transverse direction (see Fig. 4*b*) due to strains arising in an anisotropic crystal lattice. Strip-shaped crystals (Π crystals) with bend angles ~1 mrad that were preliminary subjected to special chemical polishing showed the best beam-extraction efficiency of ~85%.

Proton-beam extraction was investigated mainly at energies 70 and 50 GeV using the Π crystals with the (111) orientation and the O crystals with the (110) orientation. The characteristics of the crystals and the experimental results are given in the table.

To introduce the crystal in the channeling mode, we varied its position in both coordinate and angle. Figure 5 shows the typical orientation curve for 70-GeV protons extracted from the accelerator by the 106–24–26 scheme using Π crystal no. 1 (see table). A small asymmetry of this curve is associated with extraction of a certain fraction of particles reflected from crystal planes (this process is considered in [4]) along with channeled particles. The working position of the crystal corresponds to the peak in the orientation curve. The extraction efficiency (the ratio of the extracted-beam intensity to the intensity of the beam fraction directed to the crystal) was determined by collecting statistics over several hundred cycles. The extraction efficiencies measured and calculated using the available software packages are shown in Fig. 6 for an energy of 70 GeV and for two extraction schemes: (*a*) 106–24–26 and (*b*) 22–24–26.

For the 106–24–26 scheme, the measured efficiency reaching ~85% decreases by ~10% when the fraction of the beam directed to the crystal increases. This decrease is attributed to the direction angle drift that breaks the optimal angular orientation of the crystal with respect to the beam. In Fig. 6*a*, calculated curve *2* is higher than experimental curve *1* by approximately 3–5%; i.e., they are in satisfactory agreement with each other.

For the 22–24–26 scheme (Fig. 6*b*), efficiency increases (by ~4%) when the beam fraction directed to the crystal increases. This increase can be explained by assuming that the remaining particle beam partially touches the current partition of a septum magnet at the beginning of extraction and, hence, a certain fraction is lost. As the beam emittance decreases during extraction, these losses also decrease, and the extraction efficiency increases. This process was simulated, and it appeared that, when a certain beam fraction falls to an edge of the septum magnet at a depth of 0.3 mm, the experimentally observed dependence (curve *1*) is completely repeated (curve *2*). If the crystal position moves closer to the equilibrium orbit by $\geq$0.3 mm, the observed effect vanishes, and the extraction efficiency increases to 90% (curve *3*) at the beginning of the process. Thus, though a quite high extraction efficiency of ~85% is reached, calculations show that it can likely be increased to 90%.

In this study, we also measured other characteristics of 50-GeV proton beams extracted by the 22–24–26 scheme using crystal no. 6 (see table). Figure 7 shows the extracted-beam profiles in the

Table

Crystal number	Installation place	Type	Bend angle, mrad	Size $l \times h \times R$, mm	Efficiency, %	Energy, GeV	Extraction scheme
1	SS-106	П	1.0	$2 \times 35 \times 0.5$	85	70	106–24–26
					80	70	106–20–22–26
2	SS-106	О	0.7	$3.5 \times 5 \times 0.7$	60	70	106–24–26
3	SS-19	П	2.0	$5 \times 45 \times 0.5$	67	70	19–20–22–26
4	SS-19	О	2.1	$5 \times 5 \times 0.7$	65	70	19–20–22–26
5	MU-22	П	0.8	$1.9 \times 45 \times 0.5$	85	70	22–24–26
6	MU-22	П	0.9	$1.8 \times 45 \times 0.5$	80	50	22–24–26

output window of the accelerator vacuum chamber. It is seen that the extracted beam is quite well formed. Its horizontal and vertical sizes at half maximum are equal to 3.7 and 2.0 mm, respectively. They are much smaller than the output-window diameter of the vacuum chamber, which is equal to 38 mm.

Figure 8 illustrates the fairly stable operation of the extraction system at a time interval of 180 working cycles of the accelerator. The extraction efficiency at an energy of 50 GeV reaches 80% and the extracted-beam intensity is equal to 10^{12} protons per cycle.

Important results were also obtained when testing crystals at the unit in the test area. The schematic drawing of the testbed is given in Fig. 9.

The efficiency of crystals in this case was determined as follows. When using a kicker magnet, the entire beam was kicked on the absorber end face and the total profilometer signal corresponded to 100% intensity of the beam. The ratio of the integrated signal when kicking the beam by a crystal installed in the 84th magnetic unit to the signal obtained using the kicker magnet gives the absolute value of the efficiency of the crystal under study. In this case, the total error does not exceed 5%. The measurements of efficiency of the П crystal with a bend angle of 0.8 mrad and a length of ~1.7 mm along the beam (see Fig. 10) show the same high efficiency of 85% as the direct measurements during the beam extraction. It also follows from these results that the crystal station with a bent crystal near the beam absorber can also be efficiently used for localization of beam losses, which is especially important for superconducting accelerators.

The efficiency of a crystal 1.8 mm in length and with a bend angle of 0.8 mrad was obtained as a function of the accelerated-proton energy in the same way at the testbed (see Fig. 11). The measured and calculated efficiencies of the bent crystal are in good agreement. A decrease in efficiency with the proton energy is mainly explained by the increase in the rms angle of the multiple scattering and the decrease in the dechanneling length. The obtained dependence also shows that the same crystal can provide the extraction of beams in a quite wide energy range of 40–70 GeV with an efficiency higher than 60%.

For applying crystals at accelerators, their radiation resistance is of importance. The maximum particle flux that a silicon crystal can endure was estimated in the experiments performed at CERN and BNL at $\sim 2 \times 10^{20}$ proton/cm^2. Our experiments also corroborate this result. The crystals lose no channeling properties during two 1400-h runs. As for thermal loadings, our experiment showed that the crystal with an efficiency of 80–85% provided the extraction of beams with an intensity to 10^{12} particles per 1–2 s cycle, which meets the requirements of the majority of experiments performed at the IHEP accelerator. When the crystal is irradiated by a beam with an intensity of $\sim 10^{13}$ protons, it loses its channeling properties. To determine more precisely the upper limit of

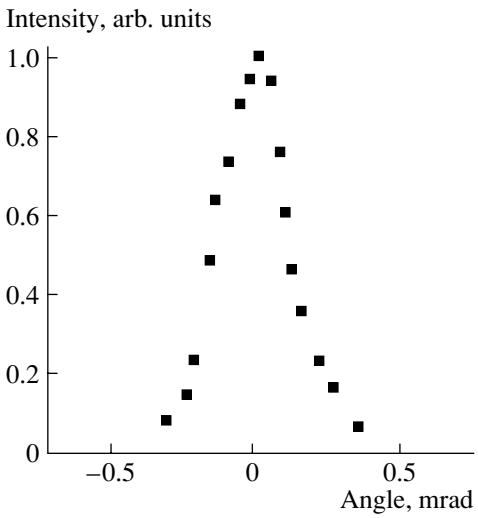

Fig. 5. Extracted-beam intensity vs. the crystal orientation angle with respect to the beam.

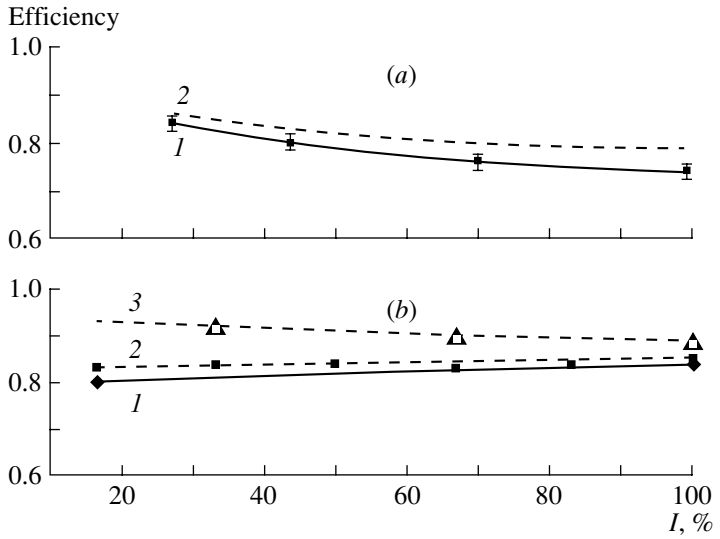

Fig. 6. Extraction efficiency at an energy of 70 GeV vs. the beam fraction directed to the crystal for the extraction schemes (*a*) 106–24–26 and (*b*) 22–24–26 (the curves are described in the text).

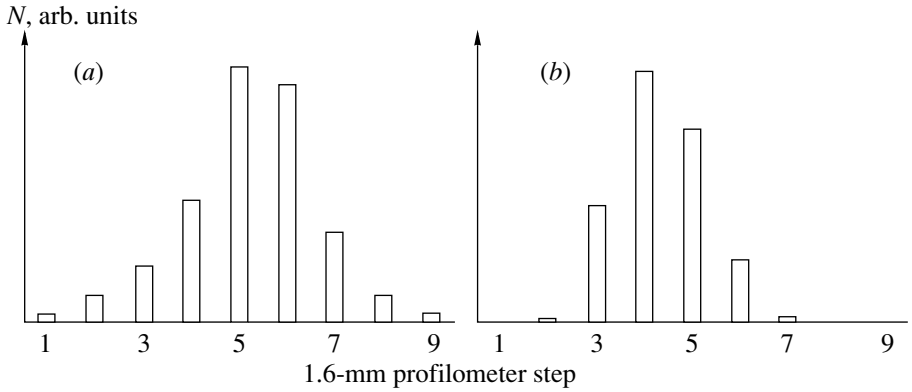

Fig. 7. Beam-density distribution along the (*a*) horizontal and (*b*) vertical coordinates in the output window of the accelerator vacuum chamber.

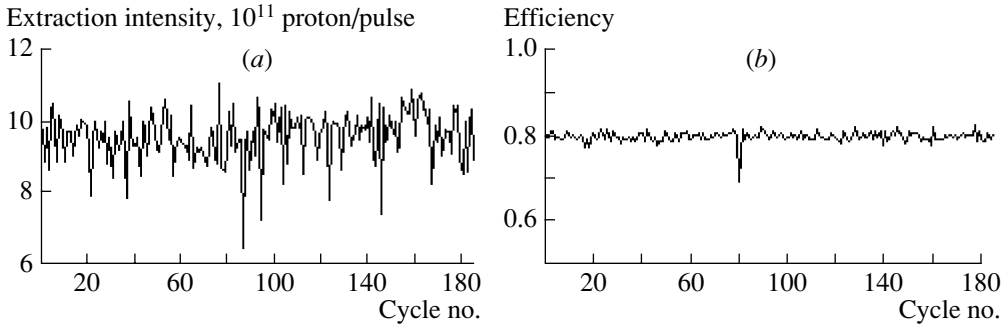

Fig. 8. (*a*) Intensity and (*b*) efficiency of the 22–24–26 extraction scheme for a 50-GeV proton beam.

intensity that can be directed to a short crystal, it is necessary to perform special investigations including the search for ways to improve the heat removal from the crystal.

The proton-beam extraction using bent crystals in principle admits the operation of several internal targets in parallel, which was experimentally corroborated in 1991 at the IHEP accelerator [17].

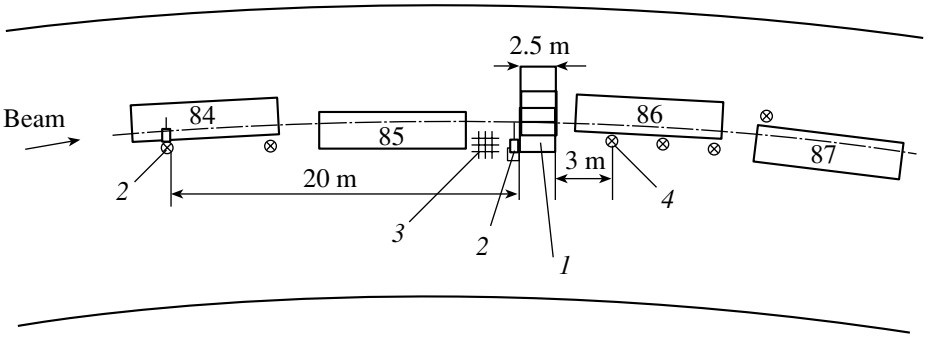

Fig. 9. Schematic drawing of the unit for testing crystals: *1* is the absorber, *2* are the crystal stations, *3* is the profilometer, *4* are the ionization chambers, and 84–87 are the magnetic units.

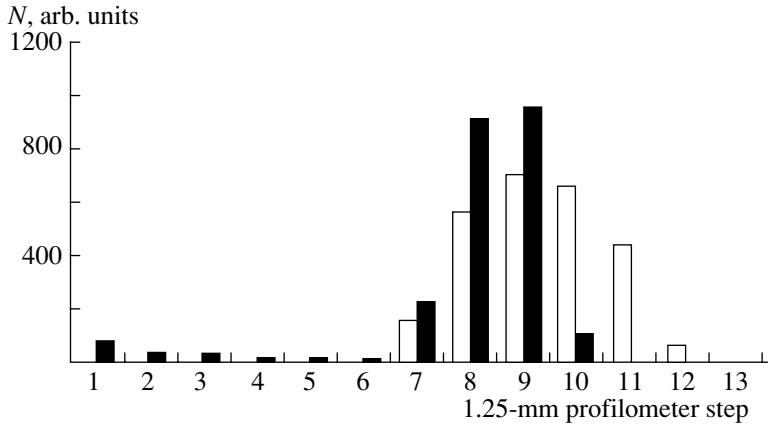

Fig. 10. Beam-density distribution over the horizontal coordinate on the absorber in the case of extraction of protons by (□) a kicker magnet and (■) an oriented crystal.

The realization of such a mode using short crystals opens the possibility for simultaneous operation of several experimental installations over the entire flattop (plateau) of the accelerator magnetic cycle, which results in a substantial reduction in expenses for realization of the experiments. We emphasize that classical resonance extraction is incompatible with the operation of internal targets in parallel. In this case, it is necessary to divide the magnetic-cycle plateau between them.

To realize the simultaneous operation of the extraction by a crystal and internal targets, the crystal stations Si_{19} or Si_{106} were used (see Fig. 3). In this case, three experimental installations could simultaneously operate in the beams, which completely satisfied the experimental requirements on the intensity, duration, and quality of a beam. Figure 12 shows the time structure of the extracted beam and the secondary-particle beams from the targets on the flattop of a magnetic cycle. The number of simultaneously performed experiments can be increased to four by using the Si_{30} crystal (see Fig. 2).

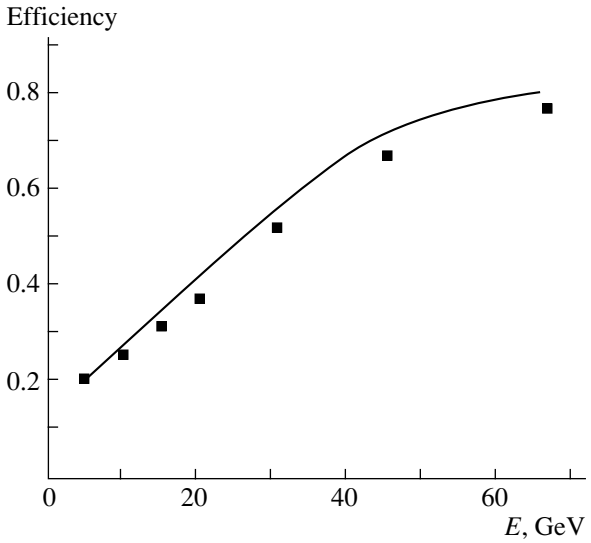

Fig. 11. (Curve) Calculated and (points) measured extraction efficiency of the crystal vs. the proton energy.

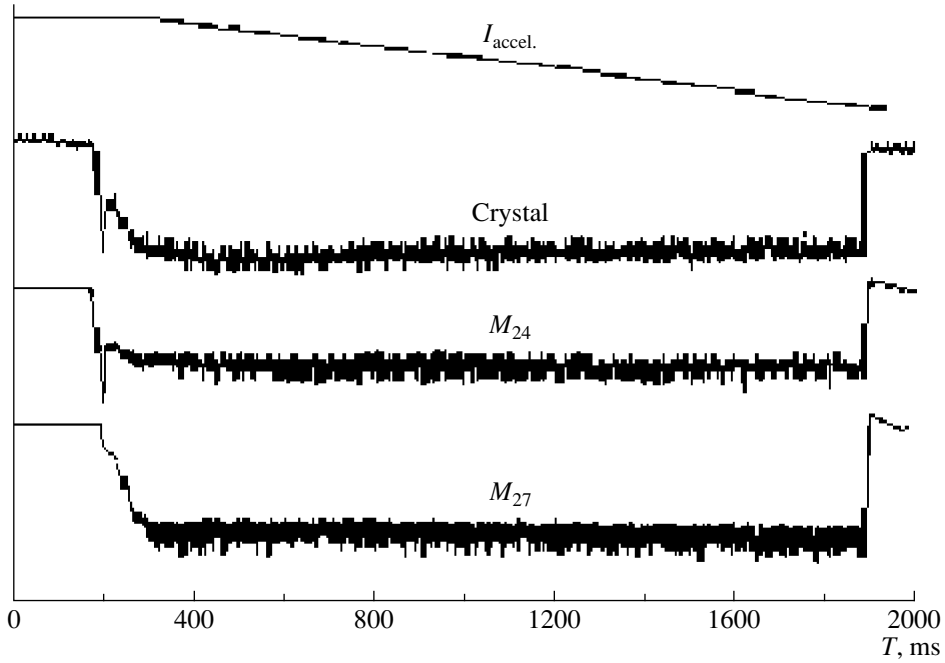

Fig. 12. Oscillograms of the signals from the monitors providing the beam to the crystal and to the internal targets.

The developed beam extraction has been used at the IHEP accelerator since the end of 1999 in each run of operation. All systems of this extraction were considered in detail in [18].

3. PROSPECTS AND NEW APPLICATIONS

The application of bent crystals for controlling high-energy particle beams becomes possible due to significant advances in the corresponding investigations. The proton-beam extraction using bent crystals that has been developed at the IHEP accelerator successfully operates and provides the realization of a wide physical research program. It would be desirable to make this extraction competitive with the resonance slow extraction by increasing the intensity of extracted beams by an order of magnitude (from 10^{12} to 10^{13} protons per cycle). It seems possible to solve this problem by replacing silicon crystals with more heat and radiation resistant crystals such as artificial diamonds, for which these parameters are higher by a factor of 3 and 6, respectively.

For extracting an accelerated beam from low-energy accelerators, it seems promising to use new crystalline structures, so-called carbon nanotubes 1–1.4 nm in diameter. The point is that the use of silicon crystals for extracting accelerated particles with energies of $\leq$1 GeV becomes difficult due to a small dechanneling length of $\sim$1 mm. In nanotubes, the dechanneling length is approximately five times larger, and their use can be decisive.

The field of applications of oriented crystals (not only bent, but also straight ones) has been extended considerably. For example, at CERN [19] and KEK [20, 21], a series of investigations on extracting positron beams was carried out using tungsten crystals with the $\langle 111 \rangle$ axial orientation as a target installed in electron beams of energies 6–40 and 3–8 GeV, respectively. It was shown that the yield of, e.g., 10-MeV positrons from such a target at an electron-beam energy of 8–10 GeV is higher than that from an amorphous target of the same size by a factor of 2 to 6.5 depending on the crystal length varying in the range of 9–2.2 mm, respectively. The results agree well with the calculations made in [22] and can serve as the basis for designing new positron sources for linear colliders.

Recently, several proposals on using oriented crystals as undulators appeared [23–27]. As is known, the standard method for generating intense x-ray beams is based on using undulators and wigglers. However, it is impossible to create such sources with a period shorter than several centimeters. Therefore, the radiation energy range cannot be expanded above 100 keV. In crystals oriented along the crystallographic planes, high-energy positrons mainly emit hard γ-ray photons (radiation in channeling). To provide the conditions for undulator radiation, it is necessary to create one more period in these crystals, which is much longer than the period of radiation in channeling. This condition can be achieved, for example, by either manufacturing a silicon crystal with

germanium atoms implanted in a certain order [24] or deforming the silicon crystal by making grooves of a given period on its lateral surfaces [26, 27]. The latter method was tested on an x-ray diffractometer, which showed that the crystallographic planes in this case are deformed by approximately a sine law with the period preset by the grooves. In addition, investigations of such crystals on a 60-GeV proton beam confirmed their channeling properties. Investigations of such crystals as sources of undulator radiation are scheduled to be performed on positron beams of energies 2–15 GeV from the IHEP accelerator. According to the calculations, the expected energy of photons in the case of operation with a deformed silicon crystal 3 mm in length with ten periods is equal to ~0.5 MeV.

REFERENCES

1. J. Lindhard, Mat.-Fys. Medd. Dan. Vid. Selsk. **34** (14), 1 (1965).
2. V. M. Biryukov, V. I. Kotov, and Y. A. Chesnokov, Usp. Fiz. Nauk **164**, 1017 (1994) [Phys. Usp. **37**, 937 (1994)].
3. V. M. Biryukov, Y. A. Chesnokov, and V. I. Kotov, *Crystal Channeling and Its Application at High-Energy Accelerators* (Springer, Berlin, 1997).
4. A. M. Taratin, Fiz. Élem. Chastits At. Yadra **29**, 1063 (1998) [Phys. Part. Nucl. **29**, 437 (1998)].
5. E. N. Tsyganov, Fermilab Preprint Nos. TM-682 and TM-684 (Batavia, 1976).
6. A. S. Vodop'yanov *et al.*, Pis'ma Zh. Éksp. Teor. Fiz. **30**, 474 (1979) [JETP Lett. **30**, 442 (1979)].
7. S. P. Moller, T. Worm, *et al.*, Nucl. Instrum. Methods Phys. Res. B **84**, 434 (1994).
8. D. G. Koshkarev, Preprint ITÉF No. 30 (Institute of Theoretical and Experimental Physics, Moscow, 1977).
9. V. V. Avdeĭchikov *et al.*, Kratk. Soobshch. Ob'edin. Inst. Yad. Issled., No. 1-84, 3 (1984).
10. A. A. Asseev, M. D. Bavizhev, *et al.*, Nucl. Instrum. Methods Phys. Res. A **309**, 1 (1991); A. A. Asseev *et al.*, Nucl. Instrum. Methods Phys. Res. A **324**, 31 (1993).
11. H. Akbari *et al.*, Phys. Lett. B **313**, 491 (1993).
12. T. Murphy *et al.*, Nucl. Instrum. Methods Phys. Res. B **90**, 128 (1994).
13. A. Taratin *et al.*, Report SSCL 28/91-15 (Texas, 1991).
14. V. M. Biryukov *et al.*, in *Proceedings of the Particle Accelerator Conference, Vancouver, Canada, 1997*, Vol. 1, p. 249.
15. A. M. Taratin, S. A. Vorobiev, M. D. Bavizhev, and I. A. Yazynin, Nucl. Instrum. Methods Phys. Res. B **58**, 103 (1991).
16. V. M. Biryukov, Phys. Rev. Lett. **74**, 2471 (1995).
17. A. A. Aseev, M. D. Bavizhev, A. N. Vasil'ev, *et al.*, Preprint IFVÉ No. 91-46 (Institute of High Energy Physics, Protvino, 1991).
18. A. G. Afonin, V. G. Baranov, V. M. Biryukov, *et al.*, Preprint IFVÉ No. 2003-33 (Institute of High Energy Physics, Protvino, 2003).
19. X. Artru, V. Baier, *et al.*, Nucl. Instrum. Methods Phys. Res. B **201**, 243 (2003).
20. K. Yoshida *et al.*, Phys. Rev. Lett. **80**, 1437 (1998).
21. H. Okuno *et al.*, Nucl. Instrum. Methods Phys. Res. B (in press); PII, S0168-583X(02) 01138-2.
22. N. Baier and V. M. Strakhovenko, Phys. Rev. ST Accel. Beams **5**, 121001 (2002).
23. A. V. Korol, A. V. Solov'ev, and W. Greiner, Int. J. Mod. Phys. E **8**, 49 (1999).
24. U. Mekkelsh and E. Uggerhoj, Nucl. Instrum. Methods Phys. Res. B **160**, 435 (2000).
25. R. O. Avakian *et al.*, Nucl. Instrum. Methods Phys. Res. B **173**, 112 (2001).
26. S. Bellucci *et al.*, Phys. Rev. Lett. **90**, 034801 (2003).
27. S. Bellucci *et al.*, Phys. Rev. ST Accel. Beams **7**, 023501 (2004).

Translated by V. Bukhanov

Physics of Atomic Nuclei, Vol. 68, No. 6, 2005, pp. 1034–1037. Translated from Yadernaya Fizika, Vol. 68, No. 6, 2005, pp. 1074–1077.
Original Russian Text Copyright © 2005 by Dorofeev, Lobanov.

PROCEEDINGS OF THE CONFERENCE "PHYSICS OF FUNDAMENTAL INTERACTIONS" DEDICATED TO THE 100th ANNIVERSARY OF A.I. ALIKHANOV'S BIRTH, SECTION OF NUCLEAR PHYSICS, DIVISION OF PHYSICAL SCIENCES, RUSSIAN ACADEMY OF SCIENCES; INSTITUTE OF THEORETICAL AND EXPERIMENTAL PHYSICS, MOSCOW, MARCH 1–5, 2004

Beta Decay in the Field of an Electromagnetic Wave and Experiments on Measuring the Neutrino Mass

O. F. Dorofeev and A. E. Lobanov*

Moscow State University, Vorob'evy gory, Moscow, 119992 Russia

Received May 24, 2004

Abstract—Investigations of the effect of an electromagnetic wave field on the beta-decay process are used to analyze the tritium-decay experimental data on the neutrino mass. It is shown that the electromagnetic wave can distort the beta spectrum, shifting the end point to the higher energy region. This phenomenon is purely classical and it is associated with the electron acceleration in the radiation field. Since strong magnetic fields exist in setups for precise measurement of the neutrino mass, the indicated field can appear owing to the synchrotron radiation mechanism. The phenomenon under consideration can explain the experimentally observed anomalies in the spectrum of the decay electrons; in particular, the effect of the "negative square of the neutrino mass." © *2005 Pleiades Publishing, Inc.*

The effect of electromagnetic fields on beta decay has long been studied. In particular, the effect of plane-wave fields on this process was considered in [1–3]. The results show that the spectrum of decay electrons depends strongly on electromagnetic radiation. However, the spectral distribution of β electrons is a characteristic most sensitive to the neutrino mass m_ν. The authors of [1–3] paid primary attention to very strong fields. In this paper, we consider very weak fields and their effect on the beta spectrum.

We assume that the effect of the external field on the nuclear matrix elements is negligible—this assumption is quite evident for low-frequency weak fields. In this case, change in the decay probability in the field is attributed only to change in the phase-space volume of the produced particles. Since the proton mass significantly exceeds the electron mass, in order to estimate the field effect, it is enough to calculate the transition matrix element with the solution of the Dirac equation for the electron in the plane wave rather than with the wave function of the free electron.

If we choose a circularly polarized wave with frequency ω and field strength E as a model of the external field and assume that $\omega \ll m_\nu$ (here, we use the system of units where $c = \hbar = 1$), the probability of allowed beta decay with the massive Dirac neutrino in the leading order in the parameter ω/m is determined by the expression

$$\frac{W}{\tilde{W}} = \frac{\xi^2}{4}\left\{\int_{t_1}^{t_2} dt \int_{y_1}^{\varepsilon_0-\mu} dy\Phi(t,y) \right. \quad (1)$$
$$\left. + \Theta(\xi_0-\xi)\int_{t_0}^{t_1} dt \int_{y_1}^{y_2} dy\Phi(t,y)\right\},$$

where

$$\Phi(t,y) = (t+y)y(\varepsilon_0-y) \quad (2)$$
$$\times \left[(\varepsilon_0-y)^2-\mu^2\right]^{1/2}\left[\xi^2+(y-t)^2\right]^{-3/2},$$
$$t_0 = 1, \quad \xi_0 = \left[2(\varepsilon_0-\mu-1)\right]^{1/2},$$
$$\beta = (1-1/t^2)^{1/2}.$$

Here,

$$\xi = eE/(m\omega), \quad \mu = m_\nu/m, \quad t = p^0/m, \quad (3)$$
$$\varepsilon_0 = (M_i - M_f)/m,$$

where e, m, and p^0 are the charge, mass, and total energy of the electron. For a neutron and, approximately, for tritium, $\tilde{W} = G_F^2 m^5(1+3\alpha_0^2)/(2\pi^2)$, where α_0 is the ratio of the axial and vector constants of the weak interaction and G_F is the Fermi constant. The integration limits in spectral distribution (1) assume the form

$$t_{1,2} = (\varepsilon_0-\mu)(1+\xi^2/2) \mp \xi(1+\xi^2/4)^{1/2} \quad (4)$$
$$\times \left[(\varepsilon_0-\mu)^2-1\right]^{1/2},$$
$$y_{1,2} = t\left[1+\xi^2/2 \mp \xi(1+\xi^2/4)^{1/2}\beta\right].$$

Figures 1–5 illustrate the spectrum behavior, where W_0 is the total beta-decay probability in the absence of an external field.

When $\xi \ll 1$,

$$t_{\max} \approx \varepsilon_0 - \mu + \xi(\varepsilon_0^2-1)^{1/2}. \quad (5)$$

*e-mail: lobanov@th466.phys.msu.ru

1063-7788/05/6806-1034$26.00 © 2005 Pleiades Publishing, Inc.

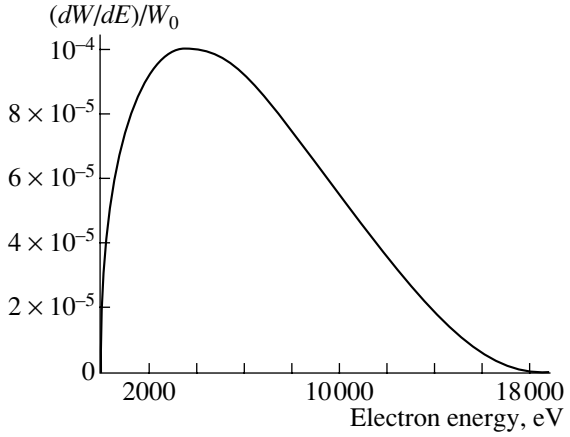

Fig. 1. Tritium beta spectrum.

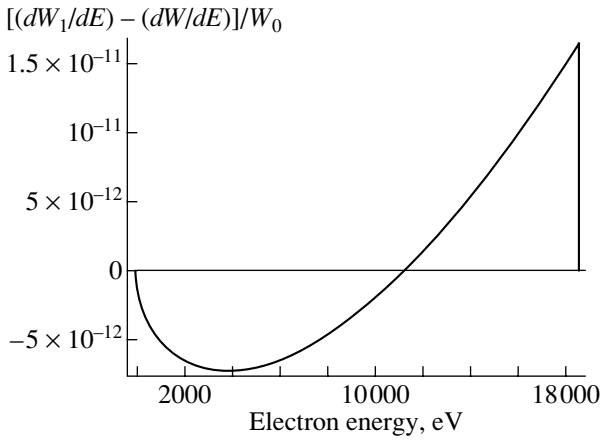

Fig. 2. Tritium beta spectrum: $m_\nu = 0$; W—$\xi = 0$; W_1—$\xi = 0.00005$.

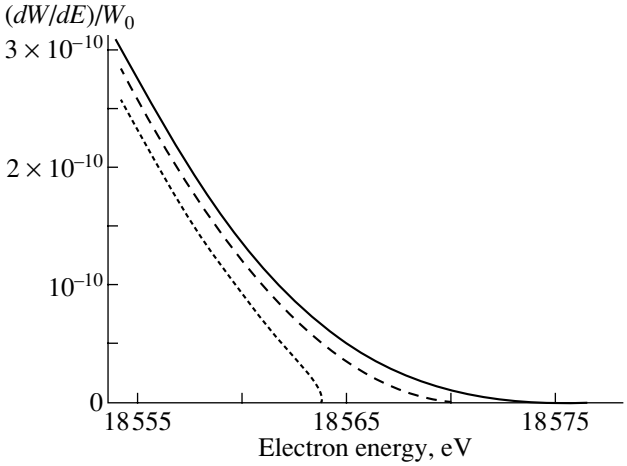

Fig. 3. Tritium beta spectrum near the end point: (dashed curve) $m_\nu = 0$, $\xi = 0$; (dotted curve) $m_\nu = 6.8$ eV, $\xi = 0$; and (solid curve) $m_\nu = 0$, $\xi = 0.00005$.

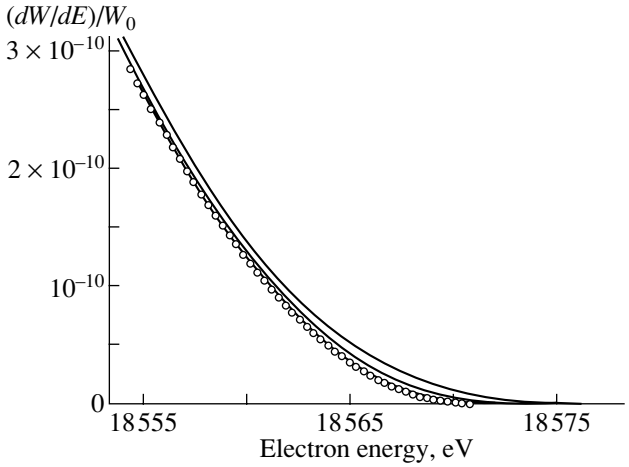

Fig. 4. Tritium beta spectrum near the end point: (points) $\xi = 0$, $m_\nu = 0$ and (solid curves) $m_\nu = 0$, $\xi = 0.00005$, 0.000034, and 0.000017.

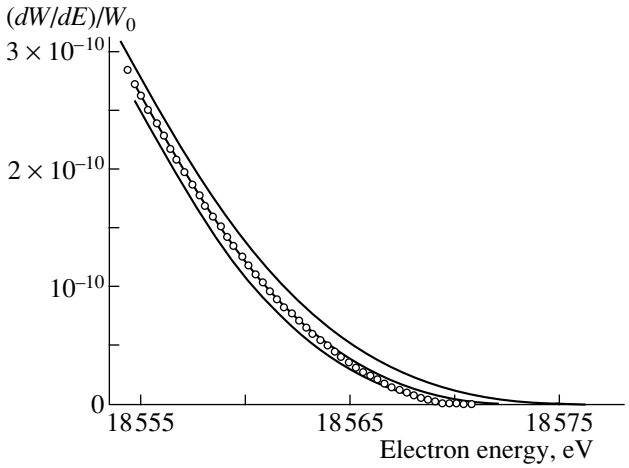

Fig. 5. Tritium beta spectrum near the end point: (points) $\xi = 0$, $m_\nu = 0$ and (solid curves) $\xi = 0.00005$, $m_\nu = 0$, 5.1, and 6.8 eV.

Relation (5) makes it possible to estimate the field strengths required to observe the effect. Assuming that the spectrum-edge shift caused by the external field is equal to the shift owing to the nonzero neutrino mass, we obtain

$$E\lambda = \frac{2\pi}{\sqrt{\varepsilon_0^2 - 1}} m_\nu. \qquad (6)$$

Here, E is the radiation field strength (in volts per meter), λ is the radiation wavelength (in meters), and m_ν is the neutrino mass (in electronvolts).

The numerical estimates show that the shift of the beta-electron spectrum for tritium, where $\varepsilon_0 \approx 1.03634$, that corresponds to a neutrino mass on the order of 1 eV (the experimental accuracy in [4, 5]) might be compensated by the SHF radiation field

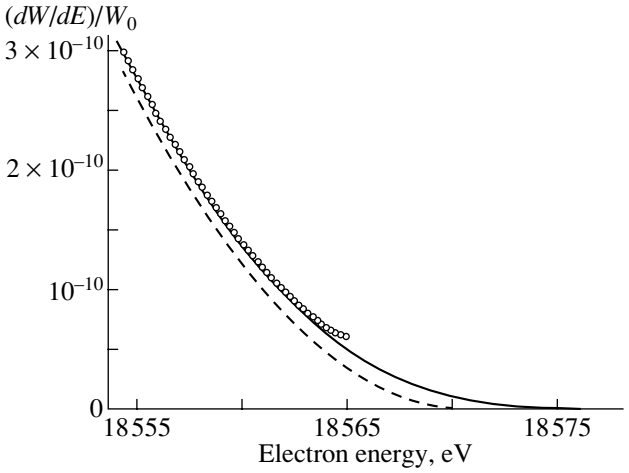

Fig. 6. Tritium beta spectrum near the end point: (dashed curve) $\xi = 0$, $m_\nu = 0$; (solid curve) $\xi = 0.00005$, $m_\nu = 0$; and (points) $\xi = 0$, $m^2_{\text{eff}} = -25\ \text{eV}^2$.

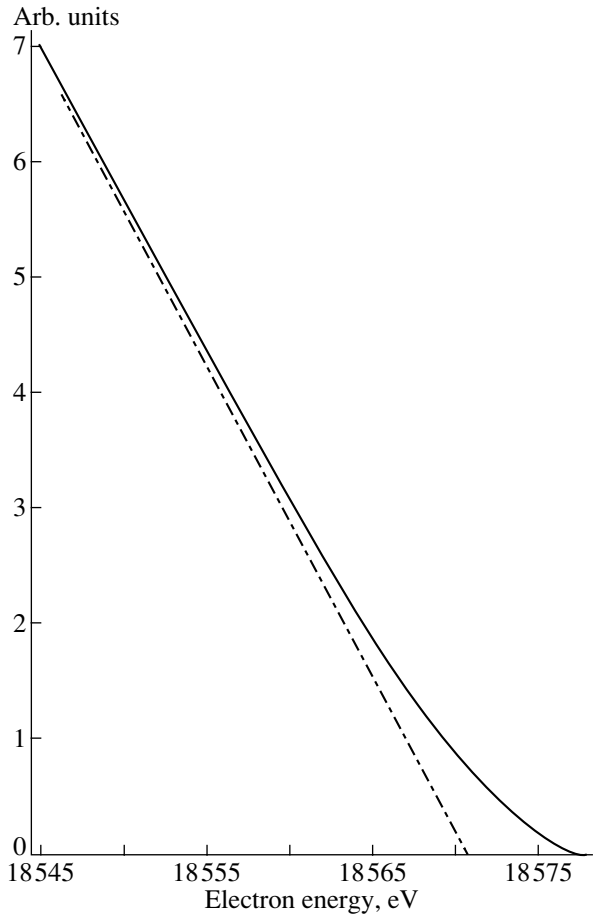

Fig. 7. Curie diagram for tritium in arbitrary units: (solid curve) $m_\nu = 0$, $\xi = 0.00005$ and (dash–dotted curve) $m_\nu = 0, \xi = 0$.

with a strength on the order of several tens of volts per meter. In the designed experiment KATRIN [6–9], where the assumed measurement accuracy is on the order of 0.1 eV, the actually observed shift might be caused by fields with a strength on the order of several volts per meter, which is comparable with the background level.

As is clear from Eq. (1), the analytical expressions for the spectrum are different for parameters t below and above t_1. It is easy to show that, for $\mu = 0, \xi \ll 1$, the spectrum in the region $t < t_1$ under the condition $\varepsilon_0 - t \ll 1$ is approximated by the expression

$$\frac{d(W_{\text{eff}}/\tilde{W})}{dt} = t\sqrt{t^2-1} \times \left[2(\varepsilon_0 - t)^2 - (\varepsilon_0 - t)\sqrt{(\varepsilon_0 - t)^2 - \mu^2_{\text{eff}}}\right], \quad (7)$$

where

$$\mu^2_{\text{eff}} = 2\xi^2 \left[\frac{\varepsilon_0}{\sqrt{\varepsilon_0^2 - 1}} \ln\left(\varepsilon_0 + \sqrt{\varepsilon_0^2 - 1}\right) - 1\right]. \quad (8)$$

It is the expression that was used in the analysis of the experimental data in [4, 5] (known as the negative neutrino mass squared, $m^2_{\text{eff}} = -m^2\mu^2_{\text{eff}}$—see Fig. 6).

The result is more obvious in the Curie diagram

$$C \sim \sqrt{\frac{dW/dt}{t(t^2-1)^{1/2}}} \quad (9)$$

presented in Fig. 7. It is clear from the diagram that the narrower the energy interval that is used to determine the spectrum edge, the larger the calculated value of ε_0. As a result, the effect of the negative mass squared is smoothed.

Thus, the experimentally observed anomaly in the tritium beta spectrum might be caused by electromagnetic radiation. We emphasize that the effect under consideration is purely classical. The characteristic parameter ξ does not contain Planck's constant, and it is the ratio of the radiation-field work on the wavelength to the electron mass. It is evident that the effect can be observed only when the mean free path of the particle in the region where the field exists is much larger than the field wavelength.

If experimental data are analyzed with regard to the described phenomenon, it is necessary to take into account both the radiation of external sources (natural and artificial) and the radiation of β electrons. Indeed, since magnetic fields on the order of several tesla exist in the chambers of experimental setups, the maximum of the radiation of the decay electrons falls into the centimeter range.

It is worth noting that a more detailed consideration should take into account the effects associated with energy losses, for example, owing to the

transition to the excited states of molecular tritium (see [10]). However, in our opinion, these effects cannot change the main conclusions of this work.

ACKNOWLEDGMENTS

We are grateful to V.M. Lobashev, A.I. Nikishov, V.N. Rodionov, N.A. Titov, and A.E. Shabad for stimulating discussions.

REFERENCES

1. I. M. Ternov, V. N. Rodionov, A. E. Lobanov, and O. F. Dorofeev, Pis'ma Zh. Éksp. Teor. Fiz. **37**, 288 (1983) [JETP Lett. **37**, 342 (1983)].
2. I. M. Ternov, V. N. Rodionov, O. F. Dorofeev, *et al.*, Yad. Fiz. **39**, 1125 (1984) [Sov. J. Nucl. Phys. **39**, 710 (1984)].
3. I. M. Ternov, V. N. Rodionov, V. G. Zhulego, *et al.*, J. Phys. G **12**, 637 (1986).
4. Ch. Weinheimer, B. Degenddag, A. Bleile, *et al.*, Phys. Lett. B **460**, 219 (1999).
5. V. M. Lobashev, V. N. Aseev, A. I. Belesev, *et al.*, Phys. Lett. B **460**, 227 (1999).
6. KATRIN Collab. (A. Osipowicz *et al.*), hep-ex/0109033.
7. Ch. Weinheimer, hep-ex/0210050.
8. N. A. Titov (for KATRIN Collab.), Yad. Fiz. **67**, 1977 (2004) [Phys. At. Nucl. **67**, 1953 (2004)].
9. V. M. Lobashev, Nucl. Phys. A **719**, 153c (2003).
10. S. Jonsell and H. J. Monkhorst, Phys. Rev. Lett. **76**, 4476 (1996).

Translated by M. Kobrinsky

Physics of Atomic Nuclei, Vol. 68, No. 6, 2005, pp. 1038–1041. Translated from Yadernaya Fizika, Vol. 68, No. 6, 2005, pp. 1078–1082.
Original Russian Text Copyright © 2005 by Sumachev.

PROCEEDINGS OF THE CONFERENCE "PHYSICS OF FUNDAMENTAL INTERACTIONS" DEDICATED TO THE 100th ANNIVERSARY OF A.I. ALIKHANOV'S BIRTH, SECTION OF NUCLEAR PHYSICS, DIVISION OF PHYSICAL SCIENCES, RUSSIAN ACADEMY OF SCIENCES; INSTITUTE OF THEORETICAL AND EXPERIMENTAL PHYSICS, MOSCOW, MARCH 1–5, 2004

New Aspects of Experimental Study of the Pion–Nucleon Interaction in the Resonance Region

V. V. Sumachev*
PNPI–ITEP Collaboration

Petersburg Nuclear Physics Institute, Russian Academy of Sciences, Gatchina, 188300 Russia

Received May 25, 2004; in final form, August 26, 2004

Abstract—New experimental data that were obtained by the PNPI–ITEP Collaboration have resolved some discrete ambiguities in the partial-wave analysis (PWA). These results were used in the new FA02 PWA performed at George Washington University. At the same time, the FA02 PWA has revealed considerable fewer N^* and Δ resonances than those listed in the RPP tables. This circumstance aggravated the known problem of so-called missing resonances. The program for further measurements of the spin rotation parameters in elastic πN scattering that are required to eliminate the remaining discrete PWA ambiguities is discussed. © *2005 Pleiades Publishing, Inc.*

INTRODUCTION

Intensive experimental studies of the πN interaction were performed until about 1980. They were completed by the global partial-wave analyses (PWAs) KN80 and CMB80 made by the Karlsruhe–Helsinki group [1] and the Carnegie Mellon–Berkeley [2] group, respectively. These and other PWAs were used to reconstruct the spectrum of the N^* and Δ baryon resonances, which was included in the review of the elementary particles RPP [3]. During the following decades (up to 2002), the πN interaction was studied less intensively, and the spectrum of the discovered baryon resonances was slightly changed in the RPP 2002 [4].

PROBLEM OF MISSING RESONANCES

Numerous attempts to create a model that would exactly reproduce the baryon resonance spectrum that was presented in the RPP [3, 4] failed. The existing models usually predicted considerably more resonances (twice or more in number) than were found in elastic πN scattering [3, 4]. This problem is known as the problem of missing resonances.

The latest FA02 PWA that was made at George Washington University (2003) [5] and included the modern experimental data appearing after 1980 revealed considerably fewer (approximately half) nonstrange baryon resonances than those presented in the RPP tables [4]. At the same time, the baryon resonances found in the FA02 PWA are in surprisingly good agreement with the Skyrme model predictions [6].

Tables 1 and 2 compare the predictions of the Skyrme model [6] for the spectrum of nonstrange baryon resonances, the $^3P_0$ model [7], the results of the PWAs KA84 [1], SM95 [8], FA02 [5], and the data from the RPP tables [4]. It is seen that the predictions of the Skyrme model coincide with the results of the FA02 PWA within 80–90%. At the moment, new aspects appear in the experimental study of πN interaction. It is clear from Tables 1 and 2 that the FA02 PWA keeps only resonances that have the highest confidence status (****) in the RPP [4] except for $D_{35}(1930)$ (which has the status ***).

Earlier, the authors of the global PWAs supposed that the appearance of new experimental data would allow more reliable determination of those baryon resonances which had low status (**) and (*) in the RPP [3]. However, the series of the PNPI–ITEP Collaboration experiments that was aimed at resolving the discrete ambiguities in the PWA procedure and that was supported by the Russian Foundation for Basic Research (project no. 99-02-16635 and others) during 1993–2001 unexpectedly led to the opposite result. Namely, they confirmed the predictions of the PWA of the VPI–GWU group for the spin rotation parameters A and R [9, 10]. This analysis did not reveal the baryon resonances with low status (**) and (*) that were presented in the RPP tables [4] (see Tables 1 and 2).

At the moment, it has become clear that the program of the PNPI–ITEP Collaboration aimed

*e-mail: sumachev@pnpi.spb.ru

Table 1. Parameters of N^* resonances

RPP (2002)	$L_{I,2J}$	Status	KA84 (1984)	$^3P_0$ model (1994)	SM95 (1995)	FA02 (2003)	Skyrme model (1985)
$N(1440)$	P_{11}	****	1410(135)	1540	1467(440)	1468(360)	
$N(1520)$	D_{13}	****	1519(114)	1495	1515(106)	1516(98)	1715
$N(1535)$	S_{11}	****	1526(120)	1460	1535(66)	1547(178)	1478
$N(1650)$	S_{11}	****	1670(180)	1535	1667(90)	1651(130)	
	S_{11}				1712(174)		
$N(1675)$	D_{15}	****	1679(120)	1630	1673(154)	1676(152)	1744
$N(1680)$	F_{15}	****	1684(128)	1770	1678(126)	1683(134)	1823
$N(1700)$	D_{13}	***	1731(110)	1625			
$N(1710)$	P_{11}	***	1723(120)	1770	$[1770 - i189]$		1427
$N(1720)$	P_{13}	****	1710(190)	1795	1820(354)	1750(256)	1982
$N(1900)$	P_{13}	**		1870			
	P_{11}			1880			
	P_{13}			1910			
	P_{13}			1950			
	P_{11}			1975			
	F_{15}			1980			
$N(1990)$	F_{17}	**	2005(350)	1980			2011
$N(2000)$	F_{15}	**	1882(95)	1995	1814(176)		
	P_{13}			2030			
	S_{11}			2030			
	D_{13}			2055			
	S_{11}			2070			
$N(2080)$	D_{13}	**	2081(265)	1960			
	D_{15}			2080			
$N(2090)$	S_{11}	*	1880(95)	1945			
	D_{13}			2095			
$N(2100)$	P_{11}	*	2050(200)	2065			
	S_{11}			2145			
	D_{13}			2165			
	D_{13}			2180			
	D_{15}			2180			
$N(2190)$	G_{17}	****	2140(390)	2090	2131(476)	2192(726)	2075
	S_{11}			2195			
$N(2200)$	D_{15}	**	2228(310)	2095			
	G_{17}			2205			
	P_{11}			2210			
$N(2220)$	H_{19}	****	2205(365)	2345	2258(334)	2270(366)	2327
	D_{15}			2235			
$N(2250)$	G_{19}	****	2268(300)	2215	2291(772)	2376(924)	2234
Total: 19			18	39	13	10	10

Table 2. Parameters of Δ resonances

RPP (2002)	$L_{I,2J}$	Status	KA84 (1984)	$^3P_0$ model (1994)	SM95 (1995)	FA02 (2003)	Skyrme model (1985)
Δ(1232)	P_{33}	****	1233(116)	1230	1233(114)	1233(118)	1424
Δ(1600)	P_{33}	***	1522(222)	1795	$[1675 - i193]$		1435
Δ(1620)	S_{31}	****	1610(139)	1555	1617(108)	1614(141)	1478
Δ(1700)	D_{33}	****	1680(230)	1620	1680(272)	1688(365)	1737
Δ(1750)	P_{31}	*		1835			
Δ(1900)	S_{31}	**	1908(140)	2035			
Δ(1905)	F_{35}	****	1905(260)	1910	1850(294)	1856(334)	1931
Δ(1910)	P_{31}	****	1888(280)	1875	2152(760)	2333(1128)	1982
Δ(1920)	P_{33}	***	1868(220)	1915			1946
Δ(1930)	D_{35}	***	1901(195)	2155	2056(590)	2046(402)	1730
Δ(1940)	D_{33}	*		2080			
Δ(1950)	F_{37}	****	1923(224)	1940	1921(232)	1923(278)	1816
	P_{33}			1985			
Δ(2000)	F_{35}	**		1990			
	D_{33}			2145			
	D_{35}			2165			
Δ(2150)	S_{31}	*		2140			
Δ(2200)	G_{37}	*	2215(400)	2230			2162
	G_{37}			2295			
	D_{35}			2325			
Δ(2300)	H_{39}	**	2217(300)	2420			2407
Δ(2350)	D_{35}	*	2305(300)	2265			
Δ(2390)	F_{37}	*	2425(300)	2370			
Δ(2400)	G_{39}	**	2468(480)	2295			2083
Δ(2420)	$H_{3,11}$	****	2416(340)	2450			2327
	F_{37}			2460			
	H_{39}			2505			
Total: 20			16	27	8	7	13

Table 3. Elastic π^+p scattering (regions of possible discrete ambiguities)

Momentum interval, MeV/c	C.m.s. angular interval, deg	Differential cross section, mb/sr
700–900	90–110	0.03–0.18
800–1000	155–175	0.08–0.60
800–1200	80–100	0.13–0.27
1600–1900	50–70	0.08–0.30
1800–2100	130–150	0.03–0.13

Table 4. Elastic π^-p scattering (regions of possible discrete ambiguities)

Momentum interval, MeV/c	C.m.s. angular interval, deg	Differential cross section, mb/sr
600–800	60–80	0.06–0.20
600–800	100–120	1.0–1.4
1200–1400	150–170	0.30–0.53
1200–1500	60–80	0.05–0.23
1200–1500	90–110	0.25–0.40
1800–2100	140–150	0.002–0.010
2000–2100	130–150	0.001–0.003

at resolving the discrete ambiguities of the available PWAs is completely justified and it should be continued up to the complete resolution of all presumably existing discrete ambiguities. It would provide an unambiguous reconstruction of the πN amplitude and finally determine the spectrum of nonstrange baryon resonances.

ON THE PROGRAM OF MEASUREMENTS OF THE SPIN ROTATION PARAMETERS A AND R IN THE RESONANCE REGION OF πN INTERACTION

Comparison of the PWA predictions in a wide range of pion momenta is conveniently performed using the Barrelet zero method [10] for the πN amplitude. Analysis of the trajectories of the πN-amplitude zeros reveals the intervals of the kinematic variables where discrete ambiguities in the PWA procedure can appear and where, therefore, the spin rotation parameters A and R should be measured in elastic πN scattering [11].

Tables 3 and 4 display the results of the analysis of the zero trajectories up to a pion momentum of 2100 MeV/c and indicate the regions of the kinematic variables where additional measurements of the spin rotation parameters A and R are required [12]. The measurements are expected to be performed at the J-PARC accelerator under construction in Japan.

REFERENCES

1. G. Höhler, *Handbook of Pion–Nucleon Scattering, Physics Data* (Fachinformationszentrum, Karlsruhe, 1979), No. 12-1.
2. R. E. Cutcosky *et al.*, Phys. Rev. D **20**, 2839 (1979).
3. C. Bricman *et al.*, Rev. Mod. Phys. **52**, S1 (1980).
4. K. Hagiwara *et al.*, Phys. Rev. D **66**, 010001 (2002).
5. R. A. Arndt *et al.*, nucl-th/0311089.
6. M. P. Mattis and M. Karliner, Phys. Rev. D **31**, 2833 (1985).
7. S. Capstick and W. Roberts, Phys. Rev. D **49**, 4570 (1994).
8. R. A. Arndt *et al.*, Phys. Rev. C **52**, 2120 (1995).
9. I. G. Alekseev *et al.*, Phys. Lett. B **485**, 32 (2000).
10. I. G. Alekseev *et al.*, Eur. Phys. J. A **12**, 117 (2001).
11. V. V. Sumachev, Doctoral Dissertation in Mathermatical Physics (St. Petersburg, 1998).
12. LOI-01 for J-PARC, http://psux1.kek.jp/~jhf-np/LOIlist/LOIlist.html

Translated by M. Kobrinsky

Physics of Atomic Nuclei, Vol. 68, No. 6, 2005, pp. 1042–1045. Translated from Yadernaya Fizika, Vol. 68, No. 6, 2005, pp. 1083–1086.
Original Russian Text Copyright © 2005 by Rybakov.

PROCEEDINGS OF THE CONFERENCE "PHYSICS OF FUNDAMENTAL INTERACTIONS" DEDICATED TO THE 100th ANNIVERSARY OF A.I. ALIKHANOV'S BIRTH, SECTION OF NUCLEAR PHYSICS, DIVISION OF PHYSICAL SCIENCES, RUSSIAN ACADEMY OF SCIENCES; INSTITUTE OF THEORETICAL AND EXPERIMENTAL PHYSICS, MOSCOW, MARCH 1–5, 2004

Chiral Self-Gravitating Cosmic Vortices

Yu. P. Rybakov*

Department of Theoretical Physics, Russian University of Peoples' Friendship, ul. Miklukho-Maklaya 6, Moscow, 117198 Russia

Received May 24, 2004

Abstract—In the framework of general relativity, an exact axisymmetric (vortex) solution of the equations of motion is obtained for the $SU(2)$ symmetric sigma model. This solution is characterized by the topological charge (winding number) and angular deficit. In the linearized approximation, the Lyapunov stability of vortices is proved and the deflection angle of a light ray in the gravitational field of the vortex (gravitational lens effect) is calculated. © *2005 Pleiades Publishing, Inc.*

1. INTRODUCTION

Cosmic strings or vortices could have arisen in the early Universe as topological defects due to a series of phase transitions associated with the spontaneous breaking of several internal symmetries [1]. In certain scenarios, cosmic strings play an important role in the formation of galaxies and stratified structures in the Universe [2, 3]. In turn, chiral fields appear due to the spontaneous breaking of chiral symmetry in the low-energy limit of QCD [4]. For this reason, it is natural to describe cosmic strings in terms of chiral fields.

In this study, in the framework of a simple $SU(2)$ sigma model, we show that the chiral field equations combined with the Einstein equations allow static vortex solutions. Such solutions can be characterized by the topological charge Q and angular deficit Δ, which increases monotonically with the distance from the vortex axis. We find that the angular deficit at spatial infinity, the topological charge, and the linear mass density of the vortex are proportional to each other.

A straightforward calculation shows that the second derivative of the vortex energy E with respect to radial variations of the metric and chiral field is positive definite. Therefore, the vortex is stable in the Lyapunov sense. Then we solve the equations for the photon geodesic in the gravitational field of a string and evaluate the deflection angle for the photon moving at a right angle to the vortex axis.

*e-mail: yrybakov@sci.pfu.edu.ru

2. STRUCTURE OF THE VORTEX SOLUTION

We assume that the Lagrangian density has the form

$$\mathcal{L} = -\frac{1}{4\lambda^2}\mathrm{tr}\,(\ell_\mu \ell^\mu) + \frac{1}{2\varkappa}R. \qquad (1)$$

Here, λ is the length parameter of the model (we use the system of units in which $\hbar = c = 1$); $\varkappa = 8\pi G$, where G is the gravitational constant; R is the scalar curvature of the gravitational field; $\ell_\mu = U^+\partial_\mu U$ is the left chiral current in terms of the matrix $U \in SU(2)$; and Greek indices run the values 0, 1, 2, and 3. When the Z axis is directed along the vortex, the axisymmetric metric has the form

$$ds^2 = e^{2\mu}dt^2 - e^{2\alpha}dx^2 - e^{2\beta}d\varphi^2 - e^{2\gamma}dz^2, \qquad (2)$$

where φ is the azimuth angle, $0 \le \varphi < 2\pi$, and x is the generalized radial variable, $-\infty \le x \le \infty$. In this case, the value $x = -\infty$ is associated with the vortex axis, and the value $x = \infty$, with spatial infinity. The metric functions μ, α, β, and γ in Eq. (2) depend only on x and it is assumed that they satisfy the Bronnikov condition for the coordinates [5]:

$$\alpha = \mu + \beta + \gamma. \qquad (3)$$

We assume that, in the transverse section of the vortex, the chiral field $U(x, \varphi)$ has a "hedgehog" structure [6]; that is, it is invariant under the group

$$G = T(z) \otimes \mathrm{diag}\,[SO(2)_I \otimes SO(2)_S], \qquad (4)$$

which involves translations along the Z axis and combined rotations about the third axis in both isotopic (I) and coordinate (S) spaces. The hedgehog fields have the form

$$U = \exp(i\tau\Theta),\ \tau = \tau_1\cos\psi + \tau_2\sin\psi,\ \psi = k\varphi, \qquad (5)$$

1063-7788/05/6806-1042$26.00 © 2005 Pleiades Publishing, Inc.

where τ_1 and τ_2 are the Pauli matrices, $\Theta = \Theta(x)$ is the chiral angle, and k is an integer (that is assumed to be positive) that is the winding number or the topological charge characterizing the mapping $Q = \deg\left(S^2 \to S^2\right)$. The latter statement can be deduced as follows. Let the angles Θ and ψ be the coordinates on the sphere $S^2 \subset SU(2)$ and

$$Q = \frac{1}{4\pi}\int\limits_{S^2} d\Theta d\psi \sin\Theta. \tag{6}$$

Then, the equality $Q = -k$ is a consequence of the boundary conditions

$$\Theta(\infty) = 0, \quad \Theta(-\infty) = \pi. \tag{7}$$

Since the corresponding charge for the mapping $S^3 \to S^3$ in the Skyrme model is treated as the baryon number, we relate k to the linear density of the baryon charge of the vortex.

Since metric (2) and chiral field (5) are invariant under transformations (4), we make use of the Coleman–Palais principle [7] for the determination of the critical points of invariant functionals so that only invariant variations are taken into consideration. Substituting Eqs. (2) and (5) into the expression for the action

$$\mathcal{A} = \int d^4x\sqrt{-g}\mathcal{L} \tag{8}$$

of system (1), we separate the radial part in expression (8) that is given by the functional

$$E = \frac{\pi}{\lambda^2}\int dx e^{\mu+\gamma} \tag{9}$$
$$\times\left[-\frac{2\lambda^2}{\varkappa}e^{\beta-\alpha}\left(\beta'\gamma' + \mu'\beta' + \mu'\gamma'\right)\right.$$
$$\left. + e^{\beta-\alpha}\Theta'^2 + k^2 e^{\alpha-\beta}\sin^2\Theta\right],$$

which is the expression for the vortex energy per unit length.

It should be noted that functional (9) and coordinate condition (3) are invariant under the replacement $\mu \rightleftarrows \gamma$. For this reason, a particular solution can be taken in the form $\mu = \gamma$. In what follows, it is convenient to introduce the variables

$$w = \alpha - \beta - 2\gamma, \quad u = 4(\beta+\gamma), \quad v = 4\beta. \tag{10}$$

Functional (9) in terms of these variables has the form

$$E = \frac{\pi}{\lambda^2}\int dx\left[\left(\frac{1}{\nu}\left(v'^2 - u'^2\right) + \Theta'^2\right)e^{-w}\right. \tag{11}$$
$$\left. + k^2\sin^2\Theta e^{w+u-v}\right],$$

where $\nu = 8\varkappa/\lambda^2$.

Since the equation for the field Θ is a consequence of the Einstein equations, it is sufficient to vary functional (11) with respect to the variables w, u, and v. In view of Eqs. (10) and (3), we obtain the condition $w = 0$ and the system of equations

$$\frac{1}{\nu}\left(u'^2 - v'^2\right) = \Theta'^2 - k^2\sin^2\Theta\, e^{u-v}, \tag{12}$$

$$\frac{2}{\nu}u'' = -k^2\sin^2\Theta\, e^{u-v}, \tag{13}$$

$$\frac{2}{\nu}v'' = -k^2\sin^2\Theta\, e^{u-v}. \tag{14}$$

Here, we consider the simplest symmetric solution of Eqs. (12)–(14) that satisfies the condition

$$u = v. \tag{15}$$

In this case, Eq. (12) with boundary conditions (7) allows a solution analogous to the domain-wall solution in the sine-Gordon model:

$$\Theta(x) = 2\arctan e^{-kx}. \tag{16}$$

When solving the remaining Eqs. (13) and (14), it is necessary to take into consideration the condition that space at the vortex axis is locally Euclidean. Therefore, as $x \to -\infty$, we arrive at

$$e^{\alpha}dx \to de^{\beta} = e^{\beta}d\beta. \tag{17}$$

Then, we substitute Eq. (16) into (13) or (14); i.e., we set

$$\sin\Theta = 2e^{-kx}\left(1 + e^{-2kx}\right)^{-1}. \tag{18}$$

Taking Eqs. (10), (15), and (17) into account, we obtain the metric parameters

$$\alpha = \beta = x - \frac{\varkappa}{\lambda^2}\ln\left(1 + e^{2kx}\right) + C, \tag{19}$$

where C is the integration constant and

$$\mu = \gamma = 0. \tag{20}$$

It should be noted that, outside the vortex axis (at $x \neq -\infty$), the resulting metric that is given by Eqs. (19) and (20) is characterized by the angular deficit

$$\Delta(x) = 2\pi\left(1 - e^{\beta-\alpha}\beta'\right),$$

that is, by the deviation of the circumference-to-radius ratio from 2π. Thus, the space outside the vortex axis is of the conical type, which is typical for cosmic strings [1]. Using Eq. (19), we compute the angular deficit at spatial infinity:

$$\Delta \equiv \lim_{x\to\infty} 2\pi\left(1 - \beta'\right) = \frac{4\pi\varkappa}{\lambda^2}k. \tag{21}$$

It is instructive to compare expression (21) with the vortex energy E. Substitution of Eqs. (15) and (18) into formula (11) gives

$$E = \frac{\pi}{\lambda^2}\int dx\left(\Theta'^2 + k^2\sin^2\Theta\right) = \frac{4\pi}{\lambda^2}k. \qquad (22)$$

A comparison of expressions (21) and (22) shows that the angular deficit at spatial infinity is proportional to the linear density of the vortex energy:

$$\Delta = \varkappa E = 8\pi G E. \qquad (23)$$

This result is also a well-known feature of cosmic strings [1].

3. STABILITY OF CHIRAL COSMIC VORTICES

We check the Lyapunov stability [8] of the solution under radial perturbations, taking the energy E of the perturbed vortex as the Lyapunov functional. Considering quantities α, β, γ, μ, and Θ as functions of time t and the generalized radial variable x, we derive the integral of motion for action (8):

$$E = \frac{\pi}{\lambda^2}\int dx e^{\gamma}\Bigg[-\frac{2\lambda^2}{\varkappa}e^{\beta} \qquad (24)$$
$$\times\Bigg[\left(\dot\alpha\left(\dot\beta+\dot\gamma\right)+\dot\beta\dot\gamma\right)e^{\alpha-\mu}$$
$$+\left(\mu'\left(\beta'+\gamma'\right)+\beta'\gamma'\right)e^{\mu-\alpha}\Bigg] + k^2\sin^2\Theta\, e^{\alpha+\mu-\beta}$$
$$+e^{\beta}\left(\dot\Theta^2 e^{\alpha-\mu}+\Theta'^2 e^{\mu-\alpha}\right)\Bigg],$$

where a dot denotes the derivative with respect to time t. To make sure that the minimum of functional (24) corresponds to the unperturbed solution, we introduce variations of the metric and chiral angle Θ:

$$\delta\alpha = a, \quad \delta\beta = b, \quad \delta\gamma = c, \qquad (25)$$
$$\delta\mu = d, \quad \delta\Theta = \eta.$$

Since the first variation of functional (24) vanishes for the unperturbed solution ($\delta E = 0$), we should evaluate the second variation $\delta^2 E$ under the coordinate condition

$$d + c = 0 \qquad (26)$$

imposed on perturbations. Under this condition, the functional $\delta^2 E$ has the form

$$\delta^2 E = \frac{\pi}{\lambda^2}\int dx\left[\frac{4\lambda^2}{\varkappa}\left[c'^2 - e^{2\alpha}\left(\dot a\dot b + \dot a\dot c + \dot b\dot c\right)\right]\right. \qquad (27)$$
$$+2e^{2\alpha}\dot\eta^2 + \Theta'^2(b-a)^2 + 4\Theta'\eta'(b-a) + 2\eta'^2$$
$$\left.+k^2\left[(b-a)^2\sin^2\Theta + 2\eta^2\cos 2\Theta - 2\eta(b-a)\sin 2\Theta\right]\right].$$

Linearized equations for perturbations are readily obtained from the expression for functional (27). It is important that these equations allow the integral of motion

$$a + b + 2c = 0, \qquad (28)$$

which implies the hyperbolic equation for perturbation c:

$$e^{2\alpha}\ddot c - c'' = 0. \qquad (29)$$

Equation (29) indicates that c perturbations are stable in the corresponding functional metric. Excluding these perturbations with the use of Eq. (28) and taking into account the equation $\Theta' = -k\sin\Theta$ for the unperturbed chiral angle Θ, we reduce Eq. (27) to the form

$$\delta^2 E = \frac{\pi}{\lambda^2}\int dx\left[\frac{\lambda^2}{\varkappa}e^{2\alpha}\left(\dot a^2 + \dot b^2\right)\right. \qquad (30)$$
$$+\frac{\lambda^2}{2\varkappa}\left(a'+b'\right)^2 + e^{2\alpha}\dot\eta^2$$
$$\left.+\left[\eta' + k\eta\cos^2\Theta - k(b-a)\sin\Theta\right]^2\right].$$

Thus, the second variation of the vortex energy (30) is reduced to the sum of positive functionals. Therefore, cosmic strings are stable in the linearized approximation.

4. LIGHT DEFLECTION IN THE GRAVITATIONAL FIELD OF THE VORTEX

Assuming that a ray of light travels in a plane orthogonal to the vortex and taking time t as a parameter, we write the geodesic equation in the form

$$\ddot x + \alpha'\left(\dot x^2 - \dot\varphi^2\right) = 0, \qquad (31)$$
$$\ddot\varphi + 2\alpha'\dot\varphi\dot x = 0, \qquad (32)$$

where the function $\alpha(x)$ is defined by expression (19). From formulas (2), (31), and (32) and the equations $dz = ds^2 = 0$ and $\alpha' = \dot\alpha/\dot x$, we derive the integrals of motion

$$e^{2\alpha}\left(\dot x^2 + \dot\varphi^2\right) = 1, \quad \dot\varphi e^{2\alpha} = e^{\alpha_0} = \text{const}. \qquad (33)$$

From formula (33) it follows that $\alpha_0 = \alpha(x_0)$, where x_0 is the coordinate of the ray point closest to the vortex. Then, the ray trajectory is determined by the equation

$$\varphi' = \dot\varphi/\dot x = \left(e^{2(\alpha-\alpha_0)} - 1\right)^{-1/2}. \qquad (34)$$

From fromula (19) it follows that

$$\alpha' = 1 - \frac{2k\varkappa}{\lambda^2}\left(1 + e^{-2kx}\right)^{-1}. \qquad (35)$$

Considering that the value of k is sufficiently small (such that $\alpha' > 0$) and using formulas (34) and (35), we derive the expression for the total deflection angle $\delta\varphi$:

$$\delta\varphi = -\pi + 2\int_{\alpha_0}^{\infty} \frac{d\alpha}{\alpha'}\left(e^{2(\alpha-\alpha_0)} - 1\right)^{-1/2}. \qquad (36)$$

In particular, formula (36) at $\alpha' \approx 1$ implies that

$$\delta\varphi \approx \frac{2k\pi\varkappa}{\lambda^2}\left(1 + e^{-2kx_0}\right)^{-1}. \qquad (37)$$

Expression (37) for the deflection angle of light in the gravitational field of the vortex agrees well with the result obtained by Vilenkin [1] for $\exp(-2kx_0) \ll 1$, that is, for a sufficiently large topological charge k at $x_0 > 0$.

5. CONCLUSIONS

As was emphasized in [1], the hypothesis of cosmic strings (vortices) can be considered as plausible if the dimensionless string parameter is on the order of

$$GE \sim 10^{-6}.$$

With the length parameter $\lambda = 2/F_\pi$, where $F_\pi \approx 186$ MeV is the pion decay constant [6], that is standard for low-energy pion physics, formula (22) provides the following estimate for the topological charge of a vortex:

$$k \sim 10^{33}.$$

We note that the hypothesis of existing cosmic strings is supported by the gravitational lense effect reported in [9–13]. In addition, the existence of cosmic strings is supported by other effects. First, fast moving strings can generate "wakes," which give rise to flat structures in the Universe [14]. Second, cosmic strings can give rise to additional electromagnetic radiation of charged particles that can account for the observed anisotropy of the cosmic background radiation [15].

ACKNOWLEDGMENTS

I am grateful to T.I. Belova, A.E. Kudryavtsev, and V.P. Pavlov for stimulating discussions. This work was supported in part by the scientific program "Russian Universities" (project no. UR.01.01.035).

REFERENCES

1. A. Vilenkin and E. P. S. Shellard, *Cosmic Strings and Other Topological Defects* (Cambridge Univ. Press, Cambridge, 1994).
2. Ya. B. Zel'dovich, Mon. Not. R. Astron. Soc. **192**, 603 (1980).
3. A. Vilenkin, Phys. Rev. Lett. **46**, 1169 (1981).
4. N. I. Karchev and A. A. Slavnov, Teor. Mat. Fiz. **65**, 192 (1985).
5. K. A. Bronnikov, Probl. Teor. Gravitatsii Elem. Chastits **10**, 37 (1979).
6. I. Zahed and G. E. Brown, Phys. Rep. **142**, 1 (1986).
7. R. Palais, Commun. Math. Phys. **69**, 19 (1979).
8. V. I. Zubov, *A. M. Lyapunov's Methods and Their Applications* (Leningrad. Gos. Univ., Leningrad, 1957) [in Russian].
9. M. Sazhin *et al.*, Mon. Not. R. Astron. Soc. **343**, 353 (2003).
10. Andrew A. de Laix, Phys. Rev. D **56**, 6193 (1997).
11. D. L. Ossipov, Grav. Cosmol. **2**, 61 (1996).
12. P. V. Bliokh and A. A. Minakov, *Gravitational Lenses* (Naukova Dumka, Kiev, 1989) [in Russian].
13. A. F. Zakharov, *Gravitational Lenses and Microlenses* (Yanus, Moscow, 1997) [in Russian].
14. M. S. Turner and J. A. Tyson, Rev. Mod. Phys. **71**, S145 (1999).
15. D. P. Bennett, A. Stebbins, and F. R. Bouchet, Astrophys. J. **399**, 5 (1992).

Translated by R. Rogalyov

Physics of Atomic Nuclei, Vol. 68, No. 6, 2005, pp. 1046–1053. From Yadernaya Fizika, Vol. 68, No. 6, 2005, pp. 1087–1094.
Original English Text Copyright © 2005 by Blaschke, Prozorkevich, Reichel, Smolyansky.

PROCEEDINGS OF THE CONFERENCE "PHYSICS OF FUNDAMENTAL INTERACTIONS" DEDICATED TO THE 100th ANNIVERSARY OF A.I. ALIKHANOV'S BIRTH, SECTION OF NUCLEAR PHYSICS, DIVISION OF PHYSICAL SCIENCES, RUSSIAN ACADEMY OF SCIENCES; INSTITUTE OF THEORETICAL AND EXPERIMENTAL PHYSICS, MOSCOW, MARCH 1–5, 2004

Kinetic Description of Vacuum Creation of Massive Vector Bosons*

D. B. Blaschke[1),2)], A. V. Prozorkevich, A. V. Reichel[1)], and S. A. Smolyansky**

Saratov State University, Saratov, Russia

Received May 24, 2004

Abstract—In the simple model of massive vector field in a flat spacetime, we derive the kinetic equation of non-Markovian type describing the vacuum pair creation under action of external fields of different nature. We use for this aim the nonperturbative methods of kinetic theory in combination with a new element when the transition of the instantaneous quasiparticle representation is realized within the oscillator (holomorphic) representation. We study in detail the process of vacuum creation of vector bosons generated by a time-dependent boson mass in accordance with the framework of a conformal-invariant scalar-tensor gravitational theory and its cosmological application. It is indicated that the choice of the equation of state allows one to obtain a number density of vector bosons that is sufficient to explain the observed number density of photons in the cosmic microwave background radiation. © *2005 Pleiades Publishing, Inc.*

1. INTRODUCTION

The vacuum creation of massive vector bosons in intense fields of different nature is widely discussed in the literature [1–3] because of its twofold role. On the one hand, massive vector bosons play an important role in different physical problems [4] and particularly in cosmology (e.g., [5, 6]). On the other hand, the massive vector field is the simplest example of a quantum field theory with higher spin and attracts close attention nowadays [7].

In this contribution, we give a kinetic description of the vacuum creation of charged massive vector bosons under the influence of a time-dependent spatially uniform electric field of arbitrary polarization. We also consider the possibility of a time-dependent mass that represents a new independent mechanism of vacuum particle production. The use of kinetic methods in the formulation allows one to obtain a rather general solution of the nonperturbative problem for an arbitrary time dependence of the strong external fields. The nonperturbative approach is particularly appropriate for fast changing fields such as, for example, in the case of time-dependent vector-boson masses in the vicinity of the cosmological singularity (see Section 4).

The construction of a kinetic theory of vacuum particle creation on a dynamical basis requires the time-dependent quasiparticle representation (QPR) [8, 9]. We use the oscillator representation for this aim [9] as the most effective instrument for the derivation of dynamical equations in the QPR (Section 2). We introduce here two types of QPR: the complete one (based on the full diagonalization of all physical quantities in the Fock and spin spaces) and the incomplete one which leaves the spin projection uncertain. Further, in Section 3, we use these results for the derivation of the kinetic equations (KE). A new feature of the obtained system of KE is the presence of a tensor distribution function in a rotating coordinate system with the orientation defined by a time-dependent kinematic momentum that results in a new type of non-Markovian processes. A significant simplification is achieved when the non-Markovian effects are neglected. The case of the absence of an electric field is considered in detail when the vacuum creation is caused entirely by the time dependence of the mass. The system of KE splits into separate equations for the transverse and longitudinal components, which can be investigated numerically. As an application, we reinvestigate in Section 4 the creation of massive vector bosons in the early Universe within a conformal invariant scalar-tensor theory of gravitation as suggested earlier by Pervushin and collaborators [5, 10]. In this approach, the time dependence of the scalar field entails a cosmological evolution of all particle masses, which, according to F. Hoyle and J.V. Narlikar, may serve as an explanation for the cosmological redshift alternative to the Hubble

*This article was submitted by the authors in English.

[1)]Fachbereich Physik, Universität Rostock, Germany.

[2)]Fakultät für Physik, Universität Bielefeld, Germany; Joint Institute for Nuclear Research, Dubna, Russia.

**e-mail: smol@sgu.ru

expansion. In the present approach, we are able to remove the singularity in the density of the produced longitudinal vector bosons reported previously [5]. We present a solution of the KE for a toy model, where the time dependence of the scalar field is given, and show that the density of vector bosons created in the early Universe corresponds to the number density of cosmic microwave background (CMB) photons. In Section 5, we summarize and present the conclusion.

We use the metric $g^{\mu\nu} = \mathrm{diag}(1, -1, -1, -1)$ and the natural units $\hbar = c = 1$.

2. THE QUASIPARTICLE REPRESENTATION

We consider here the vacuum creation of charged massive vector bosons in the flat Minkowski spacetime by the action of two mechanisms: (i) a time variation of boson mass $m(t)$ and (ii) the action of some classical spatially homogeneous time-dependent electric field with 4-potential (in the Hamilton gauge)

$$A^\mu(t) = \left(0, A^1(t), A^2(t), A^3(t)\right), \qquad (1)$$

where the corresponding field strength is $\mathbf{E} = -\dot{\mathbf{A}}$ and the overdot denotes the time derivative.

Thus, the field can be considered either as an external field or as a result of the mean-field approximation, based on the substitution of the quantized electric field $\tilde{A}^k(t)$ with its mean value $\langle \tilde{A}^k(t) \rangle = A^k(t)$, where the symbol $\langle \ldots \rangle$ denotes some averaging operation. The time dependence of the vector-boson mass can be interpreted as a result of the coupling to some average Higgs field. In the kinetic theory, the consideration of fluctuations leads to collision integrals [11]. Thus, the mean-field approximation corresponds to the neglect of dissipative effects.

We will restrict ourselves to the simplest version of the theory with the Lagrange density

$$\mathcal{L}(x) = -D^*_\mu u^*_\nu D^\mu u^\nu + m^2 u^*_\nu u^\nu, \qquad (2)$$

where $D_\mu = \partial_\mu + ieA_\mu$, and e is the charge of the vector field, including its sign. Equation (2) leads to the equation of motion

$$(D_\mu D^\mu + m^2) u_\nu = 0 \qquad (3)$$

with the additional constraint

$$D_\mu u^\mu = 0. \qquad (4)$$

The transition to the QPR can be realized in different ways, e.g., by means of the time-dependent Bogoliubov transformation [2] or with help of the holomorphic (oscillator) representation (OR) [9]. We choose the OR, being a simpler method. The OR can be introduced in the spatially homogeneous case, and it is based on the replacement of the canonical momentum by the kinematic one $\mathbf{p} \to \mathbf{P} = \mathbf{p} - e\mathbf{A}$ in the dispersion law of the free particle $\omega(\mathbf{p}, t) = \sqrt{m^2 + \mathbf{P}^2}$ in the standard decomposition of the free field operators and momenta in the discrete momentum space [12]:

$$u_\mu(x) = \frac{1}{\sqrt{V}} \sum_{\mathbf{p}} \frac{1}{\sqrt{2\omega(\mathbf{p}, t)}} \mathrm{e}^{i\mathbf{p}\cdot\mathbf{x}} \times \left\{ a^{(-)}_\mu(\mathbf{p}, t) + b^{(+)}_\mu(-\mathbf{p}, t) \right\}, \qquad (5)$$

$$\pi_\mu(x) = -\frac{i}{\sqrt{V}} \sum_{\mathbf{p}} \sqrt{\omega(\mathbf{p}, t)} \mathrm{e}^{-i\mathbf{p}\cdot\mathbf{x}} \times \left\{ a^{(+)}_\mu(\mathbf{p}, t) - b^{(-)}_\mu(-\mathbf{p}, t) \right\},$$

where $V = L^3$ and $p_i = (2\pi/L) n_i$ with an integer n_i for each $i = 1, 2, 3$. The substitution into the Hamiltonian

$$H = -\int d\mathbf{x} \left(\pi^*_\mu \pi^\mu + \mathbf{D}^* u^*_\mu \mathbf{D} u^\mu + m^2 u^*_\mu u^\mu \right) \qquad (6)$$

brings it at once to a diagonal form in the Fock space, which corresponds to the QPR

$$H = -\sum_{\mathbf{p}} \omega(\mathbf{p}, t) \Big[a^{(+)}_\mu(\mathbf{p}, t) a^{(-)\mu}(\mathbf{p}, t) + b^{(-)}_\mu(-\mathbf{p}, t) b^{(+)\mu}(-\mathbf{p}, t) \Big]. \qquad (7)$$

However, this quadratic form is not positively defined. In order to exclude the $\mu = 0$ component with the help of the additional condition (4), it is necessary to derive the equations for the amplitudes $a^\pm, b^\pm$.

Substituting (5) into the Hamiltonian equations

$$\dot{u}_\mu = \frac{\delta H}{\delta \pi^\mu} = -\pi^*_\mu, \qquad (8)$$

$$\dot{\pi}_\mu = -\frac{\delta H}{\delta u^\mu} = m^2 u^*_\mu - \mathbf{D}^* \mathbf{D}^* u^*_\mu,$$

we find the Heisenberg-type equation of motion for the time-dependent creation and annihilation amplitudes

$$\dot{a}^{(\pm)}_\mu(\mathbf{p}, t) = \frac{1}{2} \Delta(\mathbf{p}, t) b^{(\mp)}_\mu(-\mathbf{p}, t) \pm i\omega(\mathbf{p}, t) a^{(\pm)}_\mu(\mathbf{p}, t), \qquad (9)$$

$$\dot{b}^{(\pm)}_\mu(-\mathbf{p}, t) = \frac{1}{2} \Delta(\mathbf{p}, t) a^{(\mp)}_\mu(\mathbf{p}, t) \pm i\omega(\mathbf{p}, t) b^{(\pm)}_\mu(-\mathbf{p}, t),$$

where

$$\Delta(\mathbf{p}, t) = \frac{\dot{\omega}(\mathbf{p}, t)}{\omega(\mathbf{p}, t)}. \qquad (10)$$

Analogous equations were obtained in [9] for the case of scalar QED on the basis of the principle of least action.

Thus, the Hamiltonian formalism in the OR leads to the exact equations of motion (9) for the creation and annihilation operators of quasiparticles, depending on the "natural" representation of the quasiparticle energy $\omega(\mathbf{p},t)$ in the external field (1).

The additional conditions (4) may be transformed now with the help of Eqs. (9) to the following form ($i=1,2,3$):

$$\omega(\mathbf{p},t)a_0^{(\pm)}(\mathbf{p},t)=P_i a_i^{(\pm)}(\mathbf{p},t), \qquad (11)$$
$$\omega(\mathbf{p},t)b_0^{(\pm)}(-\mathbf{p},t)=-P_i b_i^{(\pm)}(-\mathbf{p},t).$$

These equations allow one to exclude the $\mu=0$ component in the Hamiltonian (7), which gives

$$H=\sum_{\mathbf{p}}\omega(\mathbf{p},t) \qquad (12)$$
$$\times\left\{a_i^{(+)}(\mathbf{p},t)a_i^{(-)}(\mathbf{p},t)+b_i^{(-)}(-\mathbf{p},t)b_i^{(+)}(-\mathbf{p},t)\right.$$
$$-\frac{1}{\omega^2(\mathbf{p},t)}\left[\left(P_i a_i^{(+)}(\mathbf{p},t)\right)\left(P_k a_k^{(-)}(\mathbf{p},t)\right)\right.$$
$$\left.\left.+\left(P_i b_i^{(-)}(-\mathbf{p},t)\right)\left(P_k b_k^{(+)}(-\mathbf{p},t)\right)\right]\right\}.$$

The next step is the additional diagonalization of the quadratic form (12) by means of the linear transformations [12]

$$\mathbf{a}^{(\pm)}(\mathbf{p},t)=E\boldsymbol{\alpha}^{(\pm)}(\mathbf{p},t) \qquad (13)$$
$$\equiv \mathbf{e}_1\alpha_1^{(\pm)}(\mathbf{p},t)+\mathbf{e}_2\alpha_2^{(\pm)}(\mathbf{p},t)+\mathbf{e}_3\frac{\omega}{m}\alpha_3^{(\pm)}(\mathbf{p},t),$$
$$\mathbf{b}^{(\pm)}(-\mathbf{p},t)=E\boldsymbol{\beta}^{(\pm)}(-\mathbf{p},t)\equiv \mathbf{e}_1\beta_1^{(\pm)}(-\mathbf{p},t)$$
$$+\mathbf{e}_2\beta_2^{(\pm)}(-\mathbf{p},t)+\mathbf{e}_3\frac{\omega}{m}\beta_3^{(\pm)}(-\mathbf{p},t),$$

where $[\mathbf{e}_1(\mathbf{p},t),\mathbf{e}_2(\mathbf{p},t),\mathbf{e}_3(\mathbf{p},t)]$ determine the local rotating basis built on the vector $\mathbf{e}_3=\mathbf{P}/|P|$. These real unit vectors form the triad

$$e_{ik}e_{jk}=e_{ki}e_{kj}=\delta_{ij}, \qquad e_{ik}=(\mathbf{e}_i)_k. \qquad (14)$$

The presence of the factor ω/m in the nonunitary matrix E in Eq. (13) leads to a violation of the unitary equivalence between the (a,b) and (α,β) representations.

The transformation (13) leads to the positively defined Hamiltonian

$$H=\sum_{\mathbf{p}}\omega(\mathbf{p},t) \qquad (15)$$
$$\times\left[\alpha_i^{(+)}(\mathbf{p},t)\alpha_i^{(-)}(\mathbf{p},t)+\beta_i^{(-)}(-\mathbf{p},t)\beta_i^{(+)}(-\mathbf{p},t)\right].$$

Let us write the equations of motion for these new amplitudes as the result of a combination of Eqs. (9) and (13):

$$\dot\alpha_i^{(\pm)}(\mathbf{p},t)=\frac{1}{2}\Delta(\mathbf{p},t)\beta_i^{(\mp)}(-\mathbf{p},t) \qquad (16)$$
$$\pm i\omega(\mathbf{p},t)\alpha_i^{(\pm)}(\mathbf{p},t)+\eta_{ij}(\mathbf{p},t)\alpha_j(\mathbf{p},t),$$
$$\dot\beta_i^{(\pm)}(-\mathbf{p},t)=\frac{1}{2}\Delta(\mathbf{p},t)\alpha_i^{(\mp)}(\mathbf{p},t)$$
$$\pm i\omega(\mathbf{p},t)\beta_i^{(\pm)}(-\mathbf{p},t)+\eta_{ij}(\mathbf{p},t)\beta_j(-\mathbf{p},t).$$

The spin rotation matrix η_{ij} is defined as

$$\eta(\mathbf{p},t)=\begin{bmatrix}0 & \dot{\mathbf{e}}_1\cdot\mathbf{e}_2 & \frac{\omega}{m}\dot{\mathbf{e}}_1\cdot\mathbf{e}_3\\ -\dot{\mathbf{e}}_1\cdot\mathbf{e}_2 & 0 & \frac{\omega}{m}\dot{\mathbf{e}}_2\cdot\mathbf{e}_3\\ -\frac{m}{\omega}\dot{\mathbf{e}}_1\cdot\mathbf{e}_3 & -\frac{m}{\omega}\dot{\mathbf{e}}_2\cdot\mathbf{e}_3 & -\Delta_m,\end{bmatrix}, \qquad (17)$$

where $\Delta_m=-\dot m/m+\Delta$. Together with the Hamiltonian (7), the operators of total momentum and charge also take a diagonal form. However, the spin operator

$$S_i=\varepsilon_{ijk}\int d\mathbf{x}\left[u_k^*\pi_j^*+\pi_j u_k-u_j^*\pi_k^*-\pi_k u_j\right] \qquad (18)$$

has a nondiagonal form in spin space in terms of the operators $\alpha^{(\pm)}$ and $\beta^{(\pm)}$:

$$S_k=i\varepsilon_{ijk}\sum_{\mathbf{p}}\left[\alpha_i^{(+)}(\mathbf{p},t)\alpha_j^{(-)}(\mathbf{p},t)\right. \qquad (19)$$
$$\left.-\beta_i^{(-)}(-\mathbf{p},t)\beta_j^{(+)}(-\mathbf{p},t)\right].$$

In particular, the spin projection onto the momentum 3-axis is

$$S_3=i\sum_{\mathbf{p}}\left[\alpha_1^{(+)}(\mathbf{p},t)\alpha_2^{(-)}(\mathbf{p},t)\right. \qquad (20)$$
$$-\alpha_2^{(+)}(\mathbf{p},t)\alpha_1^{(-)}(\mathbf{p},t)+\beta_2^{(-)}(-\mathbf{p},t)\beta_1^{(+)}(-\mathbf{p},t)$$
$$\left.-\beta_1^{(-)}(-\mathbf{p},t)\beta_2^{(+)}(-\mathbf{p},t)\right].$$

Thus, this representation can be called an incomplete quasiparticle one with nonfixed spin projection. The operator (20) can be diagonalized with a linear transformation to the circularly polarized waves basis [12]

$$c_i^{(\pm)}(\mathbf{p},t)=R_{ik}^{(\pm)}\alpha_k^{(\pm)}(\mathbf{p},t), \qquad (21)$$
$$d_i^{(\pm)}(-\mathbf{p},t)=R_{ik}^{(\pm)*}\beta_k^{(\pm)}(-\mathbf{p},t)$$

with the unitary matrix

$$R^{\pm}=\frac{1}{\sqrt{2}}\begin{bmatrix}1 & \mp i & 0\\ \pm i & 1 & 0\\ 0 & 0 & \sqrt{2}\end{bmatrix}. \qquad (22)$$

As a result, the new amplitudes $c^{(\pm)}, d^{(\pm)}$ in the QPR correspond to charged vector quasiparticles with the

total energy, 3-momentum, charge, and spin projection on the chosen direction:

$$H(t) = \sum_{\mathbf{p}} \omega(\mathbf{p},t) \times \left[c_i^{(+)}(\mathbf{p},t)c_i^{(-)}(\mathbf{p},t) + d_i^{(-)}(-\mathbf{p},t)d_i^{(+)}(-\mathbf{p},t)\right], \quad (23)$$

$$\mathbf{\Pi}(t) = \sum_{\mathbf{p}} \mathbf{P}\left[c_i^{(+)}(\mathbf{p},t)c_i^{(-)}(\mathbf{p},t) - d_i^{(-)}(-\mathbf{p},t)d_i^{(+)}(-\mathbf{p},t)\right], \quad (24)$$

$$Q = e\sum_{\mathbf{p}}\left[c_i^{(+)}(\mathbf{p},t)c_i^{(-)}(\mathbf{p},t) - d_i^{(-)}(-\mathbf{p},t)d_i^{(+)}(-\mathbf{p},t)\right], \quad (25)$$

$$S_3(t) = \sum_{\mathbf{p}}\left[c_1^{(+)}(\mathbf{p},t)c_1^{(-)}(\mathbf{p},t) - d_1^{(-)}(-\mathbf{p},t)d_1^{(+)}(-\mathbf{p},t) + d_2^{(-)}(-\mathbf{p},t)d_2^{(+)}(-\mathbf{p},t) - c_2^{(+)}(\mathbf{p},t)c_2^{(-)}(\mathbf{p},t)\right]. \quad (26)$$

This representation can be named the complete quasiparticle one. The equations of motion for these amplitudes follow from Eqs. (16), (21):

$$\dot{c}_i^{(\pm)}(\mathbf{p},t) = \frac{1}{2}\Delta(\mathbf{p},t)d_i^{(\mp)}(-\mathbf{p},t) \pm i\omega(\mathbf{p},t)c_i^{(\pm)}(\mathbf{p},t) + g_{ij}^{(\pm)}(\mathbf{p},t)c_j^{(\pm)}(\mathbf{p},t), \quad (27)$$

$$\dot{d}_i^{(\pm)}(-\mathbf{p},t) = \frac{1}{2}\Delta(\mathbf{p},t)c_i^{(\mp)}(\mathbf{p},t) \pm i\omega(\mathbf{p},t)d_i^{(\pm)}(-\mathbf{p},t) + \overset{*(\pm)}{g}_{ij}(\mathbf{p},t)d_j^{(\pm)}(-\mathbf{p},t).$$

The matrix g_{ij} is defined as

$$g^{(\pm)} = \begin{bmatrix} \pm i\dot{\mathbf{e}}_1\cdot\mathbf{e}_2 & 0 & \frac{\omega}{m}\dot{\mathbf{e}}^{(\mp)}\cdot\mathbf{e}_3 \\ 0 & \mp i\dot{\mathbf{e}}_1\cdot\mathbf{e}_2 & \frac{\omega}{m}\dot{\mathbf{e}}^{(\pm)}\cdot\mathbf{e}_3 \\ -\frac{m}{\omega}\dot{\mathbf{e}}^{(\mp)}\cdot\mathbf{e}_3 & -\frac{m}{\omega}\dot{\mathbf{e}}^{(\pm)}\cdot\mathbf{e}_3 & -\Delta_m \end{bmatrix}, \quad (28)$$

where $\mathbf{e}^{(\pm)} = (\mathbf{e}_1 \pm i\mathbf{e}_2)/\sqrt{2}$.

The transition to this representation from the initial (a,b) one is defined by the combination of the transformations (13) and (21):

$$\mathbf{c}^{(\pm)}(\mathbf{p},t) = U^{(\pm)}(\mathbf{p},t)\mathbf{a}^{(\pm)}(\mathbf{p},t), \quad (29)$$
$$\mathbf{d}^{(\pm)}(-\mathbf{p},t) = U^{(\pm)*}(\mathbf{p},t)\mathbf{b}^{(\pm)}(-\mathbf{p},t)$$

with nonunitary operator

$$U^{(\pm)}(\mathbf{p},t) = R^{(\pm)}E^{-1}(\mathbf{p},t) = \begin{bmatrix} e_1^{(\mp)} & e_2^{(\mp)} & e_3^{(\mp)} \\ e_1^{(\pm)} & e_2^{(\pm)} & e_3^{(\pm)} \\ \frac{m}{\omega}e_{31} & \frac{m}{\omega}e_{32} & \frac{m}{\omega}e_{33} \end{bmatrix}. \quad (30)$$

The quantization problem is to be solved while taking into account the equation of motion (27). It leads to the following noncanonical commutation relations:

$$\left[c_i^{(-)}(\mathbf{p},t), c_j^{(+)}(\mathbf{p}',t)\right] = \left[d_j^{(-)}(\mathbf{p},t), d_i^{(+)}(\mathbf{p}',t)\right] = Q_{ik}^{(-)}(\mathbf{p},t)Q_{jk}^{(+)}(\mathbf{p},t)\delta_{\mathbf{pp}'}, \quad (31)$$

where the matrices $Q_{ij}^{(\pm)}(\mathbf{p},t)$ are defined by the equations

$$\dot{Q}_{ij}^{(\pm)}(\mathbf{p},t) = g_{ik}^{(\pm)}(\mathbf{p},t)Q_{kj}^{(\pm)}(\mathbf{p},t) \quad (32)$$

with the initial conditions

$$\lim_{t\to-\infty} Q_{ij}^{(\pm)}(\mathbf{p},t) = \delta_{ij}; \quad (33)$$

i.e., the commutation relations (31) transform to the canonical form only in the asymptotic limit $t \to -\infty$.

3. KINETIC EQUATION

The standard procedure of the derivation of KE [8] is based on the Heisenberg-type equations of motion (9) or (27). Let us introduce the one-particle correlation functions of vector particles and antiparticles in the initial (a,b) representation

$$F_{\mu\nu}(\mathbf{p},t) = \langle 0_{\text{in}}|a_\mu^{(+)}(\mathbf{p},t)a_\nu^{(-)}(\mathbf{p},t)|0_{\text{in}}\rangle, \quad (34)$$
$$\tilde{F}_{\mu\nu}(\mathbf{p},t) = \langle 0_{\text{in}}|b_\mu^{(-)}(-\mathbf{p},t)b_\nu^{(+)}(-\mathbf{p},t)|0_{\text{in}}\rangle,$$

where the averaging procedure is performed over the in-vacuum state [2]. Differentiating the first one with respect to time, we obtain

$$\dot{F}_{\mu\nu}(\mathbf{p},t) = \frac{1}{2}\Delta(\mathbf{p},t)\left\{F_{\mu\nu}^{(+)}(\mathbf{p},t) + F_{\mu\nu}^{(-)}(\mathbf{p},t)\right\}, \quad (35)$$

where the auxiliary correlation functions are introduced as

$$F_{\mu\nu}^{(\pm)}(\mathbf{p},t) = \langle 0_{\text{in}}|a_\mu^{(\pm)}(\pm\mathbf{p},t)b_\nu^{(\pm)}(\pm\mathbf{p},t)|0_{\text{in}}\rangle. \quad (36)$$

The equations of motion for these functions can be obtained by analogy with Eq. (35). We write them out in the integral form

$$F_{\mu\nu}^{(\pm)}(\mathbf{p},t) = \frac{1}{2}\int_{-\infty}^{t} dt'\Delta(\mathbf{p},t') \quad (37)$$

$$\times \left[F_{\mu\nu}(\mathbf{p},t') + \tilde{F}_{\mu\nu}(\mathbf{p},t')\right] e^{\mp 2i\theta(\mathbf{p};t,t')},$$

where

$$\theta(\mathbf{p};t,t_0) = \int\limits_{t_0}^{t} dt'\omega(\mathbf{p},t'). \tag{38}$$

In Eq. (37), the asymptotic condition $F^{(\pm)}_{\mu\nu}(\mathbf{p},-\infty) = 0$ (the absence of quasiparticles at the initial time) has been introduced. The substitution of Eq. (37) into Eq. (35) leads to the resulting KE

$$\dot{F}_{\mu\nu}(\mathbf{p},t) = \frac{1}{2}\Delta(\mathbf{p},t) \int\limits_{-\infty}^{t} dt'\Delta(\mathbf{p},t')[F_{\mu\nu}(\mathbf{p},t') + \tilde{F}_{\mu\nu}(\mathbf{p},t')]\cos[2\theta(\mathbf{p};t,t')]. \tag{39}$$

This KE is an almost natural generalization of the corresponding KE for scalar particles [8].

Thus, the OR turns out to be an effective method for the diagonalization of the Hamiltonian in the Fock space. It is sufficient for the derivation of the KE (39). However, at this stage, there are a number of problems that are specific for the vector-field theory: the energy is not positively defined, the spin operator has a nondiagonal form in the space of spin states, etc. (Section 2). This circumstance hampers the physical interpretation of the distribution function (34). In order to overcome this difficulty, it is necessary to pass on to the complete QPR in which the system has well-defined values of energy, spin, etc. The simplest way of deriving the KE is the QPR, based on the application of the transformations (29) directly into the KE (39).

3.1. Kinetic Equation in QPR

By analogy with the definitions (34), let us introduce the correlation functions of vector particles and antiparticles in the complete QPR:

$$f_{ik}(\mathbf{p},t) = \langle 0_{\rm in}|c^{(+)}_i(\mathbf{p},t)c^{(-)}_k(\mathbf{p},t)|0_{\rm in}\rangle, \tag{40}$$
$$\tilde{f}_{ik}(\mathbf{p},t) = \langle 0_{\rm in}|d^{(-)}_i(-\mathbf{p},t)d^{(+)}_k(-\mathbf{p},t)|0_{\rm in}\rangle.$$

They are connected with the primordial correlation functions (34) by relations of the type

$$f_{ik}(\mathbf{p},t) = U^{+}_{\rm in}(\mathbf{p},t)U^{-}_{km}(\mathbf{p},t)F_{nm}(\mathbf{p},t), \tag{41}$$

where $F_{nm}(\mathbf{p},t)$ is the "spatial" part of the tensor function $F_{\mu\nu}(\mathbf{p},t)$ (34) $(m,n = 1,2,3)$.

To obtain the resulting KE in the complete QPR, we differentiate the function $f_{ik}(\mathbf{p},t)$ (41) with respect to time and take into account the KE (39):

$$\dot{f}_{ik}(t) = \dot{U}^{(+)}_{ij}(t)U^{(+)-1}_{km}(t)f_{jm}(t) \tag{42}$$
$$+ \dot{U}^{(-)}_{kj}(t)U^{(-)-1}_{jm}(t)f_{im}(t) + \frac{1}{2}U^{(+)}_{ij}(t)U^{(-)}_{kl}(t)\Delta(t) \times \int\limits_{-\infty}^{t} dt'\Delta(t')U^{(+)-1}_{jm}(t')U^{(-)-1}_{ln}(t') \times [f_{mn}(t') + \tilde{f}_{mn}(t')]\cos[2\theta(\mathbf{p};t,t')].$$

In comparison with non-Markovian effects of vacuum tunneling of scalar particles [13], the considered case has its own characteristics related to the dynamics of spin twist.

The system of the integro-differential Eqs. (42) can be reduced to a system of 27 coupled ordinary differential equations that is convenient for numerical calculations. We will not analyze here this rather complicated case and will restrict ourselves below to the consideration of a simple particular case having cosmological motivation.

3.2. Deformation of the Energy Gap

Let us consider the vacuum creation of vector bosons in the case when it is caused by an arbitrary time-dependent deformation of energy gap, i.e., $m = m(t)$ and $A^k(t) = 0$. This is an isotropic case with $P_k = p_k$ and $\dot{\mathbf{e}}_i = 0$. As a result, the KE (42) takes the following form:

$$\dot{f}_{ik}(\mathbf{p},t) = -\Delta_m(\mathbf{p},t)[\delta_{i3}f_{3k}(\mathbf{p},t) + \delta_{k3}f_{i3}(\mathbf{p},t)] + \frac{1}{2}\Delta(\mathbf{p},t) \times \int\limits_{-\infty}^{t} dt'\Delta(\mathbf{p},t')M_{ikjl}(\mathbf{p},t,t') \times [f_{jl}(\mathbf{p},t') + \tilde{f}_{jl}(\mathbf{p},t')]\cos[2\theta(\mathbf{p};t,t')], \tag{43}$$

where

$$M_{ikjl}(t,t') = \delta^{\perp}_{ij}\delta^{\perp}_{kl} + \frac{\omega(t')}{\omega(t)}\frac{m(t)}{m(t')} \times \left[\delta_{i3}\delta_{j3}\delta^{\perp}_{kl} + \delta_{k3}\delta_{l3}\delta^{\perp}_{ij} + \frac{\omega(t')}{\omega(t)}\frac{m(t)}{m(t')}\delta_{i3}\delta_{k3}\delta_{j3}\delta_{l3}\right] \tag{44}$$

and $\delta^{\perp}_{ik} = \delta_{ik} - \delta_{i3}\delta_{k3}$.

As to be expected, the distribution functions $f_{\alpha\beta}(\mathbf{p},t)$ and $F_{\alpha\beta}(\mathbf{p},t)$ satisfy the same KE (39) for $\alpha = 1,2$. The feature of the complete QPR becomes apparent only in the component of tensor distribution function $f_{ik}(\mathbf{p},t)$ that contains the preferred values of spin index $i,k = 3$. Let us select the KE for the

diagonal components of the correlation functions (40) having a direct physical meaning as the distribution functions of the transversal ($i = 1, 2$) and longitudinal components:

$$\dot{f}_i(\mathbf{p},t) = \frac{1}{2}\Delta(\mathbf{p},t)\int\limits_{-\infty}^{t} dt'\Delta(\mathbf{p},t') \qquad (45)$$
$$\times\left[1+2f_i(\mathbf{p},t')\right]\cos[2\theta(\mathbf{p};t,t')],$$
$$\dot{f}_3(\mathbf{p},t) = -2\Delta_m(\mathbf{p},t)f_3(\mathbf{p},t) \qquad (46)$$
$$+\frac{1}{2}\Delta(\mathbf{p},t)\frac{m^2(t)}{\omega^2(t)}\int\limits_{-\infty}^{t} dt'\Delta(\mathbf{p},t')\frac{\omega^2(t')}{m^2(t')}$$
$$\times\left[2f_3(\mathbf{p},t')+Q(\mathbf{p},t')\right]\cos[2\theta(\mathbf{p};t,t')].$$

Here, the shorthand notation $f_{ii} = f_i$ has been introduced for the diagonal components of the matrix correlation functions (40), and we have

$$\Delta = \frac{m\dot{m}}{\omega^2}, \qquad \Delta_m = -\Delta\frac{\mathbf{p}^2}{m^2}. \qquad (47)$$

It is possible to show that the distribution functions of the longitudinal ($i = 3$) and transversal ($i = 1, 2$) components are connected by the relation

$$f_3(\mathbf{p},t) = Q(\mathbf{p},t)f_1(\mathbf{p},t), \qquad (48)$$

where $Q(\mathbf{p},t)$ is the function occurring in the commutator of the creation and annihilation operators for the longitudinal bosons,

$$[c_3^{(-)}(\mathbf{p},t), c_3^{(+)}(\mathbf{p}',t)] = Q(\mathbf{p},t)\delta_{pp'},$$

$$Q(\mathbf{p},t) = \exp\left[-2\int\limits_{t_0}^{t}\Delta_m(t')dt'\right] \qquad (49)$$
$$= \left[\frac{m(t)}{m(t_0)}\frac{\omega(t_0)}{\omega(t)}\right]^2.$$

The remarkable feature of the KE (45) and (46) is the fact that they are not coupled and that the longitudinal distribution function has some additive homogeneous contribution. The presence of this term in the KE (46) is a new element of the kinetic theory of vacuum particle creation in comparison with, e.g., the case of the scalar field [8, 13]. This term leads to some exponential factors of the type

$$\exp\left\{-2\int\limits_{t_0}^{t} dt'\Delta_m(\mathbf{p},t')\right\}, \qquad (50)$$

which provide an additional influence on the vacuum tunneling process.

Owing to Eq. (48), it is sufficient to solve the one equation (45). We use now the well-known procedure

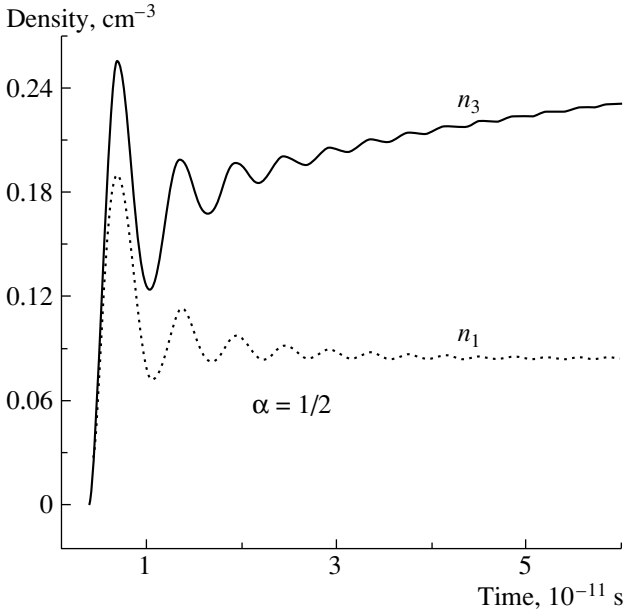

Fig. 1. Time evolution of the particle number density with initial condition $m_0 t_0 = 1$ for $\alpha = 1/2$.

of the reduction of the KE from the integro-differential form to the corresponding system of ordinary differential equations [14] in order to study the KE (45) numerically and to investigate the asymptotic behavior of its solutions for large momenta:

$$\dot{f}_1 = \frac{1}{2}\Delta u_1, \qquad \dot{u}_1 = \Delta(1+2f_1) - 2\omega v_1, \quad (51)$$
$$\dot{v}_1 = 2\omega u_1.$$

Here, u_1 and v_1 are some auxiliary functions responsible for the different effects of vacuum polarization (see, e.g., [14]). The main characteristic of the vacuum creation process is the total number density of vector bosons

$$n_{\mathrm{tot}}(t) = 2\sum_{i=1}^{3} n_i(t) \qquad (52)$$
$$= \frac{1}{\pi^2}\int\limits_0^\infty p^2 dp\left[2f_1(p,t)+f_3(p,t)\right],$$

where isotropy of the system was taken into account, $p = |\mathbf{p}|$. The general factor 2 in Eq. (52) corresponds to equal numbers of particles and antiparticles. In order to prove the convergence of the integral (52), we use the procedure of n-wave regularization [2, 15]. According to this procedure, all unknown functions in Eqs. (51) are subject to formal decompositions in asymptotic series with respect to the inverse powers of the momentum modulus, i.e.,

$$y(p,t) = \sum_{n=0}^{\infty} y^{(n)}(t)p^{-n}. \qquad (53)$$

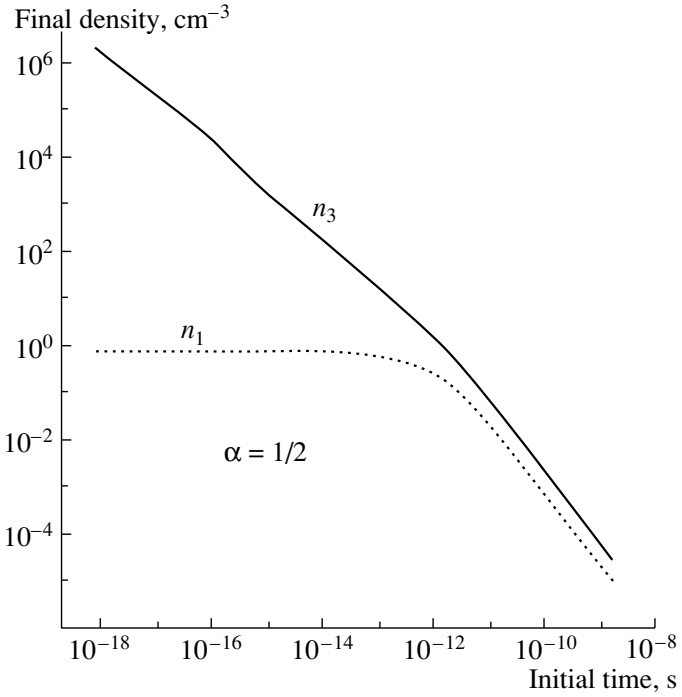

Fig. 2. The dependency of the final particle number density on the initial time for $\alpha = 1/2$.

The substitution of series (53) into (51) produces the following leading terms:

$$f_1^{(6)} = \frac{1}{16}(m\dot{m})^2, \qquad u_1^{(4)} = \frac{1}{4}(\dot{m}^2 + m\ddot{m}), \quad (54)$$
$$v_1^{(3)} = \frac{1}{2}m\dot{m};$$

consequently, the integral (52) is convergent.

4. VECTOR-BOSON PRODUCTION IN THE EARLY UNIVERSE

In order to estimate the vector-boson creation in the early Universe, we consider a conformal-invariant cosmological model [10], thus assuming that the spacetime is conformally flat and that the expansion of the Universe in the Einstein frame can be replaced by the change of masses in the Jordan frame due to the evolution of the cosmological (scalar) dilaton background field [5].

For our numerical studies, we use as a generic form of the conformal time dependence of the scalar field (mass) in the early Universe

$$m = \left(\frac{t}{t_H}\right)^{\alpha} m_W, \qquad (55)$$

where $t_H = (\alpha H)^{-1}$ is the age of the Universe, H is the Hubble constant, and $m_W = 80$ GeV is the W-boson mass. The parameter α depends on the choice of the cosmic equation of state (EoS), where, e.g., $\alpha = 1/2$ would correspond to a stiff fluid. Such an EoS will be adopted for the dominance of a massless scalar field in the Universe. Due to back reactions and dynamical mass generation during the cosmic evolution, the detailed mass history remains to be worked out. The central question, however, is whether the number density of produced W bosons could be of the same order as that of the CMB photons, $n_{\mathrm{CMB}} \sim 430\ \mathrm{cm}^{-3}$. If this question could be answered positively, the vacuum pair creation of W bosons from a time-dependent scalar field (mass term) could be suggested as a mechanism for the generation of matter and radiation in the early Universe. The non-Abelian nature of the W bosons could even imply consequences for the generation of the baryon (and lepton) asymmetry due to topological effects [16].

The numerical analysis of Eqs. (51) is performed by a standard Runge–Kutta method on a one-dimensional momentum grid. As one can see from Fig. 1, the creation process ends very quickly and the particle density saturates at some final value. The dependence of the corresponding final value of density on the initial time is shown in Fig. 2. The final density n_1 of particles with spin projection ± 1 reaches a maximum when we let the initial time go to very early times, when the Universe was born. However, in the same limit, the density n_3 of particles with zero projection of spin grows beyond all bounds. The choice of the EoS changes drastically the quantity of created particles, thus giving values which are too

small ($\alpha = 1/2$) or too large ($\alpha = 1/3$) in comparison with the observed CMB photon densities. In order to improve this model, we should use an improved EoS, assuming that the scalar field as a source of the particle masses can change during its time evolution. We can also consider the back-reaction problem by taking into account that the created particles can influence mass evolution. Furthermore, we could use another spacetime model, e.g., Kasner spacetime [17] instead of the conformal flat de Sitter one. The main achievement relative to the earlier work [5] is that, in the present approach, there is no divergence in the distribution function; thus, we do not need to introduce some ambiguous regularization procedure.

5. SUMMARY

The present work is dedicated to the kinetic description of vacuum creation of massive vector bosons caused either by the time dependence of energy gap or by the action of the nonstationary electric field. The statement of the problem is stimulated by modern cosmological problems related to the need for an explanation of the nature of the recent accelerating expansion of the Universe characteristic features of CMB radiation. The resulting KE (42) of non-Markovian type is obtained on a strong nonperturbative basis within the framework of the OR, which provides a short way to the QPR, in the language of which the kinetic theory is constructed. We apply then this KE for the analysis of the important particular case of an isotropic gas of vector bosons with the time-dependent mass which can be justified on the basis of conformal-invariant scalar-tensor gravitation theories. We show that the kinetic theory leads to a reasonable density of vector bosons in an early period of the Universe evolution which is sufficient for the explanation of the present density of CMB photons.

The obtained results constitute a foundation for the subsequent investigation of the dynamics of vector bosons created from the vacuum (the equation of state, the long wavelength acoustic excitations, the back-reaction problem, etc.).

ACKNOWLEDGMENTS

This work was partly supported by the Russian Federation State Committee for Higher Education (grant no. E02-3.3-210) and the Russian Foundation for Basic Research (project no. 03-02-16877). A.V.R. acknowledges support by DAAD grant no. A/03/01292 and S.A.S. by DFG grant no. 436 RUS 117/78/04.

REFERENCES

1. A. I. Nikishov, Zh. Éksp. Teor. Fiz. **120**, 227 (2001) [JETP **93**, 197 (2001)].
2. A. A. Grib, S. G. Mamaev, and V. M. Mostepanenko, *Vacuum Quantum Effects in Strong External Fields* (Energoatomizdat, Moscow, 1988; Friedmann Lab., St. Petersburg, 1994).
3. H.-P. Pavel and V. N. Pervushin, Int. J. Mod. Phys. A **14**, 2285 (1999).
4. V. M. Mostepanenko, V. M. Frolov, and V. A. Sheliuto, Yad. Fiz. **37**, 1261 (1983) [Sov. J. Nucl. Phys. **37**, 750 (1983)].
5. D. Blaschke, S. I. Vinitsky, A. A. Gusev, *et al.*, Yad. Fiz. **67**, 1074 (2004) [Phys. At. Nucl. **67**, 1050 (2004)].
6. A. A. Grib and A. V. Nesteruk, Yad. Fiz. **35**, 216 (1982) [Sov. J. Nucl. Phys. **35**, 122 (1982)].
7. S. I. Kruglov, Int. J. Theor. Phys. **40**, 515 (2001).
8. S. M. Schmidt, D. Blaschke, G. Röpke, *et al.*, Int. J. Mod. Phys. E **7**, 709 (1998).
9. V. N. Pervushin, V. V. Skokov, A. V. Reichel, *et al.*, Int. J. Mod. Phys. A (in press); hep-ph/0307200.
10. V. N. Pervushin, D. V. Proskurin, and A. A. Gusev, Grav. Cosmol. **8**, 181 (2002).
11. S. A. Smolyansky, A. V. Reichel, D. V. Vinnik, and S. M. Schmidt, in *Progress in Nonequilibrium Green's Functions II*, Ed. by M. Bonitz and D. Semkat (World Sci., Singapore, 2003), p. 384.
12. N. N. Bogoliubov and D. V. Shirkov, *Introduction to the Theory of Quantized Fields* (Nauka, Moscow, 1984; Wiley, New York, 1980).
13. S. Schmidt, D. Blaschke, G. Röpke, *et al.*, Phys. Rev. D **59**, 094005 (1999).
14. D. V. Vinnik, V. A. Mizerny, A. V. Prozorkevich, *et al.*, Yad. Fiz. **64**, 836 (2001) [Phys. At. Nucl. **64**, 775 (2001)].
15. Ya. B. Zeldovich and A. A. Starobinsky, Zh. Éksp. Teor. Fiz. **61**, 2161 (1971) [Sov. Phys. JETP **34**, 1159 (1971)]; S. G. Mamaev and N. N. Trunov, Yad. Fiz. **30**, 1301 (1979) [Sov. J. Nucl. Phys. **30**, 677 (1979)].
16. D. Blaschke and M. P. Dąbrowski, hep-th/0407078.
17. S. A. Smolyansky, A. V. Prozorkevich, D. V. Vinnik, and A. V. Reichel, in *Proceedings of the International Workshop "Hot Point in Astrophysics", Dubna, 2000*, p. 364.

Physics of Atomic Nuclei, Vol. 68, No. 6, 2005, pp. 1054–1063. Translated from Yadernaya Fizika, Vol. 68, No. 6, 2005, pp. 1095–1104.
Original Russian Text Copyright © 2005 by Bornyakov.

PROCEEDINGS OF THE CONFERENCE "PHYSICS OF FUNDAMENTAL INTERACTIONS" DEDICATED TO THE 100th ANNIVERSARY OF A.I. ALIKHANOV'S BIRTH, SECTION OF NUCLEAR PHYSICS, DIVISION OF PHYSICAL SCIENCES, RUSSIAN ACADEMY OF SCIENCES; INSTITUTE OF THEORETICAL AND EXPERIMENTAL PHYSICS, MOSCOW, MARCH 1–5, 2004

Lattice QCD

V. G. Bornyakov

Institute for High Energy Physics, Protvino, Moscow oblast, 142284 Russia

Received May 24, 2004; in final form, October 4, 2004

Abstract—Possibilities that are provided by a lattice regularization of QCD for studying nonperturbative properties of QCD are discussed. A review of some recent results obtained from computer calculations in lattice QCD is given. In particular, the results for the QCD vacuum structure, the hadron mass spectrum, and the strong coupling constant are considered. © *2005 Pleiades Publishing, Inc.*

1. INTRODUCTION

Quantum chromodynamics (QCD) is a theory that describes strong interactions of elementary particles. With the aid of perturbation-theory methods, physicists have obtained many pieces of corroborative evidence that QCD correctly describes strong interactions at high energies. However, it is well known that, at low energies, the strong coupling constant α_s grows, which renders perturbation theory inapplicable. It follows that, in order to perform calculations at low energies, it is necessary to develop a nonperturbative method that would make it possible to solve problems such as the calculation of fundamental QCD parameters (α_s and quark masses), the calculation of the hadron-mass spectrum, and elaboration of the theory of color confinement. It is the method of computer calculations within lattice formulations of QCD that makes it possible to solve these problems without recourse to uncontrollable approximations. Thirty years ago, Wilson [1] formulated basic ideas of the lattice approach to studying QCD. About twenty-five years ago, Creutz [2] used this approach to perform the first computer calculations of the string tension within the $SU(2)$ non-Abelian gauge model. Considerable advances have been made in the development of lattice QCD since then, and many results that deepened our understanding of the nonperturbative properties of QCD have been obtained along these lines. The most remarkable of these results include the calculation of the string tension, the glueball spectrum, the strong coupling constant, and the phase-transition temperature.

The above results were obtained in the so-called quenched approximation, where the contribution of quark loops is disregarded, which was because of the lack of adequate computer facilities. Only within the last five to seven years has a systematic study of lattice QCD been initiated in the unquenched approximation. Computers that are used in current investigations are about 10^4 to 10^5 times more powerful than those in the first studies and the community of researchers involved in these investigations includes about 150 physicists in Europe alone. The results obtained in lattice calculations are extensively used in phenomenological calculations. A new breakthrough is expected in the next two to three years, when computers of speed up to 10 teraflops become available for use in studying lattice QCD. The problems to be addressed in this connection can be formulated as follows:

(i) testing QCD as a theory of strong interactions;

(ii) solving the problems of confinement and spontaneous chiral-symmetry breaking;

(iii) calculating fundamental QCD parameters;

(iv) calculating other physical quantities that are of importance for understanding strong interactions;

(v) seeking new physics.

This article presents a brief review of the modern state of lattice calculations and their prospects. For deeper insights into lattice QCD, the interested reader is referred to the review articles quoted in [3].

The present review is organized as follows. In Section 2, we recall basic definitions in lattice theory. Section 3 is devoted to describing errors in lattice calculations. Some important physics results obtained within lattice QCD are described in Section 4. In the Conclusion, we discuss the prospects for lattice QCD.

2. BASIC DEFINITIONS

The lattice formulation of quantum field theory has the following special features. The theory is formulated in Euclidean space. The expression for the

generating functional $\mathcal{Z}$ becomes similar to that for the partition function; that is,

$$\mathcal{Z} = \int\int \mathcal{D}A\mathcal{D}\varphi e^{-S(A,\varphi)}, \qquad (1)$$

where S is the action of the theory in Euclidean space, $A_\mu(x)$ is a gauge field, and $\varphi(x)$ is a matter field. The analogy with statistical physics becomes perfect upon going over to a discrete spacetime. In this case, one considers a finite volume in a four-dimensional Euclidean space, $0 < x_1, x_2, x_3, x_4 \le L$, and assumes that the coordinates take discrete values. Thus, we arrive at a four-dimensional lattice specified by the nodes at the points $s = (s_1, s_2, s_3, s_4)$, $1 \le s_k \le N = L/a$, where a is a lattice constant. The lattice gauge field $U_\mu(s)$ is defined on the edges of the lattice, taking values in the gauge group, while the matter fields are defined at the nodes of the lattice. The generating functional of the theory then reduces to a finite-dimensional integral,

$$\mathcal{Z} = \int \prod_{s,\mu} dU_\mu(s) \prod_{s'} d\varphi(s') e^{-S(U,\varphi)}. \qquad (2)$$

A transition from a path integral to a finite-dimensional integral makes it possible to calculate quantum expectation values numerically. The continuum limit corresponds to $N \to \infty$ and $a \to 0$ at $L = Na =$ const. Actual calculations are performed at finite N and a, and systematic errors are evaluated in a standard way by varying the number of lattice nodes (N^4) and the lattice constant (a).

The QCD Lagrangian has the form

$$\mathcal{L} = \frac{1}{2g^2}\mathrm{Tr}F_{\mu\nu}^2(x) + \sum_f \bar\psi_f(x)(\gamma_\mu D_\mu + m_f)\psi_f(x), \qquad (3)$$

where ψ_f and $\bar\psi_f$ are quarks fields of flavor f, $F_{\mu\nu}$ is the strength tensor of the gauge field, D_μ is a covariant derivative, γ_μ are the Dirac matrices, and m_f is the quark mass. The choice of a lattice analog of this Lagrangian is ambiguous. The following conditions are imposed on the lattice Lagrangian:

(i) gauge invariance;

(ii) correct continuum limit (naive limit): for $a \to 0$ and fixed values of the coupling constant and the quark mass, the lattice Lagrangian must go over to the continuum-limit Lagrangian (3);

(iii) locality.

These conditions hold for an infinite number of lattice Lagrangians. The simplest and most natural form of the lattice action was proposed by Wilson [1]:

$$S = S_\mathrm{W}^G + S_\mathrm{W}^F. \qquad (4)$$

Here,

$$S_\mathrm{W}^F = a^4 \sum_s \bar\psi(s)\psi(s) + \kappa a^3 \qquad (5)$$
$$\times \sum_s \bar\psi[(\gamma_\mu - 1)U_\mu(s)\psi(s+\hat\mu)$$
$$- (\gamma_\mu + 1)U_\mu^\dagger(s-\hat\mu)\psi(s-\hat\mu)]$$

is the fermion component of the action for one flavor and

$$S_\mathrm{W}^G = \beta \sum_\mathrm{P} \left(1 - \frac{1}{3}\mathrm{Re\ Tr}U_\mathrm{P}\right) \qquad (6)$$

is the gauge-field action. In these expressions, κ is a parameter that determines the quark mass, while $\beta = 6/g^2$ is the lattice coupling constant. The plaquette matrix U_P is constructed in a standard way from the edge variables, $U_\mu(s) = e^{iaA_\mu(s)}$, where $A_\mu(s)$ is an $SU(3)$ gauge field. Upon going over to the (naive) continuum limit, we have

$$S_\mathrm{W}^G \xrightarrow[a\to 0]{} \frac{1}{2g^2}\int \mathrm{tr}F_{\mu\nu}^2 d^4x + O(a^2), \qquad (7)$$
$$S_\mathrm{W}^F \xrightarrow[a\to 0]{} \int \bar\psi(\gamma_\mu D_\mu + m)\psi d^4x + O(a);$$

that is, the Wilson fermion action tends to its continuum limit more slowly than the gauge-field action. This drawback was removed in the "improved" Sheikholeslami–Wohlert (SW) action for fermion fields [4]. It has the form

$$S^F = S_\mathrm{W}^F - \frac{i}{2}\kappa g a^5 c_\mathrm{SW} \qquad (8)$$
$$\times \sum_s \bar\psi(s)\sigma_{\mu\nu}\hat F_{\mu\nu}(s)\psi(s) \equiv \bar\psi M(U)\psi,$$

where $\hat F_{\mu\nu}$ is the lattice gauge-field strength tensor, $\sigma_{\mu\nu} = [\gamma_\mu, \gamma_\nu]/(2i)$, and the parameter c_SW is determined nonperturbatively [5]. The action S^F tends to the continuum limit within $O(a^2)$. This form of fermion action has been widely used over the last five years. The Kogut–Susskind fermion action [6] is yet another popular choice. Its chiral properties are better than the chiral properties of the action in (8), but the former has a significant drawback, flavor-symmetry breaking. From the theoretical point of view, the lattice fermion action whose matrix M satisfies the Ginsparg–Wilson relation [7]

$$M\gamma_5 + \gamma_5 M = \frac{a}{2r}M\gamma_5 M, \quad 0 < r < 1, \qquad (9)$$

is the best one. Such a fermion action possesses chiral symmetry even at a nonzero lattice spacing. Its realizations were found quite recently [8], and its

properties are being vigorously studied, but its practical applications have so far been hindered by some technical difficulties [9].

Numerical integration can be performed only with respect to gauge fields. Integration with respect to fermion fields is performed analytically,

$$\int \mathcal{D}\psi\mathcal{D}\bar{\psi}e^{-\bar{\psi}M(U)\psi} = \det M(U), \tag{10}$$

$$\int \mathcal{D}\psi\mathcal{D}\bar{\psi}\bar{\psi}^a(s')\psi^b(s)e^{-\bar{\psi}M(U)\psi} = (M^{-1}_{s,s'}(U))^{ba}\det M(U). \tag{11}$$

As a result, the integral to be evaluated with the aid of computers has the form

$$\langle\mathcal{O}\rangle = \frac{1}{\mathcal{Z}}\int \mathcal{D}U\mathcal{O}(\mathcal{U})e^{-S_{\text{eff}}(U)}, \tag{12}$$

where

$$\mathcal{Z} = \int \mathcal{D}U e^{-S_{\text{eff}}(U)}, \tag{13}$$

$$S_{\text{eff}}(U) = S^G_{\text{W}}(U) - N_f \ln\det M(U), \tag{14}$$

$\mathcal{D}U = \prod_{x,\mu} dU_\mu(x), dU_\mu(x)$ is the Haar measure on $SU(3)$, and N_f is the number of flavors of identical mass. For an operator depending on the fermion fields—for example, $\mathcal{O} = (\bar{\psi}\psi)(s')(\bar{\psi}\psi)(s)$—one calculates the integral

$$\langle\mathcal{O}\rangle = \frac{1}{\mathcal{Z}}\int \mathcal{D}U(M^{-1}_{s,s'}(U))^{ab}(M^{-1}_{s',s}(U))^{ba}e^{-S_{\text{eff}}(U)}. \tag{15}$$

From expressions (4)–(6), it can be seen that lattice QCD is characterized by the parameters β and κ, which determine the lattice spacing and the quark mass, respectively. At the present time, the majority of the results of lattice calculations have been obtained in the quenched approximation. In the quenched approximation, one sets $\det M(U) = \text{const}$ in (14), this being equivalent to $N_f = 0$ (that is, one disregards the contributions of quark loops). This is an uncontrollable approximation, and its application was motivated by the lack of sufficiently powerful computers exclusively. Considerable advances have been made in the past years. Results were obtained for two mass-degenerate light quarks ($N_f = 2$), this corresponding to the inclusion of u and d quarks. The first investigations with the added third quark (s quark) of the same ($N_f = 3$) or a higher ($N_f = 2+1$) mass were also performed.

For the parameters corresponding to actual QCD, the calculation of integrals belonging to the type in (12) is a nontrivial problem. In order to do this, the members of lattice collaborations employ the largest supercomputers and develop new algorithms for improving the efficiency of the calculations. A discussion on these algorithms (their description can be found in the review article of Peardon [10]) is beyond the scope of the present article. We only note that, in numerical calculations, the integral in (12) is replaced by the sum over gluon-field configurations generated with the weight $\exp\{-S_{\text{eff}}\}$; that is,

$$\langle\mathcal{O}\rangle \approx \frac{1}{N_{\text{conf}}}\sum_{i=1}^{N_{\text{conf}}}\mathcal{O}_i(U), \tag{16}$$

where N_{conf} is the number of statistically independent gluon-field configurations and $\mathcal{O}(U)_i$ the value of the operator $\mathcal{O}$ on the ith configuration.

The required volume of the calculations increases faster than the number of degrees of freedom. A semiphenomenological expression for calculations in QCD with two light quarks can be represented in the form [11]

$$\text{volume of calculations} \approx 2.8\left(\frac{N_{\text{conf}}}{1000}\right)\left(\frac{m_\pi/m_\rho}{0.6}\right)^{-6} \times \left(\frac{L}{3\,\text{fm}}\right)^5\left(\frac{1/a}{2\,\text{GeV}}\right)^7 \text{teraflop}\times\text{year}, \tag{17}$$

where m_π and m_ρ are the masses of, respectively, the π and the ρ meson (the ratio m_π/m_ρ determines the quark-mass value). For example, a 1-teraflop computer must operate 100 days in order to generate 100 configurations for the parameter values of $m_\pi/m_\rho = 0.6$ (that is, the quark mass is approximately 50 MeV), $L = 3$ fm, and $1/a = 2$ GeV. We note that the high powers in (17) indicate that the volume of the calculations grows fast as we approach the continuum limit or the chiral limit.

A few words about supercomputers used in lattice calculations are in order. The operating speed of the best supercomputers grows as an exponential function of the year of production (see Fig. 1). All dedicated computers presented in this figure (with the exception of the Earth Simulator) are intended for calculations in lattice QCD. The Earth Simulator of the NEC enterprise is now the most powerful computer, its operating speed being about 40 teraflop. Previously, this supercomputer was used to explore global phenomena in nature, but it was planned to perform lattice QCD calculations with it in 2004.

3. SOURCES OF ERRORS IN LATTICE CALCULATIONS

3.1. Statistical Errors

The statistical errors decrease in proportion to $1/\sqrt{N_{\text{conf}}}$.

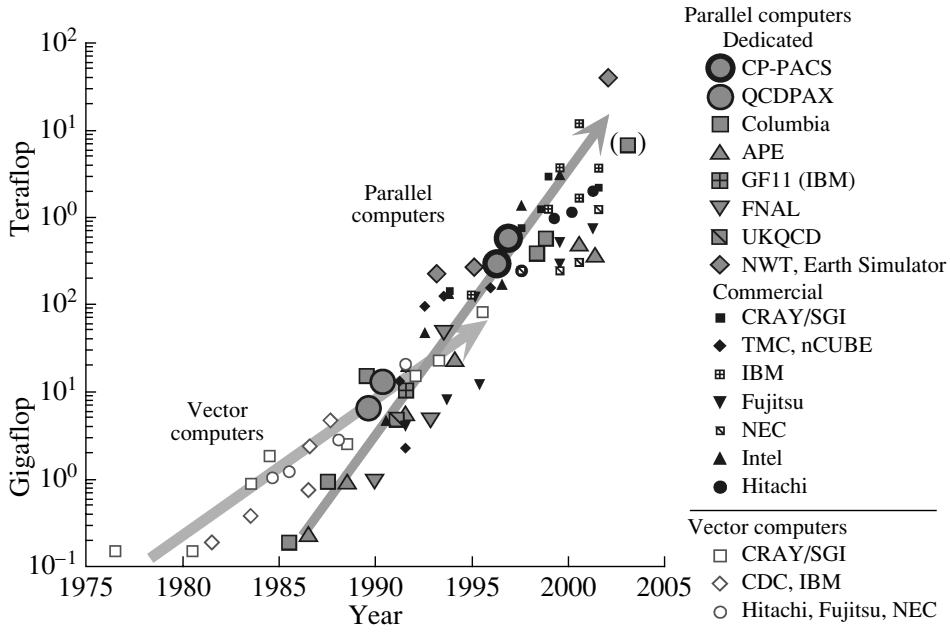

Fig. 1. Development of the computer speed for the best supercomputers [12].

3.2. Finiteness of the Lattice Spacing a

In order to obtain physical results, one must go over to the limit $a \to 0$. In practice, the calculations are performed at several values of the lattice spacing a, whereupon the results are extrapolated to $a = 0$. Typical values of a lie in the range 0.05–0.15 fm.

3.3. Effects of Finite Volume

The contributions of these effects decrease exponentially in proportion to $\exp\{-m_\pi L\}$ [13]. Typical values of L lie in the interval 2–3 fm, while the π-meson mass is two to three times higher than its physical value.

3.4. Extrapolation to the Physical Mass of Light Quarks (Chiral Extrapolation)

As the light-quark mass decreases, the volume of the calculations grows very fast for a number of reasons. In the calculations, it is necessary to find the inverse of the fermion matrix several times. The computer time required for calculating the inverse fermion matrix grows fast as its smallest eigenvalue, which is determined by the lattice quark mass $m_q a$, decreases. In addition, a decrease in m_π entails the need for increasing the lattice size (see Subsection 3.3). The calculations are performed at several values of the light-quark mass $m_{u,d}$ from the interval $0.2m_s \lesssim m_q \lesssim m_s$, whereupon the results are extrapolated to the physical value of the light-quark mass by means of chiral perturbation theory. It is believed that the extrapolation based on the chiral effective Lagrangian must be used for values of $m_{u,d} < m_s/4$. This corresponds to $m_\pi/m_\rho < 0.4$.

3.5. Heavy Quarks

The b and c quarks are very heavy, so that the necessary condition $m_Q a \ll 1$ does not hold for them. Therefore, calculations with heavy quarks cannot be performed in the same way as with light quarks. This problem was solved quite recently by using heavy-quark effective theory and nonrelativistic QCD. The basic idea is to consider heavy quarks as static or nonrelativistic ones; as a result, the appropriate action appears to be an expansion of the original action in $1/m_Q$. For the c quark, one can also use the ordinary relativistic approach under the condition that the lattice spacing in the time direction is much smaller than the lattice spacing in the spatial directions.

3.6. Matching of the Lattice Scheme with the Modified Minimal Subtraction Scheme ($\overline{MS}$)

In order to compare the results of lattice calculations for nonspectral quantities with their experimental counterparts, it is necessary to rescale lattice data to an ordinary scheme—for example, the modified minimal subtraction scheme ($\overline{MS}$). In general, we have

$$\langle 0|\mathcal{O}_i(\dots)|0\rangle^{\overline{MS}} = Z_{ij}\langle 0|\mathcal{O}_j(\dots)|0\rangle^{\text{lat}} \qquad (18)$$
$$= (\delta_{ij} + O(\alpha_s))\langle 0|\mathcal{O}_j(\dots)|0\rangle^{\text{lat}},$$

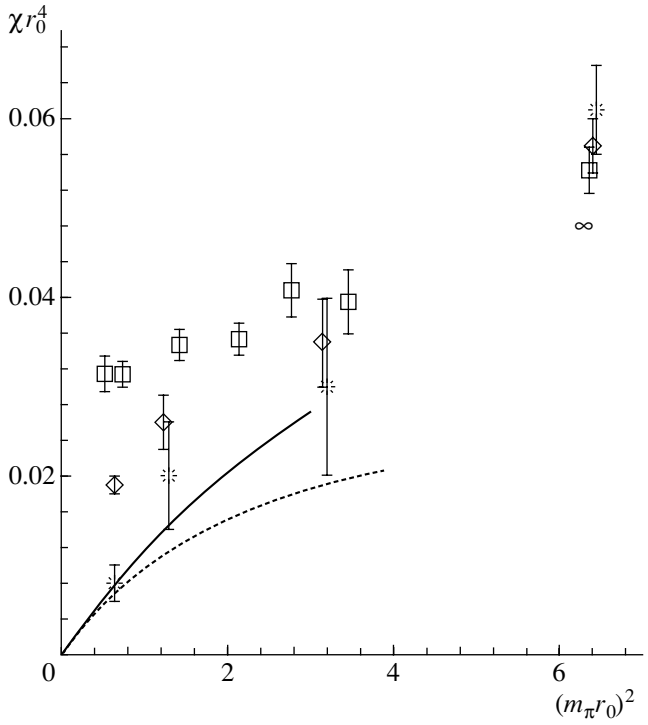

Fig. 2. Topological susceptibility for $N_f = 2 + 1$ in lattice QCD [17]: (boxes) results of the calculations for a 20^4 lattice whose nodes are spaced by 0.13 fm, (diamonds) analogous results for a lattice of dimension 28^4 and lattice spacing of 0.09 fm, and (asterisks) result of the extrapolation to the continuum limit. The solid curve represents the prediction of chiral perturbation theory [see Eq. (19)], while the dashed curve shows the phenomenological result from [18].

where Z_{ij} can be calculated by perturbation theory and are usually known only in the one-loop approximation. Since the strong coupling constant α_s is large at energy values typically used in lattice calculations, higher order corrections can make a contribution of about 10%. Therefore, the problem of nonperturbatively calculating Z_{ij} becomes important.

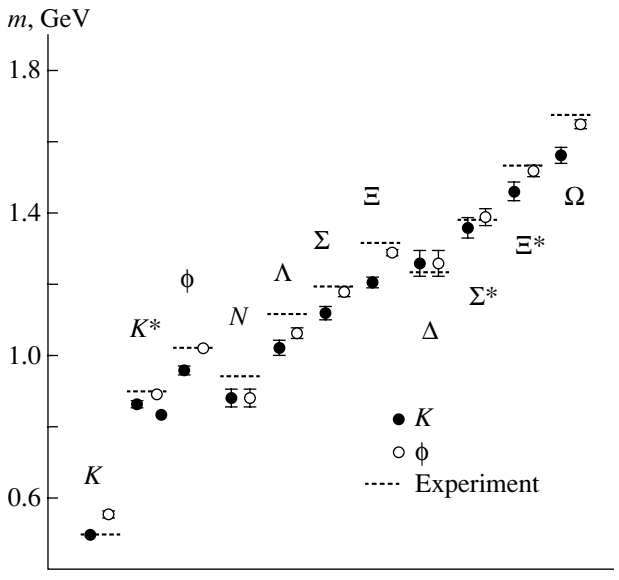

Fig. 3. Hadron mass spectrum obtained by the CP-PACS Collaboration [21] on the basis of QCD not involving dynamical quarks.The s-quark mass was fixed by using the K-meson or the ϕ-meson mass.

4. RESULTS FOR PHYSICAL QUANTITIES

The results of numerical calculations are values corresponding to physical quantities reduced to a dimensionless form by an appropriate power of the lattice spacing a. For example, this is ma for the mass m. In order to rescale physical quantities to dimensional units, it is necessary to define the lattice scale—that is, a. For this, one takes a physical quantity whose value is known from experiments—for example, the mass of a hadron. It is desirable that the chosen physical quantity be weakly dependent on the light-quark mass and be readily calculable on a lattice. In view of this, the quantity r_0, which has dimensions of length and which admits a determination from the potential of static quarks, is a popular choice. This choice is disadvantageous in that r_0 is taken from the potential model (which gives a phenomenological value of 0.5 fm) rather than being directly accessible from experimental data. The ρ-meson mass and the splitting between the P- and S-wave levels in the $b\bar{b}$ or $c\bar{c}$ quarkonia are other quantities used to fix a.

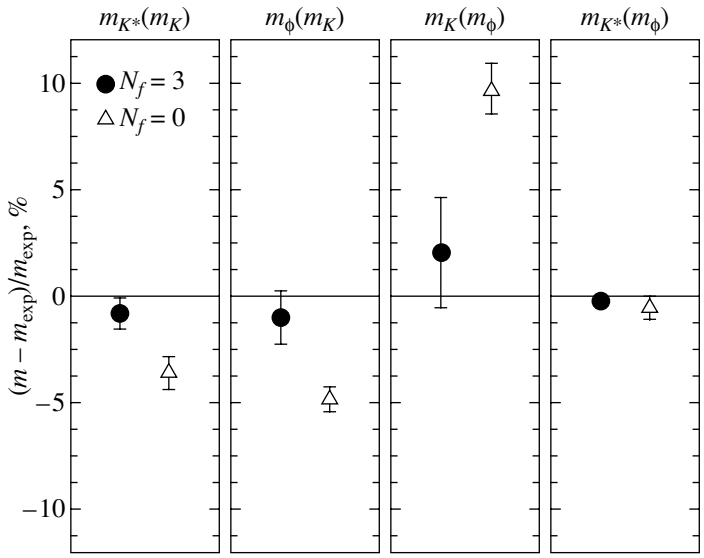

Fig. 4. Strange-meson masses in (closed circles) $N_f = 3$ and (open triangles) $N_f = 0$ lattice QCD. The s-quark mass m_s is fixed by using the K- or the ϕ-meson mass (m_K or m_ϕ in the figure) [23].

Upon determining the lattice spacing a, any mass can be expressed in GeV units. Before a comparison with experimental results, it is necessary, however, to tune the quark masses $m_{u,d}$, m_s, m_c, and m_b. For each quark mass, we then select a hadron whose mass value will be used for tuning. For this hadron, lattice results obtained for a number of values of the bare quark mass are interpolated or extrapolated in order to find the bare-quark-mass value corresponding to the correct value of the hadron mass. After that, the masses of other hadrons containing this quark can be predicted. In order to fix $m_{u,d}$, use is usually made of the π-meson mass; the masses of the K, K^*, or ϕ mesons are taken to fix m_s. In order to fix m_c (m_b), one employs the masses of the $D(B)$, $D_s(B_s)$, and $\psi(\Upsilon)$ mesons.

In the case of lattice QCD involving dynamical quarks, the above procedure of tuning the parameters of the QCD Lagrangian is complicated because the lattice spacing a changes with the bare-quark mass.

Let us consider some examples involving the calculation of physical quantities in lattice QCD.

4.1. Properties of the Vacuum

It was indicated in the Introduction that, back in the 1980s, lattice calculations produced results important for understanding nonperturbative phenomena in QCD, although these results concerned gluodynamics. These results include a confirmation of the conjecture that the potential of interaction between static quarks is linear at large distances and a calculation of the glueball spectrum in gluodynamics, of the temperature of the confinement–deconfinement phase transition, of the topological susceptibility, and of the gluon condensate. Later, the advent of more powerful computers and of more efficient computational algorithms made it possible to obtain new, more precise results for the structure of the vacuum in gluodynamics, on one hand, and to go over to a more realistic theory that takes into account dynamical quarks, on the other hand.

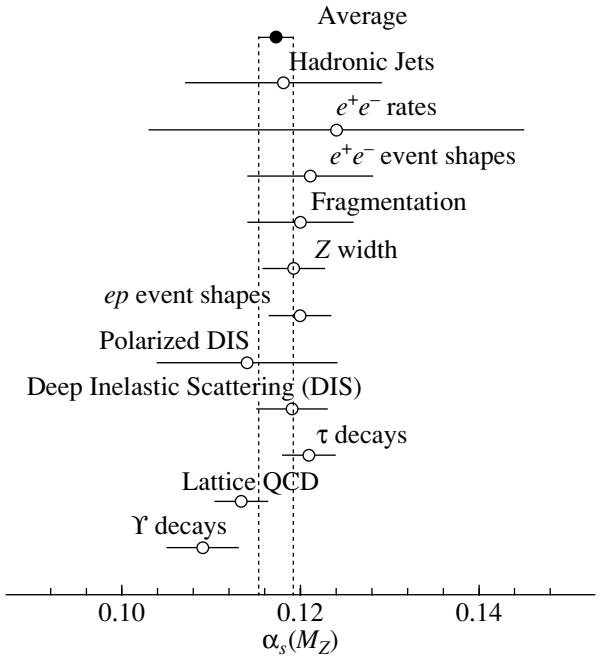

Fig. 5. Strong coupling constant $\alpha_s(M_Z)$ as determined by various methods [25].

Errors in lattice calculations (in %) for the coupling constant $\alpha_s(M_z)$, the quark masses, the $\hat{B}$ parameters, and the decay constants and form factors at zero momentum transfer at the time of the forecast (2000), in short-term forecasts (2000–2003), and in long-term forecasts (2003–2006) [28]

Quantity	2000	2000–2003	2003–2006
$\alpha_s(M_z)$	10	5	3
$\bar{m}_{u,d,s,c}$	25	10	5
$\bar{m}_b$	5	2.5	1
$\hat{B}_K$	15	10	5
Other $\hat{B}$	30	10	5
f_{D_q}	15	10	5
$f_{B_q}, f_{B_q}\sqrt{\hat{B}_q}$	20	15	7
$F(0)^{D\to M}$	25	10	5
$F(0)^{B\to M}$	35	15	7

Numerous results have been obtained that highlight the important role of topologically nontrivial configurations (monopoles, vortices) in the structure of the QCD vacuum—in particular, it was found that such configurations determine the properties of confinement and spontaneous symmetry breaking (see the review articles of Greensite and of Chernodub and Polikarpov [14]).

Owing to the application of a new algorithm for calculating the potential of interaction between static quarks, the force $F(r)$ of the interaction between static quarks in gluodynamics was calculated in [15] to a very high precision for distances of $r \approx 1$ fm. The results of this calculation proved to be in very good qualitative agreement with its counterpart predicted by the Nambu–Goto string model, $c(r) \equiv r^3F'(r)/2 = \pi(d-2)/24$, where d is the dimensionality of the space. However, the high precision of the calculation in question made it possible to pinpoint the deviation from the above relation. The origin of this deviation has yet to be clarified.

The first results obtained in lattice QCD for the topological susceptibility χ_t as a function of the light-quark mass were recently published for $N_f = 2$ [16] and $N_f = 2+1$ [17]. It was found in both cases (see Fig. 2, which shows the results for $N_f = 2+1$ QCD) that the numerical results obtained at small values of the quark mass and upon extrapolation to the continuum limit comply well with the predictions of chiral perturbation theory [19]:

$$\chi_t = \frac{f_\pi^2 m_\pi^2}{4}, \quad N_f = 2; \tag{19}$$

$$\chi_t = \frac{f_\pi^2 m_\pi^2}{4(1+m_u/2m_s)}, \quad N_f = 2+1.$$

The value obtained to a high precision for the temperature T_c of the phase transition in gluodynamics is 270 MeV. For QCD involving dynamical quarks, the results are not quite reliable, the phase-transition temperature being estimated at 150 to 170 MeV [20].

4.2. Hadron Spectrum

A calculation of hadron masses may serve as a test of lattice QCD. It is of importance to calculate the masses with small errors of all types in order to be confident that, in calculating other quantities (for example, hadron matrix elements), the errors are under control. Moreover, the masses of some hadrons are generally used to fix the parameters of the lattice action (lattice spacing and quark masses).

The hadron masses are calculated from the two-point correlation functions; that is,

$$\langle 0|\Phi_H(t)\Phi_H^\dagger(0)|0\rangle \tag{20}$$
$$= \sum_n |\langle 0|\Phi_H|H_n\rangle|^2 e^{-m_n t} \underset{t\to\infty}{=} |\langle 0|\Phi_H|H\rangle|^2 e^{-m_H t},$$

where Φ_H is a hadron operator that has appropriate quantum numbers, m_H is the hadron mass, and $\{|H_n\rangle\}$ is the complete set of states in the channel being considered.

The desired accuracy of calculations was attained in the case of quenched lattice QCD. However, it should be recalled that the disregard of quark loops introduces uncontrollable errors, which can be removed only in lattice QCD simulations involving dynamical quarks. It was found (see Fig. 3) that, in the quenched approximation, a typical discrepancy between the lattice results and experimental values is 10%. It should be noted that, in this approximation, the result depends on the mass of the particle that is used to fix quark masses. One can see this in Fig. 3, which shows the same lattice results obtained by two methods of rescaling to dimensional units: in order to fix the s-quark mass, one uses the K- and the ϕ-meson mass in the first and the second case, respectively. Rather good agreement with experimental results for hadron masses gives reasons to hope for obtaining not very large deviations for other physical quantities as well.

If one performs calculations within full QCD—that is, with allowance for quark loops—the resulting hadron masses will approach their experimental values as the u- and d-quark masses tend to their actual values. In [22], improved agreement with experimental results for strange mesons was found in $N_f = 2$ QCD. There was no systematic improvement for baryons there, but this was due to the use

of an insufficiently large lattice in the calculations. In [23], remarkable agreement with experimental data on the strange-meson masses was attained for $N_f = 3$ QCD. In Fig. 4, which was borrowed from [23], the results obtained in the quenched approximation ($N_f = 0$) are contrasted against their counterparts in $N_f = 3$ QCD. The results differing by the method used to fix the s-quark mass are displayed there. The figure shows that, in contrast to what we have in quenched QCD, the results in $N_f = 3$ QCD do not depend on the method for fixing the quark mass. In order to obtain similar results for the masses of light baryons, the lattice size must be increased by a factor of about 1.5.

As was indicated above, calculations involving dynamical c and b quarks would require considerably reducing the lattice spacing (especially, for b quark), but this is next to impossible. Fortunately, other methods are applicable in this case—these are heavy-quark effective theory in studying hadrons that contain one heavy quark and nonrelativistic QCD in studying quarkonia. The results obtained in quenched QCD for the spectra of low-lying levels of charmonium, bottomonium, and D and B mesons agree well with experimental data. In just the same way as in the case of light hadrons, calculations within $N_f = 2, 3$ QCD led to a considerable improvement of the agreement [24].

4.3. Coupling Constant α_s

The calculation of the coupling constant for strong interactions in lattice QCD is among the indisputable successes of this approach. In Fig. 5, which was borrowed from [25], the lattice result is shown along with the results extracted from experimental data. In order to calculate α_s, one can employ different lattice quantities: the average plaquette (analog of the gluon action), the strength of static-quark interaction, the three-gluon vertex, or the gluon propagator in the Landau gauge. In order to fix the physical scale, use was made of the difference of masses in bottomonium or another physical quantity whose value is known from experimental data to a high precision and which can be calculated on a lattice to a high precision as well. In order to go over from the lattice coupling constant $\alpha_{\rm P}(q)$ to $\alpha_{\overline{MS}}(q)$, one makes use of perturbation theory:

$$\alpha_{\overline{MS}}(q) = \alpha_{\rm P}(e^{5/6}q)\left[1 + 2\frac{\alpha_{\rm P}}{\pi} + O(\alpha_{\rm P}^2)\right]. \quad (21)$$

The calculations were performed for $N_f = 0$ and for $N_f = 2$, whereupon the results were extrapolated to $N_f = 3$. Recently, the result for $N_f = 3$ was obtained directly [26]. This result for the coupling constant is in good agreement with the previous results obtained via extrapolation.

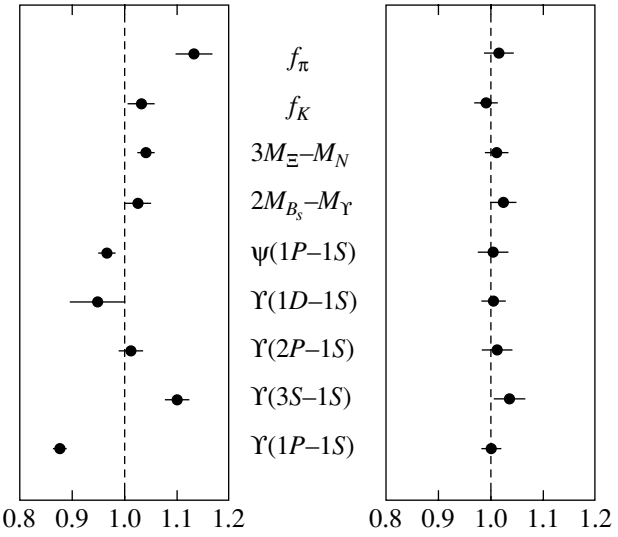

Fig. 6. Comparison of the results obtained in the quenched approximation of lattice QCD (left panel) and in $N_f = 2 + 1$ lattice QCD based on the improved Kogut–Susskind action (right panel) [6]. The ratios of the lattice results for the displayed quantities to their experimental values are given.

4.4. Hadron Matrix Elements

Lattice results for matrix elements in the decays of B, D, and K mesons are of importance for improving the accuracy in determining the elements of the Cabibbo–Kobayashi–Maskawa matrix. In particular, the element V_{td} of the Cabibbo–Kobayashi–Maskawa matrix can be determined upon measuring the mass difference between neutral B_s mesons, ΔM_s. The hadron matrix element required for calculating V_{td} is parametrized as

$$\langle \bar{B}_q^0 | \bar{b}\gamma_\mu(1-\gamma_5)q\bar{b}\gamma_\mu(1-\gamma_5)q|B_q^0\rangle = \frac{8}{3} f_{B_q}^2 B_{B_q}(\mu_b) M_{B_q}^2, \quad (22)$$

where f_{B_q} is the decay constant. In order to find the decay constants, we must calculate the expectation value

$$\langle 0|J(t)\Phi_H^\dagger(0)|0\rangle, \quad (23)$$

where J is the corresponding current. Matrix elements of the form $\langle H'|Q|H\rangle$ can also be calculated on the lattice according to the relation

$$\langle 0|\Phi_{H'}(t+t')Q(t')\Phi_H^\dagger(0)|0\rangle \underset{t,t'\to\infty}{=} \langle 0|\Phi_{H'}|H'\rangle \times \langle H'|Q|H\rangle\langle H|\Phi_H^\dagger|0\rangle e^{-m'_H t - m_H t'}. \quad (24)$$

The decay constants f_{B_q} and the B parameters were calculated by several collaborations that employed different methods to solve the heavy-quark problem.

The results obtained in the quenched approximation [27] are 10–20% less than the results obtained in $N_f = 2$ and $N_f = 2 + 1$ QCD [24]. The lattice values

$$\hat{B}_{B_d} f_{B_d}^2 = (1.26 \pm 0.10)(196 \pm 32\ \text{MeV})^2 \quad (25)$$

and

$$\frac{\hat{B}_{B_s} f_{B_s}^2}{\hat{B}_{B_d} f_{B_d}^2} = 1.56 \pm 0.26, \quad (26)$$

where $\hat{B}_{B_q}$ is the B-parameter value invariant under renormalization-group transformations, are presented in [25].

5. CONCLUSIONS

Lattice gauge theories form a very broad realm going beyond QCD. A lattice formulation ensures the well-defined mathematical basis for quantum-field theory, and this is one of the most attractive properties of the lattice approach. A lattice regularization of QCD makes it possible, at least in principle, to perform nonperturbative calculations. The advances in lattice QCD over the past decade have been made both owing to an increase in the power of computers used in such calculations and owing to the development of new concepts, computational methods, and numerical algorithms. In particular, the application of the improved fermion action made it possible to reduce considerably the values of the quark masses used in computer calculations and, to a considerable extent, to solve the chiral-limit problem.

In this review, we have not discussed the results obtained within lattice QCD for the following physical quantities:

(i) the quark masses,

(ii) the hadron structure functions,

(iii) the spectrum of exotic and hybrid particles, and

(iv) the η'-meson mass and other flavor-singlet quantities,

as well as the results obtained in QCD at nonzero baryon density.

Considerable advances have also been made in solving these problems in lattice QCD.

A few years ago, a team of experts that carried out tasks assigned by the European Commission for Future Accelerators (ECFA) presented, among other things, a forecast of the development of calculations within lattice QCD in the form of a table of errors in lattice calculations for physical quantities of importance (see table). From this table, it follows that, in the next few years, lattice calculations are expected to reach the desired precision of a few percent. The data given in the present review article demonstrate that this forecast is coming true. From Fig. 6, which was borrowed from [6], it follows that this level of precision has already been attained for many physical quantities. These results seem very optimistic. It should be noted, however, that many experts recommend taking the results reported in [6] with caution, since the possibility that the fermion action employed in that study is nonlocal cannot be ruled out on purely theoretical grounds [29].

ACKNOWLEDGMENTS

I am grateful to M.I. Polikarpov, M.N. Chernodub, and G. Schierholz for numerous stimulating discussions.

This work was supported in part by the Russian Foundation for Basic Research (RFBR, project no. 04-02-16079), RFBR–NNIO (project no. 03-02-04016), DFG-RFBR 436 RUS 113/739/0, and INTAS-00-00111.

REFERENCES

1. K. G. Wilson, Phys. Rev. D **10**, 2445 (1974).
2. M. Creutz, Phys. Rev. D **21**, 2308 (1980).
3. T. DeGrand, Int. J. Mod. Phys. A **19**, 1337 (2004); C. McNeile, hep-lat/0307027; C. Davies, hep-ph/0205181; A. S. Kronfeld, hep-lat/0205021; G. S. Bali, Phys. Rep. **343**, 1 (2001).
4. B. Sheikholeslami and R. Wohlert, Nucl. Phys. B **259**, 572 (1985).
5. K. Jansen and R. Sommer, Nucl. Phys. B **530**, 185 (1998).
6. C. T. H. Davies *et al.* (HPQCD Collab.), Phys. Rev. Lett. **92**, 022001 (2004).
7. P. H. Ginsparg and K. G. Wilson, Phys. Rev. D **25**, 2649 (1982).
8. H. Neuberger, Phys. Rev. Lett. **81**, 4060 (1998).
9. L. Giusti, Nucl. Phys. B (Proc. Suppl.) **119**, 149 (2003).
10. M. J. Peardon, Nucl. Phys. B (Proc. Suppl.) **106**, 3 (2002).
11. A. Ukawa (CP-PACS and JLQCD Collab.), Nucl. Phys. B (Proc. Suppl.) **106**, 195 (2002).
12. K. Kanaya *et al.* (CP-PACS Collab.), Fortschr. Phys. **50**, 531 (2002).
13. M. Lüscher, Commun. Math. Phys. **104**, 177 (1986).
14. J. Greensite, Prog. Part. Nucl. Phys. **51**, 1 (2003); M. N. Chernodub and M. I. Polikarpov, hep-th/9710205.
15. M. Lüscher and P. Weisz, J. High Energy Phys. **0207**, 049 (2002).
16. A. Hart and M. Teper (UKQCD Collab.), Phys. Lett. B **523**, 280 (2001).
17. C. Bernard *et al.*, Phys. Rev. D **68**, 114501 (2003).
18. S. Durr, Nucl. Phys. B **611**, 281 (2001).
19. H. Leutwyler and A. Smilga, Phys. Rev. D **46**, 5607 (1992).
20. S. D. Katz, hep-lat/0310051.

21. S. Aoki *et al.* (CP-PACS Collab.), Phys. Rev. Lett. **84**, 238 (2000).
22. S. Aoki *et al.* (JLQCD Collab.), Phys. Rev. D **68**, 054502 (2003).
23. T. Kaneko *et al.* (CP-PACS Collab.), hep-lat/0309137.
24. A. S. Kronfeld, Nucl. Phys. B (Proc. Suppl.) **129**, 46 (2004).
25. S. Eidelman *et al.*, Phys. Lett. B **592**, 1 (2004).
26. C. Davies *et al.*, Nucl. Phys. B (Proc. Suppl.) **119**, 595 (2003).
27. S. M. Ryan, Nucl. Phys. B (Proc. Suppl.) **106**, 86 (2002).
28. Report of the ECFA Working Panel, ECFA/99/200 (2000).
29. B. Bunk, M. Della Morte, K. Jansen, and F. Knechtli, hep-lat/0403022.

Translated by A. Isaakyan

Physics of Atomic Nuclei, Vol. 68, No. 6, 2005, pp. 1064–1070. Translated from Yadernaya Fizika, Vol. 68, No. 6, 2005, pp. 1105–1112.
Original Russian Text Copyright © 2005 by Sikach.

PROCEEDINGS OF THE CONFERENCE "PHYSICS OF FUNDAMENTAL INTERACTIONS" DEDICATED TO THE 100th ANNIVERSARY OF A.I. ALIKHANOV'S BIRTH, SECTION OF NUCLEAR PHYSICS, DIVISION OF PHYSICAL SCIENCES, RUSSIAN ACADEMY OF SCIENCES; INSTITUTE OF THEORETICAL AND EXPERIMENTAL PHYSICS, MOSCOW, MARCH 1–5, 2004

Covariant Methods for Calculating Differential Cross Sections and Polarization Characteristics of Reactions

S. M. Sikach*

Stepanov Institute of Physics, National Academy of Sciences of Belarus, Minsk, 220072 Belarus

Received May 24, 2004

Abstract—A covariant method for calculating reaction amplitudes in the diagonal spin basis is presented. In this basis, amplitudes represent the spin kinematics of the interacting particles in the simplest and most adequate manner. A matrix is obtained such that differential cross sections for polarized particles and amplitude combinations that are required to calculate various polarization characteristics of reactions can be expressed in an arbitrary basis in terms of the amplitudes calculated in one basis. © *2005 Pleiades Publishing, Inc.*

1. INTRODUCTION

At the moment, the standard method of direct calculation of the reaction amplitude modulus squared is almost never used, because the difficulty of calculations increases drastically when the number of particles increases even slightly or when particle polarizations should be taken into account.

The idea of direct calculation of amplitudes followed by their squaring is quite evident. However, this approach generates a number of specific problems. For this reason, works that develop various aspects of this methodology have appeared for several decades (see bibliography in the reviews [1, 2].) In these works, a covariant or noncovariant approach is used and calculations are performed in an arbitrary or a particular spin basis.

The studies by F.I. Fedorov and his disciples are among the first works in this field (see details in [3]). They are mainly devoted to the covariant calculation of amplitudes in an arbitrary spin basis. For example, the authors of [4] suggested a method that uses the main "advantage" of the squaring procedure, where all calculations are reduced to the computation of the traces of γ-matrix operators.

We illustrate this approach by the example of the fermion "sandwich"

$$\bar{u}^{\sigma'}(p',s')Qu^{\sigma}(p,s) = \mathrm{Tr}\,Qu^{\sigma}(p,s)\bar{u}^{\sigma'}(p',s'), \quad (1)$$

where Q is an arbitrary operator. The main difficulties of this approach are the determination of exact expressions for the transition operators

$$u^{\sigma}(p,s)\bar{u}^{\sigma'}(p',s'), \quad (2)$$

the calculation of phase factors, elimination of singularities, calculation of exchange diagrams, inclusion of the specific features of the spin configuration $\sigma' = -\sigma$, etc. Certain difficulties can be overcome by choosing a special spin basis. The transition to another basis is performed using Wigner D functions, but this tool is very cumbersome and noncovariant.

In this paper, we show how cross sections for polarized particles and amplitude combinations that are required to calculate other polarization characteristics of reactions can be expressed in an arbitrary basis in terms of the amplitudes (1) in the basis where they have the simplest form.

In Section 2, we consider single-particle states. We show that the consistent application of the tetrad formalism makes it possible to operate with the complete set of bispinors and to reduce the action of matrix operators to the action of tensor operators. In Section 3, we obtain matrices that enable the amplitude modulus squared in a certain spin basis to be expressed in terms of the amplitudes calculated in another spin basis. In Section 4, we consider the diagonal spin basis (DSB) introduced previously in [5]. In the DSB, the bispinors of initial and final states have a common set of spin operators and they are related to each other in the simplest way. As a result, a compact and simple solution is obtained for the key problem of this approach—the determination of the exact expression for transition operators (2). The diagonal amplitudes have clear physical interpretation and they are the best "building blocks" for the calculation of amplitude products with various spin configurations in an arbitrary spin basis. In Section 5, we show how to calculate observables in terms of the diagonal amplitudes.

*e-mail: sikach@dragon.bas-net.by

2. SINGLE-PARTICLE STATES: TETRADS

A single-particle state is determined by two 4-vectors: momentum p and spin projection axis s, where $ps = 0$. This condition is satisfied if we define s in terms of an arbitrary vector q:

$$s = \frac{(pq)p - m^2 q}{m\sqrt{(pq)^2 - m^2 q^2}}. \tag{3}$$

If

$$s_0 = v = p/m, \quad s_3 = s, \tag{4}$$

then $s_0^2 = -s_3^2 = 1$ and $s_0 s_3 = 0$. Any vector of the form $\alpha s_0 + \beta s_3$ lies in the 2-plane (s_0, s_3) in Minkowski space. The orthogonal 2-plane is defined in terms of the following two tensors:

$$g_{||}^{\mu\nu} = v^\mu v^\nu - s^\mu s^\nu, \quad \tilde{\varepsilon}_{||}^{\mu\nu} = \varepsilon^{\mu\nu\rho\sigma} v_\rho s_\sigma, \tag{5}$$

where $\varepsilon_{0123} = 1$. If an arbitrary vector r does not belong to the 2-plane (s_0, s_3), the vectors

$$s_1^\mu = (g_{||}^{\mu\nu} - g^{\mu\nu})\frac{r_\nu}{r_\perp}, \quad s_2^\mu = -\tilde{\varepsilon}_{||}^{\mu\nu}\frac{r_\nu}{r_\perp}; \tag{6}$$

$$r_\perp = \sqrt{r_\mu (g_{||}^{\mu\nu} - g^{\mu\nu}) r_\nu}$$

(where g is the Minkowski tensor) satisfy the conditions $s_1^2 = s_2^2 = -1$ and $s_1 s_2 = 0$, and both vectors are orthogonal to s_0 and s_3. Therefore, the tetrad $\{s_0, s_3, s_1, s_2\}$ forms the orthonormal basis in Minkowski space. The vectors s_1 and s_2 enter into all spin relations only in the combination $s_1 \pm i s_2$. It follows from Eqs. (6) that

$$s_1 + i\sigma s_2 = T_\sigma \frac{r}{r_\perp}, \quad T_\sigma = g_{||} - g - i\sigma\tilde{\varepsilon}_{||}. \tag{7}$$

It is clear that the tensor T_σ plays a special role in spin calculations. Apart from the evident properties $T_\sigma^* = T_{-\sigma}$, $T_\sigma^+ = T_\sigma$, and $T_\sigma^2 = -2T_\sigma$, it satisfies the relation

$$T_\sigma^{\mu\nu} T_\sigma^{\alpha\beta} = T_\sigma^{\mu\beta} T_\sigma^{\alpha\nu}, \tag{8}$$

from which it follows that

$$T_\sigma^{\mu\nu} r_\nu r_\alpha T_\sigma^{\alpha\beta} = r_\perp^2 T_\sigma^{\mu\beta}. \tag{9}$$

Changing r to r' in (7), from Eqs. (7) and (9), we obtain

$$s_1' + i\sigma s_2' = e^{i\sigma\varphi}(s_1 + i\sigma s_2), \tag{10}$$

$$e^{i\sigma\varphi} = \frac{r T_\sigma r'}{r_\perp r_\perp'}.$$

Thus, variations in r result in the rotation by the angle φ in the 2-plane (s_1, s_2) and in the appearance of an additional phase factor in spin relations.

By fixing r, we also specify a tetrad in the Minkowski space and obtain the whole set of the spin operators in the explicit form[1)]

$$\Sigma_3 = \gamma_5 \hat{s}_3, \quad \Sigma_\sigma = (\hat{s}_1 + i\sigma\hat{s}_2)/2, \tag{11}$$

which act on the bispinor $u^\sigma(p, s, r)$[2)] according to the relations

$$\begin{gathered}\Sigma_3 u^\sigma(p,s,r) = \sigma u^\sigma(p,s,r),\\ \Sigma_{-\sigma} u^\sigma(p,s,r) = u^{-\sigma}(p,s,r),\\ \Sigma_\sigma u^\sigma(p,s,r) = 0.\end{gathered} \tag{12}$$

The second relation is the known phase agreement: the action of the spin-flip operator does not result in any additional phase factor.

We emphasize an important point. Specifying the tetrad, we can write four equations for the 4-component bispinor. Namely, in addition to the Dirac equation and spin-projection equation, we obtain two equations for the spin-flip operator.

Let us consider one of the consequences. We represent the tensor g in the form

$$g^{\mu\nu} = v^\mu v^\nu - s^\mu s^\nu - s_1^\mu s_1^\nu - s_2^\mu s_2^\nu. \tag{13}$$

Then, it follows from Eqs. (11) and (13) that

$$\begin{aligned}\gamma^\mu = g^{\mu\nu}\gamma_\nu &= v^\mu \hat{v} - s^\mu \hat{s} - s_1^\mu \hat{s}_1 - s_2^\mu \hat{s}_2\\ &= v^\mu \hat{v} - \gamma_5\{s^\mu \Sigma_3 + (s_1^\mu - i\sigma s_2^\mu)\Sigma_\sigma\\ &\quad + (s_1^\mu + i\sigma s_2^\mu)\Sigma_{-\sigma}\}.\end{aligned} \tag{14}$$

Using the Dirac equation and Eqs. (12), we arrive at the relation

$$\begin{aligned}\gamma^\mu u^\sigma(p,s) &= (v^\mu - \sigma s^\mu \gamma_5) u^\sigma(p,s)\\ &\quad - (s_1^\mu + i\sigma s_2^\mu)\gamma_5 u^{-\sigma}(p,s).\end{aligned} \tag{15}$$

The repeated action of the γ matrix on Eq. (15) gives

$$\begin{aligned}&\sigma^{\mu\nu} u^\sigma(p,s)\\ &= \sigma\left([v\cdot s]^{\mu\nu}\gamma_5 + i\widetilde{[v\cdot s]}^{\mu\nu}\right) u^\sigma(p,s)\\ &\quad - [(s_1 + i\sigma s_2)\cdot(\sigma s + \gamma_5 v)]^{\mu\nu}\, u^{-\sigma}(p,s),\end{aligned} \tag{16}$$

where

$$[a\cdot b]^{\mu\nu} = a^\mu b^\nu - b^\mu a^\nu. \tag{17}$$

An arbitrary operator Q can be decomposed in terms of the complete set of the Dirac matrices

$$\Gamma = \{1, \gamma_5, \gamma^\mu, \gamma_5\gamma^\mu, \sigma^{\mu\nu}\}. \tag{18}$$

Thus, expressions (15) and (16) make it possible to reduce the action of an arbitrary matrix operator on the bispinor $Qu^\sigma(p,s)$ to a decomposition

[1)] $\gamma_5 = i\gamma^0\gamma^1\gamma^2\gamma^3$ can be represented in the form $\gamma_5 = i\hat{s}_1\hat{s}_2\hat{s}_3\hat{s}_0$.

[2)] We keep symbols s and, particularly, r only where it is necessary.

in terms of the complete set of bispinors $u^{\pm\sigma}(p,s)$, $\gamma_5 u^{\pm\sigma}(p,s)$. The decomposition coefficients are tensors whose rank is equal to the number of the free Lorentz indices of the operator Q.

3. TRANSITION MATRICES BETWEEN DIFFERENT SPIN BASES

Let the set of amplitudes in a certain spin basis be known,

$$\mathcal{M}_{\delta'\delta} = \bar{u}^{\delta'}(p',s')Qu^{\delta}(p,s), \tag{19}$$

but the axis of spin projections in the initial state is determined by the vector l. Thus, we consider the amplitude

$$\mathcal{M}'_{\delta'\sigma} = \bar{u}^{\delta'}(p',s')Qu^{\sigma}(p,l), \tag{20}$$

or, more precisely, we are finally interested in the squares of their moduli.

Using the equality

$$\sum_{\delta}\frac{1}{4}(1+\hat{v})(1+\delta\gamma_5\hat{s})u^{\sigma}(p,l) = u^{\sigma}(p,l), \tag{21}$$

we obtain the following expression for the modulus squared of amplitude (20) (we omit the arguments of the bispinors):

$$\begin{aligned}|\mathcal{M}'_{\delta'\sigma}|^2 &= \bar{u}^{\delta'}Qu^{\sigma}\bar{u}^{\sigma}\bar{Q}u^{\delta'} \qquad (22)\\ &= \sum_{\delta_1\delta_2}\bar{u}^{\delta'}Q\frac{1}{4}(1+\hat{v})(1+\delta_1\gamma_5\hat{s})u^{\sigma}\bar{u}^{\sigma}\\ &\quad\times\frac{1}{4}(1+\hat{v})(1+\delta_2\gamma_5\hat{s})\bar{Q}u^{\delta'}\\ &= \sum_{\delta_1\delta_2}\bar{u}^{\delta'}Qu^{\delta_1}\bar{u}^{\delta_1}u^{\sigma}\bar{u}^{\sigma}u^{\delta_2}\bar{u}^{\delta_2}\bar{Q}u^{\delta'}\\ &= \sum_{\delta_1\delta_2}\mathcal{M}_{\delta'\delta_1}\mathcal{K}_{\delta_1\delta_2}\mathcal{M}^{*}_{\delta'\delta_2},\end{aligned}$$

where

$$\mathcal{K}_{\delta_1\delta_2} = \bar{u}^{\delta_1}u^{\sigma}\bar{u}^{\sigma}u^{\delta_2} = \mathrm{Tr}\,u^{\sigma}\bar{u}^{\sigma}u^{\delta_2}\bar{u}^{\delta_1}. \tag{23}$$

Therefore, if we know the explicit form of matrix (23), we can calculate the modulus squared of amplitude (20) by using relation (19).

If $\delta_1 = \delta_2 = \delta$, then [6]

$$\begin{aligned}\mathcal{K}_{\delta\delta} &= \frac{1}{16}\,\mathrm{Tr}(1+\hat{v})(1+\sigma\gamma_5\hat{l})(1+\hat{v}) \qquad (24)\\ &\quad\times(1+\delta\gamma_5\hat{s}) = \frac{1}{2}\,(1-\sigma\delta(ls))\,.\end{aligned}$$

Using the spin-flip operators $\gamma_5(\hat{s}_1 - i\delta\hat{s}_2)/2$, we arrive at the expression for the configuration $\delta_1 = -\delta_2 = \delta$:

$$\begin{aligned}\mathcal{K}_{\delta-\delta} &= \frac{1}{32}\,\mathrm{Tr}(1+\hat{v})(1+\sigma\gamma_5\hat{l}) \qquad (25)\\ &\quad\times\gamma_5(\hat{s}_1 - i\delta\hat{s}_2)(1+\hat{v})(1+\delta\gamma_5\hat{s})\\ &= \frac{1}{16}\,\mathrm{Tr}\,\gamma_5(\hat{s}_1 - i\delta\hat{s}_2)(\sigma\gamma_5\hat{l} + \sigma\delta\hat{s}\hat{v}\hat{l})\\ &= -\frac{\sigma}{2}(s_1 - i\delta s_2)l.\end{aligned}$$

We derived (25) using the relation ($s_3 = s$, $s_0 = v$)

$$\gamma_5 = i\hat{s}_1\hat{s}_2\hat{s}_3\hat{s}_0. \tag{26}$$

Explicit forms (24) and (25) of the matrix elements of the matrix $\mathcal{K}_{\delta_1\delta_2}$ imply that it can be expressed in terms of the Pauli matrices σ_i:

$$\mathcal{K}_{\delta_1\delta_2} = (1 - \sigma\sigma_i(ls_i))_{\delta_1\delta_2}\,. \tag{27}$$

Relation (27) can be represented in a four-dimensional covariant form. Let us introduce the isotropic 4-vector

$$L = (1;\sigma(ls_i)) \tag{28}$$

and take into account that $\sigma_0 = 1$; then

$$\mathcal{K} = \sigma_\mu L^\mu. \tag{29}$$

Here, 1 is the 4-velocity squared, and l and s_3 are the axes of the spin projections in different spin bases.

We emphasize that Eqs. (27) and (28) contain only the vectors of the tetrad used in the calculation of amplitude (19). We can show that the final expression given by Eq. (22) is independent not only of the phase vector r, but also of the vectors s_1 and s_2, because they enter into Eq. (22) in the combinations $s_1^\mu s_1^\nu + s_2^\mu s_2^\nu = s_3^\mu s_3^\nu - g^{\mu\nu}$ and $\varepsilon^{\mu\nu\rho\sigma}s_{1\rho}s_{2\sigma} = [v_0\cdot s_3]^{\mu\nu}$.

The procedure described by Eqs. (24), (25), (27), and (29) makes it possible to build the matrix $\mathcal{K}$ for any fermion involved in the reaction; in addition, the representation by Eqs. (27) and (29) allows the application of the Fierz transformation if it is required.

We point to the following important fact. Expression (22) is also applicable when a beam is partially polarized and the states are not pure. In this case, it is necessary to make the change $\sigma l \to a$, $|a^2| < 1$ in Eqs. (24), (25), and (28) (where a is the vector of partial polarization—see [7]).

In addition to amplitude modulus squared (22), study of polarization phenomena requires the quantities $\mathcal{M}_\sigma\mathcal{M}^*_{-\sigma}$,[3)] because various polarization characteristics are expressed in terms of the real and imaginary parts of these quantities. Thus, in the general case, we should know the matrix

$$\mathcal{K}^{\sigma_1\sigma_2}_{\delta_1\delta_2} = \mathrm{Tr}\,u^{\sigma_1}\bar{u}^{\sigma_2}u^{\delta_2}\bar{u}^{\delta_1}, \tag{30}$$

and in the case $\sigma_2 = \sigma_1$, we obtain Eqs. (22) and (23).

[3)] In the amplitude notation, we retain only the spin projection of the particle whose polarization is studied.

We can show that the matrix $\mathcal{K}$ assumes the form ($\delta_{\alpha\beta}$ is the Kronecker delta)

$$\mathcal{K}^{\sigma_1\sigma_2}_{\delta_1\delta_2} = \frac{1}{2}\left\{\delta_{\sigma_1\sigma_2}\delta_{\delta_1\delta_2} - \sigma_i^{\sigma_2\sigma_1}\sigma_j^{\delta_1\delta_2}(l_i s_j)\right\}. \quad (31)$$

We recall that Eq. (31) implies the summation with respect to δ_1 and δ_2 with the amplitudes calculated in the spin basis with the tetrad $\{v, s_3, s_1, s_2\}$.

In conclusion, we note that the expression

$$\mathcal{M}'_{\sigma_1}\mathcal{M}'^{*}_{\sigma_2} = \sum_{\delta_1\delta_2}\mathcal{M}_{\delta_1}\mathcal{K}^{\sigma_1\sigma_2}_{\delta_1\delta_2}\mathcal{M}^{*}_{\delta_2} \quad (32)$$

is a new method for describing the transition from one spin basis to another without the cumbersome and noncovariant formalism of Wigner D functions.

4. DIAGONAL SPIN BASIS (DSB)

Any process can involve only an even number of fermions. If the number of free fermions is $2n$, each diagram contains n unclosed fermion lines and it is described by the structure that consists of the convolutions of n fermion sandwiches of the type

$$\bar{\Phi}^{\sigma'}(p', s')Q\Phi^{\sigma}(p, s). \quad (33)$$

For the fermion and antifermion lines, Φ are the bispinors u [see Eq. (1)] and v, respectively; for the annihilation and production of a pair, Φ are the bispinors u and v, respectively. For definiteness, we consider structures (1) and (2).

We do not discuss here the group-theoretical aspects of the DSB introduction; we only note that the vectors s and s' in the DSB are chosen so that they belong to the 2-plane (p, p') or (v, v'); $v = p/m$, $v' = p'/m'$. Satisfying this requirement, we obtain

$$s = \frac{(vv')v - v'}{\sqrt{(vv')^2 - 1}}, \quad s' = -\frac{(vv')v' - v}{\sqrt{(vv')^2 - 1}}. \quad (34)$$

Therefore, the reference vectors [see Eq. (3)] for the states at the beginning and end of the fermion line are the vectors $q = v'$ and $q' = -v$. With this sign choice, the vectors $\mathbf{s}$ and $\mathbf{s}'$ in the specified reference frames coincide with the direction of the 3-momentum of the incident particle and are opposite to that of the final particle. Here, the specified reference frames are the Breit frame for the fermion or antifermion lines (t lines) and the c.m.s. for the annihilating or produced pair (s lines).

It is clear from Eqs. (34) that the diagonality in the specified reference frames acquires the sense of helicity, and $\delta = \lambda$ and $\delta' = -\lambda'$. Thus, the DSB is the covariant description of helicity in the specified reference frames.

These are the frames where the helicities of a pair of particles, as well as spin-flip and non-spin-flip amplitudes, have clear physical meaning. Indeed, if the spins of the incident and final particles in an arbitrary reference frame are projected on the 3-momenta $\mathbf{p}$ and $\mathbf{p}'$, respectively, what can we say about the spin-flip and non-spin-flip processes? These notions in the helicity basis have merely a marking meaning.

In our opinion, owing primarily to neglect of this circumstance, the construction of operators (2) convenient in calculations continued for decades. All attempts to construct covariant operators (2) in the helicity basis are doomed to failure. The helicity of a massive particle is a "bad" quantum number, because it is not invariant under Lorentz transformations. Any declaration of the covariance of operators (2) in the helicity basis is a hidden transition to a particular reference frame. Moreover, in this case, covariance for other fermion pairs is indefinite, because each pair has its own particular reference frame. The only exception is the reactions such as $e^+e^- \to \mu^+\mu^-$. It is not surprising that these reactions are usually taken as examples for the process calculation (quarks are usually considered instead of leptons).

Prior to constructing the tetrads for the initial and final states, we introduce two orthonormal vectors symmetrized with respect to v and v' in the 2-plane (v, v'):

$$n_0 = \frac{v + v'}{2V_+}, \quad n_3 = \frac{v - v'}{2V_-}; \quad (35)$$

$$V_\pm = \sqrt{\frac{vv' \pm 1}{2}}. \quad (36)$$

It follows from Eqs. (5), (34), and (35) that

$$g^{\mu\nu}_{||} = v^\mu v^\nu - s^\mu s^\nu = v'^\mu v'^\nu - s'^\mu s'^\nu \quad (37)$$
$$= n_0^\mu n_0^\nu - n_3^\mu n_3^\nu,$$
$$\tilde{\varepsilon}^{\mu\nu}_{||} = \varepsilon^{\mu\nu\rho\sigma}v_\rho s_\sigma = \varepsilon^{\mu\nu\rho\sigma}v'_\rho s'_\sigma = \varepsilon^{\mu\nu\rho\sigma}n_{0\rho}n_{3\sigma}$$
$$= \frac{1}{2V_+V_-}\varepsilon^{\mu\nu\rho\sigma}v_\rho v'_\sigma.$$

From Eqs. (6) and (37), it follows that the choice of the common phase vector $r' = r$ results in the coincidence of the tetrads for both vectors belonging to the orthogonal 2-plane, that is

$$n_1^\mu = s_1^\mu = s'^\mu_1 = (g^{\mu\nu}_{||} - g^{\mu\nu})\frac{r_\nu}{r_\perp}, \quad (38)$$
$$n_2^\mu = s_2^\mu = s_2'^\mu = -\tilde{\varepsilon}^{\mu\nu}_{||}\frac{r_\nu}{r_\perp}.$$

Let us now consider the plane Lorentz transformation that transforms v into v'. In the representation of the

$SL(2,C)$ group, it has the form

$$\Lambda(v \to v') = \frac{1+\hat{v}'\hat{v}}{2V_+}, \tag{39}$$

and $\Lambda\hat{v}\Lambda^+ = \hat{v}'$. It also follows from Eq. (34) that $\Lambda\hat{s}\Lambda^+ = \hat{s}'$. Transformation (39) does not change the vectors that lie in the orthogonal 2-plane. Thus, the Lorentz transformation given by Eq. (39) transforms the tetrad of the incident particle into that of the final particle:

$$\Lambda(v \to v')\{\hat{v}, \hat{s}, \hat{n}_1, \hat{n}_2\}\Lambda^+(v \to v') = \left\{\hat{v}', \hat{s}', \hat{n}_1, \hat{n}_2\right\}. \tag{40}$$

In turn, this property means that the relation between the bispinors of the initial and final states in the DSB assumes the form

$$u^\delta(p', s') = \Lambda(v \to v')u^\delta(p, s). \tag{41}$$

In the DSB, we choose the normalization condition

$$\bar{u}^\delta(p)u^\delta(p) = \bar{u}^{\delta'}(p')u^{\delta'}(p') = 1. \tag{42}$$

In this case, relation (41) describes the case $m' \neq m$ as well.

In order to restore the standard normalization, it is necessary to multiply the amplitudes calculated in the DSB by the factor

$$\prod_{i=1}^{n}\sqrt{2m_i \cdot 2m_i'}, \tag{43}$$

where n is the number of unclosed fermion lines.

Using the Dirac equation and Eq. (14), we can rewrite relation (41) in various representations:

$$u^\delta(p', s') = \frac{\hat{v}'+1}{2V_+}u^\delta(p, s) = \hat{n}_0 u^\delta(p, s) = (V_+ - \delta\gamma_5 V_-)u^\delta(p, s). \tag{44}$$

Using expressions (44), we obtain the following explicit form of transition operators (2) in the DSB in terms of the projection operators of the initial (or final) state:

$$u^\delta(p, s)\bar{u}^\delta(p, s) = \frac{1}{4}(\hat{v}+1)(1+\delta\gamma_5\hat{s}). \tag{45}$$

Similarly to Eq. (44), transition operators (2) can be represented in various forms such as

$$\begin{aligned} 4u^\delta(p, s)\bar{u}^\delta(p', s') &= (\hat{v}+1)\left(\frac{1}{2V_+} - \frac{\delta\gamma_5}{2V_-}\right)(\hat{v}'+1) \\ &= (V_+ + \delta\gamma_5 V_-)(1 - \delta\gamma_5\hat{n}_0\hat{n}_3) + \hat{n}_0 + \delta\gamma_5\hat{n}_3 \\ &= \left(1 + \frac{1}{2}(V_+ + \delta\gamma_5 V_-)(\hat{n}_0 + \delta\gamma_5\hat{n}_3)\right) \\ &\times (\hat{n}_0 + \delta\gamma_5\hat{n}_3), \end{aligned} \tag{46}$$

$$\begin{aligned} 4u^\delta(p, s)\bar{u}^{-\delta}(p', s') &= \frac{\delta}{r_\perp}(\hat{v}+1) \\ &\times \left(\frac{1}{2V_-}\left(\hat{r} - \frac{r(v+v')}{vv'+1}\right)\right. \\ &\left. -\frac{\delta\gamma_5}{2V_+}\left(\hat{r} - \frac{r(v-v')}{vv'-1}\right)\right)(\hat{v}'+1) \\ &= \gamma_5(V_+ + \delta\gamma_5 V_- - \hat{n}_0)(\hat{n}_1 + i\delta\hat{n}_2) \\ &= \gamma_5\left(V_+ + \delta\gamma_5 V_- - \frac{1}{2}(\hat{n}_0 + \delta\gamma_5\hat{n}_3)\right)(\hat{n}_1 + i\delta\hat{n}_2). \end{aligned} \tag{47}$$

Expression (47) is derived from Eq. (46) using spin-flip operator (11) and the following relations valid for an arbitrary orthonormal tetrad:

$$\hat{n}_0(\hat{n}_1 + i\delta\hat{n}_2) = \delta\gamma_5\hat{n}_3(\hat{n}_1 + i\delta\hat{n}_2), \tag{48}$$
$$(\hat{n}_0 + \delta\gamma_5\hat{n}_3)^2 = 2(1 - \delta\gamma_5\hat{n}_0\hat{n}_3) = 2(1 + i\delta\hat{n}_1\hat{n}_2).$$

Since any interaction operator can be decomposed in terms of the complete set of Dirac matrices (18), it is interesting to calculate the matrix elements of this set in the DSB. It follows from Eqs. (1), (46), and (47) that

$$\begin{aligned} &\bar{u}^\delta(p', s')\{1; \gamma_5; \gamma^\mu; \gamma_5\gamma^\mu; \sigma^{\mu\nu}\}u^\delta(p, s) \\ &= \{V_+; \delta V_-; n_0^\mu; -\delta n_3^\mu; V_-[n_0 \cdot n_3]^{\mu\nu} \\ &\quad - i\delta V_+\widetilde{[n_0 \cdot n_3]}^{\mu\nu}\}, \end{aligned} \tag{49}$$

$$\begin{aligned} &\bar{u}^{-\delta}(p', s')\{1; \gamma_5; \gamma^\mu; \gamma_5\gamma^\mu; \sigma^{\mu\nu}\}u^\delta(p, s) \\ &= \{0; 0; \delta V_-(n_1 + i\delta n_2)^\mu; -V_+(n_1 + i\delta n_2)^\mu; \\ &\quad \delta\left[n_3 \cdot (n_1 + i\delta n_2)\right]^{\mu\nu}\}. \end{aligned} \tag{50}$$

Matrix elements (49) and (50) can be interpreted as the spin characteristics of the exchange particles for scalar, pseudoscalar, vector, axial, and tensor interactions, respectively.

It follows from Eq. (50) that the exchange (emission, absorption) by the pseudoscalar particle does not change the fermion spin projection in the DSB. Therefore, the choice of the DSB not only results in simple calculation expressions, but also adequately corresponds to the physical essence of the described processes. In order to confirm this statement, let us consider the matrix elements of the nucleon current in the DSB:

$$\begin{aligned} J_\mu^{\delta,\delta'} &= \bar{u}^{\delta'}(p', s') \\ &\times \left(F_1(q^2)\gamma_\mu - \frac{F_2(q^2)}{2m}\sigma_{\mu\nu}q^\nu\right)u^\delta(p, s); \\ q &= p' - p. \end{aligned} \tag{51}$$

It is clear from Eqs. (49) and (50) that

$$J_\mu^{\delta,\delta} = G_E n_{0\mu}, \qquad (52)$$
$$J_\mu^{\delta,-\delta} = \delta V_- G_M (n_1 + i\delta n_2)_\mu.$$

It is noteworthy that the form factors F_1 and F_2 in the DSB are combined into the Sachs form factors

$$G_E = F_1 + \frac{q^2}{4m^2}F_2, \quad G_M = F_1 + F_2, \qquad (53)$$

which have clear physical meaning and describe the distribution of the electric and magnetic moments of the nucleon, respectively. Thus, it follows from Eq. (52) that, in the DSB, we obtain the covariant description of the situation where the non-spin-flip processes are responsible for the electric interaction, and spin-flip processes are responsible for the magnetic interaction. In these processes, a spacelike ($q^2 < 0$) virtual photon has scalar and circular polarization, respectively.

In the helicity basis, combination (53) occurs only in the Breit frame, where the Fourier transform becomes three-dimensional, because

$$\exp(-iqr) = \exp i(\mathbf{q}\cdot\mathbf{r} - q_0 t) = \exp(i\mathbf{q}\cdot\mathbf{r}).$$

Expressions (46) and (47) describe a fermion t line. In order to describe an antifermion line and s lines for an annihilating or produced pair, it is necessary to use the relation

$$v^\delta(p,s) = -\delta\gamma_5 u^{-\delta}(p,s) \qquad (54)$$

for the bispinors of the particle and antiparticle.

If the normalization $\bar u^\delta(p)u^\delta(p) = 2m$ is restored in Eqs. (46) and (47) according to Eq. (43), and the limit $m \to 0$ and (or) $m' \to 0$ is taken, we arrive at the transition operators obtained in [8] for the processes with the massless fermions.

In certain processes, it might be more convenient to use the formalism with the same basis spinor $u^\delta(n_0, n_3; n_1, n_2)$ for the beginning and end of the fermion line. This spinor satisfies the conditions

$$\hat n_0 u^\delta(n_0,n_3) = u^\delta(n_0,n_3), \qquad (55)$$
$$\gamma_5 \hat n_3 u^\delta(n_0,n_3) = \delta u^\delta(n_0,n_3).$$

It is easy to show[4)] that the plane Lorentz transformations

$$\Lambda(n_0 \to v) = \frac{1 + \hat v\hat n_0}{\sqrt{2(V_+ + 1)}}$$

and

$$\Lambda(n_0 \to v') = \frac{1 + \hat v'\hat n_0}{\sqrt{2(V_+ + 1)}}$$

transform the tetrad of the basis spinor into the tetrads of the initial and final states, respectively. Therefore, transition operators (46) and (47) can be represented in the form

$$4u^\delta(p,s)\bar u^{\delta'}(p',s') = \frac{2}{V_+ + 1}(\hat v + 1) \qquad (56)$$
$$\times\, u^\delta(n_0,n_3)\bar u^{\delta'}(n_0,n_3)(\hat v' + 1) = \frac{1}{2(V_+ + 1)}$$
$$\times\, (\hat v + 1)(\hat n_0 + 1)(\delta_{\delta'\delta} + \gamma_5 \hat n^i \sigma^i_{\delta'\delta})(\hat v' + 1).$$

The latter equality uses the Bouchiat–Michel relation [9]. The vectors v and v' in Eq. (56) can be decomposed in terms of the vectors n_0 and n_3 using relations (35).

In conclusion of this section, we give the calculation recipe for exchange diagrams in the DSB. We take the electron–electron scattering as an example. For definiteness, let particles 1 and 3, as well as particles 2 and 4, be united in a pair. In this case, the direct diagram corresponds to the expression

$$\bar u^{\delta_3}(p_3)\gamma_\mu u^{\delta_1}(p_1)\bar u^{\delta_4}(p_4)\gamma^\mu u^{\delta_2}(p_2) \qquad (57)$$
$$= \mathrm{Tr}\,\gamma_\mu u^{\delta_1}(p_1)\bar u^{\delta_3}(p_3)\,\mathrm{Tr}\,\gamma^\mu u^{\delta_2}(p_2)\bar u^{\delta_4}(p_4).$$

Then, the exchange diagram has the structure

$$\bar u^{\delta_4}(p_4)\gamma_\mu u^{\delta_1}(p_1)\bar u^{\delta_3}(p_3)\gamma^\mu u^{\delta_2}(p_2) \qquad (58)$$
$$= \mathrm{Tr}\,\gamma_\mu u^{\delta_1}(p_1)\bar u^{\delta_3}(p_3)\gamma^\mu u^{\delta_2}(p_2)\bar u^{\delta_4}(p_4);$$

that is, it is expressed in terms of the transition operators that enter into the direct diagram.

If boson pairs are involved in the process, their tetrads are constructed similarly to the fermion pairs. The circular polarization vectors for each boson pair coincide. In the process with three bosons such as the $e^+e^- \to W^+W^-Z^0$ reaction, it is convenient to choose the common reference vector $q = k_1 + k_2 + k_3 = p_1 + p_2$ and the common vector n_2, where $n_2^\mu \sim \varepsilon^{\mu\nu\rho\sigma}k_{1\nu}k_{2\rho}k_{3\sigma}$. This choice significantly simplifies the interaction operator Q, which contains up to five γ matrices.

5. CALCULATION OF OBSERVABLES IN TERMS OF THE DIAGONAL AMPLITUDES

The matrix $\mathcal{K}$ in Eq. (31) can be represented in the form

$$\mathcal{K}^{\sigma_1\sigma_2}_{\delta_1\delta_2} = \frac{1}{2}\Big\{(\sigma_0 v^\mu)^{\sigma_2\sigma_1}(\sigma_0 v_\mu)^{\delta_1\delta_2} \qquad (59)$$
$$- (\sigma_i l_i^\mu)^{\sigma_2\sigma_1}(\sigma_j s_{j\mu})^{\delta_1\delta_2}\Big\} = \frac{1}{2}(\bar\sigma l^\mu)^{\sigma_2\sigma_1}(\sigma s_\mu)^{\delta_1\delta_2}$$
$$= \frac{1}{2}(\sigma l^\mu)^{\sigma_2\sigma_1}(\bar\sigma s_\mu)^{\delta_1\delta_2}.$$

[4)] We use the relation $V_-/(V_+ + 1) = (V_+ - 1)/V_-$.

Here, $\sigma a = \sigma_0 a_0 + \sigma_i a_i$, $\bar{\sigma} a = \sigma_0 a_0 - \sigma_i a_i$ and we take into account the equality $v^\mu s_{i\mu} = v^\mu l_{i\mu} = 0$ for both tetrads. As a result, Eq. (32) assumes the form

$$\mathcal{M}'_{\sigma_1}\mathcal{M}'^{*}_{\sigma_2} = \frac{1}{2}(\bar{\sigma}l^\mu)^{\sigma_2\sigma_1} \tag{60}$$

$$\times \sum_{\delta_1\delta_2} \mathcal{M}_{\delta_1}(\sigma s_\mu)^{\delta_1\delta_2}\mathcal{M}^*_{\delta_2} = \frac{1}{2}(\sigma l^\mu)^{\sigma_2\sigma_1}$$

$$\times \sum_{\delta_1\delta_2} \mathcal{M}_{\delta_1}(\bar{\sigma} s_\mu)^{\delta_1\delta_2}\mathcal{M}^*_{\delta_2}.$$

Let us now consider the case where the final particle v' in Eq. (20) is also described in a certain basis with the tetrad $\{v', l'_i\}$. Transformations similar to Eq. (22) give[5)]

$$\mathcal{M}'_{\sigma'_1\sigma_1}\mathcal{M}'^{*}_{\sigma'_2\sigma_2} \tag{61}$$

$$= \sum_{\delta_1,\delta'_1,\delta_2,\delta'_2} \mathcal{M}_{\delta'_1\delta_1}\frac{1}{2}\Big\{\delta_{\sigma_1\sigma_2}\delta_{\delta_1\delta_2}$$

$$- \sigma_i^{\sigma_2\sigma_1}\sigma_j^{\delta_1\delta_2}(l_i s_j)\Big\}\mathcal{M}^*_{\delta'_2\delta_2}\frac{1}{2}\Big\{\delta_{\sigma'_1\sigma'_2}\delta_{\delta'_1\delta'_2}$$

$$- \sigma_a^{\sigma'_1\sigma'_2}\sigma_b^{\delta'_2\delta'_1}(l'_a s'_b)\Big\}.$$

Using Eq. (59) and a similar expression for the final particle, we obtain $\left(\mathcal{M}^+_{\delta_2\delta'_2} = \mathcal{M}^*_{\delta'_2\delta_2}\right)$

$$\mathcal{M}'_{\sigma'_1\sigma_1}\mathcal{M}'^{*}_{\sigma'_2\sigma_2} = \frac{1}{4}(\bar{\sigma}l^\mu)^{\sigma_2\sigma_1}(\sigma l'^\nu)^{\sigma'_1\sigma'_2} \tag{62}$$

$$\times \sum_{\delta_1,\delta'_1,\delta_2,\delta'_2} \mathcal{M}_{\delta'_1\delta_1}(\sigma s_\mu)^{\delta_1\delta_2}\mathcal{M}^+_{\delta_2\delta'_2}(\bar{\sigma} s'_\nu)^{\delta'_2\delta'_1}$$

$$= \frac{1}{4}(\sigma l^\mu)^{\sigma_2\sigma_1}(\bar{\sigma} l'^\nu)^{\sigma'_1\sigma'_2}$$

$$\times \sum_{\delta_1,\delta'_1,\delta_2,\delta'_2} \mathcal{M}_{\delta'_1\delta_1}(\bar{\sigma} s_\mu)^{\delta_1\delta_2}\mathcal{M}^+_{\delta_2\delta'_2}(\sigma s'_\nu)^{\delta'_2\delta'_1}.$$

On the right-hand side of Eqs. (61) and (62), the calculations might be performed in arbitrary spin bases. However, the DSB is the most suitable basis for this purpose. It follows from the discussion in Section 4 that, owing to the symmetrization of the spin states of a fermion pair [6, 10], the amplitudes have the simplest form and adequately describe the spin kinematics of the interacting particles. The same is true for the matrices $\mathcal{K}$ that enter into Eqs. (61) and (62), because they contain tetrads that are constrained by Eqs. (35), (37), and (40). In addition, form (62) is convenient for the Fierz transformations.

Finally, we emphasize the following. Methods that enable one to avoid the squaring procedure through the direct calculation of amplitudes have been developed for more than 40 years. When it is necessary to change from one basis (e.g., a basis chosen for the calculations) to another (e.g., a basis where measurements are performed), the formalism of Wigner D functions or another similar formalism is used. This procedure is the most cumbersome and time-consuming step. It follows from our considerations that it is possible to avoid this step through the "inverse trace." Instead of direct transition from one spin state to another, it is more convenient to use the squaring procedure.

[5)] We recall that the spin indices of other particles that are involved in the reaction are omitted.

REFERENCES

1. M. V. Galynskiĭ and S. M. Sikach, Fiz. Élem. Chastits At. Yadra **29**, 1133 (1998) [Phys. Part. Nucl. **29**, 409 (1998)]; M. V. Galynsky and S. M. Sikach, hep-ph/9910284.
2. A. L. Bondarev, hep-ph/9710398.
3. F. I. Fedorov, *Lorentz Group* (Nauka, Moscow, 1979) [in Russian].
4. A. A. Bogush and F. I. Fedorov, Izv. Akad. Nauk BSSR, Ser. Fiz.-Mat. Nauk, No. 2, 26 (1962).
5. S. M. Sikach, in *Covariant Methods in Theoretical Physics* (Inst. Fiz. Akad. Nauk BSSR, Minsk, 1981), p. 91 [in Russian].
6. S. M. Sikach, in *Proceedings of the 15th International Spin Physics Symposium "SPIN 2002", New York, 2002*, Ed. by Y. Makdisi *et al.* (Melville, New York, 2003), p. 661.
7. V. B. Berestetskii, E. M. Lifshitz, and L. P. Pitaevskii, *Quantum Electrodynamics* (Nauka, Moscow, 1989, Pergamon Press, Oxford, 1982), p. 723.
8. S. M. Sikach, Preprint Nos. 658, 659, IP ASB (Minsk, 1992).
9. C. Bouchiat and L. Michel, Nucl. Phys. **5**, 416 (1958).
10. S. M. Sikach, in *Proceedings of the International School–Seminar "Actual Problems of Particle Physics", Gomel, 2001*, Ed. by A. Bogush *et al.* (Dubna, 2002), Vol. 2, p. 62.

Translated by M. Kobrinsky

Physics of Atomic Nuclei, Vol. 68, No. 6, 2005, pp. 1071–1078. Translated from Yadernaya Fizika, Vol. 68, No. 6, 2005, pp. 1113–1120.
Original Russian Text Copyright © 2005 by the Editorial Board.

FUTURE PUBLICATIONS

Tensor Analyzing Power for Relativistic-Deuteron Fragmentation as a Means for Studying the Structure of the Deuteron within Light-Front Dynamics

L. S. Azhgirey, S. V. Afanas'ev, V. N. Zhmyrov, L. S. Zolin, V. I. Ivanov, A. Yu. Isupov, V. P. Ladygin, A. G. Litvinenko, V. F. Peresedov, A. N. Khrenov, and N. P. Yudin

New data on the vector (A_y) and tensor (A_{yy}) analyzing powers for the reaction $^9\mathrm{Be}(d,p)X$ at a primary deuteron momentum of 5 GeV/c for a proton emission angle of 178 mrad are obtained by using the synchrophasotron of the Joint Institute for Nuclear Research (JINR, Dubna). The experimental data on A_{yy} are analyzed within the approach based on light-front dynamics, the relativistic wave function obtained by Karmanov and his colleagues being used for the deuteron. It is shown that, in contrast to what one has from calculations with standard nonrelativistic deuteron wave functions, all relevant data can be explained in this approximation without resort to additional degrees of freedom.

Heavy Majorana Neutrinos in the Production of Dileptons in Deep-Inelastic Lepton–Proton Scattering

A. Ali, A. V. Borisov, and D. V. Zhuridov

The cross section for the deep inelastic production of likely charged leptons in the $e^+p \to \bar{\nu}_e \ell^+ \ell'^+ X$ ($\ell, \ell' = e, \mu, \tau$) processes induced by the exchange of heavy Majorana neutrinos is calculated. The effect of the interference of a few neutrino mass eigenstates is studied. The possibilities of observing these processes at future lepton–proton colliders are considered.

On the Possibility of Observing $a_0^0(980)$–$f_0(980)$ Mixing in the Reaction $\pi^- p \to \eta\pi^0 n$ on a Polarized Target

N. N. Achasov and G. N. Shestakov

It is shown that the spin asymmetry in the reaction $\pi^- p \to a_0^0(980)n \to (\eta\pi^0)_S n$ is highly sensitive to the mixing of the $a_0^0(980)$ and $f_0(980)$ resonances. At low momentum transfers (namely, in any of the intervals $0 \le -t \le 0.025, \ldots, 0.1$ GeV^2), the asymmetry normalized in such a way that it takes values between -1 and 1 must undergo a discontinuity close to unity in the region of the $\eta\pi^0$ invariant masses between 0.965 and 1.01 GeV. A large jump of the asymmetry is due exclusively to $a_0^0(980)$–$f_0(980)$ mixing. A very high resolution in the $\eta\pi^0$ invariant mass is not required for observing the discontinuity of the asymmetry. The energy dependence of the polarization effect is expected to be rather weak; therefore, the polarization effect in question can be studied at any high energy—for example, in the range between 8 and 100 GeV.

Some Features of the Momentum Spectrum of Protons from $^{16}\mathrm{O}p$ Collisions at 3.25 GeV/c per Nucleon

E. Kh. Bazarov, V. V. Glagolev, K. G. Gulamov, S. L. Lutpullaev, K. Olimov, Kh. Sh. Khamidov, A. A. Yuldashev, and B. S. Yuldashev

The momentum features of protons originating from $^{16}\mathrm{O}p$ collisions at a momentum of 3.25 GeV/c per nucleon are analyzed. It is shown that the degree of excitation of the fragmenting nucleus affects predominantly the shape of the momentum spectrum of protons emitted into the backward hemisphere in the rest frame of the target nucleus and partly the shape of the spectra of forward protons formed via the mechanisms of Fermi breakup and evaporation.

1063-7788/05/6806-1071$26.00 © 2005 Pleiades Publishing, Inc.

On the Energy Spectrum of Protons Originating from ^{16}Op Interactions at 3.25 GeV/c per Nucleon

E. Kh. Bazarov

New experimental data on the mechanisms that can be responsible for the emission of protons emerging as fragments from the interactions of oxygen nuclei in a hydrogen chamber at high energies are presented. It is shown that the anomalies observed in the energy spectrum of protons at kinetic energies in the range 70–90 MeV are associated with slow-pion absorption by a quasideuteron nucleon pair.

Interaction of Gold Nuclei with Photoemulsion Nuclei at Energies in the Range 100–1200 MeV per Nucleon and the Cascade–Evaporation Model

S. D. Bogdanov, E. Ya. Shablya, S. Vokal, V. F. Kosmach, and V. A. Plyushchev

The interaction of gold nuclei with photoemulsion nuclei at energies in the range 100–1200 MeV per nucleon was studied experimentally. A consistent comparison of the resulting experimental data with the results of the calculations based on the cascade–evaporation model is performed.

Indirect Methods for Determining Heavy-Neutrino Masses

G. G. Boyarkina and O. M. Boyarkin

Within the two-flavor approximation, equations that relate the oscillation parameters for both light and heavy neutrinos to the Yukawa coupling constants and the vacuum expectation values of the Higgs fields are derived within the left–right model. The contributions from Higgs bosons to the muon anomalous magnetic moment, to the cross sections for lepton-flavor-violating processes, and to the cross sections for low-energy light-neutrino scattering are studied in order to determine the Yukawa coupling constants. It is shown that the heavy-neutrino masses $m_{N_{1,2}}$ can be expressed in terms of only the triplet Yukawa coupling constants and the mass of the gauge W_2 boson. Data on direct and inverse muon decay and constraints on the masses of the $\delta^{(-)}$, $\Delta_{1,2}^{(--)}$, and W_2 bosons are used to obtain bounds on $m_{N_{1,2}}$ both in the absence of degeneracy and in the presence of mass degeneracy in the sector of heavy neutrinos. Only in the case of degeneracy are data concerning the explanation of the $(g-2)_\mu$ anomaly used to determine bounds on $m_{N_{1,2}}$.

Single-Spin Asymmetry in Inclusive Neutral-Pion Production in $pp_\uparrow$ Interactions at 70 GeV in the Region $-0.4 < x_F < -0.1$

A. N. Vasiliev, V. N. Grishin, A. M. Davidenko, A. A. Derevshchikov, Yu. A. Matulenko, Yu. M. Mel'nik, A. P. Meshchanin, V. V. Mochalov, L. V. Nogach, S. B. Nurushev, A. F. Prudkoglyad, P. A. Semenov, L. F. Solov'ev, V. L. Solovianov†, V. Yu. Khodyrev, K. E. Shestermanov, A. E. Yakutin, N. S. Borisov, V. N. Matafonov†, A. B. Neganov, Yu. A. Plis, Yu. A. Usov, A. N. Fedorov, and A. A. Lukhanin

The single-spin asymmetry in inclusive neutral-pion production in the reaction $p + p_\uparrow \to \pi^0 + X$ at 70 GeV was measured over the region specified by the inequalities $-0.4 < x_F < -0.1$ and $0.9 < p_T < 2.5$ GeV/c. According to the results of these measurements, the asymmetry is close to zero in the region $-0.2 < x_F < -0.1$ and grows in magnitude with decreasing x_F, amounting to $(-10.6 \pm 3.2)\%$ for $-0.4 < x_F < -0.2$.

Independent Yields of Kr and Xe Appearing as Fragments in the Photofission of ^{237}Np and ^{243}Am Odd Nuclei

Yu. P. Gangrsky, V. I. Zhemenik, G. V. Myshinsky, and Yu. E. Penionzhkevich

Results are presented that were obtained by measuring the independent yields of Kr ($A = 89$–93) and Xe ($A = 135$–142) appearing as fragments in the photofission of ^{237}Np and ^{243}Am odd nuclei. The respective experiments were performed in a beam of bremsstrahlung photons from electrons accelerated to an energy of 25 MeV at the microtron of the Laboratory of Nuclear Reactions at the Joint Institute for Nuclear Research

† Deceased.

(JINR, Dubna). Use was made of the procedure involving the transportation of fragments emitted from the target by a gas flow along a capillary and the condensation of inert gases in a cryostat at liquid nitrogen temperature. The identification of Kr and Xe appearing as fragments was performed by the gamma spectra of their daughter products. The mass-number distributions of the independent yields of Kr and Xe isotopes were obtained, along with those for fragments conjugate to them (Y and La in the fission of ^{237}Np and Nb and Pr in the fission of ^{243}Am).

Semimicroscopic Description of the Simplest Photonuclear Reactions Involving the Excitation of a Giant $E1$ Resonance

M. L. Gorelik and M. H. Urin

A quantitative interpretation of basic properties of a giant $E1$ resonance is proposed within a semimicroscopic approach based on the random-phase approximation that takes exactly into account a single-particle continuum and on a phenomenological description of the fragmentation effect. For some magic and semimagic nuclei, the calculated photoabsorption cross sections and cross sections for partial "direct + semidirect" photoneutron reactions are compared with their experimental counterparts.

Neutrino Geophysics at Baksan: Searches for Antineutrino Sources and Sources of Radiogenic Heat in the Earth

G. V. Domogatsky, V. I. Kopeikin, L. A. Mikaelyan, and V. V. Sinev

Antineutrinos produced in the Earth ("geoneutrinos") carry information that is of crucial importance for the understanding of the origin and evolution of our planet. It is shown that the Baksan Neutrino Observatory of the Institute for Nuclear Research (Moscow, Russian Academy of Sciences) may become one of the best laboratories for studying geoneutrinos with the aid of a large scintillation spectrometer. A brief history of the development of concepts of the Earth as a source of antineutrinos—it dates back to 1960, spanning a period of nearly 45 years (1960–2004)—is outlined.

Molecular Structure of Exotic Mesons

M. A. Durnev

The 0^{--} exotic meson state is considered as the P-wave molecular state of the $\rho'(1465)$ and $\eta(550)$ mesons. The mass and decay width of the 0^{--} exotic meson are calculated by the N/D dispersion method.

Searches for Effects of the Breakdown of Fundamental Symmetries in Isomeric Nuclear States

S. D. Kurgalin, I. S. Okunev, T. V. Chuvil'skaya, and Yu. M. Chuvil'sky

The results of broad searches for schemes that are convenient for observing effects of time-inversion-invariance violation (T violation) simultaneously with parity violation (PT violation) in electromagnetic transitions in nuclei are presented. The main problems in observing such effects are discussed. A scheme that seems the most promising for this and which is based on measuring the linear polarization of gamma radiation accompanying the deexcitation of isomeric states of nuclei that are oriented by a magnetic field at low temperatures is highlighted.

Yield of ^{8}Be Originating from the Fragmentation of ^{10}B in Emulsion at an Energy of 1 GeV per Nucleon

F. G. Lepekhin and B. B. Simonov

The branching fraction of the channel $^{10}\mathrm{B} \to {}^8\mathrm{Be} \to 2\alpha$ is estimated at $(18 \pm 3)\%$, while the constants characterizing angular distributions of product alpha particles and the distribution of the angles between them are found to be 20.5 ± 0.7 and 31.7 ± 2.0 mrad, respectively. These values agree with their counterparts calculated before the experiment on the basis of prevalent ideas of the limiting fragmentation of relativistic nuclei.

Hadroproduction of High-Transverse-Momentum B_c Mesons within the k_T-Factorization Approach

A. K. Likhoded, V. A. Saleev, and D. V. Vasin

Within the k_T-factorization approach, the spectra of B_c mesons at the energies of the Tevatron and LHC colliders are calculated on the basis of the fragmentation and fusion models. The calculations within the fusion model are performed under the assumption of charm excitation in the proton.

Inclusive Production of a Vector Charmonium in Electron–Photon Annihilation to Two Photons

A. V. Luchinsky

One of the processes that involve the inclusive production of a vector charmonium state, J/ψ or $\psi(2S)$, in electron–positron annihilation to two photons at $\sqrt{s} = 10.6$ GeV is considered on the basis of the color-singlet model. Analytic expressions for the respective differential cross sections, numerical values of the total cross sections, and graphs representing the distributions of product vector mesons with respect to their emission angle and energy are given. It is shown that these distributions differ substantially from the analogous distributions in the case of charmonium production in single-photon electron–positron annihilation. Owing to this, the process being considered can readily be separated despite the smallness associated with the additional factor of α.

Rare Radiative Leptonic Decays $\bar{B}^0_{d,s} \to \ell^+\ell^-\gamma$

D. I. Melikhov, N. V. Nikitin, and K. S. Toms

The rare radiative leptonic decays $\bar{B}^0_{d,s} \to \ell^+\ell^-\gamma$ are studied. The contributions to the respective amplitude from the emission of photons from the quark loop, from bremsstrahlung from leptons, and from weak-annihilation effects are taken into account in relevant calculations. Results are presented for the partial widths and distributions of leptons in the final state. It is shown that the previously disregarded contributions of vector resonances associated with virtual-photon emission from the light valence quark of the B meson have a significant effect on the dilepton-mass spectra.

Static and Statistical Properties of Hot Nuclei in the Macroscopic Temperature-Dependent Model That Takes into Account the Finiteness of Nuclear Forces

E. G. Ryabov and G. D. Adeev

The macroscopic temperature-dependent model that takes into account the finiteness of nuclear forces is used to calculate the static and statistical properties of hot rotating compound nuclei. The level-density parameter is approximated by an expression of the leptodermous type. The resulting coefficients are in good agreement with their counterparts proposed previously by A.V. Ignatyuk and his colleagues. It is shown that the simultaneous consideration of the nuclear temperature and angular-momentum effects on the quantities under study, such as the heights and positions of fission barriers and the effective moments of inertia of nuclei at the barrier, is important. The fissility parameter $(Z^2/A)_{\text{crit}}$ and the position of the Businaro–Gallone point are studied as a function of temperature. It is found that, with increasing temperature, both parameters are shifted to the region of lighter nuclei. It is shown that the inclusion of temperature leads to qualitatively the same effects as the inclusion of the angular momentum of a nucleus, but, quantitatively, thermal excitation leads to smaller effects than rotational excitation.

On the Properties of Charge-Exchange Dipole Excitations and of the $T_>$ Component of the Giant $E1$ Resonance in Spherical Nuclei

I. V. Safonov, M. L. Gorelik, and M. H. Urin

Within the semimicroscopic approach based on the random-phase approximation that takes exactly into account a single-particle continuum and on a phenomenological inclusion of the fragmentation effect, it is proposed to describe the strength functions for charge-exchange giant dipole resonances and cross sections

for photoabsorption and for partial "direct + semidirect" (γ, p) reactions in the vicinity of a giant $E1$ resonance with allowance for the isospin-splitting effect. The results of the calculations performed for some magic and semimagic nuclei without resort to free parameters are compared with available experimental data.

On Solving Nonhomogeneous Bethe–Salpeter Equations

S. S. Semikh, S. M. Dorkin, M. Bayer, and L. P. Captar'

A new method for solving nonhomogeneous Bethe–Salpeter equations is developed. The method is based on expanding the interaction amplitudes and kernels in a basis of four-dimensional spherical harmonics and is applicable both to scalar and to spinor equations. The method is explained in detail for the nonhomogeneous Bethe–Salpeter equation for scalar particles in the ladder approximation. The calculated model phase shifts are in good agreement with the results reported previously.

Project of a Large Superconductor Detector—Calorimeter Where Hot-Electron Diffusion is One-Dimensional

V. S. Shpinel

Over the past few years, radically new detectors for soft x-ray and gamma radiation have been created on the basis of superconducting tunnel transitions. These detectors made it possible to obtain a very high resolution, but the maximum area of the detectors in question was overly small for them to be applied in nuclear spectroscopy. The present study is devoted to the problem of creating a comparatively large superconductor detector for recording photons that is appropriate for applications in different regions. The detector will consist of three parts: an absorber, a calorimeter for hot electrons, and a thermometer based on a tunnel transition (normal metal–dielectric–superconductor). The absorber has a multilayer structure consisting of thin superconductor layers that are arranged in the order of the change in the superconductor energy gap Δ. This structure specifies a direction of hot-electron diffusion. Owing to the fact that quasiparticle diffusion occurs in a specific direction, the diffusion time is shorter than in the case of ordinary diffusion. It is necessary that this time be shorter than the time of electron–phonon interaction. Calculations of the diffusion time that were performed for a specific structure and data available in the literature for electron–phonon interaction show that the working area of the detector may reach 3 to 4 mm^2, while its thickness may be about 1 mm. These dimensions can be increased considerably in the case of especially pure superconductors.

Determination of the Quark–Antiquark Components of the Photon Wave Function for *u*, *d*, and *s* Quarks

A. V. Anisovich, V. V. Anisovich, L. G. Dakhno, V. A. Nikonov, and A. V. Sarantsev

Based on the data for the transitions $\pi^0, \eta, \eta' \to \gamma\gamma^*(Q^2)$ and reactions of the e^+e^- annihilations, $e^+e^- \to \rho^0, \omega, \phi$ and $e^+e^- \to$ hadrons at $1 < E_{e^+e^-} < 3.7$ GeV, we determine the light-quark components of the photon wave function $\gamma^*(Q^2) \to q\bar{q}\,(q = u, d, s)$ for the region $0 \lesssim Q^2 \lesssim 1\,(\mathrm{GeV}/c)^2$.

Study of the *pd* Reaction at Ultralow Energies Using Hydrogen Liner Plasma

V. M. Bystritsky, Vit. M. Bystritskii, G. N. Dudkin, V. V. Gerasimov, A. R. Krylov, G. A. Mesyats, B. A. Nechaev, V. M. Padalko, S. S. Parzhitsky, F. M. Pen'kov, N. A. Ratakhin, and J. Wozniak

The present work is devoted to the study of the pd reaction ($pd \to {}^3\mathrm{He} + \gamma(5.5\ \mathrm{MeV})$) in the range of astrophysical energies of collisions of protons with deuterons using a hydrogen liner in the inverse Z-pinch configuration at the pulsed-power generator MIG (HCEI, Tomsk). Fundamental characteristics of this and other reactions with light nuclei at ultralow energies are important for problems of basic physics and astrophysics. The knowledge of the energy distribution of the nuclei participating in these reactions is important due to their exponential type of dependence on the collision energy. Two experimental techniques were designed and tested for recovering the energy distribution of liner protons incident on the CD_2 target by using optical detectors and ion collectors. It is shown that the combined use of these two techniques could provide relevant information on the energy distribution of accelerated protons in a liner. Estimates of

the upper limits on the astrophysical S factor and the effective cross section for the pd reaction in the proton–deuteron collision energy range of 2.7–16.7 keV are obtained: $\bar{S}_{pd}(E_{pd} = 10.2\ \text{keV}) \leq 2.5 \times 10^{-7}$ MeV b and $\tilde{\sigma}_{pd}(2.7 \leq E_{pd} \leq 16.7\ \text{keV}) \leq 4 \times 10^{-33}\ \text{cm}^2$.

Fundamental–Electroweak Scale Hierarchy in the Standard Model

C. D. Froggatt, L. V. Laperashvili, and H. B. Nielsen

The multiple-point principle, according to which several vacuum states with the same energy density exist, is put forward as a fine-tuning mechanism predicting the ratio between the fundamental and electroweak scales in the Standard Model (SM). It is shown that this ratio is exponentially huge: $\sim e^{40}$. Using renormalization group equations for the SM, we obtain the effective potential in the two-loop approximation and investigate the existence of its postulated second minimum at the fundamental scale. The investigation of the evolution of the top-quark Yukawa coupling constant in the two-loop approximation shows that, with initial values of the top-quark Yukawa coupling in the interval $h(M_t) = 0.95 \pm 0.03$ (here, M_t is the top-quark pole mass), a second minimum of the SM effective potential can exist in the region $\phi_{\min 2} \approx 10^{16}-10^{22}$ GeV. A new bound state of six top-quarks and six antitop quarks, formed owing to Higgs boson exchanges between pairs of quarks/antiquarks, is predicted to exist. This bound state is supposed to condense in a new phase of the SM vacuum. This gives rise to the possibility of having a phase transition between vacua with and without such a condensate. The existence of three vacuum states (new, electroweak, and fundamental) solves the hierarchy problem in the SM.

Comparative Analysis of the ^{178m2}Hf Yield in Reactions with Various Projectiles

S. A. Karamian

The long-lived high-spin ^{178m2}Hf K isomer can be produced in nuclear reactions with various projectiles. The reaction yields and cross sections were measured in a series of experiments and the results are now reviewed. The systematics of isomer-to-ground state ratios is composed and real production capabilities are estimated for the best reactions. Such a summary is relevant to the significance of the isomer studies both for nuclear-science knowledge and for possible applications. Potential isomer applications were earlier stressed in popular publications with probably overestimated expectations. The real possibilities are restricted in part by the production yield and by other shortcomings as well.

Can Centauros or Chirons Be the First Observations of Evaporating Mini Black Holes?

A. D. Mironov, A. Yu. Morozov, and T. N. Tomaras

We argue that signals expected from the evaporation of mini black holes—predicted in TeV-gravity models with large extra dimensions and possibly produced in ultrahigh-energy collisions in the atmosphere—are quite similar to the characteristics of Centauro events, an old mystery of cosmic-ray physics.

Production and Decay of Charmed Baryons: Spectra of Muons and Asymmetry between μ^+ and μ^-

N. V. Nikitin and O. I. Piskounova

The spectra of muons from the decay of Λ_c baryons were calculated on the basis of the description of recent data on charmed-baryon production in hadronic interactions. Data are described in the framework of the quark–gluon string (QGS) model that allows us to consider primary proton interactions at arbitrary high energy. A Monte Carlo code was built for charmed-baryon semileptonic decay in order to obtain the kinematical characteristics of resulting particles. It is predicted that the charge asymmetry between the energy spectra of μ^+ and μ^- in the laboratory system is clearly seen as the consequence of asymmetry between the spectra of charmed baryons and antibaryons. This extension of the QGS model can be used to correct the calculations of muon and neutrino spectra in astrophysics.

Special Case of Sunset: Reduction and ε Expansion

A. Onishchenko and O. Veretin

We consider two-loop sunset diagrams with two mass scales m and M at the threshold and pseudothreshold that cannot be treated by earlier published formulas. The complete reduction to master integrals is given. The master integrals are evaluated as series in the ratio m/M and in ε with the aid of a differential-equation method. The rules of asymptotic expansion in the case where q^2 is at the (pseudo)threshold are given.

Gravity as the Affine Goldstone Phenomenon and Beyond

Yu. F. Pirogov

The two-phase structure is imposed on the world continuum, with the graviton emerging as a tensor Goldstone boson during the spontaneous transition from the affinely connected phase to the metric one. The physics principle of metarelativity, extending the respective principle of special relativity, is postulated. The theory of metagravitation as the general nonlinear model $GL(4,R)/SO(1,3)$ in the arbitrary background continuum is built. The concept of the Metauniverse as the ensemble of the regions of the metric phase inside the affinely connected phase is introduced, and the possible bearing of the emerging multiple universes to the fine tuning of our Universe is conjectured.

Dibaryon Model for Nuclear Force and the Properties of the Three-Nucleon System

V. N. Pomerantsev, V. I. Kukulin, V. T. Voronchev, and A. Faessler

The dibaryon model for NN interaction that supposes the formation of an intermediate six-quark bag dressed with a σ field is applied to the $3N$ system, where it results in a new three-body force of scalar nature between the six-quark bag and a third nucleon. A new multicomponent formalism is developed to describe three-body systems with nonstatic pairwise interactions and nonnucleonic degrees of freedom. Precise variational calculations of $3N$ bound states are carried out in the dressed-bag model including the new scalar three-body force. It is shown that this three-body force gives at least half the $3N$ total binding energy, while the weight of nonnucleonic components in the ^{3}H and ^{3}He wave functions can exceed 10%. The new force model provides a very good description of $3N$ bound states with a reasonable magnitude of the σNN coupling constant. A new Coulomb $3N$ force between the third nucleon and a dibaryon is found to be very important for a correct description of the Coulomb energy and the root-mean-square charge radius in ^{3}He. In view of the new results for the Coulomb displacement energy obtained here for $A = 3$ nuclei, an explanation for the long-term Nolen–Schiffer paradox in nuclear physics is suggested. The role of the charge-symmetry breaking effects in the nuclear force is discussed.

Measurements of the Total-Cross-Section Difference $\Delta\sigma_L(np)$ at 1.39, 1.69, 1.89, and 1.99 GeV

V. I. Sharov, N. G. Anischenko, V. G. Antonenko, S. A. Averichev, L. S. Azhgirey, V. D. Bartenev, N. A. Bazhanov, A. A. Belyaev, N. A. Blinov, N. S. Borisov, S. B. Borzakov, Yu. T. Borzunov, Yu. P. Bushuev, L. P. Chernenko, E. V. Chernykh, V. F. Chumakov, S. A. Dolgii, A. N. Fedorov, V. V. Fimushkin, M. Finger, M. Finger, Jr. , L. B. Golovanov, G. M. Gurevich, A. Janata, A. D. Kirillov, V. G. Kolomiets, E. V. Komogorov, A. D. Kovalenko, A. I. Kovalev, V. A. Krasnov, P. Krstonoshich, E. S. Kuzmin, V. P. Ladygin, A. B. Lazarev, F. Lehar, A. de Lesquen, M. Yu. Liburg, A. N. Livanov, A. A. Lukhanin, P. K. Maniakov, V. N. Matafonov, E. A. Matyushevsky, V. D. Moroz, A. A. Morozov, A. B. Neganov, G. P. Nikolaevsky, A. A. Nomofilov, Tz. Panteleev, Yu. K. Pilipenko, I. L. Pisarev, Yu. A. Plis, Yu. P. Polunin, A. N. Prokofiev, V. Yu. Prytkov, P. A. Rukoyatkin, V. A. Schedrov, O. N. Shevelev, S. N. Shilov, R. A. Shindin, M. Slunečka, V. Slunečková, A. Yu. Starikov, G. D. Stoletov, L. N. Strunov, A. L. Svetov, Yu. A. Usov, T. Vasiliev, V. I. Volkov, E. I. Vorobiev, I. P. Yudin, I. V. Zaitsev, A. A. Zhdanov, and V. N. Zhmyrov

New accurate data on the neutron–proton spin-dependent total-cross-section difference $\Delta\sigma_L(np)$ at the neutron-beam kinetic energies of 1.39, 1.69, 1.89, and 1.99 GeV are presented. In general, these data complete the measurements of the energy dependence of the $\Delta\sigma_L(np)$ over the Dubna Synchrophasotron energy region. The measurements were carried out at the Synchrophasotron of the Veksler and Baldin Laboratory of High Energies at the Joint Institute for Nuclear Research. A quasimonochromatic neutron beam was produced by breakup of extracted polarized deuterons. The deuteron (and hence neutron) polarization direction was

flipped every accelerator burst. The neutron vertical direction of polarization was rotated onto the neutron beam direction and longitudinally (L) polarized neutrons were transmitted through a large proton L-polarized target. The longitudinal target-polarization direction was reversed after one to two days of measurements. Four different combinations of the beam and target parallel and antiparallel polarization directions, both oriented along the neutron beam momentum, were used at each energy. A fast decrease in $-\Delta\sigma_L(np)$ with increasing energy above 1.1 GeV and a structure in the energy dependence around 1.8 GeV, first observed from our previous data, seem well revealed. The new results are also compared with model predictions and with phase-shift-analysis fits. The $\Delta\sigma_L$ quantities for isosinglet state $I = 0$, deduced from the measured $\Delta\sigma_L(np)$ values and known $\Delta\sigma_L(pp)$ data, are also given. The results of the measurements of unpolarized total cross sections $\sigma_{0\mathrm{tot}}(np)$ at 1.3, 1.4, and 1.5 GeV and $\sigma_{0\mathrm{tot}}(n\mathrm{C})$ at 1.4 and 1.5 GeV are presented as well. These data were obtained by using the same apparatus and high-intensity unpolarized deuteron beams extracted either from the synchrophasotron or from the nuclotron.

Physics of Atomic Nuclei, Vol. 68, No. 6, 2005, pp. 909–920. Translated from Yadernaya Fizika, Vol. 68, No. 6, 2005, pp. 948–959.
Original Russian Text Copyright © 2005 by Davidovskaya, Kashuba, Porodzinsky.

NUCLEI
Theory

Isotopic Dependence of the Shape of Se Nuclei in the Collective-Model Representation

O. I. Davidovskaya[1)*], I. E. Kashuba[1)], and Yu. V. Porodzinsky[†2)]

Received November 3, 2003; in final form, March 15, 2004

Abstract—The energy structure of low-lying excited states in the nuclei of even selenium isotopes is considered on the basis of a soft-nucleus model. The nuclei are treated as nonaxial rotors, longitudinal and transverse vibrations of their surface being taken into account in the quadrupole-deformation approximation featuring an admixture of an octupole deformation. The parameters of a phenomenological collective model for the ^{72,74,76,78,80,82}Se nuclei are found both in the case of β vibrations (longitudinal vibrations) and in the presence of additional γ vibrations (transverse vibrations) of the nuclear surface.
© 2005 Pleiades Publishing, Inc.

1. INTRODUCTION

Various modes of motion (for example, single-particle and collective ones) may coexist in nuclei. An especially wide variety of modes are expected in nuclei where the number Z of protons or the number N of neutrons (or both of them) occurs in the middle of the gap between their magic values. Nuclei of even selenium isotopes belong to this type ($Z = 34$, $N = 38-48$).

The collective character of a nuclear-motion mode manifests itself first of all in values of nuclear-surface deformation [1–3], as well as the generation of various excited-mode components in the configuration space of a generalized model [4]. The second case can be reduced to specifying the nuclear shape in terms of, for example, the total nuclear deformation β and the nonaxiality γ for various multipolarities. If the observed static quadrupole moments of excited 2_1^+ states in the nuclei of even selenium isotopes are indicative of a longitudinal deformation of these nuclei [5], then the structure of the energy spectra suggests their nonaxiality and softness with respect to β vibrations of the surface [6]. The aforementioned properties of selenium nuclei (especially of ^{76,78}Se) were confirmed by experiments devoted to studying the scattering of nuclear particles on these nuclei. We note that the choice of a collective model for treating their low-lying excited states affects significantly the quality of the description of experimental data on the dynamics of nucleon–nucleus scattering [7, 8]. In particular, the second 2^+ and 0^+ states in ^{76}Se are interpreted in the rotational–vibrational model as the beginnings of, respectively, the β and the γ vibrational band [9, 10]. Within the Davydov–Chaban and Davydov–Kashuba–Porodzinsky collective models (see [1] and [3], respectively), however, these states are considered in the quadrupole approximation ($\lambda = 2$) as the beginning of the first anomalous band in the former case and as the beginning of the first rotational–vibrational band in the latter case, the longitudinal and transverse softness of the nonaxial ^{76}Se nucleus being taken into account here.

The isotopic dependence of the parameters of the optical nucleon–nucleus potential for even selenium isotopes was previously studied in [11]. The potential of the model proposed there can be extended significantly by taking into account spectroscopic and dynamical information within a unified approach, since the same parameters of the nuclear shape are used both in nuclear spectroscopy and in problems of nucleon–nucleus scattering.

Even–even nuclei in the Ge–Se mass range are characterized by the instability of their shape and the presence of an $I = 3$ (I is the spin of a level) negative-parity level among the lowest states of the nuclei, which is a level that can be interpreted as the beginning of the octupole ($\lambda = 3$) rotational band. Various versions of the collective model [8, 9]—the harmonic and anharmonic vibrational models (HVM and AVM), the rotational–vibrational model (RVM), and the asymmetric rotational model (ARM), as well as their modifications [3, 7, 8]—were used to study the nature of 2_2^+ and 3_1^- states.

That the quadrupole-deformation parameter for the ^{76}Se nucleus has a value of $\beta \approx 0.3$ [12] casts

[†]Deceased.
[1)]Institute of Nuclear Research, National Academy of Sciences of Ukraine, pr. Nauki 47, Kiev, 03680 Ukraine.
[2)]Institute of Radiation Physics and Chemistry Problems, Belarussian Academy of Sciences, Minsk, 220109 Belarus.
[*]e-mail: odavi@kinr.kiev.ua

some doubt upon the applicability of the harmonic rotational model to this nucleus in a pure form, the more so as the large quadrupole moment of the 2_1^+ state [5] is indicative of a static deformation of the ^{76}Se nucleus. As to describing the states of the (2_2^+, 4_1^+, 0_2^+) triplet, there arise difficulties here as well. In particular, it follows from data on nucleon scattering by ^{76,80}Se nuclei [9, 10] that the 0_2^+ state is less collectivized in ^{80}Se than in ^{76}Se; that is, the nature of the 0_2^+ state is dependent on the neutronic composition of a selenium isotope, but there is no such dependence in the harmonic model. In all probability, this applies, to some extent, to other even selenium isotopes as well. In nuclei, it is therefore necessary to take into account the existence of closed structures such that the addition of a pair of neutrons to them may manifest itself in a phenomenological pattern as a smooth variation of model parameters in response to a transition from one isotope to another or in response to a variation in the spin and energy of an excited nuclear state [13, 14].

2. COLLECTIVITY OF A MODE AND SOFTNESS OF NUCLEUS

Interest in collective modes in soft nuclei is associated with unsolved problems in describing finite Fermi systems that involve large shape fluctuations. Models based on mapping fermion dynamics to boson variables [15] are used in a number of studies to describe the structure of such nuclei. The total deformation of a nucleus is then determined primarily by its deformation and the tensors of orientation of respective multipole moments [16], while the shape of the dynamical deformation is controlled by the nuclear-reaction mechanism. For nuclei whose mass numbers lie in the vicinity of $A \sim 80$, dynamical-deformation theory [17] predicts, for low-lying states, large three-dimensional deformations of nuclei. At a model level, this is manifested in the tensor character of the mass parameter $B_{\mu\nu}$ in the kinetic-energy operator in the collective Hamiltonian.

The existence of collective and noncollective modes in nuclei and the competition between these modes manifest themselves in the variation of the nuclear shape upon the transition from one isotope (or state) to another. This issue was also considered in detail in exploring the energy-band structures in ^{74}Se [18] and ^{184}Os [19], and it was shown that the inclusion of the γ softness of nuclei enhances the degree of nonconservation of the projection K of the excited-state spin onto the nuclear-symmetry axes and, hence, affects the identification of the energy bands of excited nuclear states.

Since a nuclear potential is sensitive to three-dimensional deformability [18] (and, hence, to the transverse softness of a nucleus), electromagnetic transitions in nuclei may also be different in nature, this being confirmed by calculations within the interacting-boson model [20]: for example, the electric quadrupole transition from levels of the β band to levels of the ground-state band may be noncollective, while the transition to levels of the γ band may be collective.

In describing the lowest excited nuclear states, which are characterized by the quantum numbers 2_1^+ and 0_2^+, one must of course take into account the ground-state properties of the respective nuclei [4]. In particular, the wave vector of the 0_2^+ state can be represented, irrespective of the nuclear shape, as a superposition of two components such that, of these, either can be dominant, depending on in which of the variables β and γ the nucleus being considered is softer. Data on the processes where (p, p') and (n, n') scattering on even selenium isotopes is accompanied by the excitation of the 3_1^- state are indicative of the change in the shape of the nucleus involved [10] as it is deexcited, which is confirmed within the asymmetric rotational model by the difference in the nuclear-nonaxiality parameters for the 2_1^+ and 2_2^+ states.

3. MODEL DESCRIPTION OF THE SPECTRA OF EVEN SELENIUM ISOTOPES

The isotopic dependence of the energy normalization factor $\hbar\omega_0$ and of the nonaxiality parameter γ_0 for a nucleus in the ground state (or the effective nonaxiality parameter γ_{eff}, which has the same value for all states of a given nucleus) was previously established in [6, 11] for even selenium isotopes in the quadrupole-deformation approximation ($\lambda = 2$); also, the isotopic dependence of the longitudinal-nuclear-softness parameter μ_β was found there within the Davydov–Chaban model for the ground-state and the anomalous β band. By introducing, in the Hamiltonian of the model, the γ deformability of the nuclear surface as an extra parameter (Davydov–Kashuba–Porodzinsky model), one modifies the parameters of the Davydov–Chaban model and has to assign nuclear states, in addition to the quantum number $n_\beta = 0, 1, \ldots$, which labels the energy bands of longitudinal vibrations, the quantum number $n_\gamma = 0, 1, \ldots$, which directly participates in the identification of excited nuclear states and, hence, in the construction of its energy-band structure. As a result, the energy of excited states of an even–even nucleus in the quadrupole-deformation approximation ($\lambda = 2$) can be represented in the form [3]

$$\frac{E_{I\tau n_\beta n_\gamma}}{\hbar\omega_0} = \left\{\left(\nu_{I\tau n_\beta n_\gamma} + \frac{1}{2}\right)\sqrt{4 - \frac{3}{p_{I\tau n_\gamma}}}\right.$$

$$+\frac{1}{2}\left(\frac{\mu_\beta}{p_{I\tau n_\gamma}}\right)^2 \varepsilon_{I\tau n_\gamma}\left[1+\left(\frac{\mu_\beta}{p_{I\tau n_\gamma}}\right)^4 \varepsilon_{I\tau n_\gamma}\right]\Bigg\},$$

where I is the angular momentum of the nuclear state being considered and τ is the ordinal number of the eigenvalue of the rigid-nonaxial-rotor operator for a given spin I [in our case, the inclusion of an octupole ($\lambda = 3$) deformation requires introducing the quantum number n_ξ, which takes the value of unity in describing octupole vibrations and which is equal to zero for quadrupole deformations]. The quantities $\nu_{I\tau n_\beta n_\gamma}$ are defined as the eigenvalues for parabolic-cylinder functions in the presence of longitudinal and transverse vibrations and of their coupling to the rotation of a deformed nonaxial nucleus. The energies $\varepsilon_{I\tau n_\gamma}$ are obtained by solving the eigenvalue problem specified by a set of coupled equations in the space of variables β and $(\gamma, \hat{\theta})$ and by subsequently taking into account $(\gamma, \hat{\theta})$ coupling within perturbation theory ($\hat{\theta} \equiv (\theta_1, \theta_2, \theta_3)$ are Euler angles). The quantity $p_{I\tau n_\gamma}$ can be considered as a parameter that takes into account the presence of γ vibrations ($n_\gamma \neq 0$), along with β vibrations, in the Davydov–Kashuba–Porodzinsky model and is defined as the ratio of the longitudinal-nuclear-deformation parameter $\beta_{I\tau n_\gamma}$ in the state specified by the quantum numbers I, τ, and n_γ to the value β_0 of the longitudinal-deformation parameter for the ground state of the nucleus being considered.

The levels of nuclei studied here are given in the first columns of Tables 1–6 (N_{level}). The experimental levels used as a basis in determining model parameters are labeled with an asterisk either in the $E_{\text{level}}^{\text{expt}}$ columns (Tables 1, 5, 6) if the same set of basis experimental levels, together with their quantum numbers and energies, is used for all models considered here or in the $E_{\text{level}}^{\text{theor}}$ columns (Tables 2, 3, 4) if different sets of experimental levels are used as a basis in different models.

3.1. ^{72}Se

Investigations of the ^{72}Se nucleus did not provide a clear answer to the question of whether collective models are applicable to describing the energy structure of this nucleus. In addition to the ground state of spin equal to zero and positive parity, only one state $N_{\text{level}} = 3$ (Table 1) of spin–parity 0^+, which, within the Davydov–Kashuba–Porodzinsky model, could be the beginning of the band of transverse quadrupole vibrations, was discovered among the lowest excited states [21].

Because of the absence of a state on which the band of longitudinal quadrupole vibrations could be built, the parameter μ_β cannot be unambiguously determined. First, the use of the state $N_{\text{level}} = 10$ for a basis state leads to an unjustifiable overestimation of μ_β; second, model calculations predict $I^\pi = 2^+$ for this state, while experiments lead to a dubious spin value of $I = 3$ for it, the parity remaining without a proper determination. For the state $N_{\text{level}} = 6$, the experimental value is $I = 2$ or 4; however, theoretical calculations, both those that are based on the Davydov–Chaban model and those that are based on the Davydov–Kashuba–Porodzinsky model, yield $I^\pi = 3^+$ (the latter is an elaboration of the former; therefore, the parameters of the Davydov–Chaban model are used as input values in optimizing the parameters of the Davydov–Kashuba–Porodzinsky model).

For basis levels, we choose those experimental levels that are pure in the spin I and in the quantum numbers τ and n_β within the Davydov–Chaban model and in the additional quantum number n_γ within the Davydov–Kashuba–Porodzinsky model. On the basis of these levels, model parameters and the energies of excited states were obtained for ^{72}Se (Table 1), the quantum numbers used to identify respective levels according to energy bands being indicated for these states.

The introduction of hard hexadecapole ($\lambda = 4$) deformations enables one to improve the description of the energies of high-spin ($I > 8$) levels for the lowest rotational band, but this spoils the description of the lowest states of other bands. The introduction of symmetric octupole ($\lambda = 3$) deformations [8] made it possible to describe the lowest experimental levels of negative parity ($N_{\text{level}} = 8$ and 12). However, this identification of states is ambiguous because the experimental level $N_{\text{level}} = 7$ or 8 can be associated with the $E_{\text{level}}^{\text{theor}} = 2.4156$ MeV state. There arises a similar situation in comparing the model level at $E_{\text{level}}^{\text{theor}} = 2.9909$ MeV with the energy of the experimental state $N_{\text{level}} = 11$ or 12.

The transverse-softness parameter μ_γ^{KP} from [3] involves the total deformation β_0 as a factor, differing by this factor from the analogous parameter μ_γ^{DCh} from [1]; that is, $\mu_\gamma^{\text{DCh}} = \beta_0 \mu_\gamma^{\text{KP}}$. The parameter μ_γ^{DCh} within the Davydov–Kashuba–Porodzinsky model is determined for ^{72}Se by using the level $N_{\text{level}} = 3$ as the beginning of the first γ vibrational band, which is initiated by the transverse deformability of the nuclear surface.

3.2. ^{74}Se

The energy structure of the ^{74}Se nucleus has not yet received adequate study either in a theoretical or

Table 1. Features of the excited states of the ^{72}Se nucleus (experimental and model results)

N_{level}	Experiment [21]		DChM ($\lambda = 2$)				DKPM ($\lambda = 2$ and 3)					
	$E^{\text{expt}}_{\text{level}}$, MeV	I^{π}_{level}	$E^{\text{theor}}_{\text{level}}$, MeV	I^{π}_{level}	τ	n_β	$E^{\text{theor}}_{\text{level}}$, MeV	I^{π}_{level}	τ	n_β	n_γ	n_ξ
1	0.0	0^+	0.0	0^+	1	0	0.0	0^+	1	0	0	0
2	0.86208*	2^+	0.8377	2^+	1	0	0.8265	2^+	1	0	0	0
3	0.93722	0^+					0.9372	0^+	1	0	1	0
4	1.31668*	2^+	1.3599	2^+	2	0	1.3485	2^+	2	0	0	0
5	1.63686*	4^+	1.6511	4^+	1	0	1.6360	4^+	1	0	0	0
6	1.87620	(2, 4)	1.7854	3^+	1	0	1.7732	3^+	1	0	0	0
7	2.40573	3^-										
8	2.43376	3^-					2.4156	3^-	1	0	0	1
9	2.46677*	6^+	2.4862	6^+	1	0	2.4704	6^+	1	0	0	0
10	2.58642	(3)	2.5492	2^+	1	1	2.5261	2^+	1	1	0	0
11	2.843	5^-										
12	2.965						2.9909	5^-	1	0	0	1
13	3.4248*	8^+	3.3335	8^+	1	0	3.3216	8^+	1	0	0	0
14	4.5043	10^+	4.1991	10^+	1	0	4.1943	10^+	1	0	0	0
15	5.7097	12^+	5.0734	12^+	1	0	5.0741	12^+	1	0	0	0
16	7.0381	14^+	5.9582	14^+	1	0	5.9688	14^+	1	0	0	0

Parameter	DChM ($\lambda = 2$)	DKPM ($\lambda = 2$ and 3)
$\hbar\omega_0$, MeV	1.0663	1.0663
μ_β	0.9852	0.9852
γ_0, rad/deg	0.4341/24.9	0.4341/24.9
β_0	–	0.236
$\mu_\gamma^{\text{DCh}} = \beta_0\mu_\gamma^{\text{KP}}$	–	0.2098

* Experimental levels used to determine the collective-model parameters.

in an experimental aspect. This especially concerns high-spin states and results, in particular, in some discrepancies between information contained in the compilation of Fahran [22] and information given in the study of Döring *et al.* [18]. For example, not only did the authors of [18] refine the quantum-mechanical properties of the ^{74}Se nucleus, but they also arrived at the unambiguous conclusion, on the basis of the Hartree–Fock–Bogolyubov approach, that this nucleus has a deformed shape and features a significant softness in all three spatial axes. The application of the Davydov–Chaban or the Davydov–Kashuba–Porodzinsky model to the nucleus in question also confirms the conclusions drawn in [18]: the longitudinal and the transverse softness of the ^{74}Se nucleus are both quite sizable, and there is a correction for deformations that are associated with higher multipolarities (see Table 2).

The application of the Davydov–Kashuba–Porodzinsky model to the ^{74}Se nucleus made it possible to describe the band of negative-parity levels ($N_{\text{level}} =$ 12, 15, 18, 22) by employing the assumption of its octupole deformation ($\lambda = 3$) characterized by the quantum number n_ξ [8] and to refine the spins and parities of the excited states $N_{\text{level}} = 11$, 13, 17, 20–22.

As to the level $N_{\text{level}} = 24$ (Table 2), it follows from the calculations based on the Davydov–Kashuba–Porodzinsky model that it belongs to the octupole band built on the level $N_{\text{level}} = 12$ and that it can be assigned a spin of $I = 11$ and a negative parity.

Table 2. Features of the excited states of the ^{74}Se nucleus (experimental and model results)

N_{level}	Experiment [18, 22]		DChM ($\lambda = 2$)				DKPM ($\lambda = 2$ and 3)					
	$E^{\text{expt}}_{\text{level}}$, MeV	I^{π}_{level}	$E^{\text{theor}}_{\text{level}}$, MeV	I^{π}_{level}	τ	n_β	$E^{\text{theor}}_{\text{level}}$, MeV	I^{π}_{level}	τ	n_β	n_γ	n_ξ
1	0.0	0^+	0.0	0^+	1	0	0.0	0^+	1	0	0	0
2	0.635	2^+	0.622*	2^+	1	0	0.5987*	2^+	1	0	0	0
3	0.854	0^+					0.8538	0^+	1	0	1	0
4	1.269	2^+	1.258*	2^+	2	0	1.243	2^+	2	0	0	0
5	1.363	4^+	1.417*	4^+	1	0	1.397*	4^+	1	0	0	0
6	1.6574	0^+	1.581	0^+	1	0	1.630*	0^+	1	1	0	0
7	1.838	2^+										
8	1.884	3^+	1.629	3^+	1	0	1.613	3^+	1	0	0	0
9	2.108	4^+	2.299	4^+	2	0	2.279	4^+	2	0	0	0
10	2.2314	6^+	2.251*	6^+	1	0	2.2461*	6^+	1	0	0	0
11	2.314	(2^+)	2.346	2^+	1	1	2.356	2^+	1	1	0	0
12	2.349	3^-					2.166	3^-	1	0	0	1
13	2.379	$(1, 2^+)$					2.356	2^+	1	1	0	0
14	2.661	5^+	2.560	5^+	1	0	2.552	5^+	1	0	0	0
15	2.842	5^-					2.787	5^-	1	0	0	1
16	3.198	8^+	3.130*	8^+	1	0	3.122	8^+	1	0	0	0
17	3.253	(2–6)					3.272	4^+	1	1	0	0
18	3.516	7^-					3.512	7^-	1	0	0	1
19	3.525	7^+	3.552	7^+	1	0	3.565	7^+	1	0	0	0
20	3.980	(6^+)					4.222	6^+	1	1	0	0
21	4.256	(10^+)	4.040	10^+	1	0	4.059	10^+	1	0	0	0
22	4.403	(9^-)					4.253	9^-	1	0	0	1
23	4.449	9^+	4.558	9^+	1	0	4.599	9^+	1	0	0	0
24	5.492	11^+					5.107	11^-	1	0	0	1
25	5.443	12^+	4.981	12^+	1	0	5.023	12^+	1	0	0	0

Parameter	DChM ($\lambda = 2$)	DKPM ($\lambda = 2$ and 3)
$\hbar\omega_0$, MeV	1.3592	1.4301
μ_β	0.5756	0.5499
γ_0, rad/deg	0.4341/24.9	0.4341/24.9
β_0	–	0.236
$\mu_\gamma^{\text{DCh}} = \beta_0\mu_\gamma^{\text{KP}}$	–	0.2606

* Experimental levels used to determine the collective-model parameters.

Table 3. Features of the excited states of the ^{76}Se nucleus (experimental and model results)

N_{level}	Experiment [26]		DChM ($\lambda = 2$)				DKPM ($\lambda = 2$)					DKPM ($\lambda = 2$ and 3)					
	$E^{\text{expt}}_{\text{level}}$, MeV	I^{π}_{level}	$E^{\text{theor}}_{\text{level}}$, MeV	I^{π}_{level}	τ	n_β	$E^{\text{theor}}_{\text{level}}$, MeV	I^{π}_{level}	τ	n_β	n_γ	$E^{\text{theor}}_{\text{level}}$, MeV	I^{π}_{level}	τ	n_β	n_γ	n_ξ
1	0.0	0^+	0.0	0^+	1	0	0.0	0^+	1	0	0	0.0	0^+	1	0	0	0
2	0.5591	2^+	0.5518*	2^+	1	0	0.5345 *	2^+	1	0	0	0.5414*	2^+	1	0	0	0
3	1.1223	0^+					1.1223*	0^+	1	0	1	1.1223*	0^+	1	0	1	0
4	1.2161	2^+	1.2115*	2^+	2	0	1.2246 *	2^+	2	0	0	1.2133*	2^+	2	0	0	0
5	1.3309	4^+	1.3654*	4^+	1	0	1.3944 *	4^+	1	0	0	1.4008*	4^+	1	0	0	0
6	1.6889	$(3)^+$	1.6020	3^+	1	0	1.6535 *	3^+	1	0	0	1.6480*	3^+	1	0	0	0
7	1.7876	2^+					1.5101	2^+	1	0	1	1.5145	2^+	1	0	1	0
8	2.1272	(2^+)					2.2035	4^+	1	0	1	2.2085	4^+	1	0	1	0
9	2.1706	(0^+)	1.9316	0^+	1	1	2.0182 *	0^+	2	1	0	2.0182*	0^+	1	1	0	0
10	2.2623	6^+	2.2727*	6^+	1	0	2.3900	6^+	1	0	0	2.3948	6^+	1	0	0	0
11	2.3629	$(2^+, 3, 4^+)$	2.3188	4^+	2	0	2.4032	4^+	2	0	0	2.4144	4^+	2	0	0	0
12	2.4291	3^-										2.4287	3^-	1	0	0	1
13	2.4886	$(5)^+$	2.6195	5^+	1	0	2.7651	5^+	1	0	0	2.7703	5^+	1	0	0	0
14	2.5147	(2^+)	2.6322	2^+	1	1	2.5193	2^+	1	1	0	2.5325	2^+	1	1	0	0
15	2.8248	5^-										3.0041	5^-	1	0	0	1
16	3.2250	$(4^+, 5^+)$	3.6063	4^+	1	1	3.3604	4^+	1	1	0	3.3723	4^+	1	1	0	0
17	3.2695	8^+	3.2646*	8^+	1	0	3.5244	8^+	1	0	0	3.5291	8^+	1	0	0	0
18	3.4416	7^-										3.7207	7^-	1	0	0	1
19	4.2994	10^+	4.3127	10^+	1	0	4.6863	10^+	1	0	0	4.7064	10^+	1	0	0	0
20	4.3246	9^-										4.6202	9^-	1	0	0	1
21	5.4294	12^+	5.4171	12^+	1	0	6.0191	12^+	1	0	0	6.0452	12^+	1	0	0	0

Parameter	DChM ($\lambda = 2$)	DKPM ($\lambda = 2$)	DKPM ($\lambda = 2$ and 3)
$\hbar\omega_0$, MeV	1.8476	1.796	1.796
μ_β	0.4395	0.533	0.533
γ_0, rad/deg	0.4293/24.6	0.4039/23.1	0.4039/23.1
β_0	–	0.236	0.236
$\mu_\gamma^{\text{DCh}} = \beta_0\mu_\gamma^{\text{KP}}$	–	0.2603	0.2603

* Experimental levels used to determine the collective-model parameters.

However, the experimentally observed levels of ^{74}Se do not include a level that would have a negative parity and which would be close on the energy scale to the theoretically predicted level. In all probability, this discrepancy between the experimental and the theoretical parity is due to the impossibility of observing the corresponding level because of the smallness of its intensity in relation to the intensity of the $I^\pi = 11^+$ state. The choice of various sets of basis levels affects the numerical values of the model parameters and the quality of the agreement between the theoretical values of the energies of states and their experimentally measured counterparts.

3.3. ^{76}*Se*

The energy-level bands of the ^{76}Se nucleus ($Z = 34$, $N = 42$) were studied in many reactions for example, ^{76}Ge(α, $2n\gamma$) [23], ^{76}Se(^{16}O, ^{16}O$'$) [5], and

Table 4. Features of the excited states of the ^{78}Se nucleus (experimental and model results)

N_{level}	Experiment [27]		DChM$^{(1)}$ ($\lambda = 2$)				DChM$^{(2)}$ ($\lambda = 2$)				DKPM ($\lambda = 2$ and 3)					
	$E^{\text{expt}}_{\text{level}}$, MeV	I^{π}_{level}	$E^{\text{theor}}_{\text{level}}$, MeV	I^{π}_{level}	τ	n_β	$E^{\text{theor}}_{\text{level}}$, MeV	I^{π}_{level}	τ	n_β	$E^{\text{theor}}_{\text{level}}$, MeV	I^{π}_{level}	τ	n_β	n_γ	n_ξ
1	0.0	0^+	0.0	0^+	1	0	0.0	0^+	1	0	0.0	0^+	1	0	0	0
2	0.6138	2^+	0.6137*	2^+	1	0	0.6089 *	2^+	1	0	0.6009*	2^+	1	0	0	0
3	1.3086	2^+	1.3091*	2^+	2	0	1.3035 *	2^+	2	0	1.2889*	2^+	2	0	0	0
4	1.4986	(0^+)									1.4985	0^+	1	0	1	0
5	1.5026	(4^+)	1.5071*	4^+	1	0	1.5162*	4^+	1	0	1.4974*	4^+	1	0	0	0
6	1.7587	$(0^+, 1, 2)$	1.7478	3^+	1	0	1.7570	3^+	1	0	1.7385	3^+	1	0	0	0
7	1.9960	(2^+)									1.9317	2^+	1	0	1	0
8	2.1903		2.1481	0^+	1	1										
9	2.3346	$(0^+, 1, 2)$					2.3279*	0^+	1	1	2.3279*	0^+	1	1	0	0
10	2.5076	3^-									2.5076	3^-	1	0	0	1
11	2.5374	$(0^+$,1,2)	2.5748	4^+	2	0										
12	2.5387	(6^+)	2.5085*	6^+	1	0	2.2552*	6^+	1	0	2.5211*	6^+	1	0	0	0
13	2.6476	$(0^+, 1, 2)$					2.6271	4^+	2	0	2.6497	4^+	1	0	1	0
14	2.6801	$(1, 2)$									2.6047	4^+	2	0	0	0
15	2.8901		2.8891	5^+	1	0										
16	2.9145										2.9203	5^+	1	0	0	0
17	2.9477						2.9475	5^+	1	0						
18	3.0903						3.1033	2^+	1	1	3.0877	2^+	1	1	0	0
19	3.2551										3.2717	5^-	1	0	0	1
20	3.5736	(8^+)	3.6049*	8^+	1	0	3.6973	8^+	1	0	3.6544	8^+	1	0	0	0

Parameter	DChM$^{(1)}$ ($\lambda = 2$)	DChM$^{(2)}$ ($\lambda = 2$)	DKPM ($\lambda = 2$ and 3)
$\hbar\omega_0$, MeV	2.0581	2.2631	2.2631
μ^{DCh}_β	0.4368	0.4125	0.4125
γ_0, rad/deg	0.4383/25.1	0.4415/25.3	0.4415/25.3
β_0	0.236	0.236	0.236
$\mu^{\text{DCh}}_\gamma = \beta_0\mu^{\text{KP}}_\gamma$	–	–	0.1966

* Experimental levels used to determine the collective-model parameters.

^{76}Se(p, n) [25] and were analyzed on the basis of various collective models [6–11, 23–25], which furnished evidence in support of its large static nonaxiality and its three-dimensional deformability (softness).

Interest in the ^{76}Se nucleus is motivated by its nucleonic composition and by the energy of the first 2^+ state: it is minimal among the other even selenium isotopes, with the result that collective degrees of freedom are more readily excited in this nucleus than in the nuclei of the other isotopes, the effect of closed

Table 5. Features of the excited states of the ^{80}Se nucleus (experimental and model results)

N_{level}	Experiment [28, 29]		DChM ($\lambda = 2$)				DKPM ($\lambda = 2$)					DKPM ($\lambda = 2$ and 3)					
	$E^{\text{expt}}_{\text{level}}$, MeV	I^{π}_{level}	$E^{\text{theor}}_{\text{level}}$, MeV	I^{π}_{level}	τ	n_β	$E^{\text{theor}}_{\text{level}}$, MeV	I^{π}_{level}	τ	n_β	n_γ	$E^{\text{theor}}_{\text{level}}$, MeV	I^{π}_{level}	τ	n_β	n_γ	n_ξ
1	0.0	0^+	0.0	0^+	1	0	0.0	0^+	1	0	0	0.0	0^+	1	0	0	0
2	0.666118*	2^+	0.66180	2^+	1	0	0.66610	2^+	1	0	0	0.65628	2^+	1	0	0	0
3	1.44922	2^+	1.5472	2^+	2	0	1.5472	2^+	2	0	0	1.5256	2^+	2	0	0	0
4	1.4790	0^+					1.4793	0^+	1	0	1	1.4792	2^+	1	0	1	0
5	1.70122*	4^+	1.7015	4^+	1	0	1.7015	4^+	1	0	0	1.6775	4^+	1	0	0	0
6	1.96005	2^+					1.9749	2^+	1	0	1	1.9680	2^+	1	0	1	0
7	2.1210	($\leq$4)	2.0375	3^+	1	0	2.0375	3^+	1	0	0	2.0116	3^+	1	0	0	0
8	2.6271*	(0, 1, 2)	2.6272	0^+	1	1	2.6272	0^+	1	1	0	2.6272	0^+	1	1	0	0
9	2.7166	3^-										2.73323	3^-	1	0	0	1
10	2.8253	(2–6)					2.8249	4^+	1	0	1	2.8058	4^+	1	0	1	0
11	2.9475	($\leq$4)	2.9197	4^+	2	0	2.9197	4^+	2	0	0	2.8906	4^+	2	0	0	0
12	3.314		3.3341	5^+	1	0	3.3341	5^+	1	0	0	3.2981	5^+	1	0	0	0
13	3.491		3.4761	2^+	1	1	3.4761	2^+	1	1	0	3.4570	2^+	1	1	0	0
14	3.567											3.6067	5^-	1	0	0	1

Parameter	DChM ($\lambda = 2$)	DKPM ($\lambda = 2$)	DKPM ($\lambda = 2$ and 3)
$\hbar\omega_0$, MeV	2.5564	2.5564	2.5564
μ_β	0.4108	0.4108	0.4108
γ_0, rad/deg	0.4189/24	0.4189/24	0.4189/24
β_0	0.236	0.236	0.236
$\mu^{\text{DCh}}_\gamma = \beta_0\mu^{\text{KP}}_\gamma$	–	0.2466	0.2466

* Experimental levels used to determine the collective-model parameters.

shells manifesting itself quite clearly here. In [6, 11], the ^{76}Se nucleus was considered as a nonaxial rotor that is soft in β vibrations; the inclusion of its transverse softness and of an octupole deformation, along with a quadrupole deformation, makes it possible to identify up to five energy bands. The description of so great a number of excited states of the nucleus enables one to employ, with a rather high degree of reliability, a phenomenological model in analyzing cross sections for nuclear processes, including neutron–nucleus scattering.

Experimental data on the energies $E^{\text{expt}}_{\text{level}}$ and the spin–parities I^{π}_{level} of states of the ^{76}Se nucleus [26] are displayed in Table 3, along with their counterparts calculated within the Davydov–Chaban and the Davydov–Kashuba–Porodzinsky model, the identification quantum numbers τ, n_β, n_γ, and n_ξ, which are used to associate an excited nuclear state with one energy band or another, being indicated. In particular, the band of quadrupole longitudinal vibrations is built on the experimental level $N_{\text{level}} = 9$ rather than on the level $N_{\text{level}} = 3$, as was assumed previously [8] in the case of a different choice of input values for the model parameters. If the levels $N_{\text{level}} = 2, 4, 5, 10, 17$ are chosen for a basic set of levels, the ground-state and the anomalous band are described well within the Davydov–Chaban model, but the β band ($N_{\text{level}} = 9$, 14, 16) is described more poorly. By introducing the additional parameter μ_γ (Davydov–Kashuba–

Table 6. Features of the excited states of the ^{82}Se nucleus (experimental and model results)

N_{level}	Experiment [30]		DChM ($\lambda = 2$)				DKPM ($\lambda = 2$ and 3)					
	$E^{\text{expt}}_{\text{level}}$, MeV	I^{π}_{level}	$E^{\text{theor}}_{\text{level}}$, MeV	I^{π}_{level}	τ	n_β	$E^{\text{theor}}_{\text{level}}$, MeV	I^{π}_{level}	τ	n_β	n_γ	n_ξ
1	0.0	0^+	0.0	0^+	1	0	0.0	0^+	1	0	0	0
2	0.65469*	2^+	0.6547	2^+	1	0	0.6392	2^+	1	0	0	0
3	1.4099	0^+					1.4103	0^+	1	0	1	0
4	1.73113	2^+	1.5373	2^+	2	0	1.6053	2^+	2	0	0	0
5	1.73505*	4^+	1.7350	4^+	1	0	1.7506	4^+	1	0	0	0
6	2.55009	$(2, 4^+)$	2.0745	3^+	1	0	2.1431	3^+	1	0	0	0
7	3.105	(4^+)	3.0857	4^+	2	0	3.1671	4^+	2	0	0	0
8	3.449*	0^+	3.4490	0^+	1	1	3.5094	0^+	1	1	0	0
9	3.624		3.5349	5^+	1	0	3.6417	5^+	1	0	0	0
10	4.134	2^+					4.1465	2^+	1	1	0	0
11	4.396	2^+	4.2747	2^+	1	1						

Parameter	DChM ($\lambda = 2$)	DKPM ($\lambda = 2$ and 3)
$\hbar\omega_0$, MeV	3.4306	3.4327
μ_β	0.3498	0.4005
γ_0, rad/deg	0.4262/24.42	0.4376/25.07
β_0	0.236	0.236
$\mu_\gamma^{\text{DCh}} = \beta_0\mu_\gamma^{\text{KP}}$	–	0.2446

* Experimental levels used to determine the collective-model parameters.

Porodzinsky model), varying μ_β, and taking the experimental level $N_{\text{level}} = 9$ for the beginning of the band of longitudinal vibrations and the level $N_{\text{level}} = 3$ for the beginning of the band of transverse vibrations, one can improve the situation on average and describe four bands in the quadrupole approximation [Davydov–Kashuba–Porodzinsky model ($\lambda = 2$)] or five energy bands if an octupole deformation, with the quantum number n_ξ of an octupole longitudinal softness, is taken into account [Davydov–Kashuba–Porodzinsky model ($\lambda = 2, 3$)].

3.4. ^{78}Se

The description of the energy bands of ^{78}Se on the basis of a collective Hamiltonian is illustrated in Table 4, where the results of the calculations on the basis of the Davydov–Chaban model for various sets of basis levels (DChM$^{(1)}$ and DChM$^{(2)}$) are given in addition to experimental data from [27]. The calculations according to the Davydov–Kashuba–Porodzinsky model ($\lambda = 2, 3$) in the quadrupole approximation with allowance for octupole vibrations of the nuclear surface (on the basis of the procedure employed in [8]) make it possible to identify more reliably low-lying excited states of both negative and positive parity.

If the levels $N_{\text{level}} = 2, 3, 5, 12, 20$ are chosen for a basis set (the case of DChM$^{(1)}$), the model parameters are determined by taking into account only the longitudinal softness, and the states of the ^{78}Se nucleus are identified by using the parameter values found in this way. In particular, the experimental level $N_{\text{level}} = 8$ was interpreted as the level on which the band of longitudinal quadrupole vibrations is built. The levels $N_{\text{level}} = 6$ and $N_{\text{level}} = 11$ are assumed to be levels of the anomalous rotational band, which also contains the level $N_{\text{level}} = 15$, and are therefore assigned the spin–parities of 3^+ and 4^+.

But if ones employs the levels $N_{\text{level}} = 2, 3, 5, 9, 12$ for a basis (DChM$^{(2)}$ case), there will arise different parameter values. Thus, the choice of basis set of levels plays a significant role both in determining the model parameters and in identifying states, this

being illustrated by a comparison of the results for the DChM$^{(1)}$ and DChM$^{(2)}$ sets in Table 4.

The calculation of the energy structure of the ^{78}Se nucleus within the Davydov–Kashuba–Porodzinsky model is based on the use of the DChM$^{(2)}$ parameters, the parameter of the quadrupole transverse softness being chosen in the course of the ensuing analysis. Within this procedure, the experimental level $N_{\text{level}} = 4$ is treated as the beginning of the energy band of transverse quadrupole vibrations, which also contains the levels $N_{\text{level}} = 4$, 7, 13. Negative-parity states (in Table 4, these are $N_{\text{level}} = 10$, 19) can also be described within the Davydov–Kashuba–Porodzinsky model if longitudinal octupole deformations characterized by the quantum number of $n_\xi = 0$ or 1 are assumed to be present additionally in the nucleus and if the model parameters are appropriately determined for these deformations [8].

3.5. ^{80}Se

In contrast to what we had for the nuclei considered above, experimental data for the ^{80}Se nucleus do not contain information about high-spin states [28, 29] in its energy spectrum of excitations (Table 5). For this reason, it is difficult to construct the lowest rotational band and, hence, to determine the respective parameters within the Davydov–Chaban or Davydov–Kashuba–Porodzinsky model.

If, for all models, the experimental levels $N_{\text{level}} =$ 2, 3, and 5 are used for basis levels, the parameter values of $\hbar\omega_0 = 2.9160$ MeV, $\mu_\beta = 0.3791$, and $\gamma_0 =$ 0.4428 are obtained on the basis of the Davydov–Chaban model. There are no experimental data on states of spin $I > 4$ in the ^{80}Se nucleus. In choosing the parameters of the Davydov–Chaban model, we are therefore deprived of experimental guidelines for the energies of levels belonging to the lowest rotational band. In view of this, the experimental levels $N_{\text{level}} = 2$, 5, 8 were used for basis ones. For the Davydov–Chaban model, we thereby obtained the parameter values that are quoted in Table 5 and which were used, without varying them further, in the calculations based on the Davydov–Kashuba–Porodzinsky model for $\lambda = 2$ and for $\lambda = 2$, 3 (the inclusion of octupole vibrations was performed according to [8]).

In accordance with our calculations, the $N_{\text{level}} = 8$ state was considered as the beginning ($I^\pi = 0^+$) of the energy band of longitudinal quadrupole vibrations. But the use of the $E^{\text{expt}}_{\text{level}} = 1.87334$ MeV level ($I^\pi = 0^+$ or 2^+) [29] for the beginning of this band leads to an anomalously large value of μ_β, this contradicting the foundations of the model in question. The $N_{\text{level}} = 7$, 11 and 12 experimental states are identified as levels of the $n_\beta = 0$ anomalous rotational band, while the $N_{\text{level}} = 13$ experimental level, together with the $N_{\text{level}} = 8$, forms the second band ($n_\beta = 1$) of longitudinal quadrupole vibrations within the Davydov–Chaban and the Davydov–Kashuba–Porodzinsky model. As to the $N_{\text{level}} = 10$ level [$E^{\text{expt}}_{\text{level}} = 2.8253$ MeV ($I^\pi = 2$–6)], it is assumed to belong to the band of transverse quadrupole vibrations characterized by the quantum numbers $I^\pi = 4^+$ and $n_\gamma = 1$.

An analysis of the energy bands of the ^{80}Se nucleus within the Davydov–Chaban or the Davydov–Kashuba–Porodzinsky model gives evidence in support of its longitudinal and transverse polarizability. If the parameters of the Davydov–Chaban model are taken for a basis and if the $N_{\text{level}} = 4$ experimental level is considered as the beginning of the transverse-quadrupole-deformation band, the transverse-nuclear-softness parameters μ_γ can be determined within the Davydov–Kashuba–Porodzinsky model both in the approximation including only a quadrupole deformation and in the approximation allowing for an admixture of octupole ($\lambda = 3$) vibrations, the latter providing the description of negative-parity states ($N_{\text{level}} = 9$ and 14 in Table 5). In order to attain this, it was sufficient to take into account only symmetric octupole vibrations characterized by the quantum numbers $n_\xi = 0$ and 1.

3.6. ^{82}Se

In the lower part of the energy spectrum of the ^{82}Se nucleus [30], the sequence of spins is identical to that in the spectrum of the ^{76}Se nucleus. However, the levels detected experimentally do not contain an $I > 4$ state. For this reason, it is difficult to construct reliably energy bands on the basis of collective models. The experimental and theoretical features of the ^{82}Se nucleus are given in Table 6, the values obtained for the model parameters being indicated.

In analyzing the spectrum of ^{82}Se levels, there arise ambiguities in associating some states with specific energy bands. Such ambiguities can be removed only by performing a global analysis of the whole spectrum. For example, the $N_{\text{level}} = 8$ level of spin–parity 0^+ was chosen for the beginning of the band of longitudinal quadrupole vibrations, while the $N_{\text{level}} = 9$ level was assigned a spin–parity $I^\pi = 5^+$ and was identified, both within the Davydov–Chaban and within the Davydov–Kashuba–Porodzinsky model, as that which belongs to the anomalous rotational band.

We considered the $N_{\text{level}} = 3$ level as the beginning of the band of transverse quadrupole vibrations and

determined the transverse-nuclear-softness parameter $\mu_\gamma^{\mathrm{DCh}}$ by using this level. The order of levels on which the bands of longitudinal and transverse quadrupole vibrations of the ^{82}Se nucleus are built is identical to that in ^{76}Se; that is, the beginning of the band of transverse vibrations ($N_{\mathrm{level}} = 3$) is below the beginning of the band of longitudinal vibrations ($N_{\mathrm{level}} = 8$).

4. DISCUSSION OF THE RESULTS

Information about the dependence of the nuclear shape on the choice of collective model (the Davydov–Chaban model versus the Davydov–Kashuba–Porodzinsky model) is given in Tables 1–6. Our analysis of this information has revealed that, by introducing, in a collective model, the additional parameter of nuclear softness, $\mu_\gamma^{\mathrm{DCh}}$, in the form of γ deformability, one can include, in the consideration, a much greater number of the energy bands of excited states and identify nuclear states more precisely than in a phenomenological model that takes into account only the longitudinal softness of the nucleus. According to the definition of the parameters of longitudinal and transverse softness (μ_β and $\mu_\gamma^{\mathrm{DCh}}$, respectively) [3], they include, in addition to the parameters of longitudinal and transverse deformations (β_0 and γ_0, respectively) in the ground state, structural parameters such as the mass parameter B of a nucleus and its stiffness parameters C_β and C_γ. In the majority of the cases, levels predicted within the Davydov–Chaban model and within the Davydov–Kashuba–Porodzinsky model have identical sets of quantum numbers and are close in excitation energy, this confirming the genealogical relationship between the models.

The $\xi = (N - Z)/A$ (ξ is the doubled z component of the total isospin of a nucleus per nucleon) dependences of the parameters $\hbar\omega_0$, $\mu_\gamma^{\mathrm{DCh}}$, γ_0, and μ_β obtained for selenium isotopes (Fig. 1–4) on the basis of the Davydov–Chaban model and on the basis of the Davydov–Kashuba–Porodzinsky model are qualitatively similar. This is not so only within individual segments for these functions. By way of example, we indicate that, in both models, the quantity $\hbar\omega_0$ (Fig. 1) is an increasing smooth function of the variable ξ, a numerical distinction being observed only for the isotope (^{78}Se) having the minimum value of $\mu_\gamma^{\mathrm{DCh}}$ (Fig. 2) and the maximum value of the nonaxiality parameter γ_0 (Fig. 3).

As to the behavior of the longitudinal-softness parameter μ_β as a function of ξ (Fig. 4), it is represented, within the models considered here, by decreasing smooth dependences, which differ significantly only

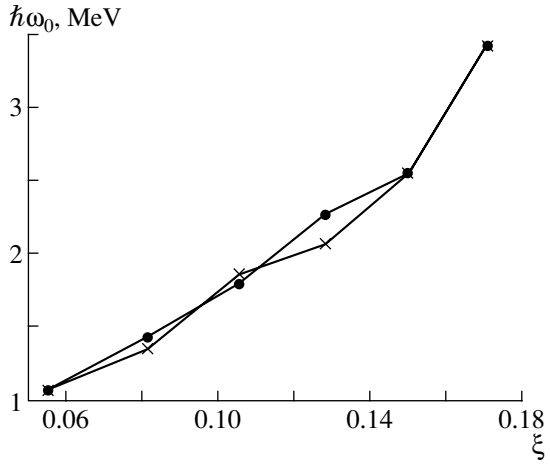

Fig. 1. Parameter $\hbar\omega_0$ determined on the basis of the (crosses) Davydov–Chaban and (closed circles) Davydov–Kashuba–Porodzinsky models as a function of $\xi = (N - Z)/A$.

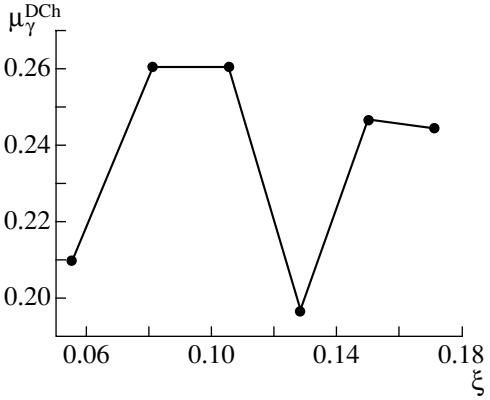

Fig. 2. Parameter $\mu_\gamma^{\mathrm{DCh}}$ determined on the basis of the Davydov–Kashuba–Porodzinsky model as a function of $\xi = (N - Z)/A$.

for ^{76}Se, this being due, in all probability, to sizable changes in the parameters γ_0 and μ_γ for this nucleus. In the Davydov–Chaban model ($\gamma_0 = \gamma_{\mathrm{eff}}$) and in the Davydov–Kashuba–Porodzinsky model, the parameter γ_0 is nearly constant for all selenium isotopes and is about 25° (there is a shallow minimum for ^{76}Se). In the Davydov–Chaban model, the dimensionless parameter μ_β changes from 0.9852 for ^{72}Se to 0.3498 for ^{82}Se. If the transverse nuclear softness is taken additionally into account, the parameter μ_β changes insignificantly in relation to the predictions of the Davydov–Chaban model, this being illustrated in Fig. 4 by means of a comparison of the results obtained within the Davydov–Chaban model and within the Davydov–Kashuba–Porodzinsky model.

With increasing ξ, the dimensionless parameter

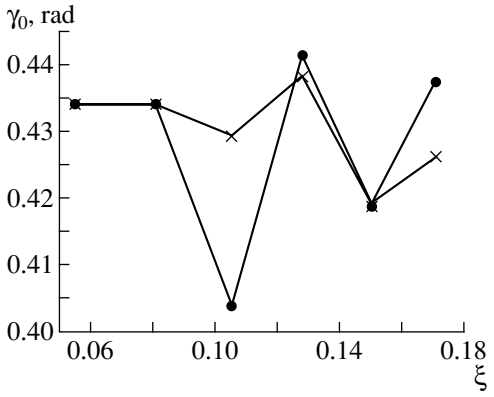

Fig. 3. Parameter γ_0 determined on the basis of the (crosses) Davydov–Chaban and (closed circles) Davydov–Kashuba–Porodzinsky models as a function of $\xi = (N - Z)/A$.

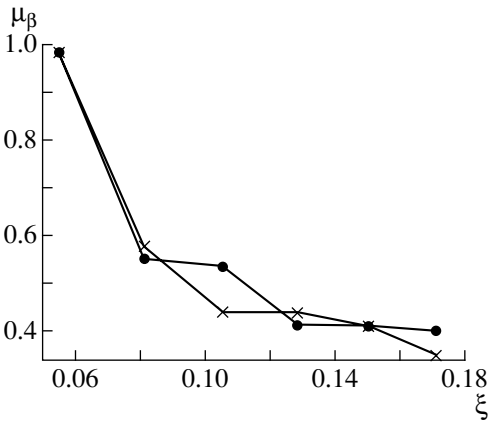

Fig. 4. Parameter μ_β determined on the basis of the (crosses) Davydov–Chaban and (closed circles) Davydov–Kashuba–Porodzinsky models as a function of $\xi = (N - Z)/A$.

of transverse nuclear softness, $\mu_\gamma^{\mathrm{DCh}}$, changes only slightly in relative units (approximately within 15%), from 0.2098 for ^{72}Se to 0.2446 for ^{82}Se.

In studying the probabilities of electric quadrupole transitions between the lowest states ($0_1^+ \to 2_1^+$, $2_1^+ \to 2_2^+$), one can also see a monotonic variation of the reduced probabilities $B(E2)$ [11] versus ξ, this suggesting a collective character of selenium nuclear states and, hence, the applicability of the Davydov–Kashuba–Porodzinsky model to them.

REFERENCES

1. A. S. Davydov, *Excited States of Nuclei* (Atomizdat, Moscow, 1967) [in Russian].
2. J. M. Eisenberg and W. Greiner, *Nuclear Theory* (North-Holland, Amsterdam,1976; Atomizdat, Moscow, 1973–1976), Vols. I–III.
3. I. E. Kashuba and Yu. V. Porodzinskiĭ, Ukr. Fiz. Zh. **44**, 677 (1999).
4. R. V. Jolos and Yu. V. Palchikov, Yad. Fiz. **63**, 633 (2000) [Phys. At. Nucl. **63**, 570 (2000)].
5. R. Lecomte, P. Paradis, J. Barrette, *et al.*, Nucl. Phys. A **284**, 123 (1977).
6. I. E. Kashuba and É. Yu. Kotishevskaya, Izv. Akad. Nauk SSSR, Ser. Fiz. **39**, 617 (1975).
7. I. E. Kashuba, I. A. Korzh, and T. I. Yakovenko, Ukr. Fiz. Zh. **45**, 1295 (2000).
8. Yu. V. Porodzinskij and E. Sh. Sukhovitskij, Yad. Fiz. **59**, 247 (1996) [Phys. At. Nucl. **59**, 228 (1996)].
9. R. G. Kurup, R. W. Finlay, J. Rapaport, and J. P. Delaroche, Nucl. Phys. A **420**, 237 (1984).
10. J. P. Delaroche, R. L. Varner, T. B. Clegg, *et al.*, Nucl. Phys. A **414**, 113 (1984).
11. A. A. Golubova, I. E. Kashuba, Yu. V. Porodzinskiĭ, and E. Sh. Sukhovitskiĭ, Yad. Fiz. **51**, 660 (1990) [Sov. J. Nucl. Phys. **51**, 418 (1990)].
12. R. C. Barrett and D. F. Jackson, *Nuclear Sizes and Structure* (Clarendon Press, Oxford, 1977; Naukova Dumka, Kiev, 1981).
13. I. E. Kashuba, Ukr. Fiz. Zh. **46**, 519 (2001).
14. I. E. Kashuba and O. I. Davidovskaya, Yad. Fiz. **65**, 1446 (2002) [Phys. At. Nucl. **65**, 1411 (2002)].
15. O. K. Vorov and V. G. Zelevinskiĭ, Izv. Akad. Nauk SSSR, Ser. Fiz. **51**, 66 (1987).
16. N. S. Zelenskaya and I. B. Teplov, Izv. Akad. Nauk SSSR, Ser. Fiz. **54**, 2183 (1990).
17. K. Kumar, Prog. Theor. Phys. Suppl., Nos. 74–75, 198 (1983).
18. J. Döring, G. D. Johns, M. A. Riley, *et al.*, Phys. Rev. C **57**, 2912 (1998).
19. C. Wheldon, G. D. Dracoulis, R. T. Newman, *et al.*, Nucl. Phys. A **699**, 415 (2002).
20. W.-T. Chou, R. F. Casten, and P. von Brentano, Phys. Rev. C **45**, 9 (1992).
21. W.-T. Chou and M. M. King, Nucl. Data Sheets **73**, 215 (1994).
22. A. R. Farhan, Nucl. Data Sheets **74**, 529 (1995).
23. T. Matsuzaki and H. Taketani, Nucl. Phys. A **390**, 413 (1982).
24. C. Wong, S. M. Grimes, C. H. Poppe, *et al.*, Phys. Rev. C **26**, 889 (1982).
25. Yu. V. Porodzinskiĭ and E. Sh. Sukhovitskiĭ, Yad. Fiz. **55**, 2368 (1992) [Sov. J. Nucl. Phys. **55**, 1315 (1992)].
26. B. Singh, Nucl. Data Sheets **74**, 63 (1995).
27. B. Singh and D. A. Viggars, Nucl. Data Sheets **33**, 189 (1981).
28. B. Singh and D. A. Viggars, Nucl. Data Sheets **36**, 127 (1982).
29. B. Singh, Nucl. Data Sheets **66**, 623 (1992).
30. M. M. King and W.-T. Chou, Nucl. Data Sheets **76**, 285 (1995).

Translated by A. Isaakyan

Physics of Atomic Nuclei, Vol. 68, No. 6, 2005, pp. 921–927. Translated from Yadernaya Fizika, Vol. 68, No. 6, 2005, pp. 960–966.
Original Russian Text Copyright © 2005 by Goncharova, Pronkina.

NUCLEI
Theory

Magnetic Resonances in the Electroexcitation of the ^{26}Mg Nucleus

N. G. Goncharova and N. D. Pronkina*

Institute of Nuclear Physics, Moscow State University, Vorob'evy gory, Moscow, 119899 Russia

Received March 5, 2004; in final form, July 13, 2004

Abstract—On the basis of spectroscopic information about direct pickup reactions, the multipole magnetic resonances $M2$, $M4$, and $M6$ of the ^{26}Mg nucleus are calculated within the *particle–core coupling* version of the multiparticle shell model. The excitation-energy distribution of the form factors for the multipole magnetic $1\hbar\omega$ resonances is obtained for momentum transfers to a nucleus up to 2 fm^{-1}. A comparison of the results of the calculations for the $M6$ form factors with corresponding experimental data confirms that the adopted model approximations are realistic. © *2005 Pleiades Publishing, Inc.*

1. INTRODUCTION

Investigation of multipole giant resonances in effective cross sections for the excitation of nuclei is one of the important tools for deducing information about the internal structure of nuclei and about the role of various components of the intranuclear current in the formation of the response of a nucleus to an excitation. Experimental investigations of cross sections for the electroexcitation of nuclei at large angles made it possible to single out, for some nuclei, the contributions of magnetic $1\hbar\omega$ resonances from a general pattern of the response of a nucleus to an excitation. In contrast to what we have in analyzing experimental data on hadron–nucleus reactions, a theoretical interpretation of electroexcitation does not require invoking model assumptions on the reaction mechanism, but, in order to construct it, one must have an adequate description of the ground state of a target nucleus and of its excited states. While the problem of obtaining qualitative wave functions for the initial and final states of a nucleus can adequately be solved for nuclei close to magic ones by using the random-phase approximation within the multiparticle-shell model, attempts at theoretically describing giant multipole resonances in nuclei whose ground states are far from closed shells and subshells run into a number of difficulties. A possible way to solving the problem of microscopically describing giant multipole resonances in such nuclei is provided by the multiparticle-shell-model version referred to as the *particle–core coupling* version [1]. This approach, which takes into account the fractional-parentage structure of the ground state of a target nucleus, has already proved to be quite efficient in studying giant multipole resonances in $1p$-shell nuclei, as well as in some sd-shell nuclei, for which the excitation-energy distribution of the multipole strength was adequately interpreted upon taking into account deviations of the ground state from a closed shell.

The present article is devoted to theoretically studying magnetic $1\hbar\omega$ resonances in the cross sections for the excitation of the ^{26}Mg nucleus.

A number of giant multipole resonances are excited in inelastic electron scattering on nuclei; the higher the momentum transfer to the nucleus involved, the higher the average multiplicity of resonances that dominate the respective cross section. While dipole resonances in the photo- and electroexcitation of nuclei have received adequate study both in an experimental and in a theoretical aspect, $1\hbar\omega$ resonances of higher multipole order are understood much more poorly. Over the past 10 to 15 years, the commissioning and running of intermediate-energy accelerators, along with recording of secondary electrons at a scattering angle of 180°, have greatly contributed to making considerable advances in studying magnetic multipole resonances of the vibrational type, especially maximum-spin resonances (stretched states). Great interest in this type of giant multipole resonances is motivated by the fact that only the spin component of the nucleon current in the target nucleus is involved in their excitation. In addition, these states provide a good test for model approximations because the basis of doorway configurations is bounded. The excitation of $M6$ magnetic resonances in the ^{26}Mg nucleus was experimentally investigated in [2, 3] up to excitation energies of 20 MeV. In [4], the $M6$ states in the ^{26}Mg nucleus were theoretically calculated by using the basis of $(d_{5/2})^9 1f_{7/2}$ states. The contributions to the same region from cross sections for magnetic resonances of lower multipole order have not yet been taken

*e-mail: natacha@msx.ru

1063-7788/05/6806-0921$26.00 © 2005 Pleiades Publishing, Inc.

into account, although the $M4$ transitions of $p_{3/2}$ nucleons to $d_{5/2}$ holes in the valence shell of the ^{26}Mg nucleus contribute to the cross section for backward electron scattering in the same region of momentum transfers to the nucleus as the transitions $d_{5/2} \to f_{7/2}$. The excitation-energy and momentum-transfer distributions of $M2$ and $M4$ resonances, which dominate backward electron scattering at momentum transfers to the nucleus in the range between about 0.8 and 1.2 fm^{-1}, have received no study thus far.

The objective of the present study was to construct a theoretical description of all magnetic $1\hbar\omega$ resonances in the electroexcitation of the ^{26}Mg nucleus and to analyze their contributions to the cross section at momentum transfers to the nucleus that range up to 2 fm^{-1}.

2. FORM FACTORS FOR GIANT MULTIPOLE RESONANCES IN (e, e') CROSS SECTIONS

Investigation of inelastic electron scattering is the most reliable means for exploring magnetic multipole resonances in cross sections for nuclear excitations, since an analysis of (e, e') reactions does not involve the problem of interaction dynamics. All of the observed maxima in the effective cross sections for electroexcitation reactions—that is, giant multipole resonances—result from nuclear-charge and nuclear-current interactions with an electromagnetic field. The effective differential cross section for electron–nucleus scattering is related to the features of the nuclear structure through the longitudinal and transverse form factors (F_L and F_T, respectively) as [5]

$$\frac{d\sigma}{d\Omega} = \frac{4\pi\sigma_{\rm M}}{\eta_T}\left\{F_L^2(q,\omega) + \left(\frac{1}{2} + \tan^2\frac{\theta}{2}\right)F_T^2(q,\omega)\right\}, \quad (1)$$

where $\sigma_{\rm M}$ is the Mott cross section for scattering on a pointlike charge, η_T is the nuclear-recoil factor, q is the momentum transfer to the nucleus involved, and ω is the excitation energy of the nucleus.

Nuclear-charge-density distributions have been studied in detail in the scattering of electrons into the forward hemisphere, in which case the effective scattering cross section is dominated by the longitudinal form factor. At the present time, it is more important to study electron scattering into the backward hemisphere, since the special features of intranuclear-current interaction with an external field manifest themselves in this process. The effective cross section for electron scattering at an angle of 180° is related to the properties of the target nucleus through the transverse form factor squared, which is the sum of the squares of the transverse multipole form factors,

$$F_T^2(q,\omega) = \sum_{J=1}^{J_{\max}}\{F_{EJ}^2 + F_{MJ}^2\}. \quad (2)$$

The form factors for giant multipole resonances can be expressed in terms of the matrix elements of the operators of spin and orbital multipole intranuclear-nucleon-current components. (Giant multipole resonances determine the response of a nucleus to an excitation in the excitation-energy region below 50 MeV; in this energy region, the role of meson-exchange currents in the formation of cross sections is much less important than the role of the nucleon components of the intranuclear current.) If the approximation of pointlike nucleons is used in calculating the operators of nucleon currents, a finite nucleon size is taken into account by introducing the coefficient $f_{\rm sn}$ in the formula for nuclear form factors [6]. The calculation of the matrix elements of single-particle operators in the approximation of harmonic-oscillator wave functions requires, in addition, taking into account the correction $f_{\rm c.m.}$, which is associated with center-of-mass motion; that is, [5, 6]

$$F_{MJ}(q,\omega) \quad (3)$$
$$= f_{\rm sn}f_{\rm c.m.}(2J_i+1)^{-1/2}\langle J_fT_f \parallel \hat{O}_J^{\rm mag} \parallel J_iT_i\rangle,$$

where J_f and T_f are, respectively, the spin and the isospin of the final state of the target nucleus, while J_i and T_i stand for their counterparts in its initial state.

The operator of an excitation that is characterized by a multipolarity J and an isospin T can be represented as the sum of single-particle operators; that is,

$$\hat{B}^{JT}_{M_JM_T} = \sum_i \hat{b}^{JT}_{M_TM_J}(i) = \sum_i \hat{O}^{JM_J}_{TM_T} \quad (4)$$
$$= \sum_i \hat{R}^J_{M_J}(i)\hat{\tau}^T_{M_{TI}}(i),$$

where τ is an operator in isospin space: $\tau^0 = I$, $\tau^1 = \tau$.

The matrix elements in (3) and (4) can be reduced to the sum of the matrix elements of one-nucleon operators; that is,

$$\langle J_fI_fM_{T_f} \parallel \hat{B}^J_{TM_T} \parallel J_iI_iM_{T_i}\rangle \quad (5)$$
$$= \sum_{i,j_i,j_f}\langle j_f \parallel \hat{O}^J_{TM_T}(i) \parallel j_i\rangle$$
$$\times \sqrt{2}\sqrt{2(2J_i+1)}Z^J_{TM_{TI}}(j_fj_i),$$

where Z is the spectroscopic transition amplitude.

The operator of an excitation of magnetic transitions characterized by a multipolarity J is the sum of

three operators; of these, two operators reflect virtual-photon coupling to the spin nucleon current of the nucleus ($\hat{A}_{J-1} + \hat{A}_{J+1}$), while the third ($\hat{B}_J$) takes into account coupling to the orbital (convection) current. Specifically, we have

$$\hat{O}_J^{\mathrm{mag}}(q) = \frac{iq}{2m_N}\sum_{i=1}^{A}\left\{\left(\frac{\mu_s + \mu_v\hat{\tau}_3}{2}\right)\right. \quad (6)$$
$$\times\left[\sqrt{\frac{J+1}{2J+1}}j_{J-1}(qr_i)[Y_{J-1}\times\hat{\sigma}_i]_J\right.$$
$$\left.\left. - \sqrt{\frac{J}{2J+1}}j_{J+1}(qr_i)[Y_{J+1}\times\hat{\sigma}_i]_J\right]\right.$$
$$\left. - \frac{2}{q}\left(\frac{1+\hat{\tau}_3}{2}\right)j_J(qr_i)[Y_J\times\hat{\nabla}_i]_J\right\}$$
$$= \hat{A}_{J-1} + \hat{A}_{J+1} + \hat{B}_J.$$

Here, m_N is the nucleon mass, $\mu_s = \frac{1}{2}(\mu_p + \mu_n)$, and $\mu_v = \frac{1}{2}(\mu_p - \mu_n)\hat{\tau}_3$, with μ_p and μ_n being, respectively, the proton and neutron magnetic moments.

The dependence of the matrix elements of single-particle operators on the special features of the structure of a concrete nucleus is controlled by the spectroscopic multipole-transition amplitude

$$Z^J_{TM_T} = \langle J_f I_f M_{T_f} \parallel \hat{A}^J_{TM_T}(j_f j_i) \parallel J_i I_i M_{T_i}\rangle, \quad (7)$$

where the excitation operator $\hat{A}$, which acts on the ground state of the nucleus, is related to nucleon (quasiparticle) creation ($\hat{a}^+$) and annihilation ($\hat{a}$) operators by the equation

$$\hat{A}^{JM_J}_{TM_T} = \sum_{t_{3f}t_{3i}}(-1)^{1/2-t_{3f}} \quad (8)$$
$$\times\langle 1/2 t_{3f} 1/2 - t_{3i}|TM_T\rangle$$
$$\times\sum_{m_f m_i}(-1)^{j_i - m_i}\langle j_f m_f j_i m_i|JM_J\rangle$$
$$\times\hat{a}^+_{j_f m_f t_{3f}}\hat{a}_{j_i m_i t_{3i}} = [\hat{a}^+_{j_f m_f t_{3f}}\times\hat{a}_{j_i m_i t_{3i}}]^{JM_J}_{TM_T}.$$

3. METHOD OF THE CALCULATIONS

Within the *particle–core coupling* version, the wave functions for the initial and final states of the nucleus can be represented in the form of an expansion in basis configurations:

$$|J_i T_i\rangle = \sum C_i^{J'T',j_i}|(J'T'E')\times(j) : J_i T_i\rangle, \quad (9)$$

$$|J_f T_f\rangle = \sum \alpha_f^{J'T',j_f}|(J'T'E')\times(j') : J_f T_f\rangle. \quad (10)$$

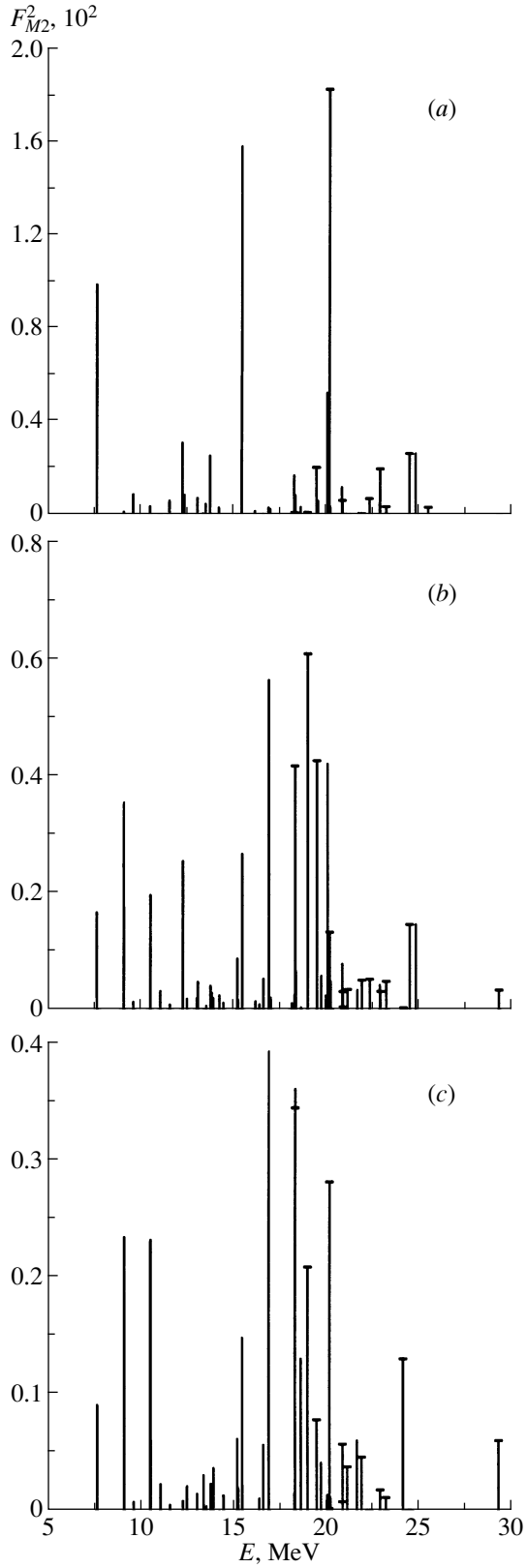

Fig. 1. Results of the calculation for the $M2$ resonance at momentum transfers of $q =$ (*a*) 0.8, (*b*) 1.2, and (*c*) 1.8 fm^{-1}. Lines with and without a transverse dash represent, respectively, the $T = 2$ and the $T = 1$ isospin branch.

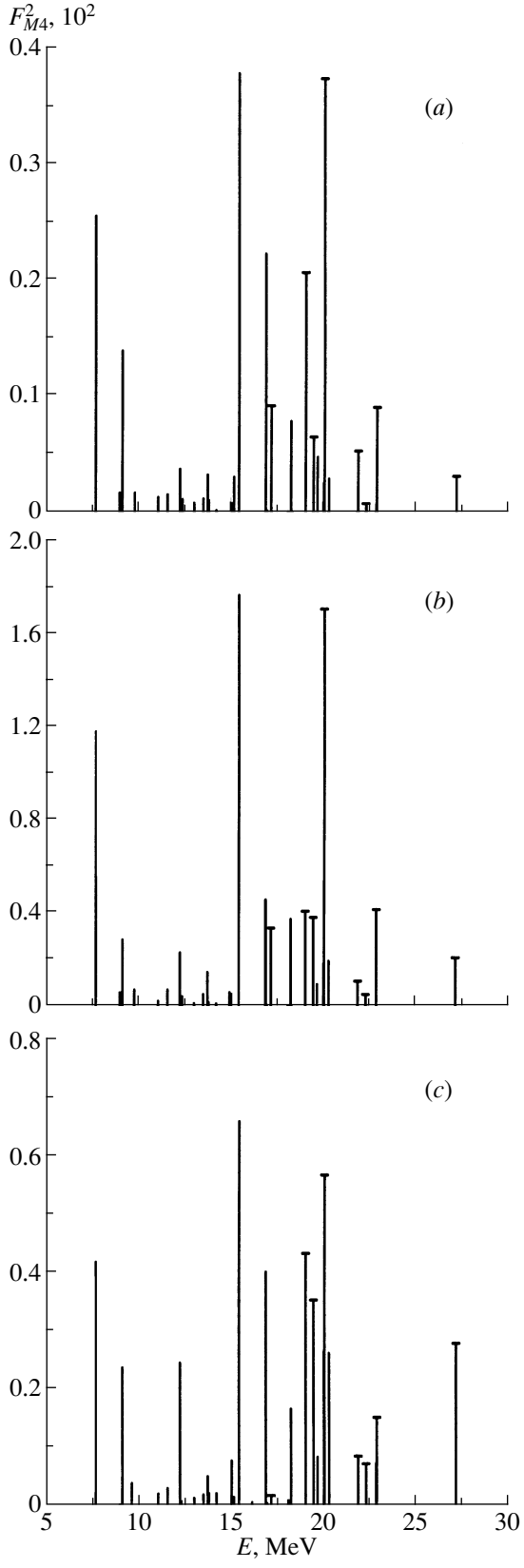

Fig. 2. Results of the calculation for the $M4$ resonance at momentum transfers of $q = (a)$ 0.8, (b) 1.2, and (c) 1.8 fm^{-1}. The notation for the isospin branches is identical to that in Fig. 1.

The fractional-parentage coefficients C stem from expanding the known ground-state wave function for nucleus A in the products of the wave functions for the final nucleus $(A-1)$ and the nucleon wave function. In theoretically studying giant multipole resonances in $1p$-shell nuclei, transition matrix elements were calculated on the basis of the known fractional-parentage structure of the ground states [1]. In calculating giant multipole resonances of the ^{26}Mg nucleus, the fractional-parentage coefficients were estimated with the aid of experimental data on the spectroscopy of direct nucleon-pickup reactions [7]. The coefficients α result from diagonalizing the Hamiltonian in the basis of *particle–core coupling* configurations.

Within the *particle–core coupling*, the spectroscopic amplitudes (7) are functions of the fractional-parentage coefficients C and α; that is,

$$Z^J_{TM_T}(j_f j_i) = \sqrt{(2T_i+1)(2J_f+1)} \times \langle T_i M_{T_i} T0 | T_f M_{T_f}\rangle \sum_{J'T'} C_i^{J'T',j_i} \alpha_f^{J'T',j_f} \times (-1)^{J'-J_i+j_f-J} W(J_i J_f j_i j_f; JJ') \times (-1)^{T'-T_i+1/2-T} W(T_i T_f \tfrac{1}{2}\tfrac{1}{2}; TT'), \quad (11)$$

where W are Racah coefficients.

The Hamiltonian was diagonalized in the bases of the excited-state wave functions (10) for $J_f = 2, 4, 6$ and final-state isospins of $T_f = 1, 2$.

In the matrix elements of the total Hamiltonian, we took into account the energies E' of states of nucleus $(A-1)$ that have a significant fractional-parentage relation to the ground state of the ^{26}Mg nucleus:

$$\hat{H}_{ij} = (E' + \varepsilon_j + E_c)\delta_{ij} + \hat{V}_{ij}. \quad (12)$$

Here, $\hat{V}_{ij}$ is the operator of residual nucleon–core interaction, while ε_j are single-particle nucleon energies. The matrix elements of residual interactions between the states in (10) were calculated by the formula

$$\langle (J''T''E''), j_2 : J_f T_f | \hat{V}_{\rm int} | (J'T'E'), j_1 : J_f T_f\rangle = \sum_{J,T,j,j'} \langle J'T'E' | J_i T_i, j^{-1}\rangle \langle J_i T_i, j'^{-1} | J''T''E''\rangle \times (2J+1)(2T+1)\sqrt{(2J'+1)(2T'+1)(2J''+1)} \times \sqrt{(2T''+1)}\, W(J_i j J_f j_1; J'J) W(J_i j' J_f j_2; J''J) \times W(T_i 1/2\, T_f 1/2; T'T) W(T_i 1/2\, T_f 1/2; T''T) \times \langle j^{-1} j_1 : JT | V_{\rm int} | j'^{-1} j_2 : JT\rangle. \quad (13)$$

The calculation of the matrix elements of particle–hole interactions in (13) was performed with a zero-range potential.

4. MAGNETIC RESONANCES OF THE ^{26}Mg NUCLEUS

The results of the calculations for the $M2$ and $M4$ resonances are displayed in Figs. 1 and 2 for the momentum transfers of $q = 0.8$, 1.2, and 1.8 fm^{-1}. The resonances of isospin $T = 1$ and T = 2 are singled out in the figures. The excitation-energy distributions of the form factors for the $M2$ and $M4$ transitions in Figs. 1 and 2 reflect the main source of the fragmentation of the magnetic-resonance strengths in the ^{26}Mg nucleus, which features an unfilled valence shell—this is the distribution of the hole state over the energies of $A = 25$ nuclei. According to data on direct reactions, the separation of a neutron from a ^{26}Mg nucleus leads, with the highest probability, to the $5/2^+$ state of the ^{25}Mg nucleus at an energy of 7.79 MeV—this is an isobaric analog of the ^{25}Na ground state.

The first of the above momentum-transfer values (0.8 fm^{-1}) approximately corresponds to the maximum of the sum of the squares of the form factors for the $M2$ resonances. The position of this maximum is determined by the dominant role of the contributions to the total $M2$ form factor from the transitions $d_{5/2} \to f_{7/2}$. The square of the $M2$ form factor for this single-particle transition at $q = 0.8$ fm^{-1} is almost an order of magnitude greater than the contributions of other single-particle transitions of a $d_{5/2}$ nucleon. The wave functions associated with the peaks of the $M2$ resonances at energies of about 15.5 and 20.2 MeV are dominated by the configurations $|(5/2^+,\ E = 7.79\ \text{MeV},\ T' = 3/2) \times 1f_{7/2} : J = 2, T\rangle$, the isospin being $T = 1$ and $T = 2$ for, respectively, the first and the second peak. The lowest (in energy) peak of the $M2$ resonance corresponds to the configuration $|(5/2^+,\ E = 0,\ T' = 1/2) \times 1f_{7/2} : J = 2,\ T = 1\rangle$.

Magnetic quadrupole transitions from the $d_{5/2}$ subshell make a significant contribution to electroexcitation at the higher momentum-transfer values inclusive (Figs. 1*b*, 1*c*), which correspond to the maxima of the contributions from the $M4$ and $M6$ resonances. The distribution of the $M2$ transitions in Fig. 1*b* is fragmented to a much greater extent than in the momentum-transfer region around $q = 0.8$ fm^{-1}. This fact reflects the more important role of $d_{5/2} \to 2p_{3/2}$, $d_{5/2} \to f_{5/2}$, and $d_{5/2} \to 2p_{1/2}$ transitions, for which single-particle form factors are close to their maximum values at this value of the momentum transfer to the nucleus. At the momentum transfer of 1.2 fm^{-1}, the strongest maxima among the $M2$ resonances are associated with states dominated by the configurations $|(5/2^+,\ E = 7.79\ \text{MeV},\ T' = 3/2) \times 1f_{5/2} : J = 2,\ T\rangle$ and $|(5/2^+,\ E = 7.79\ \text{MeV},\ T' = 3/2) \times 2p_{3/2} : J = 2,\ T\rangle$. (The momentum-transfer distributions of the form factors for single-particle $M2$ transitions from the sd shell are given in [8].)

The role of transitions from the $1p$ shell in the form factors for $M2$ resonances is quite modest. The contributions of the $p_{3/2} \to d_{5/2}$, $p_{3/2} \to d_{3/2}$, $p_{3/2} \to 2s_{1/2}$, and $p_{1/2} \to d_{3/2}$ transitions to the total $M2$ form factor is as small as about 12% at $q = 0.8$ and 1.2 fm^{-1}. The first of these transitions makes a nearly 100% contribution to the peak at an energy of 24.5 MeV. The fraction of these transitions grows with increasing momentum transfer to the nucleus, since the single-particle form factors for the $p_{3/2} \to d_{3/2}$ and $p_{1/2} \to d_{3/2}$ transitions become greater at $q = 1.2$ fm^{-1}. At $q = 1.8$ fm^{-1}, the fraction of transitions from the p shell reaches 16% in the total $M2$ form factor, playing a dominant role in the states at $E = 18.7$, 24.5, and 29.4 MeV. It should be emphasized that information about the spectroscopy of pickup reactions producing final nuclei in negative-parity states is rather contradictory at the present time. Here, we make use of averaged data.

Figure 2*a* shows the distribution of the $M4$ strength at the momentum-transfer value of $q = 0.8$ fm^{-1}. This strength is strongly fragmented, the total contribution of $M4$ resonances to the electroexcitation at $q = 0.8$ fm^{-1} being approximately 4 times less than the contribution to the cross section from the dominant $M2$ resonances. Upon the increase in the momentum transfer to $q = 1.2$ fm^{-1}, $M4$ transitions begin to play a leading role in electroexcitation (Fig. 2*b*). The origin of the main $M4$ maxima in Fig. 2*b* is similar to the origin of the main peaks of $M2$ resonances in Fig. 1*a*: the wave functions are dominated by the $|(5/2^+,\ E = 7.79\ \text{MeV},\ T' = 3/2) \times 1f_{7/2} : J = 4,\ T\rangle$ configurations of isospin $T = 1$ and $T = 2$; the wave function for the peak at the lowest energy is associated almost completely with the $|(5/2^+,\ E = 0,\ T' = 1/2) \times 1f_{7/2} : J = 4,\ T = 1\rangle$ configuration.

The isospin splitting of peaks into the $T = 1$ and $T = 2$ components of close configuration structures is about 4 to 6 MeV for almost all magnetic resonances considered here. As in the case of $M2$ resonances, the contribution of transitions from the $1p$ shell to the total form factor grows with increasing q, reaching 12% at $q = 1.8$ fm^{-1}.

Figures 1*c* and 2*c* display the contributions to electroexcitation from $M2$ and $M4$ magnetic $1\hbar\omega$ resonances in the region around $q = 1.8$ fm^{-1}, which is dominated by $M6$ excitations.

In this momentum-transfer region, the $p_{3/2} \to d_{5/2}$ transition plays a special role in $M4$ excitation.

$M6$ resonances in the ^{26}Mg nucleus at $q = 1.8$ fm^{-1}

Experimental data [2]			Model results		
T	E, MeV	F^2, 10^3	T	E, MeV	F^2, 10^3
1	7.5	0.020	1	8.49	0.705
1	9.2	0.180	1	10.46	0.079
1	12.5	0.231	1	12.41	0.044
1	12.9	0.110	1	13.22	0.063
1	13.0	0.050	1	14.36	0.022
1	14.0	0.080	1	14.58	0.181
1	14.5	0.130	1	16.31	0.467
1	15.4	0.140	2	17.90	0.895
1	15.5	0.250	1	19.13	0.056
1	16.5	0.300	2	20.93	0.263
2	18.0	0.810			

If the spin of the excitation is $J = 4$, this transition, as well as the $M6$ transition considered below, is a maximum-spin transition. As in the case of $M6$ excitations, the $M4$ resonance is formed in $p_{3/2} \to d_{5/2}$ transitions by the spin operator $\hat{A}_{J-1}$ exclusively. In the calculation with harmonic-oscillator wave functions, the $M4$ form factor for this transition has only one maximum, in just the same way as the $M6$ form factor for the $d_{5/2} \to f_{7/2}$ transition. Although $p_{3/2} \to d_{5/2}$ transitions in the ^{26}Mg nucleus are partly suppressed since the $d_{5/2}$ subshell is filled, the spectroscopic factor for the direct pickup reaction leading to the production of the $3/2^-$ state of the ^{25}Mg nucleus at $E' = 11.7$ MeV is not small [7], and this is the reason why, in the region of target-nucleus excitation energies above 20 MeV, the contribution of transitions from the p shell to magnetic multipole form factors is sizable within the *particle-core coupling* approach.

Experimental data on the distribution of the $M6$ strength [2] and the theoretical results of the present study are quoted in the table.

A comparison of the results obtained on the basis of the *particle–core coupling* approach with experimental data shows that this model approximation reproduces experimental data fairly well. The use of data concerning the distribution with respect to the energies of $5/2^+$ states in $A = 25$ nuclei and underlying the construction of the basis for 6^- configurations of the excited nucleus ^{26}Mg here leads to eight peaks associated with the isospin of $T = 1$ and two peaks associated with the isospin of $T = 2$. (All of the excitations forming the $M6$ resonance are associated with the $d_{5/2} \to f_{7/2}$ transition.)

The 6^- states of isospin $T = 2$ are constructed on the basis of the 7.79- and 10.62-MeV configurations. These are the isospin-3/2 states of the ^{25}Mg nucleus, the respective spectroscopic factors for direct pickup reactions being 3.86 and 0.81, respectively. Unfortunately, the experimental distribution of the 6^- states in the ^{26}Mg nucleus is known only over the energy region $E < 20$ MeV. Calculations reveal that a 6^-, $T = 2$ peak dominated by the $|(5/2^+,\ E = 10.62$ MeV, $T' = 3/2) \times 1f_{7/2} : J = 6,\ T = 2\rangle$ configuration must manifest itself at higher excitation energies as well.

One drawback of the present theoretical calculation is worthy of note—it overestimates the form factor for the lower (on the energy scale) peak corresponding to the contribution of the $|(5/2^+,\ E = 0,\ T' = 1/2) \times 1f_{7/2} : J = 6,\ T = 1\rangle$ configuration.

In our opinion, the fragmentation of the $M6$ resonance in the cross section for the electroexcitation of the ^{26}Mg nucleus is a compelling piece of evidence that the distribution of doorway states over the energies of levels of $(A-1)$ nuclei plays a dominant role in the formation of the response of this nucleus to a multipole excitation.

5. CONCLUSIONS

(i) A deviation of the ground states of A-nucleon nuclei from closed shells or subshells manifests itself over a broad energy range of states excited in $(A-1)$ nuclei in direct pickup reactions. The spectroscopic factors of pickup reactions can be used in calculating wave functions for the excited states of the target nucleus within the *particle–core coupling* version of the multiparticle shell model.

(ii) The spreading of hole states over the excitation energies of $(A-1)$ nuclei is, along with isospin splitting, a source of the fragmentation of the multipole strengths in open-shell nuclei.

(iii) Our calculation of the $M2$, $M4$, and $M6$ resonances in the electroexcitation of the ^{26}Mg nucleus has revealed a high degree of the fragmentation of the multipole strengths in the excitation-energy range between 7 and 29 MeV.

(iv) A comparison of the results of the calculations within the *particle–core coupling* approach with experimental data on the distribution of the $M6$ strength has proven the validity of our model assumptions.

ACKNOWLEDGMENTS

This work was funded by a presidential grant (no. NSh-1619.2003.2) for support of leading scientific schools.

REFERENCES

1. N. G. Goncharova and N. P. Yudin, Phys. Lett. B **29B**, 272 (1969); N. G. Goncharova, in *Proceedings of the X International Seminar "Electromagnetic Interactions at Low and Medium Energies", Moscow, 2003,* p. 23.
2. B. L. Clausen, R. J. Peterson, and R. A. Lindgren, Phys. Rev. C **38**, 589 (1988).
3. B. L. Clausen, R. J. Peterson, C. Kormanyos, *et al.*, Phys. Rev. C **48**, 1632 (1993).
4. J. A. Carr, Phys. Rev. C **49**, 2505 (1994).
5. T. de Forest and J. D. Walecka, Adv. Phys. **15**, 57 (1966).
6. T. W. Donnelly and J. D. Walecka, Annu. Rev. Nucl. Sci. **25**, 329 (1975).
7. P. M. Endt, Nucl. Phys. A **521**, 131 (1990).
8. A. A. Dzhioev and N. G. Goncharova, Izv. Akad. Nauk, Ser. Fiz. **66**, 21 (2002).

Translated by A. Isaakyan

Physics of Atomic Nuclei, Vol. 68, No. 6, 2005, pp. 928–939. Translated from Yadernaya Fizika, Vol. 68, No. 6, 2005, pp. 967–977.
Original Russian Text Copyright © 2005 by Kuterbekov, Kukhtina, Penionzhkevich, Zholdybayev.

NUCLEI
Theory

Energy and Mass Dependences of the Parameters of the Semimicroscopic Folding Model for Alpha Particles at Low and Intermediate Energies

K. A. Kuterbekov[1)*], I. N. Kukhtina, Yu. E. Penionzhkevich, and T. K. Zholdybayev[1)]

Joint Institute for Nuclear Research, Dubna, Moscow oblast, 141980 Russia

Received July 6, 2004

Abstract—The energy and mass dependences of the parameters of the semimicroscopic alpha-particle potential are investigated for the first time in the region of low and intermediate energies. Within the semimicroscopic folding model, both elastic and inelastic differential and total cross sections for reactions on various nuclei are well described by using global parameters obtained in this study. © *2005 Pleiades Publishing, Inc.*

1. INTRODUCTION

The results of a global analysis of both the angular distributions for the elastic and inelastic scattering of alpha particles and light exotic nuclei and the total reaction cross sections are an important source of information about the nuclear-matter distributions in nuclides and about the properties of the potential representing nucleus–nucleus interaction. At low and intermediate energies, the semimicroscopic folding model based on the double-folding method [1–4] is a popular method for analyzing experimental angular distributions.

In connection with the well-justified model assumption that an alpha particle is a core of exotic light nuclei (^{6,8}He), it is of importance to perform a systematic analysis of experimental data on the interaction of low- and intermediate-energy alpha particles with a broad range of stable nuclei and to derive generalized dependences for the parameters of the semimicroscopic folding model.

The energy dependence of a number of parameters of the simple double-folding model was investigated for alpha particles in [5].

With the aim of global searches for unified parameters of the semimicroscopic folding model, experimental differential and total reaction cross sections for alpha-particle interactions with $A = 12$–208 nuclei at energies in a broad range are systematically analyzed here for the first time within the double-folding model [6] on the basis of the total M3Y effective interaction and nucleon densities calculated for all colliding nuclei by the density-functional method [7].

A theoretical model that claims to be a complete description of experimental data must reproduce, with the same set of input parameters, both the absolute values of differential cross sections and the total reaction cross sections. The choice of optimum parameters for the double-folding model [6] makes it possible to extract, in the following, reliable information about the structural features of the nuclei under study by using a comparative analysis of experimental data on the scattering of alpha particles and exotic light nuclei.

In the present article, the energy and mass dependences of the parameters of the semimicroscopic folding model are proposed for the first time for alpha particles of energy in a broad range.

2. EXPERIMENTAL DATA USED FOR AN ANALYSIS

In order to construct the sought global dependence of the parameters of the semimicroscopic folding model, we chose input experimental data that include the results of our studies and data available from the literature [5, 8–20].

The main characteristics of experimental conditions under which the angular distributions used were obtained are given in Table 1. The experimental angular distributions presented in [11, 14, 16, 18, 20] and included in the analysis were obtained at the isochronous cyclotron U-150M, reaction products being recorded and identified by means of a system based on the CAMAC–PC/AT complex [21].

[1)]Institute of Nuclear Physics, National Nuclear Center of the Republic of Kazakhstan, Almaty, 480082 Republic of Kazakhstan.

[*]e-mail: kuterbekov@inp.kz

Table 1. Main features of experiments that studied elastic alpha-particle scattering

Nucleus	E_α, MeV	Target		Angular range (c.m. frame), deg	References
		thickness, mg/cm^2	enrichment, %		
For the energy dependence					
^{90}Zr	21.0	0.73	97.0	48–177	[8]
^{90}Zr	23.4	0.73	97.0	48–177	[8]
^{90}Zr	25.0	0.73	97.0	48–177	[8]
^{90}Zr	31.0	1.0	98.0	10–98	[9]
^{90}Zr	35.4	0.520	97.65	10–100	[10]
	35.4	0.855	97.67	6–47	
^{90}Zr	40.0 ± 0.2	0.84–2.47	97.6	5–175	[5]
	40.0 ± 0.5	2.13 ± 0.08	95.0	10–70	[11]
^{90}Zr	50.1 ± 0.5	2.13 ± 0.08	95.0	15–80	[11]
^{90}Zr	59.1 ± 0.3	0.84–2.47	97.6	5–175	[5]
^{90}Zr	65.0	5.0–8.5	95.0	10–76	[12]
^{90}Zr	79.5 ± 0.4	0.84–2.47	97.6	5–175	[5]
^{90}Zr	99.5 ± 0.5	0.84–2.47	97.6	5–175	[5]
^{90}Zr	118.0 ± 0.5	0.84–2.47	97.6	5–175	[5]
^{90}Zr	141.7 ± 0.2	5.9	99.0	5–95	[13]
For the mass dependence					
^{12}C	50.5 ± 0.5	1.1–2.0	98.9	13–173	[14]
	139.0 ± 0.5	0.88	CH	5–70	[15]
^{24}Mg	50.5 ± 0.5	1.0–3.2	99.1	12–172	[14, 16]
^{28}Si	50.5 ± 0.5	0.59–0.76	92.17	11–171	[14, 16]
^{40}Ca	141.7 ± 0.2	2.1	96.0	5–80	[13]
^{46}Ti	140.1 ± 0.5	5.0	83.8	5–70	[17]
^{48}Ti	50.5 ± 0.5	4.50 ± 0.08	99.2	24–64	[14]
	140.1 ± 0.5	5.0	99.1	5–70	[17]
^{50}Ti	50.5 ± 0.5	3.15 ± 0.08	83.2	32–84	[18]
	140.1 ± 0.5	5.0	83.2	5–75	[17]
^{58}Ni	50.5 ± 0.5	0.56	99.5	20–65	[14]
	139.0 ± 0.5	1.6 ± 0.3	99.0	5–80	[19]
^{68}Zn	50.5 ± 0.5	3.48 ± 0.08	91.2	16–76	[14, 20]
^{70}Zn	50.5 ± 0.5	3.10 ± 0.08	95.0	16–66	[14, 20]
^{90}Zr	50.1 ± 0.5	2.13 ± 0.08	95.0	16–75	[11]
	141.7 ± 0.2	5.9	99.0	5–95	[13]
^{94}Zr	50.1 ± 0.5	2.60 ± 0.08	91.2	12–75	[11]
^{120}Sn	50.5 ± 0.5	2.20 ± 0.08	99.2	10–63	[14, 20]
^{124}Sn	50.5 ± 0.5	2.00 ± 0.08	95.1	10–65	[14, 20]
^{208}Pb	139.0 ± 0.5	2.09 ± 0.20	99.0	10–95	[19]

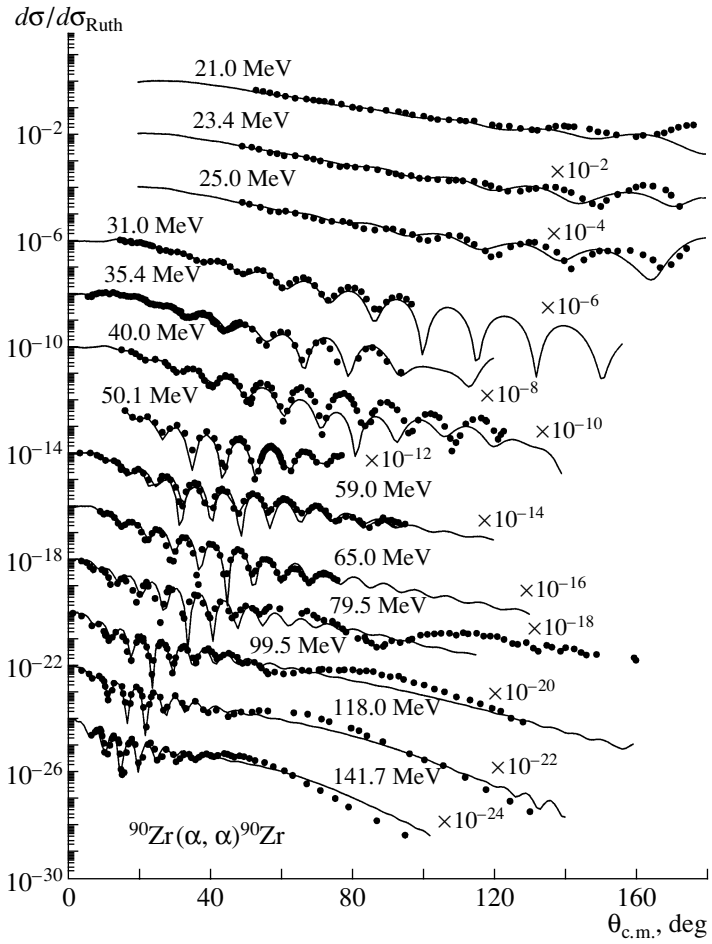

Fig. 1. Angular distributions of the differential cross sections for elastic alpha-particle scattering on ^{90}Zr at energies in the range 21.0–147.7 MeV: (points) experimental data and (solid curves) results of the calculations within the semimicroscopic folding model.

In [11, 14, 16, 18, 20], the systematic error in the absolute differential cross sections for scattering received contributions primarily from the uncertainties in the target thickness (4–6%), the solid angle of the spectrometer (1%), and the calibration of the current integrator and did not exceed 10%. The statistical error of the data under analysis was 1–5%; only in individual cases—at the minima of the angular distributions at large angles—did it become as large as 6 to 15%. All of the targets used were self-sustaining and were prepared by the thermal-evaporation method. The target thicknesses were determined by using the energy losses of alpha particles from ^{241}Am, ^{243}Am, ^{244}Cm, and ^{239}Pu radioactive sources. According to data reported in the literature [5, 8–10, 12, 13, 15, 17, 19], the errors in the absolute values of the differential cross sections in the angular distributions for scattering were in the range 5–10%.

The experimental values of the total reaction cross sections σ_R, the errors in them being 4–7% in the energy region under consideration, were borrowed from [11] and from other sources available in the literature [22–25].

3. ANALYSIS OF DATA AND GLOBAL DEPENDENCE OF THE PARAMETERS OF THE SEMIMICROSCOPIC FOLDING MODEL

3.1. Semimicroscopic Folding Model

The semimicroscopic optical potential $U(R)$ is constructed within the double-folding model on the basis of the total M3Y effective interaction and nucleon densities calculated by the density-functional method [7]. In the first order in the effective forces, the potential simulating the interaction of two colliding nuclei can be represented as the sum

$$U(\mathbf{R}) = U^E(\mathbf{R}) + U^D(\mathbf{R}), \qquad (1)$$

where

$$U^D(\mathbf{R}) = \iint \rho^{(1)}(\mathbf{r}_1)V^D(\mathbf{s})\rho^{(2)}(\mathbf{r}_2)d\mathbf{r}_1 d\mathbf{r}_2 \qquad (2)$$

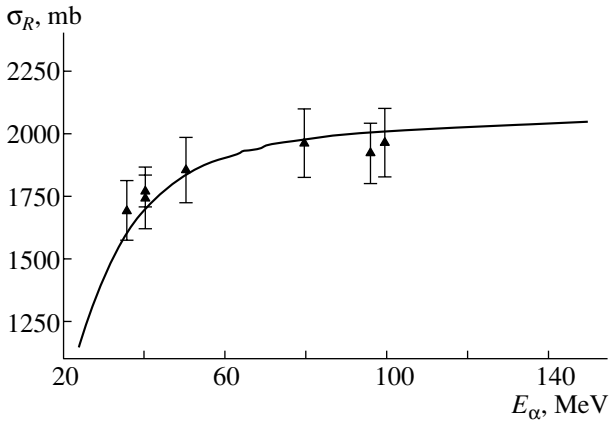

Fig. 2. Total reaction cross sections for alpha-particle interactions with ^{90}Zr nuclei: (▲) experimental data and their evaluation from [11, 22, 23] and (curve) theoretical values obtained on the basis of the semimicroscopic folding model.

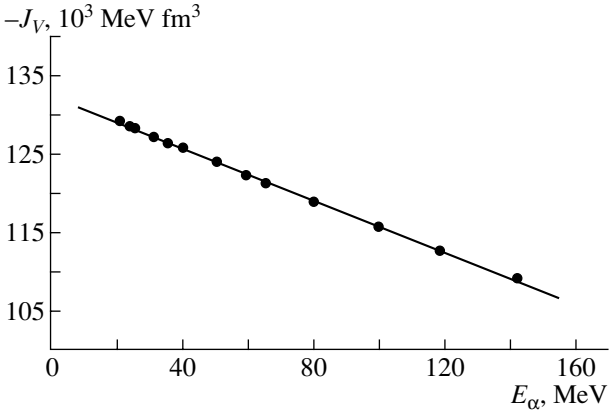

Fig. 3. Energy dependence of the volume integral J_V of the folded potential: (points) values calculated within the semimicroscopic folding model and (straight line) linear approximation.

is the direct potential in the double-folding model [1]. In expression (2), the factor $V^D(\mathbf{s})$ is the direct component of the effective interaction ($\mathbf{s} = \mathbf{r}_2 - \mathbf{r}_1 + \mathbf{R}$) and $\rho^{(i)}(\mathbf{r}_i)$ stands for the densities of colliding nuclei ($i = 1, 2$). A detailed scheme for computing the exchange potential $U^E(\mathbf{R})$ was formulated in [6]. The main contribution to it comes from one-nucleon-exchange effects [26], which are described within the density-matrix formalism; that is,

$$U^E(\mathbf{R}) = \iint \rho^{(1)}(\mathbf{r}_1, \mathbf{r}_1 + \mathbf{s}) V^E(\mathbf{s}) \rho^{(2)}(\mathbf{r}_2, \mathbf{r}_2 - \mathbf{s}) \times \exp(i\mathbf{k}(\mathbf{R}) \cdot \mathbf{s}/\eta) d\mathbf{r}_1 d\mathbf{r}_2, \quad (3)$$

where V^E (**s**) is the exchange component of effective nucleon–nucleon forces, $\rho^{(i)}$ (**r**, **r**') ($i = 1, 2$) are the density matrices for colliding nuclei of mass number A_1 and A_2, and $\mathbf{k}(\mathbf{R})$ is the local momentum of relative motion in the system of colliding nuclei. For this momentum, we have the relation

$$k^2(\mathbf{R}) = (2m\eta/\hbar^2)[E - U(\mathbf{R}) - V_{\text{Coul}}(\mathbf{R})], \quad (4)$$

where $\eta = A_1A_2/(A_1 + A_2)$, E is the c.m. energy, and $V_{\text{Coul}}(\mathbf{R})$ is the Coulomb potential. Thus, we see that, owing to the inclusion of one-nucleon-exchange effects, the total potential becomes energy-dependent. The parameters of effective nucleon–nucleon forces, together with the proton and neutron densities in colliding nuclei, appear to be input data for calculating the potentials in question.

In the semimicroscopic folding model, the total optical potential involves, in addition to a real part, an imaginary part, which is responsible for the absorption of the incident particle in inelastic channels. In the case being considered, the absorption potential $W(R)$ was taken to be dependent on the calculated

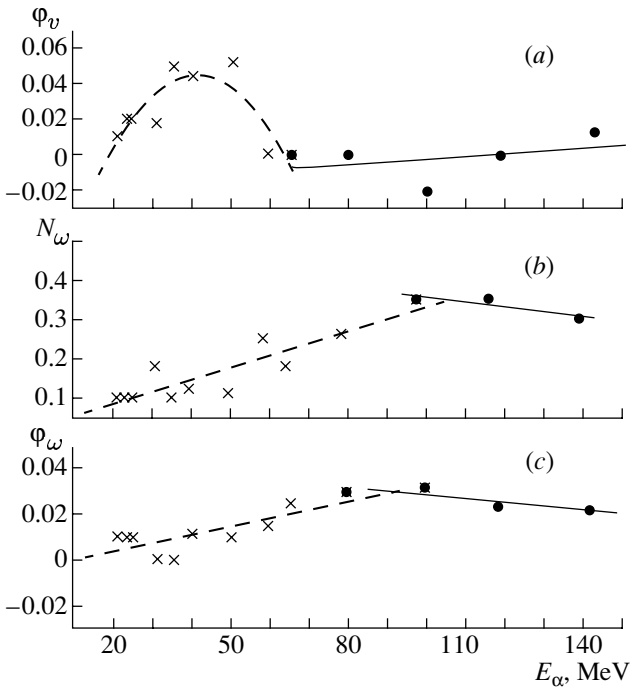

Fig. 4. Energy dependence of the parameters of the semimicroscopic-folding-model potential. The crosses and closed circles represent optimum values. In Fig. 4*a*, the dashed curve and the solid straight line are the approximations of the parameter φ_v by, respectively, the dependence in (8) and the linear dependence in (9). In Figs. 4*b* and Fig. 4*c*, the straight lines are the approximations of the parameters N_w and φ_w, respectively, by a linear dependence.

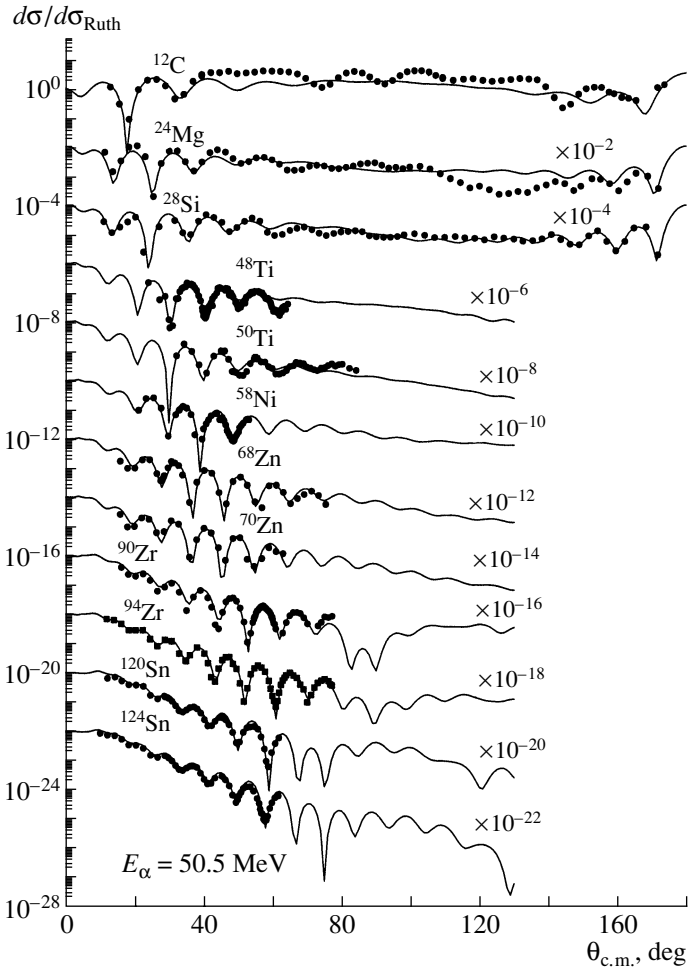

Fig. 5. Angular distributions of the differential cross sections for elastic alpha-particle scattering on $A = 12$–124 nuclei at $E_\alpha = 50.5$ MeV: (points) experimental data and (curves) results based on the semimicroscopic folding model.

real part in the form [2]

$$W(R) = i[N_w U(R) - \varphi_w R dU(R)/dR], \quad (5)$$

where $U(R)$ is the doubly folded potential (1), while N_w and φ_w are parameters that characterize, respectively, the volume and the surface component of the absorption potential. A surface term that mimics the contribution of the dynamical polarization potential [4] was included in the real part of the potential. The total optical potential in the semimicroscopic folding model has the form

$$U_{\rm tot}(R) = U(R) - \varphi_v R dU(R)/dR + i[N_w U(R) - \varphi_w R dU(R)/dR], \quad (6)$$

where φ_v, N_w, and φ_w are adjustable parameters.

In calculating the angular distributions for inelastic scattering, the inelastic-transition form factor was taken in the form $\varphi_L dU_{\rm tot}(R)/dR$ [27].

The optimum parameters of the semimicroscopic folding model were fitted in such a way as to attain, under the condition that the linear dependence of the volume integral J_V on the real part of the semimicroscopic-folding-model potential is preserved, the best agreement within a global analysis of experimental angular distributions for elastic scattering and available data on the total reaction cross section.

At the final stage of this study, we determine analytic dependences for the parameters of the semimicroscopic folding model, respecting the above criteria.

The theoretical values of the elastic-scattering cross section were calculated on the basis of a modified version of the ECIS-88 code (ECIS-PM) [28]. In this version, the semimicroscopic potentials were computed by formula (6). The fitting of the theoretical values of the angular distributions for elastic scattering and of the total reaction cross sections σ_R to experimental data was performed by varying the parameters φ_v, N_w, and φ_w. It should be noted that, in a global analysis of the differential and total reaction

Table 2. Parameters of the alpha-particle-interaction semimicroscopic potential, volume integrals $-J_V$, and rms radii $\langle r^2_{\mathrm{SFM}}\rangle^{1/2}$ of the folded potentials for ^{90}Zr at various alpha-particle energies

E_α, MeV	φ_v	N_w	φ_w	$-J_V$, 10^3 MeV fm^3	$\langle r^2_{\mathrm{SFM}}\rangle^{1/2}$, fm
21	0.010	0.10	0.010	129.3	4.989
23.4	0.020	0.10	0.010	128.7	4.990
25	0.020	0.10	0.010	128.4	4.990
31	0.017	0.18	0	127.3	4.990
35.4	0.050	0.10	0	126.5	4.991
40	0.045	0.12	0.012	125.7	4.992
50.1	0.052	0.11	0.010	123.9	4.993
59.1	0	0.25	0.015	122.3	4.994
65	0	0.18	0.025	121.3	4.994
79.5	0	0.26	0.030	118.9	4.996
99.5	−0.020	0.35	0.032	115.7	4.999
118	0	0.35	0.024	112.8	5.001
141.5	0.013	0.30	0.022	109.3	5.006

Table 3. Rms radii (in femtometers) of the neutron-, proton-, and nuclear-matter-density distributions for the $A = 12$–124 nuclei (also given here are the differences $\Delta r_{np} = \langle r_n^2\rangle^{1/2} - \langle r_p^2\rangle^{1/2}$ at $E_\alpha = 50.5$ MeV)

Nucleus	$\langle r_n^2\rangle^{1/2}$	$\langle r_p^2\rangle^{1/2}$	$\langle r_m^2\rangle^{1/2}$	Δr_{np}
^{12}C	2.40	2.41	2.40	−0.01
^{24}Mg	2.84	2.86	2.85	−0.02
^{28}Si	2.95	2.98	2.97	−0.03
^{48}Ti	3.73	3.69	3.71	0.04
^{50}Ti	3.75	3.69	3.72	0.06
^{58}Ni	3.76	3.76	3.76	0.00
^{68}Zn	3.87	3.81	3.84	0.06
^{70}Zn	3.97	3.86	3.93	0.11
^{90}Zr	4.26	4.19	4.23	0.07
^{94}Zr	4.37	4.24	4.31	0.13
^{120}Sn	4.71	4.59	4.66	0.12
^{124}Sn	4.77	4.61	4.70	0.16

cross sections, the parameters of the semimicroscopic folding model are determined unambiguously.

In the present study, the nucleon densities were computed by using the Gaussian representation (with the rms radius being set to 1.57 fm [29]) for alpha particles and by the density-functional method [7] for target nuclei.

3.2. Energy Dependence

In order to obtain the energy-dependent component of the global dependence of the parameters of the semimicroscopic folding model for alpha particles, we analyzed 15 experimental angular distributions for the elastic scattering of 21.0- to 141.7-MeV alpha particles on ^{90}Zr nuclei. The ^{90}Zr nucleus was chosen for obtaining the energy dependence in question, since, in the region of stable $A = 12$–208 nuclei, the features of ^{90}Zr as a good average test nucleus and its behavior in nuclear processes have been extensively and thoroughly studied [10, 11, 30–35] for many purposes, including that of deriving global dependences of the macroscopic-optical-potential parameters [5, 29, 36].

For the optimum values found for the parameters of the semimicroscopic folding model, Fig. 1 shows the result of our analysis of the angular distributions for elastic alpha-particle scattering on ^{90}Zr target nuclei at various energies. It can be seen that the experimental data are well described over a broad angular range.

As an additional criterion for selecting the optimum parameters of the semimicroscopic folding model, we use the values of the total reaction cross section σ_R. One can see from Fig. 2 that the σ_R values calculated for scattering on ^{90}Zr with the generalized parameters of the semimicroscopic folding model faithfully reproduce the evaluated total reaction cross sections and the trend of their variation with increasing alpha-particle energy, this confirming that the theoretical cross sections calculated on the basis of the above approach are realistic.

The volume integral of a folded potential is one of the criteria for evaluating the resulting semimicroscopic potentials. Figure 3 shows the energy dependence of the volume integral J_V (in 10^3 MeV fm^3 units) of the folded potential. One can see a clear-cut linear dependence on the energy E_α:

$$-J_V = 132.411 - 0.166E_\alpha. \qquad (7)$$

The optimum values obtained for the parameters of the semimicroscopic folding model are given in Table 2. The dependence of the parameters of the semimicroscopic folding model on the energy E_α is illustrated in Fig. 4.

Table 4. Parameters of the semimicroscopic alpha-particle-interaction potential, volume integrals $-J_V$, and rms radii $\langle r^2_{\rm SFM}\rangle^{1/2}$ of the folded potentials for the $A = 12$–124 nuclei at $E_\alpha = 50.5$ MeV

Nucleus	φ_v	N_w	φ_w	$-J_V$, 10^3 MeV fm^3	$\langle r^2_{\rm SFM}\rangle^{1/2}$, fm
^{12}C	0	0.37	0	17.36	3.45
^{24}Mg	0	0.27	0.012	30.82	3.77
^{28}Si	0	0.26	0.010	41.16	3.99
^{48}Ti	0	0.25	0	60.40	4.27
^{50}Ti	0	0.26	0.021	62.75	4.30
^{58}Ni	−0.011	0.22	0.012	80.13	4.50
^{68}Zn	−0.015	0.21	0.022	93.95	4.69
^{70}Zn	−0.010	0.24	0.023	96.69	4.73
^{90}Zr	0.052	0.11	0.010	123.9	4.99
^{94}Zr	0.053	0.13	0.010	129.6	5.07
^{120}Sn	0.051	0.104	0.007	165.2	5.39
^{124}Sn	0.051	0.13	0.007	170.5	5.44

For the $A = 90$ nucleus being considered, the rms radii (Table 2) of the folded potentials change insignificantly with increasing alpha-particle energy.

From the data in Table 2, one can see that the parameter φ_v increases as the energy of scattered alpha particles increases up to 50.1 MeV; at higher energies, we have $\varphi_v = 0$ everywhere, with the exception of the points at 99.5 and 141.5 MeV. The parameter N_w grows gradually with increasing energy. The parameter φ_w vanishes at the energies of 31.0 and 35.4 MeV; at higher energies, it increases monotonically in the energy range from 40.0 to 99.5 MeV by a factor of about 2.7 and then decreases at the energies of 118.0 and 141.5 MeV.

The least squares approximation of the parameter φ_v by an analytic function of the energy E_α (Fig. 4*a*) has the form

$$\varphi_v = -0.111 + 0.0076E_\alpha - 0.0001E_\alpha^2 \qquad (8)$$

at energies up to 65 MeV and the form

$$\varphi_v = -0.0017 + 0.00016E_\alpha \qquad (9)$$

at energies above 65 MeV. For the parameter N_w, we obtained a linear dependence on the energy E_α (Fig. 4*b*):

$$N_w = 0.023 + 0.003E_\alpha \qquad (10)$$

at energies up to 110 MeV and

$$N_w = 0.481 - 0.0012E_\alpha \qquad (11)$$

at energies above 110 MeV.

The analytic approximation of the parameter φ_w by a linear function of the energy E_α (Fig. 4*c*) has the form

$$\varphi_w = -0.0036 + 0.0004E_\alpha \qquad (12)$$

at energies up to 80 MeV and

$$\varphi_w = 0.044 - 0.0002E_\alpha \qquad (13)$$

at energies above 80 MeV.

3.3. Mass Dependence

3.3.1. Mass dependence at low energies

At low energies, the mass dependence of the parameters of the semimicroscopic folding model was studied for the scattering of alpha particles having an energy of about 50.5 MeV and interacting with ^{12}C, ^{24}Mg, ^{28}Si, ^{48,50}Ti, ^{58}Ni, ^{68,70}Zn, ^{90,94}Zr, and ^{120,124}Sn nuclei. This was done on the basis of experimental data reported in [11, 14, 16, 18, 20] and obtained at the isochronous cyclotron of the Institute of Nuclear Physics at the National Nuclear Center of the Republic of Kazakhstan. We used the same algorithm for fitting the parameters of the semimicroscopic folding model as in analyzing the energy dependence.

One can clearly see from Fig. 5 that the description of the experimental angular distributions for the elastic scattering of 50.5-MeV alpha particles on $A = 12$–124 nuclei is quite satisfactory.

In the alpha-particle-energy region being studied, the trend of the variation of available experimental values of the total reaction cross sections σ_R versus the mass number A is well described with the resulting set of semimicroscopic-folding-model parameters (Fig. 6). For want of measured data on σ_R at $E_\alpha \sim 50.5$ MeV, the experimental values of σ_R at the energies of 40 and 69.6 MeV from [22] and [25], respectively, were used to test its mass dependence. From Fig. 6, one can see that the theoretical dependence of σ_R agrees satisfactorily with the aforementioned experimental data.

In Table 3, the rms radii of the neutron-, proton-, and nuclear-matter-density distributions are presented for target nuclei, along with the differences Δr_{np}. One can see that, for the ^{12}C, ^{24}Mg, and ^{28}Si nuclei, the rms radii of the proton-density distributions exceed the rms radii of the neutron-density distributions, while, for remaining ($A = 48$–124) nuclei, with the exception of the ^{58}Ni nucleus, we have the inverse situation.

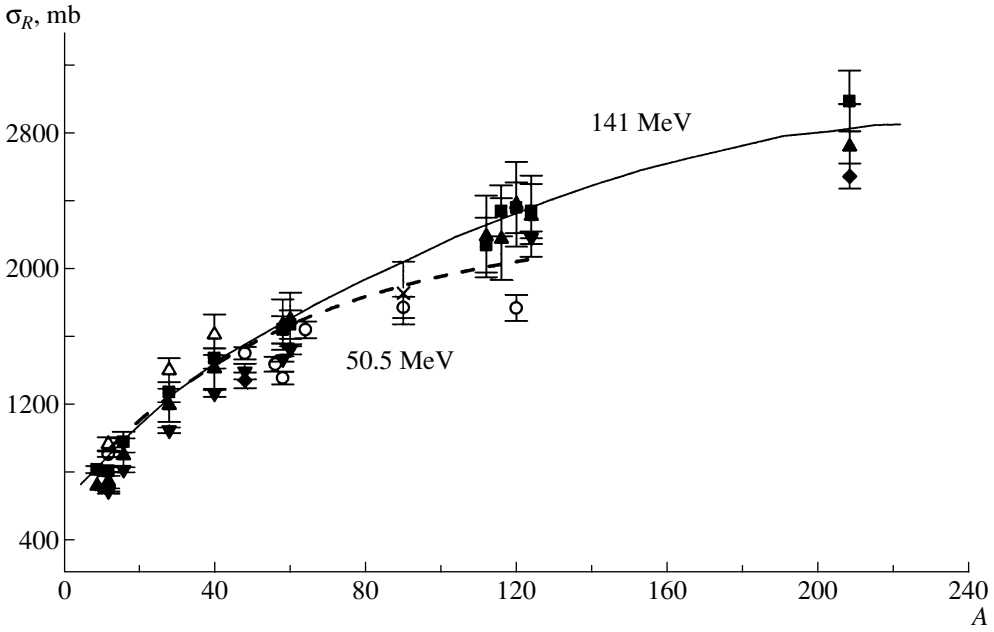

Fig. 6. Total cross sections for the reactions of alpha particles with $A = 12$–208 target nuclei at $E_\alpha =$ (dashed curve) 50.5 and (solid curve) 141 MeV according to the calculations within the semimicroscopic folding model. The displayed experimental data were obtained at (open circles) 40 MeV [22], (right open triangles) 69.6 MeV [25], (closed boxes) 117.2 MeV [25], (inverted closed triangles) 129.3 MeV [25], (closed diamonds) 159.7 MeV [25], (right closed triangles) 163.9 MeV [25], and (crosses) 96 MeV [11].

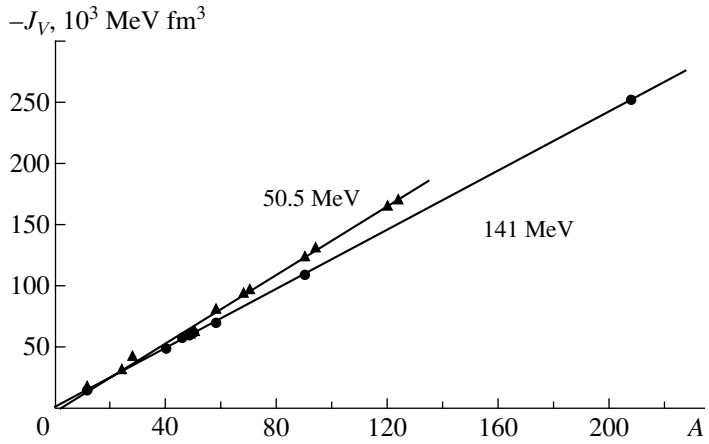

Fig. 7. Volume integral J_V of the real part of the semimicroscopic potential as a function of the mass number: (closed triangles and circles) results of the calculation within the semimicroscopic folding model at, respectively, 50.5 and 141 MeV and (straight lines) approximation by a linear dependence.

In Table 4, the optimum parameter values and the integrated properties of the potentials describing the interaction of 50.5-MeV alpha particles with $A = 12$–124 nuclei are given according to calculations within the semimicroscopic folding model. One can see that the volume integral J_V (in 10^3 MeV fm^3 units) increases in magnitude with increasing mass number at a fixed projectile energy E_α. Analytically, this dependence can be represented in the form (Fig. 7)

$$-J_V = -1.420 + 1.386A. \qquad (14)$$

The rms radii (Table 4) of the folded potentials also increase with increasing mass number A at the energy of $E_\alpha = 50.5$ MeV.

It was established that there is no significant correlation between the parameters of the semimicroscopic folding model and that the parameter set presented in Table 4 is optimal for each target nucleus.

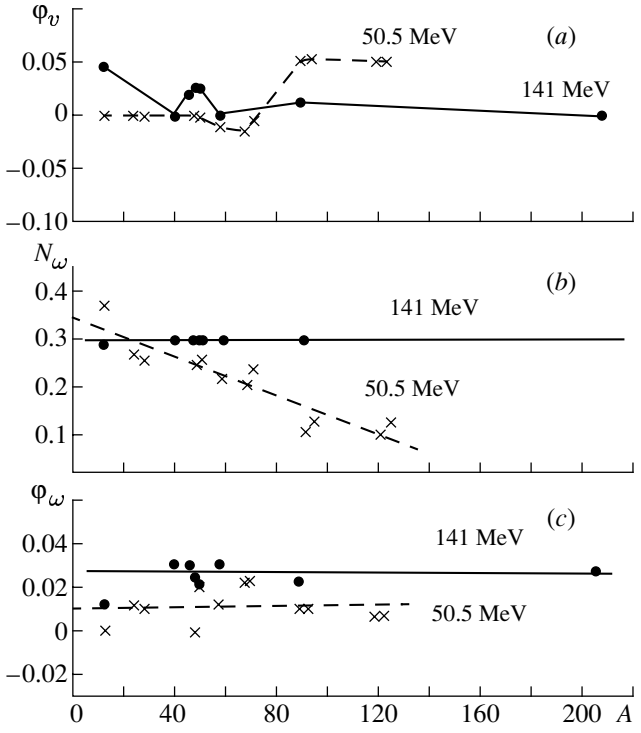

Fig. 8. Mass dependence of the parameters of the potential obtained on the basis of the semimicroscopic folding model. The crosses and closed circles represent results of the calculation within this model at the energies of 50.5 and 141 MeV, respectively. The broken lines in Fig. 8*a* correspond to the mass dependence of the parameter φ_v (see main body of the text); the straight lines in Figs. 8*b* and 8*c* are the approximations of the parameters N_w and φ_w, respectively, by a linear dependence.

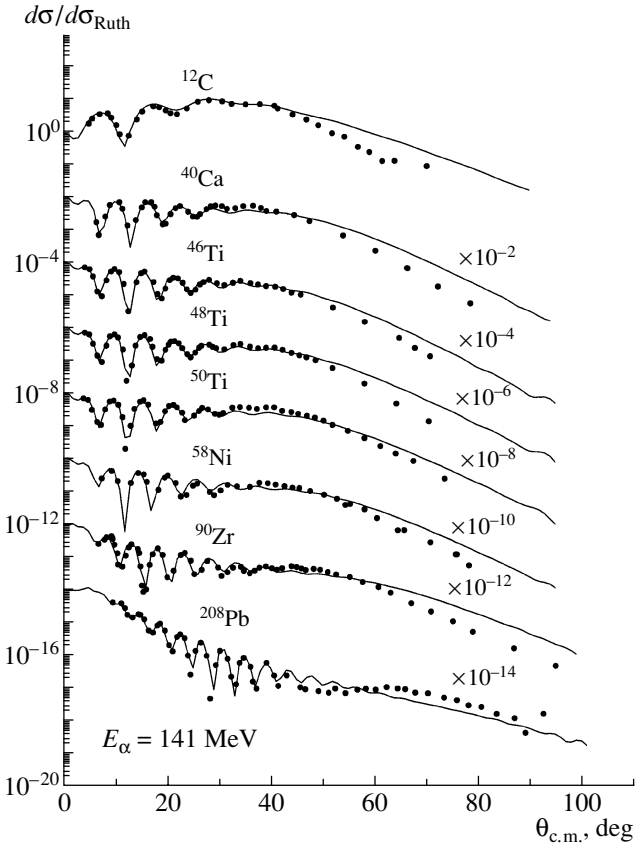

Fig. 9. Angular distributions of the differential cross sections for elastic alpha-particle scattering on $A = 12$–208 nuclei at $E_\alpha \sim 141$ MeV: (points) experimental data and (curves) results based on the semimicroscopic folding model.

The parameter φ_v affects the phase shifts to the right or to the left in the angular distribution, depending on the sign of this parameter. With increasing mass number of the target nucleus, the trend of the variation of the parameter φ_v at $E_\alpha = 50.5$ MeV is as follows (Fig. 8*a*): for the $A = 12$–50 target nuclei, the parameter φ_v vanishes—that is, there is no phase shift; for the $A = 58$–70 target nuclei, the parameter φ_v is negative—that is, the theoretical curve would be shifted to the right with respect to experimental points if the parameter φ_v were absent; and for medium-mass nuclei ($A = 90$–124), the parameter φ_v is on the contrary positive, leading to a shift to the left. Tracing the variation in the parameters of the imaginary part of the potential, one would observe their monotonic decrease. Since the mass-number dependence of the parameter φ_v at the fixed energy of $E_\alpha = 50.5$ MeV is complicated, we perform an interpolation of its optimum values in Fig. 8*a*. An analytic approximation of the parameters N_w and φ_w by a linear function of the mass number A (Figs. 8*b*, 8*c*) was constructed by the least squares method. The result is

$$N_w = 0.3469 - 0.0021A, \qquad (15)$$
$$\varphi_w = 0.01030 - 0.00001A.$$

3.3.2. Mass dependence at intermediate energies

In the region of intermediate energies, the mass dependence of the parameters of the semimicroscopic folding model for alpha particles of energy $E_\alpha \sim 141$ MeV that interact with ^{12}C, ^{40}Ca, ^{46,48,50}Ti, ^{58}Ni, ^{90}Zr, and ^{208}Pb nuclei were obtained on the basis of experimental data borrowed from [13, 15, 17, 19].

From Fig. 9, one can see that the results of theoretical calculations agree well with experimental data on the differential cross sections for the elastic scattering of alpha particles of energy about 141 MeV on $A = 12$–208 nuclei.

As in the case of the calculations at the energy of 50.5 MeV, the theoretical values obtained for the total reaction cross sections σ_R within the semimicroscopic folding model at an energy of $E_\alpha \sim 141$ MeV

Table 5. Rms radii (in femtometers) of the neutron-, proton-, and nuclear-matter-density distributions for the $A = 12$–208 nuclei (also given here are the differences $\Delta r_{np} = \langle r_n^2\rangle^{1/2} - \langle r_p^2\rangle^{1/2}$ at $E_\alpha \sim 141$ MeV)

Nucleus	$\langle r_n^2\rangle^{1/2}$	$\langle r_p^2\rangle^{1/2}$	$\langle r_m^2\rangle^{1/2}$	Δr_{np}
^{12}C	2.40	2.41	2.40	−0.01
^{40}Ca	3.34	3.38	3.36	−0.04
^{46}Ti	3.70	3.68	3.69	0.02
^{48}Ti	3.73	3.69	3.71	0.04
^{50}Ti	3.75	3.69	3.72	0.06
^{58}Ni	3.76	3.76	3.76	0.00
^{90}Zr	4.26	4.19	4.23	0.07
^{208}Pb	5.60	5.44	5.54	0.16

Table 6. Parameters of semimicroscopic alpha-particle-interaction potential, volume integrals $-J_V$, and rms radii $\langle r_{\mathrm{SFM}}^2\rangle^{1/2}$ of the folded potentials for the $A = 12$–208 nuclei at $E_\alpha \sim 141$ MeV

Nucleus	φ_v	N_w	φ_w	$-J_V$, 10^3 MeV fm^3	$\langle r_{\mathrm{SFM}}^2\rangle^{1/2}$, fm
^{12}C	0.045	0.30	0.012	15.15	3.504
^{40}Ca	0	0.30	0.03	49.31	4.273
^{46}Ti	0.02	0.30	0.03	57.78	4.258
^{48}Ti	0.026	0.30	0.025	60.08	4.550
^{50}Ti	0.026	0.30	0.022	62.30	4.563
^{58}Ni	0	0.30	0.03	71.27	4.603
^{90}Zr	0.013	0.30	0.022	109.3	5.021
^{208}Pb	0	0.30	0.027	253.3	6.203

are in satisfactory agreement with available experimental data on the total reaction cross sections at the energies of 117.2, 129.3, 159.7, and 163.9 MeV from [25] (see Fig. 6).

In Table 5, the rms radii of the neutron-, proton-, and nuclear-matter-density distributions are presented for target nuclei along with the differences Δr_{np}. These results were obtained on the basis of the semimicroscopic folding model at $E_\alpha \sim 141$ MeV. One can see that, for the ^{12}C and ^{40}Ca nuclei, the rms radii of the proton-density distributions exceed the rms radii of the neutron-density distributions, while, for the remaining ($A = 46$–208) nuclei, with the exception of the ^{58}Ni nucleus, the situation is inverse.

For the parameters of the semimicroscopic folding model, Table 6 gives values that leads to the best agreement with experimental data at an energy of $E_\alpha \sim 141$ MeV. The integrated properties of the interaction potentials are also presented there.

One can see from Table 6 that the trends of the variation in the volume integral J_V and in the rms radii at $E_\alpha \sim 141$ MeV are similar to those at low energies.

The mass-number dependence of the volume integral J_V (in 10^3 MeV fm^3 units) can be represented in a linear form (Fig. 7),

$$-J_V = 1.228 + 1.211A. \qquad (16)$$

At intermediate energies, the parameter φ_v decreases with increasing mass number of target nuclei from the interval $A = 12$–208 (Fig. 8*a*). The parameter N_w does not change. Figure 8*a* shows an interpolation of the mass-number dependence of the optimum values of the parameter φ_v at the fixed energy of $E_\alpha \sim 141$ MeV. The least squares analytic approximations of the parameters N_w and φ_w by a linear function of the mass number A (Fig. 8*b*, 8*c*) have the form

$$N_w = 0.3, \quad \varphi_w = 0.027 - 0.000006A. \qquad (17)$$

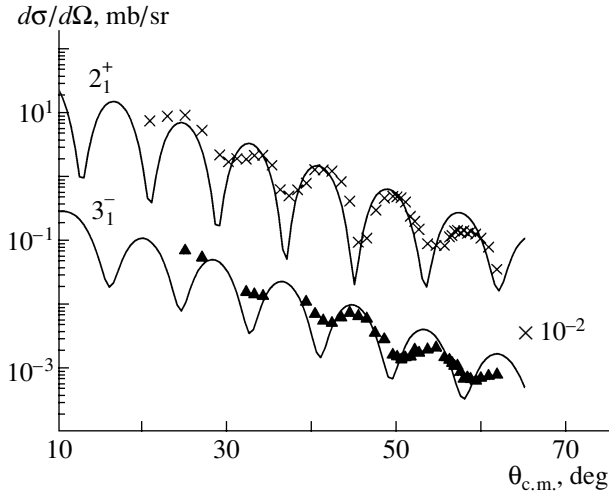

Fig. 10. Angular distributions of the cross sections for inelastic alpha-particle scattering on ^{124}Sn nuclei that is accompanied by the excitation of the low-lying states at 1.130 MeV (2_1^+) and 2.530 MeV (3_1^-): (crosses and closed triangles) experimental data at $E_\alpha = 50.5 \pm 0.5$ MeV and (curves) respective results of the calculations based on the semimicroscopic folding model.

4. APPLICATION TO INELASTIC SCATTERING

Within the semimicroscopic folding model, we have obtained a good description of the differential and total reaction cross sections and the trend of the variation in the volume integral of the folded potential. We have verified how the resulting generalized potential describes the experimental angular distributions for inelastic alpha-particle scattering. In testing the global dependences of the parameters of the semimicroscopic folding model, we have obtained quite a satisfactory description of the angular distributions for inelastic scattering accompanied by the excitation of low-lying collective nuclear states for the example of the ^{124}Sn isotope (Fig. 10).

5. CONCLUSIONS

In this study, the energy and mass dependences of the parameters of the semimicroscopic folding model for the interactions of low- and intermediate-energy alpha particles with a broad class of $A = 12$–208 nuclei have been obtained for the first time. In order to construct these dependences, we have performed a global analysis of a set of experimental data that includes angular distributions for scattering processes, total reaction cross sections, and the trend of the variation in the volume integrals. This has made it possible to perform a global search for unified parameters of the semimicroscopic folding model in the energy range under consideration. From our analysis, it has been found that the semimicroscopic folding model reproduces quite well the shape and the magnitude of the differential and total cross sections for the reactions on $A = 12$–208 nuclei over the entire angular range at low and intermediate energies of incident alpha particles. We note that, for composite particles, the identification and localization of the parameters of the semimicroscopic folding model can be performed in a reasonable approximation by using the criteria indicated above.

ACKNOWLEDGMENTS

We are grateful to S.A. Fayans† for support of this study.

This work was supported in part by the Russian Foundation for Basic Research (project no. 03-01-00657).

†Deceased.

REFERENCES

1. G. R. Satchler, *Direct Nuclear Reactions* (Oxford Univ. Press, New York, 1983).
2. S. A. Fayans, O. M. Knyazkov, I. N. Kuchtina, *et al.*, Phys. Lett. B **357**, 509 (1995).
3. O. M. Knyazkov, A. A. Kolozhvari, I. N. Kuchtina, and S. A. Fayans, Yad. Fiz. **59**, 466 (1996) [Phys. At. Nucl. **59**, 439 (1996)].
4. D. B. Bolotov, O. M. Knyazkov, I. N. Kuchtina, and S. A. Fayans, Yad. Fiz. **63**, 1631 (2000) [Phys. At. Nucl. **63**, 1546 (2000)].
5. L. W. Put and A. M. J. Paans, Nucl. Phys. A **291**, 93 (1977).
6. O. M. Knyazkov, I. N. Kuchtina, and S. A. Fayans, Phys. Part. Nucl. **30**, 870 (1999); **28**, 1061 (1997).
7. A. B. Smirnov, S. V. Tolokonnikov, and S. A. Fayans, Yad. Fiz. **48**, 1661 (1988) [Sov. J. Nucl. Phys. **48**, 995 (1988)]; S. A. Fayans, A. P. Platonov, G. Graw, and D. Hofer, Nucl. Phys. A **577**, 557 (1994); S. A. Fayans, S. V. Tolokonnikov, E. L. Trykov, and D. Zawischa, Phys. Lett. B **338**, 1 (1994).
8. M. Wit, J. Schiele, and K. A. Eberhard, Phys. Rev. C **12**, 1447 (1975).
9. E. J. Martens and A. M. Bernstein, Nucl. Phys. A **117**, 241 (1968).
10. D. Rychel, R. Gyufko, B. van Kruchten, *et al.*, Z. Phys. A **326**, 455 (1987); B. J. Lund, N. P. T. Bateman, S. Utku, *et al.*, Phys. Rev. C **51**, 635 (1995).
11. A. D. Duisebaev, K. A. Kuterbekov, I. N. Kuchtina, *et al.*, Yad. Fiz. **66**, 627 (2003) [Phys. At. Nucl. **66**, 599 (2003)].
12. C. R. Bingham, M. L. Halbert, and R. H. Bassel, Phys. Rev. **148**, 1174 (1966).
13. D. A. Goldberg, S. M. Smith, and G. F. Burdzik, Phys. Rev. C **10**, 1362 (1974).
14. N. Burtebaev, A. Duisebaev, G. N. Ivanov, *et al.*, Preprint No. 88-01, IYaF AN KazSSR (Inst. Nucl. Phys., Akad. Nauk KazSSR, Alma-Ata, 1988); N. N. Pavlova, S. Ya. Aisina, K. A. Kuterbekov, *et al.*, Preprint IYaF AN KazSSR (Inst. Nucl. Phys., Akad. Nauk KazSSR, Alma-Ata, 1990); K. A. Kuterbekov, S. Ya. Aisina, N. N. Pavlova, *et al.*, Preprint, IYaF AN KazSSR (Inst. Nucl. Phys., Akad. Nauk KazSSR, Alma-Ata, 1991).
15. S. M. Smith, G. Tibell, A. A. Cowley, *et al.*, Nucl. Phys. A **207**, 273 (1973).
16. A. D. Duisebaev, N. Burtebaev, and G. N. Ivanov, Izv. Akad. Nauk KazSSR, Ser. Fiz.-Mat., No. 6, 49 (1984).
17. P. L. Robertson, D. A. Goldberg, N. S. Wall, *et al.*, Phys. Rev. Lett. **42**, 54 (1979).
18. K. A. Kuterbekov, A. D. Duisebaev, and N. Burtebaev, Izv. Akad. Nauk, Ser. Fiz. **59**, 112 (1995).
19. D. A. Goldberg, S. M. Smith, H. G. Pugh, *et al.*, Phys. Rev. C **7**, 1938 (1973).
20. N. T. Burtebaev, K. A. Kuterbekov, and I. N. Kukhtina, Yad. Fiz. **51**, 1301 (1990) [Sov. J. Nucl. Phys. **51**, 827 (1990)].
21. A. Duisebaev, B. A. Duisebaev, K. M. Ismailov, *et al.*, Izv. Minist. Nauki i Obraz. - Akad. Nauk Resp. Kaz., Ser. Fiz.-Mat., No. 2, 104 (2002).

22. G. Igo and B. Wilkins, Phys. Rev. **131**, 1251 (1963).
23. R. M. DeVries and J. C. Peng, Phys. Rev. C **22**, 1055 (1980).
24. G. Hauser, R. Lohken, R. Rebel, *et al.*, Nucl. Phys. A **128**, 81 (1969).
25. A. Auce, R. F. Carlson, A. J. Cox, *et al.*, Phys. Rev. C **50**, 871 (1994); A. Ingemarson, J. Nyberg, P. U. Renberg, *et al.*, Nucl. Phys. A **676**, 3 (2000).
26. A. K. Ghaudhuri, D. N. Basu, and B. Sinha, Nucl. Phys. A **439**, 415 (1985).
27. I. Tanihata, T. Kobayashi, O. Yamakawa, *et al.*, Phys. Lett. B **206**, 592 (1988).
28. J. Raynal, Phys. Lett. B **196**, 7 (1987).
29. M. Nolte, H. Machner, and J. Bojowald, Phys. Rev. C **36**, 1312 (1987).
30. R. B. Firestone, *Table of Isotopes*, 8th ed. (Wiley, New York, 1999).
31. D. J. Horen, G. R. Satchler, S. A. Fayans, and E. L. Trykov, Nucl. Phys. A **600**, 193 (1996).
32. C. Mahaux and R. Sartor, Nucl. Phys. A **568**, 1 (1994).
33. E. A. Romanovsky, O. V. Bespalova, S. A. Goncharov, *et al.*, Yad. Fiz. **63**, 468 (2000) [Phys. At. Nucl. **63**, 399 (2000)].
34. O. V. Bespalova, E. A. Romanovsky, and T. I. Spasskaya, Izv. Akad. Nauk, Ser. Fiz. **67**, 66 (2003).
35. E. Gadioli and P. E. Hodgson, *Pre-Equilibrium Nuclear Reaction* (Oxford Univ., New York, 1992).
36. K. A. Kuterbekov, I. N. Kukhtina, T. K. Zholdybayev, *et al.*, Preprint No. E7-2002-220, JINR (Joint Inst. Nucl. Res., Dubna, 2002).

Translated by A. Isaakyan

Physics of Atomic Nuclei, Vol. 68, No. 6, 2005, pp. 940–947. Translated from Yadernaya Fizika, Vol. 68, No. 6, 2005, pp. 978–985.
Original Russian Text Copyright © 2005 by Berezhnoy, Mikhailyuk, Pilipenko.

NUCLEI
Theory

Elastic and Inelastic Scattering of 800-MeV Protons on ^{16}O and ^{20}Ne Nuclei

Yu. A. Berezhnoy, V. P. Mikhailyuk[1)], and V. V. Pilipenko[2)]

Kharkov National University, pl. Svobody 4, Kharkov, 61077 Ukraine

Received October 9, 2003; in final form, May 7, 2004

Abstract—Differential cross sections and polarization observables for the elastic and inelastic scattering of 800-MeV protons on ^{16}O and ^{20}Ne nuclei are calculated on the basis of the theory of multiple diffractive scattering and the α-cluster model involving dispersion. The single-particle nucleon-density distributions obtained within the α-cluster model involving dispersion are used in the calculations. The differential cross sections and polarization calculated for elastic and inelastic p^{16}O and p^{20}Ne scattering are compatible with available experimental data. The spin-rotation functions calculated for elastic p^{16}O and p^{20}Ne scattering within the independent-nucleon model differ qualitatively from their counterparts calculated within the α-cluster model involving dispersion. © *2005 Pleiades Publishing, Inc.*

At the present time, cluster models are being successfully employed in various microscopic theories (see, for example, [1–3] and references therein). A cluster structure manifests itself in a number of light nuclei. The ^{12}C nucleus is the most well known α-cluster nucleus. A cluster structure also manifests itself in the ^{9}Be [4–6], ^{13}C [7], ^{16}O [3, 8, 9], and ^{20}Ne [10–12] nuclei.

In the simplest version of the α-cluster model, it is assumed that the positions of the alpha particles in a nucleus are fixed [13]. The possible exchange of nucleons between the alpha-particle clusters and the antisymmetrization of nuclear wave functions over all filled nucleon states are taken into account in a more realistic alpha-particle model [14].

In [8, 9, 11, 15], the α-cluster model involving dispersion was proposed for the ^{12}C, ^{16}O, and ^{20}Ne nuclei. It is assumed in this model that the carbon and oxygen nuclei consist of three and four α-particle clusters located at the vertices of an equilateral triangle and a regular tetrahedron, respectively. These alpha-particle clusters can execute vibrations with respect to their most probable equilibrium positions at the vertices of the above geometric bodies.

Two approaches were proposed in [11, 12] for describing the properties of the ^{20}Ne nucleus. The neon nucleus was considered to consist of a core (^{16}O nucleus) and a complementary alpha-particle cluster, which occurs, with the highest probability, within or beyond the core.

On the basis of the α-cluster model involving dispersion and the theory of multiple diffractive scattering, various observables for particles of energy in the region $E \geq 100$ MeV per nucleon that are elastically scattered by ^{12}C, ^{16}O, and ^{20}Ne nuclei were calculated in [8, 9, 11, 12, 15]. The results of the calculations were compatible with available experimental data.

In [8, 9], we also calculated observables for elastic and inelastic proton scattering by ^{12}C and ^{16}O nuclei, relying on the theory of multiple diffractive scattering on target nucleons and employing single-particle nucleon-density distributions determined for these nuclei on the basis of the α-cluster model involving dispersion. In those studies, we showed that the observables calculated on the basis of the α-cluster model involving dispersion are in better agreement with available experimental data than their counterparts determined within the independent-nucleon model, the calculated spin-rotation functions being qualitatively different. In the present study, the approach proposed in [8, 9] is developed for the case of ^{20}Ne nuclei.

According to the α-cluster model involving dispersion, the multiparticle density of the ^{16}O nucleus can be written as

$$\rho_{\Delta}^{(\mathrm{O})}(\boldsymbol{\xi},\boldsymbol{\eta},\boldsymbol{\zeta}) = \int d^3\xi' d^3\eta' d^3\zeta' \rho_0(\boldsymbol{\xi}',\boldsymbol{\eta}',\boldsymbol{\zeta}') \quad (1)$$
$$\times \Phi_{\Delta}(\boldsymbol{\xi}-\boldsymbol{\xi}',\boldsymbol{\eta}-\boldsymbol{\eta}',\boldsymbol{\zeta}-\boldsymbol{\zeta}'),$$

[1)]Institute for Nuclear Research, National Academy of Sciences of Ukraine, pr. Nauki 47, Kiev, 03680 Ukraine.

[2)]Kharkov Institute for Physics and Technology, Akademicheskaya ul. 1, Kharkov, 61108 Ukraine.

1063-7788/05/6806-0940$26.00 © 2005 Pleiades Publishing, Inc.

$$\rho_0(\boldsymbol{\xi},\boldsymbol{\eta},\boldsymbol{\zeta}) = \frac{1}{(4\pi)^2}\delta(\xi-d)\,\delta\left(\eta-\frac{\sqrt{3}}{2}d\right) \quad (2)$$
$$\times\,\delta\left(\zeta-\sqrt{\frac{2}{3}}d\right)\delta(\boldsymbol{\xi}\cdot\boldsymbol{\eta})\delta(\boldsymbol{\xi}\cdot\boldsymbol{\zeta})\delta(\boldsymbol{\eta}\cdot\boldsymbol{\zeta}),$$

$$\Phi_\Delta(\boldsymbol{\xi},\boldsymbol{\eta},\boldsymbol{\zeta}) = \frac{1}{8(\pi\Delta^2)^9} \quad (3)$$
$$\times\exp\left(-\left(\xi^2+\frac{4}{3}\eta^2+\frac{3}{2}\zeta^2\right)\Big/\left(2\Delta^2\right)\right),$$

where $\boldsymbol{\xi},\boldsymbol{\eta},\boldsymbol{\zeta}$ are the Jacobi coordinates of the α clusters of the ^{16}O nucleus. The parameters d and Δ characterize, respectively, the distance between the alpha-particle clusters and the probability of their shift from their most probable equilibrium positions at the vertices of a regular tetrahedron.

The charge form factor of the ^{16}O nucleus is given by the formula

$$F^{(\mathrm{O})}(\mathbf{q}) = \exp\left(-\frac{1}{6}q^2\langle r^2\rangle_\alpha-\frac{3}{16}q^2\Delta^2\right) \quad (4)$$
$$\times\, j_0\left(\sqrt{\frac{3}{8}}qd\right),$$

where $j_0(x)$ is a spherical Bessel function, $\langle r^2\rangle_\alpha^{1/2} = 1.61$ fm is the root-mean-square radius of the alpha-particle clusters forming ^{16}O nucleus, and $\mathbf{q}$ is the momentum transfer. The parameters values of $d = 3.157$ fm and $\Delta = 0.643$ fm, which were obtained in [8, 9], make it possible to describe the measured form factor of the ^{16}O nucleus in the momentum-transfer range $q \le 3$ fm^{-1}.

It is well known that the charge-density distribution within a nucleus is determined by the inverse Fourier transform of the charge form factor. The charge-density distribution within the ^{16}O nucleus can be represented in the form

$$\rho^{(\mathrm{O})}(r) = \frac{1}{4r\beta\sqrt{\pi^3\alpha}}\sinh\left(\frac{r\beta}{2\alpha}\right)\exp\left(-\frac{r^2+\beta^2}{4\alpha}\right), \quad (5)$$

where $\alpha = \frac{1}{6}\langle r^2\rangle_\alpha + \frac{3}{16}\Delta^2$ and $\beta = \sqrt{\frac{3}{8}}d$.

In [11], the ^{20}Ne nucleus was treated as that which consists of a core in the form of a ^{16}O nucleus (its size differs from the size of the free ^{16}O nucleus) and a complementary alpha-particle cluster, which occurs, with the highest probability, within the core. In this approach, the multiparticle density of the ^{20}Ne nucleus can be represented in the form

$$\rho_\Delta^{(\mathrm{Ne})}(\boldsymbol{\xi},\boldsymbol{\eta},\boldsymbol{\zeta},\boldsymbol{\chi}) = \rho_\Delta^{(\mathrm{O})}(\boldsymbol{\xi},\boldsymbol{\eta},\boldsymbol{\zeta})\rho_\alpha(\boldsymbol{\chi}), \quad (6)$$

where $\boldsymbol{\chi}$ is the coordinate of the complementary alpha-particle cluster. The density of the complementary alpha-particle cluster $\rho_\alpha(\boldsymbol{\chi})$ is

$$\rho_\alpha(\boldsymbol{\chi}) = \frac{1}{(\lambda\sqrt{\pi})^3}\exp\left(-\frac{\chi^2}{\lambda^2}\right), \quad (7)$$

where the parameter λ characterizes the shift of the complementary alpha-particle cluster from the center of mass of the core.

In this approach, the elastic-scattering form factor for the ^{20}Ne nucleus can be represented in the form [11]

$$F^{(\mathrm{Ne})}(\mathbf{q}) = \exp\left(-\frac{1}{6}q^2\langle r^2\rangle_\alpha\right) \quad (8)$$
$$\times\left[\frac{4}{5}\exp\left(-\frac{3}{16}q^2\Delta^2\right)j_0\left(\sqrt{\frac{3}{8}}qd\right)\right.$$
$$\left.+\,\frac{1}{5}\exp\left(-\frac{q^2\lambda^2}{4}\right)\right].$$

The charge-density distribution in the ^{20}Ne nucleus is given by

$$\rho_1(r) = \frac{4}{5}\rho^{(\mathrm{O})}(r) + \frac{1}{40(\pi\alpha')^{3/2}}\exp\left(-\frac{r^2}{4\alpha'}\right), \quad (9)$$

where $\alpha' = \frac{1}{6}\langle r^2\rangle_\alpha + \frac{1}{4}\lambda^2$.

The values of the core (^{16}O nucleus) parameters d and Δ differ from those obtained in [8, 9] for the free ^{16}O nucleus. Comparing the calculated and measured form factors for the ^{20}Ne nucleus, we obtained the following values for the parameters of the α-cluster density: $d = 3.595$ fm, $\Delta = 0.998$ fm, and $\lambda = 1.7$ fm.

We note that, for the ^{20}Ne nucleus, one can choose a number of configurations that make it possible to obtain an analytic expression for the amplitude of elastic particle scattering by ^{20}Ne nuclei within the α-cluster model involving dispersion. In [12], the ^{20}Ne nucleus was considered as that which is formed by a core and a supplementary alpha-particle cluster, which occurs, with the highest probability, beyond the core.

In this approach, the multiparticle density in the ^{20}Ne nucleus has the form (6), while the density $\rho_\alpha(\boldsymbol{\chi})$ is

$$\rho_\alpha(\boldsymbol{\chi}) = \frac{2}{3\mu^5\pi^{3/2}}\chi^2\exp\left(-\frac{\chi^2}{\mu^2}\right), \quad (10)$$

where the parameter μ characterized the shift of the complementary alpha-particle cluster from the center of mass of the core.

Parameters of the nucleon–nucleon amplitude

	g_c, fm^2	h_c, fm^4	a_c, fm^2	g_s, fm^3	h_s, fm^5	a_s, fm^2
pp	$2.336 + 0.023i$	$0.064 + 0.248i$	0.199	$0.541 - 0.205i$	-0.0392	0.053
pn	$1.863 + 0.553i$	$0.044 + 0.204i$	0.202	$0.436 - 0.249i$	-0.0035	0.137

In this case, the charge form factor of the ^{20}Ne nucleus is

$$F^{(\mathrm{Ne})}(\mathbf{q}) = \exp\left(-\frac{1}{6}q^2\langle r^2\rangle_\alpha\right) \times \left[\frac{4}{5}\exp\left(-\frac{3}{16}q^2\Delta^2\right) j_0\left(\sqrt{\frac{3}{8}}qd\right) + \frac{1}{5}\left(1-\frac{1}{6}q^2\mu^2\right)\exp\left(-\frac{q^2\mu^2}{4}\right)\right], \quad (11)$$

while the charge-density distribution in the ^{20}Ne nucleus has the form

$$\rho_2(r) = \frac{4}{5}\rho^{(\mathrm{O})}(r) + \frac{1}{40(\pi\alpha'')^{3/2}} \times \left[1-\frac{\mu^2}{4\alpha''}\left(1-\frac{r^2}{6\alpha''}\right)\right]\exp\left(-\frac{r^2}{4\alpha''}\right), \quad (12)$$

where $\alpha'' = \frac{1}{6}\langle r^2\rangle_\alpha + \frac{1}{4}\mu^2$. The parameters of the α-cluster density in the ^{20}Ne nucleus, which were found in this approach from a comparison of the calculated and measured form factors of this nucleus, are $d = 3.848$ fm, $\Delta = 0.853$ fm, and $\mu = 1.06$ fm.

The single-particle nucleon-density distribution $\rho(\mathbf{r})$ in the ^{16}O and ^{20}Ne nuclei can be determined by formulas (5), (9), and (12), in which it is necessary to consider that nucleons have finite sizes. This can be done approximately by changing, in these formulas, the quantity $\langle r^2\rangle_\alpha$ by $\langle r^2\rangle_\alpha - \langle r^2\rangle_p$, where $\langle r^2\rangle_p^{1/2} = 0.814$ fm is the root-mean-square proton radius.

According to the theory of multiple diffractive scattering, the amplitude for proton scattering by a nucleus of mass number A has the form

$$F(\mathbf{q}) = \frac{ik}{2\pi}\int d^2b\exp(i\mathbf{q}\cdot\mathbf{b})\,\langle f|[1-\Omega(\mathbf{b};\{\mathbf{s}_j\})]|i\rangle\,, \quad (13)$$

$$\Omega(\mathbf{b},\{\mathbf{s}_j\}) = \prod_{j=1}^{A}\Omega_j(\mathbf{b}-\mathbf{s}_j), \quad (14)$$

$$\Omega_j(\mathbf{b}) = 1 - \frac{1}{2\pi ik}\int d^2q\exp(i\mathbf{q}\cdot\mathbf{b})f_j(\mathbf{q}), \quad (15)$$

where k is the wave vector; $\mathbf{b}$ is the impact parameter lying in the plane orthogonal to the incident-beam axis; $\mathbf{s}_j$ is the projection of the radius vector $\mathbf{r}_j$ of the jth scatterer onto this plane; $|f\rangle$ and $|i\rangle$ are the vectors of, respectively, the initial and the final state of the nucleus; and $f_j(\mathbf{q})$ is the amplitude of nucleon–nucleon scattering.

Disregarding small charge-exchange effects—that is, considering separately the amplitudes for proton–proton and proton–neutron scattering—and omitting spin–spin terms in the nucleon–nucleon amplitude, we can represent the amplitude $f_j(\mathbf{q})$ in the form

$$f_j(\mathbf{q}) = f_{c,j}(\mathbf{q}) + qf_{s,j}(\mathbf{q})(\boldsymbol{\sigma}\cdot\mathbf{n}), \quad (16)$$

$$f_{c,j}(\mathbf{q}) = \frac{ik}{2\pi}(g_{c,j} + h_{c,j}q^2)\exp(-a_{c,j}q^2), \quad (17)$$

$$f_{s,j}(\mathbf{q}) = \frac{ik}{2\pi}(g_{s,j} + h_{s,j}q^2)\exp(-a_{s,j}q^2), \quad (18)$$

where $\boldsymbol{\sigma}$ is the spin operator of the incident proton; $\mathbf{n} = [\mathbf{k}\times\mathbf{k}']/|[\mathbf{k}\times\mathbf{k}']|$; and $\mathbf{k}$ and $\mathbf{k}'$ are the wave vectors of, respectively the incident and the scattered proton.

For the parameters of the amplitude given by Eqs. (16)–(18), we took, in our calculations, values that were obtained in [16] from a partial-wave analysis of elastic nucleon–nucleon scattering. The values of the parameters of the nucleon–nucleon amplitude are given in the table.

The amplitude for elastic proton scattering on the nucleus characterized by the mass number A and the charge number Z can be represented in the form

$$F(\mathbf{q}) = \frac{ik}{2\pi}\exp\left(\frac{q^2}{4\gamma A}\right) \times \int d^2b\exp(i\mathbf{q}\cdot\mathbf{b})\,[1-\Omega(\mathbf{b})]\,, \quad (19)$$

$$\Omega(\mathbf{b}) = [1-E_p(\mathbf{b})]^Z\,[1-E_n(\mathbf{b})]^N\,. \quad (20)$$

Here, $N = A - Z$; $\gamma = 0.358$ fm^{-2} for the ^{16}O nucleus and $\gamma = 0.293$ fm^{-2} for the ^{20}Ne nucleus; and the functions $E_j(\mathbf{b})(j = p, n)$ are given by

$$E_j(\mathbf{b}) = \frac{1}{2\pi ik}\int d^2q\exp(-i\mathbf{q}\cdot\mathbf{b})f_j(\mathbf{q})S(\mathbf{q}), \quad (21)$$

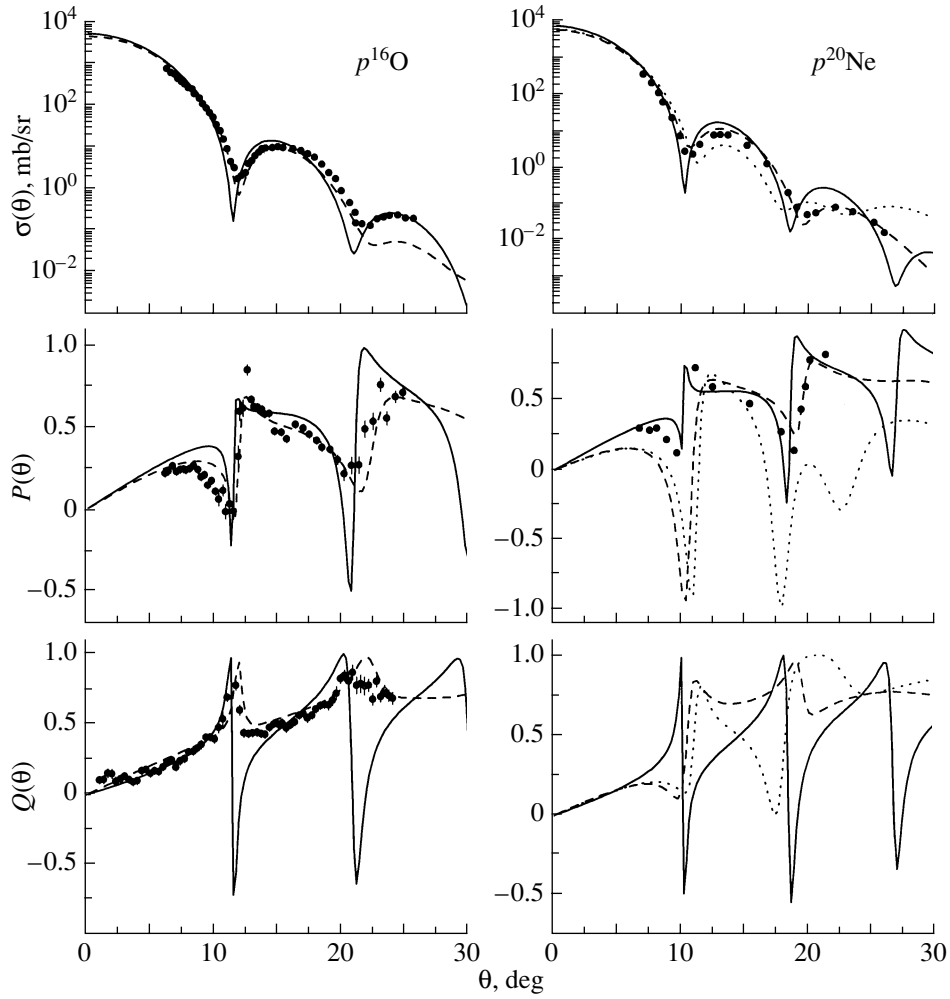

Fig. 1. Differential cross sections $\sigma(\theta)$ and polarization observables $P(\theta)$ and $Q(\theta)$ for the elastic scattering of 800-MeV protons by ^{16}O and ^{20}Ne nuclei. The displayed experimental data were borrowed from [17, 18]. The notation for the curves is explained in the main body of the text.

where the elastic form factor $S(\mathbf{q})$ has the form

$$S(\mathbf{q}) = \int d^3r \exp(i\mathbf{q}\cdot\mathbf{r})\rho(\mathbf{r}). \qquad (22)$$

The nucleon-density distributions characterizing the oxygen and neon nuclei and appearing in (22) are determined by relation (5) for the ^{16}O nucleus and by relation (9) or (12) for the ^{20}Ne nucleus. It should be emphasized that the single-particle densities used in the ensuing calculations for the ^{16}O and ^{20}Ne nuclei do not include any adjustable parameters. The parameters d, Δ, λ, and μ appearing in the expressions for the densities of the ^{16}O and ^{20}Ne nuclei are determined independently from a comparison of the calculated and measured charge form factors of the nuclei in question. Additionally, the expressions used in this study for the single-particle densities in the ^{16}O and ^{20}Ne nuclei were obtained with the aid of the α-cluster model involving dispersion, in contrast to conventional approaches, which employ a direct parametrization of nuclear densities.

On the basis of the developed approach, the differential cross sections $\sigma(\theta) \equiv d\sigma/d\Omega$ [mb/sr], the polarization $P(\theta)$, and the spin-rotation function $Q(\theta)$ were calculated for the elastic scattering of protons of energy $E_p = 800$ MeV by ^{16}O and ^{20}Ne nuclei. The results of these calculations, along with experimental data borrowed from [17, 18], are presented in Fig. 1 (solid curves). In Fig. 1, we also show the same observables computed on the basis of the theory of multiple diffractive scattering and the α-cluster model involving dispersion (dashed curves).

For the ^{20}Ne nucleus, the dashed curves represent the results of calculations where the density $\rho_1(r)$ is used in the form (9)—that is, it is assumed that the

^{20}Ne nucleus is formed by a ^{16}O core and a supplementary alpha-particle cluster, which occurs, with the highest probability, within the core. The dotted curves in Fig. 1 were calculated under the assumption that the supplementary alpha-particle cluster is located, with the highest probability, beyond the core [formulas (6), (10)]. One can see from Fig. 1 that the approach where it is assumed that the supplementary alpha-particle cluster is situated, with the highest probability within the core—that is, it executes vibrations with respect to its most probable position at the core center of mass—enables one to describe correctly the measured observables for elastic proton scattering by ^{20}Ne nuclei.

In performing numerical calculations, we have taken into account the distinctions between the proton–proton and proton–neutron amplitudes. It turns out that the use of an averaged nucleon–nucleon amplitude in similar calculations makes it possible to obtain results that differ only slightly from those given in Fig. 1. Moreover, the use of the averaged nucleon–nucleon amplitude enables one to generalize, quite readily, the approach described above to the case of inelastic proton scattering on nuclei. In the case where use is made of individual proton–proton and proton–neutron amplitudes, such a generalization would involve problems associated with the symmetrization of the expressions for the profile functions $\Omega(\mathbf{b})$ or with their Z ordering [19]. However, it turns out concurrently that the observables of the scattering process that are calculated on the basis of the theory of multiple diffractive scattering with and without allowance for Z ordering differ only slightly.

The averaged nucleon–nucleon amplitude has the form

$$f(\mathbf{q}) = \frac{N}{A} f_n(\mathbf{q}) + \frac{Z}{A} f_p(\mathbf{q}). \tag{23}$$

The transition nuclear density $\rho_{\text{tr}}(\mathbf{r})$ must appear in expressions (13)–(15) if low-lying vibrational states are excited in nuclei. In the case of the excitation of one-phonon states, their orbital angular momentum being denoted by L, the transition nuclear density can be represented in the form

$$\rho_{\text{tr}}(\mathbf{r}) = \rho_{\text{tr}}^{L}(r) Y_{LM}(\hat{\mathbf{r}}), \tag{24}$$

$$\rho_{\text{tr}}^{L}(r) = C_L \frac{d\rho(r)}{dr}, \tag{25}$$

where $\rho(r)$ is the single-particle nuclear density, which is determined by relation (5) for the ^{16}O nucleus and by the relation relation (9) or (12) for the ^{20}Ne nucleus; $\rho_{\text{tr}}^{L}(r)$ is the radial part of the transition density; $Y_{LM}(\hat{\mathbf{r}})$ are spherical harmonics; $\hat{\mathbf{r}} = \mathbf{r}/r$; and C_L is a parameter that characterizes the dynamical deformation of the nucleus being considered.

The parameter C_L can be determined from the relation

$$C_L = [\text{Br}(EL)]^{1/2} \Bigg/ \left[Ze\sqrt{2L+1} \int_0^\infty dr \frac{d\rho(r)}{dr} r^{L+2} \right], \tag{26}$$

where $\text{Br}(EL)$ is the reduced electromagnetic-transition branching ratio.

In this study, we considered the inelastic scattering of 800-MeV protons by ^{16}O and ^{20}Ne nuclei that is accompanied by the excitation of low-lying 2^+ and 3^- levels for ^{16}O and 2^+ and 4^+ levels for ^{20}Ne nuclei. The expressions for the inelastic-scattering amplitude within this approach are given in [16]. The experimentally measured values of the electromagnetic-transition branching ratios $\text{Br}(EL)$ and the calculated values of the parameters C_L are the following: $\text{Br}(E2) = 36.4\ e^2\ \text{fm}^4$ [20] and $C_2 = 0.45213$ for the 2^+ level of the ^{16}O nucleus at 6.92 MeV, $\text{Br}(E3) = 1500\ e^2\ \text{fm}^6$ [21] and $C_3 = 0.74986$ for the 3^- level of ^{16}O nucleus at 6.13 MeV, and $\text{Br}(E2) = 287\ e^2\ \text{fm}^4$ [10] and $C_2 = 0.9574$ for the 2^+ level of the ^{20}Ne nucleus at 1.63 MeV. For the 4^+ level of the ^{20}Ne nucleus at 4.25 MeV, the constant C_4 was treated in the calculations as an adjustable parameter. Its numerical value was taken to be $C_4 = 0.312$.

On the basis of the approach described above, the differential cross section $\sigma(\theta) \equiv d\sigma/d\Omega$ [mb/sr], the polarization $P(\theta)$, and the spin-rotation function $Q(\theta)$ were calculated for the inelastic scattering of 800-MeV protons by ^{16}O nuclei (Fig. 2, solid curves).

The results of the calculations of the same quantities for inelastic p^{20}Ne scattering at an energy of $E_p = 800$ MeV are shown in Fig. 3. The solid curves in Fig. 3 represent the results of the calculations in which it is assumed that the ^{20}Ne nucleus is formed by a core (^{16}O nucleus) and a complementary alpha-particle cluster, which is located, with the highest probability, within the core, while the dashed curves correspond to the calculations performed under the assumption that a complementary alpha-particle cluster is located, with the highest probability, beyond the core.

Our calculations reveal that the approach used above makes it possible to describe available experimental data without employing adjustable parameters. The assumption that the ^{16}O and ^{20}Ne nuclei possess an α-cluster structure enables one (over the applicability range of the α-cluster model—that is, for momentum-transfer values in the range $q \leq 3\ \text{fm}^{-1}$) to describe better data on the differential

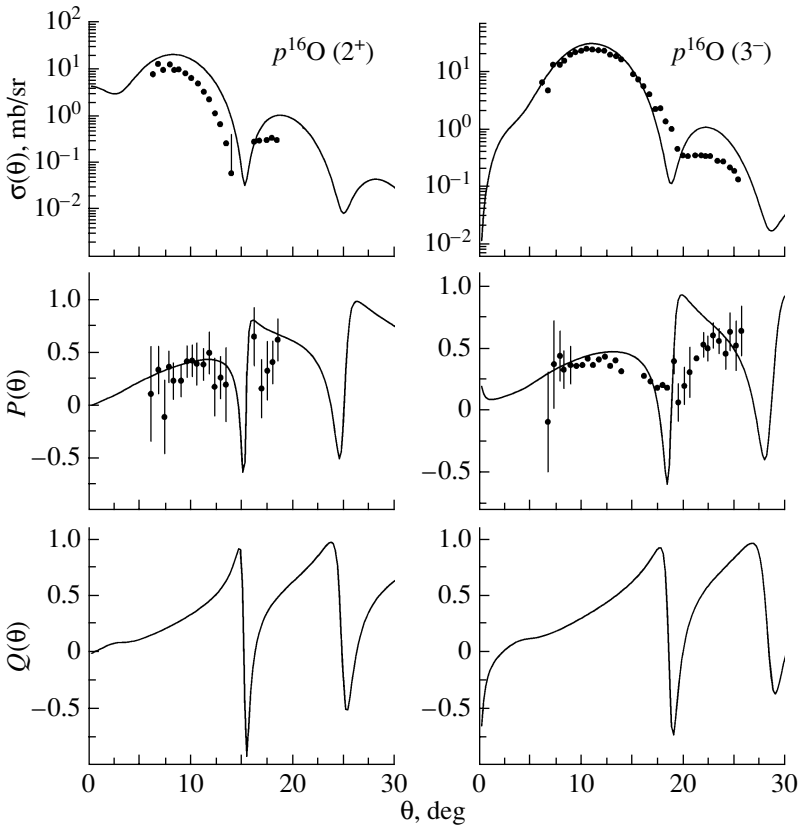

Fig. 2. Differential cross sections $\sigma(\theta)$ and polarization observables $P(\theta)$ and $Q(\theta)$ for inelastic proton scattering on the ^{16}O nuclei at an energy of 800 MeV versus the scattering angle θ. The displayed experimental data were borrowed from [17].

cross sections for the elastic scattering of 800-MeV protons by these nuclei and on the polarization observables for the ^{16}O target nucleus. The description of the polarization $P(\theta)$ for elastic proton scattering on ^{20}Ne nuclei for the case where the neon nucleus is considered as that which consists of a core and a complementary alpha-particle cluster occurring, with the highest probability, within the core is of the same quality as that where the alpha-particle cluster is off the core (Fig. 1, dashed and dotted curves, respectively); however, the independent-nucleon model seems preferable at small scattering angles (Fig. 1, solid curves). Also, it turns out that, for elastic proton scattering on both ^{16}O and ^{20}Ne nuclei, the spin-rotation functions calculated within the independent-nucleon model differ qualitatively from their counterparts calculated on the basis of the α-cluster model involving dispersion.

The calculated observables of inelastic proton scattering on ^{16}O and ^{20}Ne nuclei are also in good agreement with available experimental data, the agreement being better for p^{20}Ne than for p^{16}O scattering. In all probability, the reason is that, with increasing number of intranuclear nucleons, the cluster structure of nuclei becomes more pronounced. Experimental measurements of the spin-rotation functions for elastic proton scattering on ^{20}Ne nuclei and for inelastic p^{16}O and p^{20}Ne scattering would provide a more reliable answer to this question.

It should be noted that, in many studies, the elastic and inelastic scattering of intermediate-energy protons by ^{12}C and ^{16}O nuclei and by lighter nuclei (^{6}Li, ^{6}He, ^{9}Be, etc.) was studied on the basis of the theory of multiple diffractive scattering by using various versions of the α-cluster model, as well as by using the single-particle densities of such nuclei (see, for example, [4, 5, 22–24] and references therein).

For example, the effect of both alpha-particle and two-particle nucleon–nucleon correlations on the differential cross sections for proton–nucleus scattering was studied in [22], where it was shown that, in the scattering of intermediate-energy particles on nuclei, the effects of nucleon correlations are relatively small, the behavior of the calculated differential cross sections being determined primarily by single-particle nuclear densities.

By and large, the results of the calculations performed in the present study are compatible with the conclusions drawn in [22]. Indeed, the behavior of

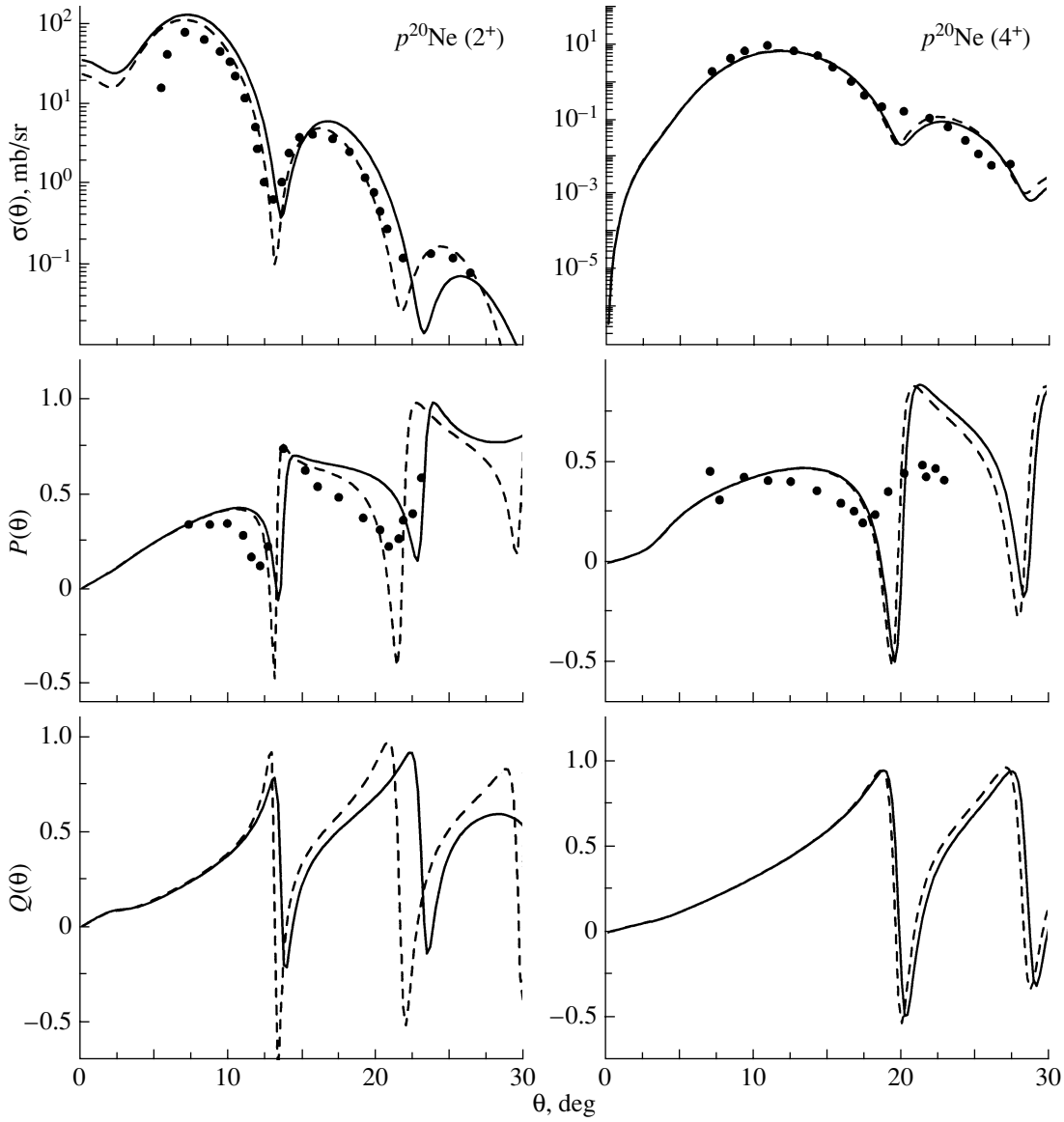

Fig. 3. As in Fig. 2, but for ^{20}Ne nuclei. The displayed experimental data were borrowed from [18]. The description of the curves is given in the main body of the text.

the differential cross sections calculated within the α-cluster model involving dispersion exhibits only slight distinctions from the behavior of the analogous quantities calculated by using the single-particle densities of the ^{16}O and ^{20}Ne nuclei. As was noted above, however, the spin-rotation functions calculated within the independent-nucleon model differ qualitatively from those calculated on the basis of the α-cluster model involving dispersion.

It should be noted that, in [19, 25], the observables of the scattering of intermediate-energy protons on nuclei were calculated on the basis of the theory of multiple diffractive scattering with allowance for two-nucleon correlations, the effects of Z ordering being taken into account in determining the required scattering amplitudes. In those calculations, densities found by the Hartree–Fock method with various Skyrme forces were used for target nuclei; also, intermediate excitations of target nuclei were taken into account. Polarization observables calculated within this approach [25] for the elastic scattering of 800 MeV protons on ^{16}O nuclei were in worse agreement with available experimental data than their counterparts calculated on the basis of the α-cluster model involving dispersion.

REFERENCES

1. K. Wildermuth and Y. C. Tang, *A Unified Theory of the Nucleus* (Vieweg, Braunschweig, 1977; Mir, Moscow, 1980).

2. Y. Fujiwara, H. Horiuchi, K. Ikeda, *et al.*, Prog. Theor. Phys. Suppl. **68**, 29 (1980).
3. M. Dufour and P. Descouvemont, Nucl. Phys. A **605**, 160 (1996).
4. M. A. Zhusupov and E. T. Ibraeva, Yad. Fiz. **61**, 51 (1998) [Phys. At. Nucl. **61**, 46 (1998)].
5. M. A. Zhusupov and E. T. Ibraeva, Fiz. Élem. Chastits At. Yadra **31**, 1427 (2000) [Phys. Part. Nucl. **31**, 723 (2000)].
6. Ya. A. Berezhnoy and V. P. Mikhaluyk, Yad. Fiz. **67**, 1147 (2004) [Phys. At. Nucl. **67**, 1448 (2004)].
7. Ya. A. Berezhnoy and V. P. Mikhaluyk, Yad. Fiz. **67**, 625 (2004) [Phys. At. Nucl. **67**, 606 (2004)].
8. Yu. A. Berezhnoy, V. P. Mikhailyuk, and V. V. Pilipenko, J. Phys. G **18**, 85 (1992).
9. Yu. A. Berezhnoĭ, V. P. Mikhailyuk, and V. V. Pilipenko, Yad. Fiz. **55**, 1885 (1992) [Sov. J. Nucl. Phys. **55**, 1044 (1992)].
10. Y. Abgrall, P. Gabinski, and J. Labarsouqe, Nucl. Phys. A **232**, 235 (1974).
11. Yu. A. Berezhnoy and V. P. Mikhailyuk, Int. J. Mod. Phys. E **8**, 485 (1999).
12. Yu. A. Berezhnoĭ and V. P. Mikhailyuk, Izv. Akad. Nauk, Ser. Fiz. **65**, 721 (2001).
13. E. V. Inopin and B. I. Tishchenko, Zh. Éksp. Teor. Fiz. **38**, 1160 (1960) [Sov. Phys. JETP **11**, 840 (1960)].
14. D. M. Brink, H. Friedrich, A. Weiguny, and C. W. Wong, Phys. Lett. B **33B**, 143 (1970).
15. Yu. A. Berezhnoy, V. V. Pilipenko, and G. A. Khomenko, J. Phys. G **10**, 63 (1984).
16. V. V. Pilipenko and A. P. Soznik, Yad. Fiz. **44**, 369 (1986) [Sov. J. Nucl. Phys. **44**, 235 (1986)].
17. R. W. Fergerson, M. L. Barlett, G. W. Hoffman, *et al.*, Phys. Rev. C **33**, 239 (1986).
18. G. S. Blanpied, G. A. Balchin, G. E. Langston, *et al.*, Phys. Rev. C **30**, 1233 (1984).
19. V. I. Kuprikov and V. V. Pilipenko, Yad. Fiz. **63**, 852 (2000) [Phys. At. Nucl. **63**, 782 (2000)].
20. M. Stroetzel, Phys. Lett. B **26B**, 376 (1968).
21. H. Miska, H. D. Graf, and A. Richter, Phys. Lett. B **58B**, 155 (1975).
22. G. D. Alkhazov, S. L. Belostotsky, and A. A. Vorobyov, Phys. Rep. **42**, 89 (1978).
23. G. D. Alkhazov, S. L. Belostotsky, A. A. Vorobyov, *et al.*, Yad. Fiz. **42**, 8 (1985) [Sov. J. Nucl. Phys. **42**, 4 (1985)].
24. G. D. Alkhazov *et al.*, Nucl. Phys. A **712**, 269 (2002).
25. V. V. Pilipenko and V. I. Kuprikov, Ukr. Fiz. Zh. **48**, 1024 (2003).

Translated by A. Isaakyan

Physics of Atomic Nuclei, Vol. 68, No. 6, 2005, pp. 948–959. Translated from Yadernaya Fizika, Vol. 68, No. 6, 2005, pp. 986–997.
Original Russian Text Copyright © 2005 by Akopdzhanov, Anikeev, Bezzubov, Vasilyev, Gilitsky, Gurzhiev, Denisov, Durum, Zvyagintsev, Kozelov, Kozlovsky, Korablev, Koreshev, Kurbakov, Lipaev, Onuchin, Rybin, Sapunov, Soldatov, Stoyanova, Trushin, Schukin, Yakimchuk.

ELEMENTARY PARTICLES AND FIELDS
Experiment

Measurement of the Charge Asymmetry of the Dalitz Plot Parameters for $K^{\pm} \to \pi^{\pm}\pi^0\pi^0$ Decays

G. A. Akopdzhanov, V. B. Anikeev, V. A. Bezzubov, I. A. Vasilyev, Yu. V. Gilitsky, S. N. Gurzhiev, S. P. Denisov, A. A. Durum, S. A. Zvyagintsev, A. V. Kozelov*, E. A. Kozlovsky, V. M. Korablev, V. I. Koreshev, V. I. Kurbakov, V. V. Lipaev, V. A. Onuchin, A. M. Rybin, Yu. M. Sapunov†, M. M. Soldatov, D. A. Stoyanova, K. I. Trushin, A. A. Schukin, and V. I. Yakimchuk

State Research Center Institute for High Energy Physics, Protvino, Moscow oblast, 142280 Russia

Received November 30, 2004

Abstract—The results are presented for the charge asymmetry of the Dalitz plot parameters g, h, and k measured for $K^{\pm} \to \pi^{\pm}\pi^0\pi^0$ decays. The experiment has been carried out in the 35-GeV/c kaon beams at the IHEP accelerator. The g, h, and k parameters appear to be identical for K^+ and K^- decays within the experimental uncertainty. In particular, a value of $(0.2 \pm 1.9) \times 10^{-3}$ is obtained for the charge asymmetry $A_g = (g^+ - g^-)/(g^+ + g^-)$ of the Dalitz plot slope. © *2005 Pleiades Publishing, Inc.*

1. INTRODUCTION

Since direct CP violation has been observed in neutral kaon decays [1–3], it can be expected in the decays of charged K mesons. For example, this effect can manifest itself as the charge asymmetry of the Dalitz plot parameters of $K^{\pm} \to \pi^{\pm}\pi^0\pi^0$ decays. These parameters are coefficients in a series expansion of the squared modulus of the matrix element [4]:

$$|M(u,v)|^2 \propto 1 + gu + hu^2 + kv^2, \qquad (1)$$

where u and v are the standard invariant variables [4].

Theoretical estimates of the charge asymmetry of the Dalitz plot slope parameter for $K^{\pm} \to \pi^{\pm}\pi^0\pi^0$ decays are rather uncertain and lie in the range between 10^{-6} and 10^{-3} [5–8]. The analysis of the available experimental data on these decays [4, 9] provides an estimate of $\Delta g = g^+ - g^- = 0.066 \pm 0.017$. It is unlikely that CP violation is so strong, and the mentioned difference between the g^+ and g^- parameters must be caused by the underestimation of the systematic uncertainty of the experiments in which decays of kaons of only one sign were studied.

The $K \to 3\pi$ decays were studied for both K^+ and K^- mesons in [10–12]. Ford *et al.* [10] studied $K^{\pm} \to \pi^{\pm}\pi^+\pi^-$ decays and found $A_g = -0.0070 \pm 0.0053$ for the charge asymmetry $A_g = (g^+ - g^-)/(g^+ + g^-)$ of the Dalitz plot slope. Smith *et al.* [11] estimated $A_g = 0.0019 \pm 0.0123$ for $K^{\pm} \to \pi^{\pm}\pi^0\pi^0$ decays. Preliminary analysis of our experimental data [12] that was based on a fraction of statistics provided an estimate of $A_g = -0.0003$ with a statistical error of 0.0025 and a systematic uncertainty below 0.0015 for $K^{\pm} \to \pi^{\pm}\pi^0\pi^0$ decays. In this paper, we report our final results obtained for the charge asymmetry of the Dalitz plot parameters.

2. EXPERIMENTAL SETUP

The experiment was carried out at the TNF-IHEP setup[1)] [13]; its layout is shown in Fig. 1. To study $K^{\pm}$ meson decays, 35-GeV/c hadron beams that were produced by 70-GeV protons on an external aluminum target 7 mm in diameter and 300 mm long were used. We used scintillation counters $S1$–$S4$ and beam hodoscopes $BH1$–$BH4$ to monitor the beam intensity and to measure beam particle trajectories. The mean hadron flux in the beamline was 4×10^6 per accelerator spill of 1.7 s. K mesons were identified with three threshold and two differential gas Cherenkov counters marked in Fig. 1 as $C1$–$C3$ and $D1$ and $D2$, respectively. The admixture of other particles in the K-meson peak at an operating pressure of 2 atm was far below 1% (Fig. 2). In addition, the threshold counters were used to select electrons in

†Deceased.
*e-mail: kozelov@mx.ihep.su

1)The Tagged Neutrino Facility (TNF) at the Institute for High Energy Physics.

1063-7788/05/6806-0948$26.00 © 2005 Pleiades Publishing, Inc.

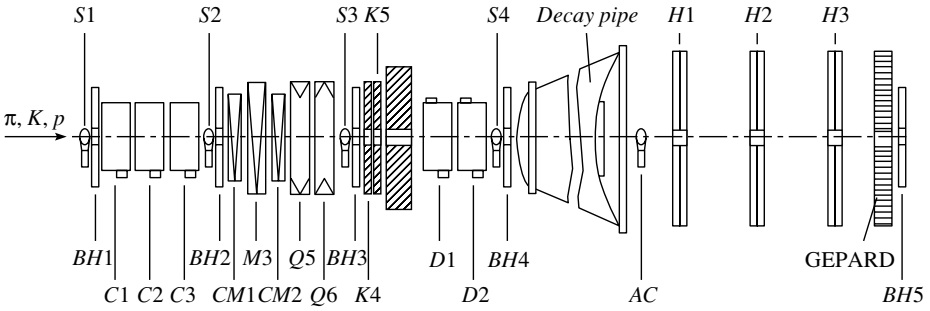

Fig. 1. Layout of the experimental setup: M are the magnets; Q are the quadrupole lenses; CM are the correcting magnets; K are the collimators, S are the scintillation counters, C and D are the threshold and differential Cherenkov counters; BH are the beam hodoscopes; AC is the anticoincidence counter; and H are the scintillation hodoscopes.

the 10-GeV/c beam when the GEPARD electromagnetic calorimeter was calibrated.

A "decay pipe" 58.5 m long, in which about 20% of the kaons decayed, was located downstream of the $BH4$ hodoscope. Its flanges had thin Mylar windows for a beam. The exit flange 3.6 m in diameter was manufactured from stainless steel 4 mm thick ($0.23X_0$). The probability of the conversion of a high-energy photon into an e^+e^- pair in this flange is 0.16.

Undecayed kaons were detected by an anticoincidence scintillation counter AC. In order to accurately measure the position of the beam passing through the whole setup, the $BH5$ beam hodoscope was mounted behind the calorimeter. The $BH5$ hodoscope operated in the counting mode; thus, we could detect all charged particles hitting it.

The products of kaon decays were detected by three scintillation hodoscopes $H1-H3$ [14] and the GEPARD calorimeter. Each hodoscope measuring the X and Y coordinates of the particles had two octagonal planes with a distance of 3.85 m between their opposite sides (Fig. 3). Each plane was divided into independent half-planes. The hodoscope elements had a cross-section of 14×12 mm, and their length was from 1.8 to 0.7 m. Scintillation light was detected by FEU-84-3 photomultiplier tubes.

The GEPARD calorimeter contained 1968 76×76-mm cells (Fig. 4). Each cell comprised 40 alternating Pb (3 mm) and scintillator (5 mm) layers. Thus, the total radiation length is $\approx 21X_0$. Scintillation light was collected onto the FEU-84-3 photomultiplier tubes using wavelength shifting light guides. The GEPARD calorimeter was calibrated by two methods: first, by irradiating each cell with the 10-GeV electron beam at the beginning of data collection and, second, by analyzing reconstructed events of $K^\pm \to \pi^\pm\pi^0$ decays during the experiment. Both methods yielded results that were in good agreement with each other. The π^0 mass resolution appeared to be equal to 12.3 MeV (Fig. 5).

The Level 1 trigger was based on signals from the scintillation and Cherenkov counters. It was formed according to the logical formula

$$T1 = S1 \times S2 \times S3 \times S4 \times (D1 + D2) \times \overline{C1} \times \overline{C2} \times \overline{C3} \times \overline{AC}.$$

The Level 2 trigger analyzed the GEPARD energy deposition [15]. To this end, the calorimeter was divided into 16 trigger channels, and the Level 2 trigger was formed if the pulse height corresponding to the energy deposition in at least three trigger channels exceeded ~ 0.8 GeV.

The stability of the beam and detector parameters was carefully controlled throughout the period of data collection. To reduce the systematic uncertainty in measuring the charge asymmetry in the Dalitz-plot

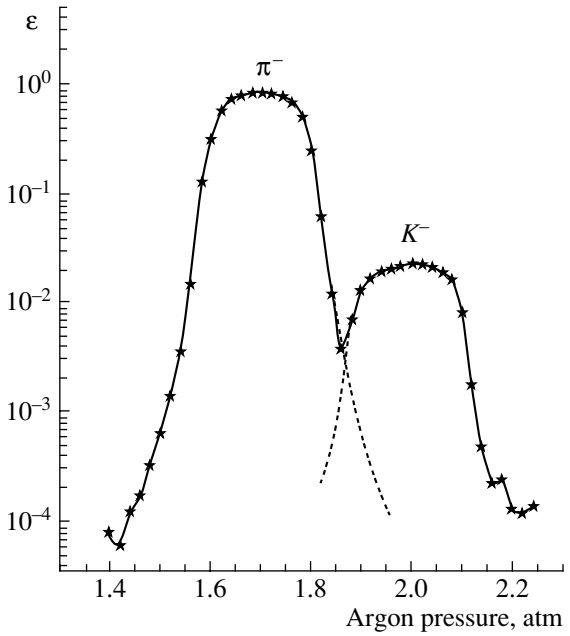

Fig. 2. Rate efficiency of the differential Cherenkov counters for the negatively charged particle versus argon pressure.

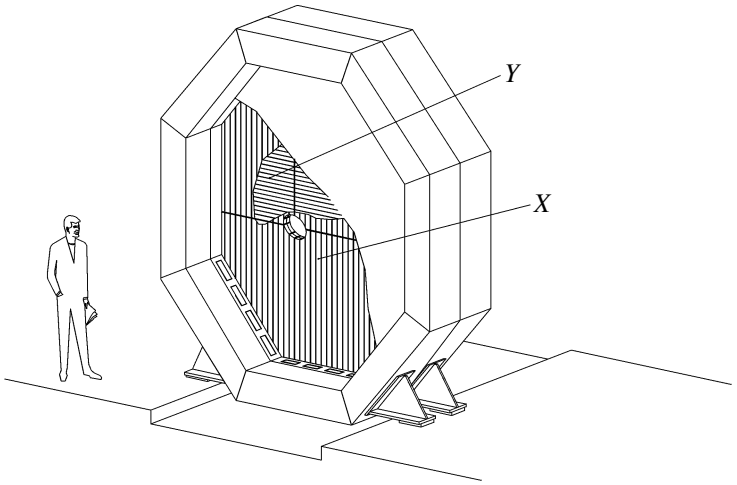

Fig. 3. General view of the scintillation hodoscope.

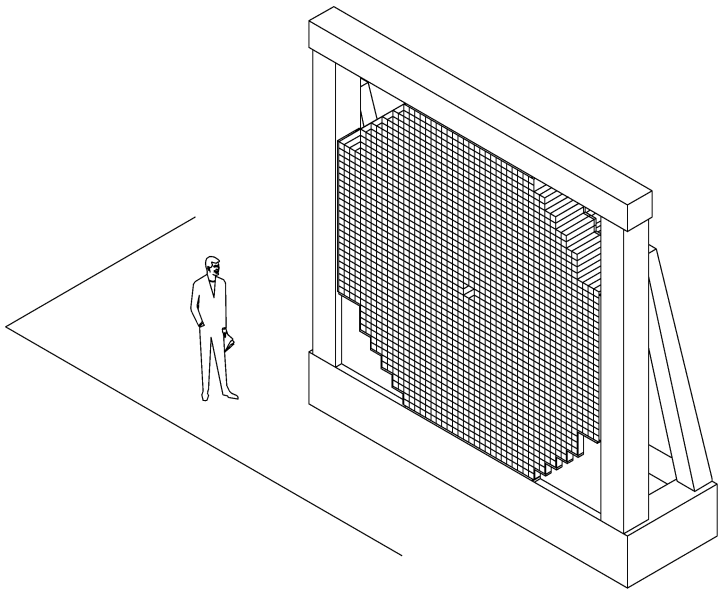

Fig. 4. Structure of the GEPARD electromagnetic calorimeter.

parameters, the sign of the beam-particle charge was reversed every day. Figures 6 and 7 show the raw data prior to their processing in order to illustrate the operational stability of our setup.

3. EVENT RECONSTRUCTION AND SELECTION CRITERIA FOR $K^{\pm} \to \pi^{\pm}\pi^0\pi^0$

The event reconstruction procedure started with finding energy-deposition clusters in the GEPARD electromagnetic calorimeter. The coordinates found for the cluster centers were used in the procedure of the reconstruction of the decay-product tracks. To reduce the possible combinatorial background, tracks are considered as reconstructed if they had no less than three hits in each of the X and Y projections in the $H1$–$H3$ hodoscopes and the GEPARD calorimeter. The vertex coordinates were calculated using the reconstructed tracks. In further processing, we considered only the events for which the hypothesis on the intersection of the secondary particle track with the beam axis had a C.L. of more than 5% and the vertex itself was inside the fiducial volume of the decay pipe. In addition, the events subjected to further processing satisfied one of the following criteria:

- Five clusters with the energy depositions above 1 GeV were reconstructed in the calorimeter and each of the reconstructed tracks was associated with one of these clusters.

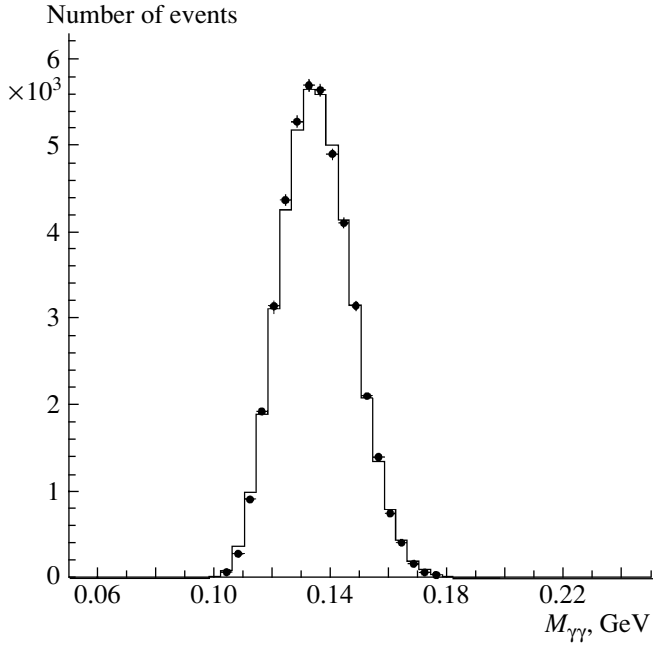

Fig. 5. Invariant mass distribution of a photon pair from the $K^{\pm} \to \pi^{\pm}\pi^0$ decays for the (points) experimental data and (histogram) MC simulated events.

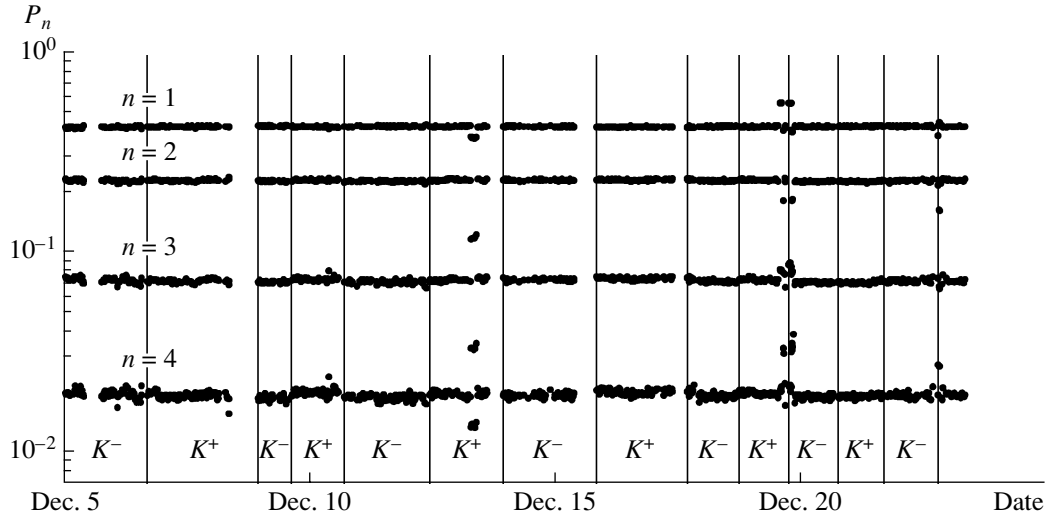

Fig. 6. Time variations of the probability P_n of reconstructing n tracks in a certain run of the data collection (P_n is averaged over $\sim 10^5$ events).

- Four clusters with the energy deposition above 1 GeV were found in the calorimeter and one of the tracks was not associated with these clusters.

The last two criteria are introduced because there is a noticeable probability of the conversion of a photon from the $\pi^0 \to \gamma\gamma$ decay into a e^+e^- pair in the exit flange of the decay pipe (see Section 2), and a charged pion can induce considerable energy deposition in the calorimeter.

Events that had passed this preliminary selection were subjected to a kinematic fit; it enabled us to resolve the ambiguities caused by the combinatorial background (e.g., to associate one of the reconstructed tracks with a $\pi^{\pm}$ meson) and to calculate the kinematic variables u and v.

The fitting procedure involved 21 measured variables: the energies and coordinates of four photons, the mean energy and parameters of the K-meson track, and the parameters of the $\pi^{\pm}$-meson track. The

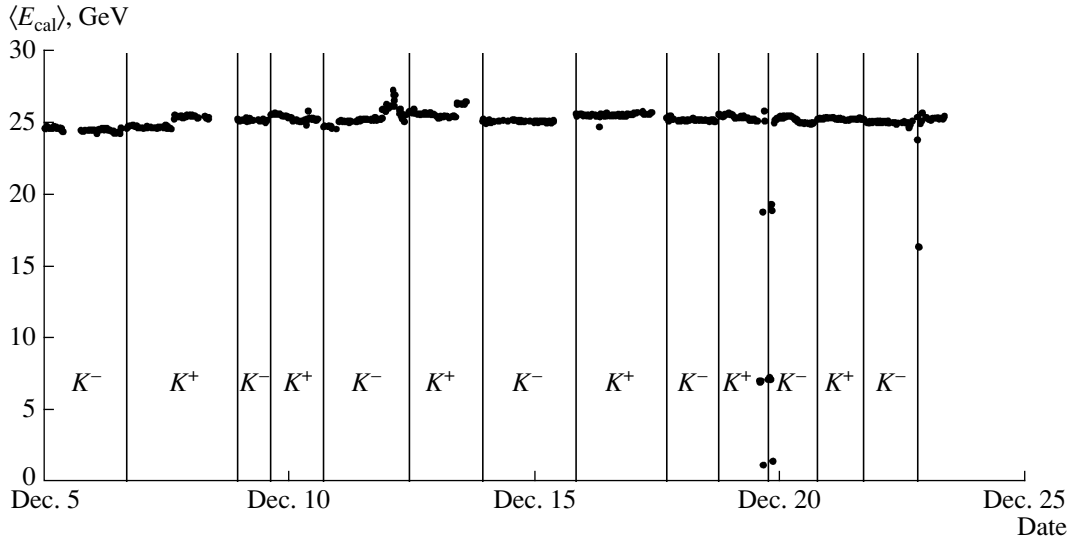

Fig. 7. Time variations of the mean energy per event recorded by the GEPARD calorimeter in a certain run of the data collection (the energy is averaged over $\sim 10^5$ events).

parameters of the energy-deposition clusters were accepted as the coordinates and energies of photons; these parameters were corrected for the transverse profile of the electromagnetic shower and for the spatial nonuniformity of the calorimeter. The energy of the $\pi^{\pm}$ meson was the only unknown parameter.

Seven constraints were imposed on the fitted parameter values: four equations corresponding to the energy–momentum conservation, two equations for the effective masses of a photon pair, and an additional equation describing the intersection of the trajectories of a kaon and a charged pion. The decay-vertex coordinates were not fixed. The parameters were determined by minimizing the functional under the constraints using the Lagrange multiplier method. The reduction of the relative variation of each fitted parameter down to 10^{-5} at the last iteration was a prerequisite to the procedure convergence. For each event, we tested all possible combinations that enabled us to associate one of the tracks with the positive π meson and to combine four photons into pairs corresponding to two π^0 mesons. The combinations providing the least χ^2 value were considered as the best. Figure 8 shows the χ^2 distribution for the experimental and simulated events. Events with $\chi^2 > 20$ were rejected because the number of experimental events systematically exceeded that of simulated events owing to background events in this region. Simulation of the detection of $K^{\pm} \to \pi^{\pm}\pi^0\pi^0$ decays in the setup demonstrated that this χ^2 cutoff reduced the statistics of desired events by only 28%, while it considerably reduced the background level.

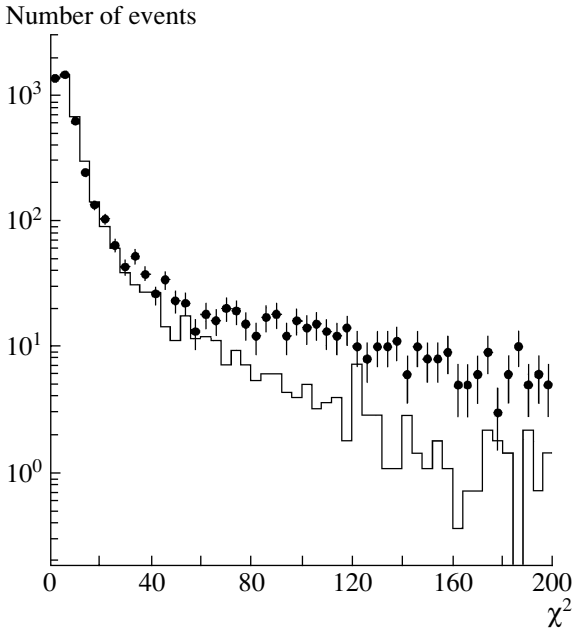

Fig. 8. χ^2 distributions corresponding to the (points) experimental data and (histogram) MC simulated events for $K^{\pm} \to \pi^{\pm}\pi^0\pi^0$ decays.

The setup operation was simulated by the Monte Carlo (MC) method with the GEANT 3.21 code. In addition to the detailed description of the setup geometry, the data obtained in the experiment were taken into account. Among these data were the calibration coefficients for each channel of the electromagnetic calorimeter, the dependence of the detection efficiency of the scintillation hodoscopes on the particle coordinates, and the correlations between the spatial and angular coordinates of kaons and their momenta. Figure 9 enables one to compare the distributions

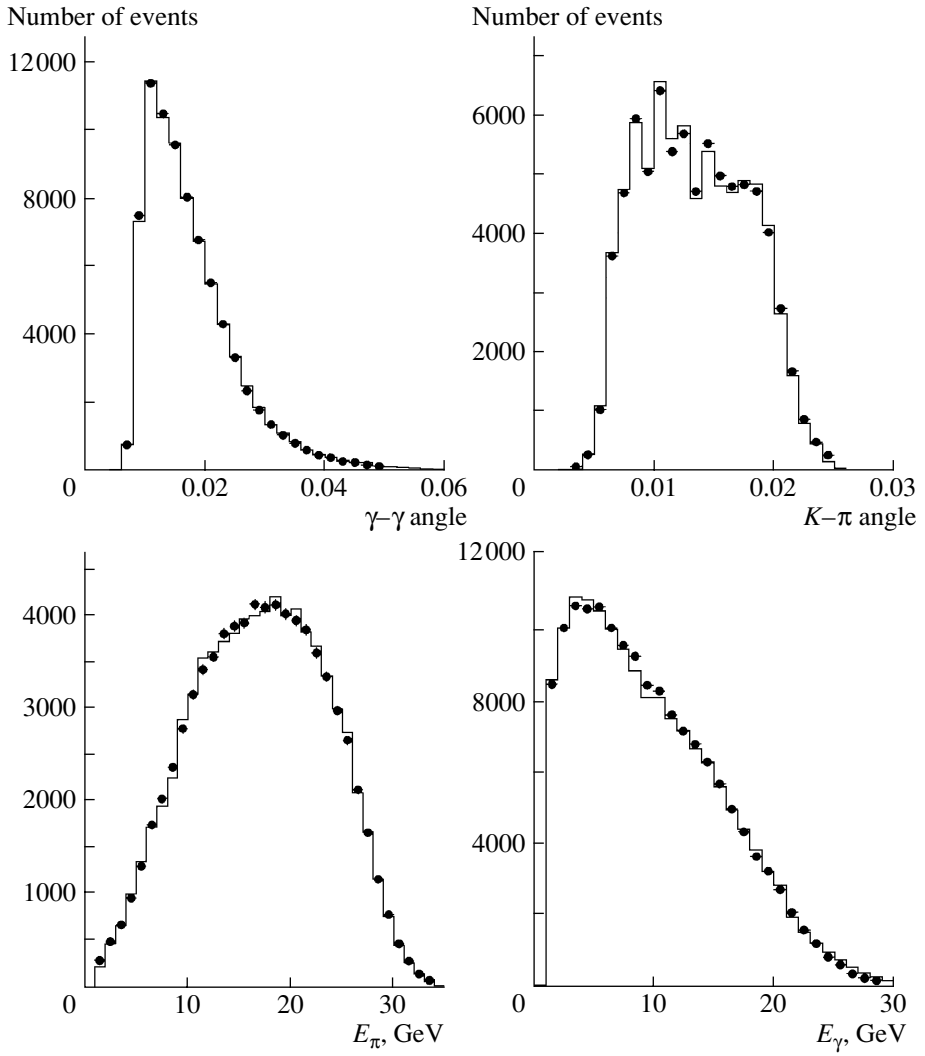

Fig. 9. Event distributions corresponding to the (points) experimental data and (histogram) MC simulated events versus certain kinematic variables of $K^{\pm} \to \pi^{\pm}\pi^0$ decays.

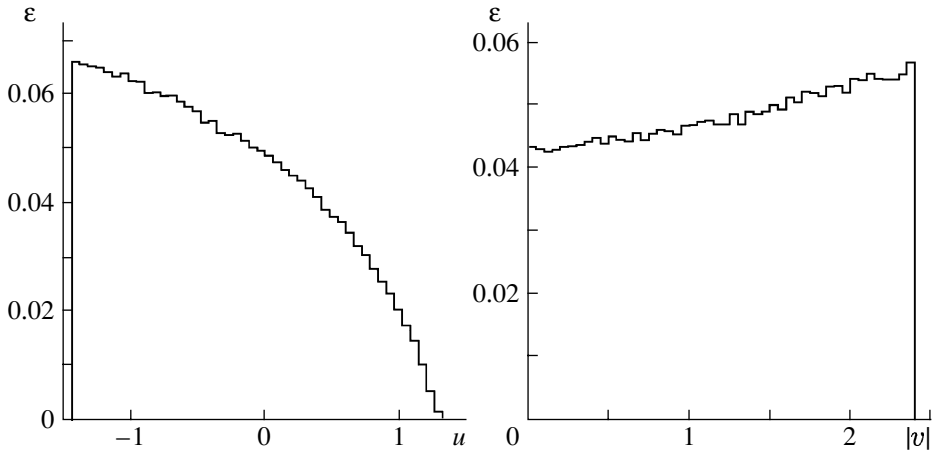

Fig. 10. Setup acceptance vs. the Dalitz variables u and $|v|$.

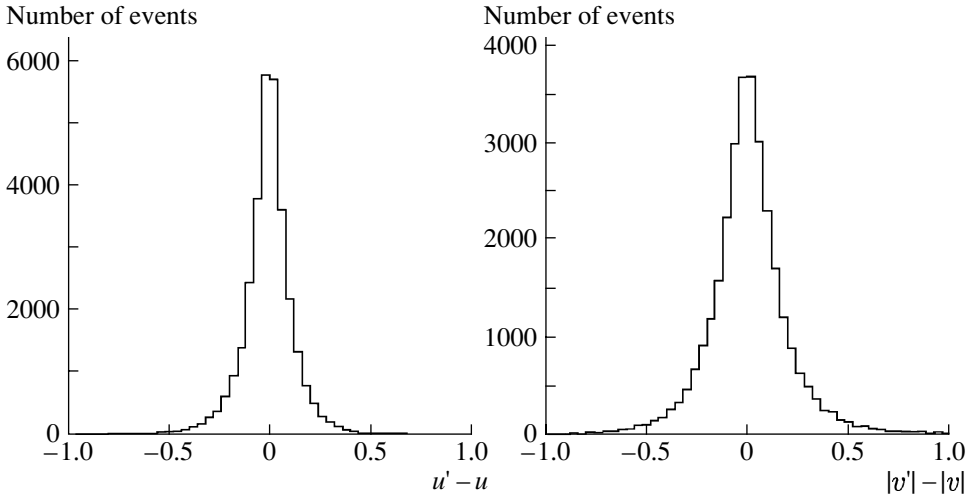

Fig. 11. Dalitz variable resolutions (u and v are the "true" values, whereas u' and v' are the reconstructed ones).

of the experimental and simulated events for $K^{\pm} \to \pi^{\pm}\pi^0$ decays. We note that the simulating code adequately describes the processes in the experimental setup. Figures 10 shows the setup acceptance as a function of the Dalitz variables u, v. Figure 11 demonstrates the (u, v) resolutions obtained within the MC simulation of the $K^{\pm} \to \pi^{\pm}\pi^0\pi^0$ decay.

Figure 12 shows the event distributions versus the χ^2 probability $P(\chi^2)$ calculated for the six degrees of freedom. These distributions were obtained both for the experimental data and for MC simulated events of $K^{\pm} \to \pi^{\pm}\pi^0\pi^0$ decays. Only the events with $P(\chi^2) > 0.1$ were used in further analysis, because the $P(\chi^2)$ values corresponding to these experimental and simulated data were in agreement with each other. To avoid uncertainties associated with the possible nonuniformity of the pulse heights, the corresponding energies were additionally recalculated in each of the Level 2 trigger channels. An event was accepted if the number of channels with energy above 1 GeV was greater than two. This criterion did not noticeably reduce the number of $K^{\pm} \to \pi^{\pm}\pi^0\pi^0$ events. However, it was of importance for the selection of $K^{\pm} \to \pi^{\pm}\pi^0$ events that were used to calibrate the calorimeter, to adjust the simulation code, and to estimate the systematic uncertainties.

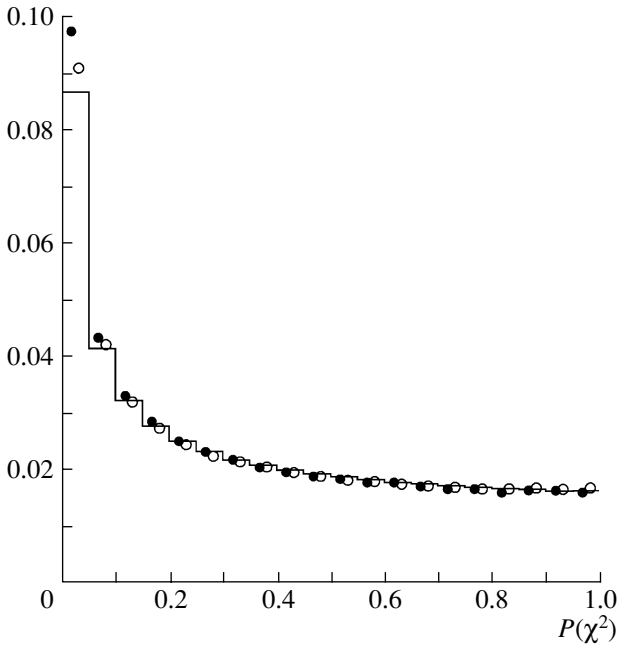

Fig. 12. $P(\chi^2)$ distributions corresponding to (histogram) the MC simulated events and to the experimental data for (closed circles) K^+ and (open circles) K^- for $K^{\pm} \to \pi^{\pm}\pi^0\pi^0$ decays. The χ^2 values are obtained from the kinematic fit.

The final data sample comprised $N^+ = 278\,398$ and $N^- = 341\,015$ events. The table shows the fraction of events satisfying the above criteria, and their number is related to the one at the previous step and to the total number of detected events.

In spite of careful selection of the events, there is an admixture of background events in the data sample of the $K^{\pm} \to \pi^{\pm}\pi^0\pi^0$ decays chosen for physical analysis. Other decay modes of the $K^{\pm}$ mesons, the interaction of beam particles with the setup material, and overlapping of events because of the finite time resolution of the recording instruments can be physical sources of the background. The simulation of various processes of particle interaction and decays indicates that, with the above selection criteria, the main sources of the background events are the $K^{\pm} \to \pi^{\pm}\pi^0$ (0.21%) and $K^{\pm} \to \pi^{\pm}\pi^+\pi^-$ (0.03%) decays. Their contribution is independent of the sign of the kaon charge and hence cannot cause a false charge

Event selection criteria	Fraction of events (%)	
	from previous step	from total number of triggers
One or more tracks are reconstructed in $H1-H3$	95.6	95.6
Position of the decay vertex is inside the fiducial length of the decay pipe	68.8	65.7
Number of clusters and tracks corresponds to $K^\pm \to \pi^\pm\pi^0\pi^0$	6.81	4.48
Passing the kinematic fit with $\chi^2 < 20$	17.8	0.80
C.L. $P(\chi^2)$ of the kinematic fit is >0.1	73.6	0.59
Programmable Level 2 trigger is true	99.8	0.59

asymmetry in the Dalitz plot parameters. The background from other sources does not exceed 0.01%.

It should be noted that the finite calorimeter resolution results in a noticeable probability (∼10%) of "wrong combinations" of photons produced in π^0-meson decays, while the inefficiency of the hodoscopes can allow the reconstruction of a false track (∼5%). However, these effects are taken into account in the event simulation and are independent of the sign of the particle charge. Therefore, they do not introduce a noticeable uncertainty to the final result.

4. RESULTS AND DISCUSSION

4.1. Estimate of the Difference in the Dalitz Plot Parameters

In order to determine the difference between the Dalitz-plot parameters for $K^\pm \to \pi^\pm\pi^0\pi^0$ decays, the following functional is minimized:

$$\chi^2(\Delta g, \Delta h, \Delta k) = \sum_{i,j} \frac{(r_{ij} - 1 - \alpha_{ij}\Delta g - \beta_{ij}\Delta h - \gamma_{ij}\Delta k)^2}{\sigma_{ij}^2}, \quad (2)$$

where $r_{ij} = (n_{ij}^+/N^+)/(n_{ij}^-/N^-)$, $\sigma_{ij}^2 = r_{ij}^2(1/n_{ij}^+ + 1/n_{ij}^-)$, and $n_{ij}^\pm$ is the number of events in the Dalitz plot bins with the measured coordinates u_i' and v_j' (Fig. 13). The coefficients α_{ij}, β_{ij}, and γ_{ij} are defined in formula (A.2) presented in the Appendix and are calculated using the MC simulated events. In this way, we obtained the following estimates for Δg, Δh, and Δk, as well as for the elements of the correlation matrix:

$$\begin{cases} \Delta g = -0.0009 \pm 0.0067, \\ \Delta h = -0.0007 \pm 0.0062, \\ \Delta k = -0.0014 \pm 0.0017, \end{cases} \quad \begin{pmatrix} 1.00 & 0.93 & 0.35 \\ & 1.00 & 0.32 \\ & & 1.00 \end{pmatrix}. \quad (3)$$

The presented uncertainties are statistical. The χ^2 value per degree of freedom is $\chi^2/\text{ndf} = 319/(279 - 3) = 1.16$.

Figure 14 shows the ratios $r_i(u') = (\sum_j n_{ij}^+/N^+)/(\sum_j n_{ij}^-/N^-)$ and $r_j(v') = (\sum_i n_{ij}^+/N^+)/(\sum_i n_{ij}^-/N^-)$ of the normalized distributions that are measured for $K^\pm \to \pi^\pm\pi^0\pi^0$ decays and obtained separately as functions of u' and $|v'|$, respectively. Figure 15 demonstrates the $r_{ij}(u')$ ratio versus u' for various $|v'|$ intervals.

Since some theoretical models predict that CP violation in $K^\pm \to 3\pi$ decays can be associated only with the charge asymmetry of the g parameter, we also estimated Δg supposing that $\Delta h = \Delta k \equiv 0$. The latter supposition does not contradict our results. This approach provides the estimate

$$\Delta g = 0.0002 \pm 0.0024 \quad \text{for} \quad \chi^2/\text{ndf} = 319/(279 - 1) = 1.15. \quad (4)$$

Within the statistical uncertainties of our experiment, the presented results indicate no differences between the g, h, and k values for kaons of different signs. Nevertheless, it does not guarantee the identity of the event distributions in the corresponding Dalitz plots. In order to check the identity of the event distributions over $(u', |v'|)$ and $(u', |v'|)$ disregarding a particular form of the matrix element given by Eq. (1), we used the Kolmogorov nonparametric criterion. This analysis provided the following

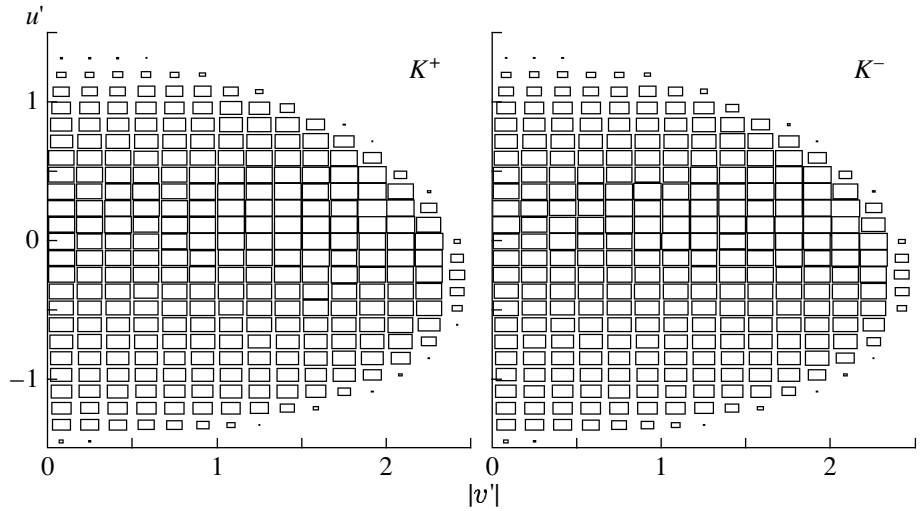

Fig. 13. Two-dimensional Dalitz plots for events of the $K^{\pm} \to \pi^{\pm}\pi^0\pi^0$ decays.

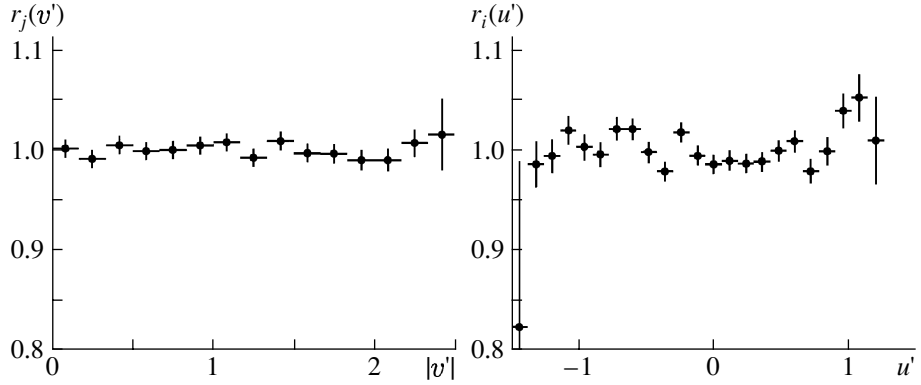

Fig. 14. Ratios of normalized event distributions for the $K^{\pm} \to \pi^{\pm}\pi^0\pi^0$ decays projected on the $|v'|$ and u' axes.

results. The probabilities that the u', $|v'|$, and $(u', |v'|)$ distributions were indistinguishable appeared to be 0.32, 0.85, and 0.55, respectively. In order to compare the two-dimensional $(u', |v'|)$ distributions, we used the modified Kolmogorov criterion from the HBOOK code, which processed the events combined into a histogram.

4.2. Estimate of Systematic Uncertainties

Although all measures were taken to provide the identity of the properties of the beams of positive and negative kaons, the mean values of the beam entrance angle with respect to the setup could differ by $\Delta A_X = 5$ μrad and $\Delta A_Y = 7$ μrad, and the mean kaon energies could differ by 50 MeV. The systematic uncertainties that were associated with these values were estimated by the Monte Carlo method as

$$\delta_A(\Delta g) = 0.0004, \qquad \delta_A(\Delta h) = 0.0003,$$
$$\delta_A(\Delta k) = 0.0001,$$

$$\delta_E(\Delta g) = 0.0006, \qquad \delta_E(\Delta h) = 0.0004,$$
$$\delta_E(\Delta k) = 0.0001.$$

The uncertainties inherent in the α, β, and γ coefficients in functional (2) are associated with the uncertainties of the g, h, and k parameters [see Eqs. (A.1) and (A.2) in the Appendix]. Two methods were used to evaluate the effect of these uncertainties on the differences Δg, Δh, and Δk: the Monte Carlo method and analytical method using the approximation of the ideal resolution in the u and v variables [see Eqs. (A.3) and (A.4)]. The results obtained by both methods are in agreement with each other:

$$\frac{\delta(\Delta g)}{\Delta g} \approx \sqrt{(0.2\delta g)^2 + (0.6\delta h)^2 + (1.6\delta k)^2},$$
$$\frac{\delta(\Delta h)}{\Delta h} \approx \sqrt{(0.5\delta g)^2 + (1.0\delta h)^2 + (1.5\delta k)^2},$$
$$\frac{\delta(\Delta k)}{\Delta k} \approx \sqrt{(0.4\delta g)^2 + (0.5\delta h)^2 + (2.9\delta k)^2}.$$

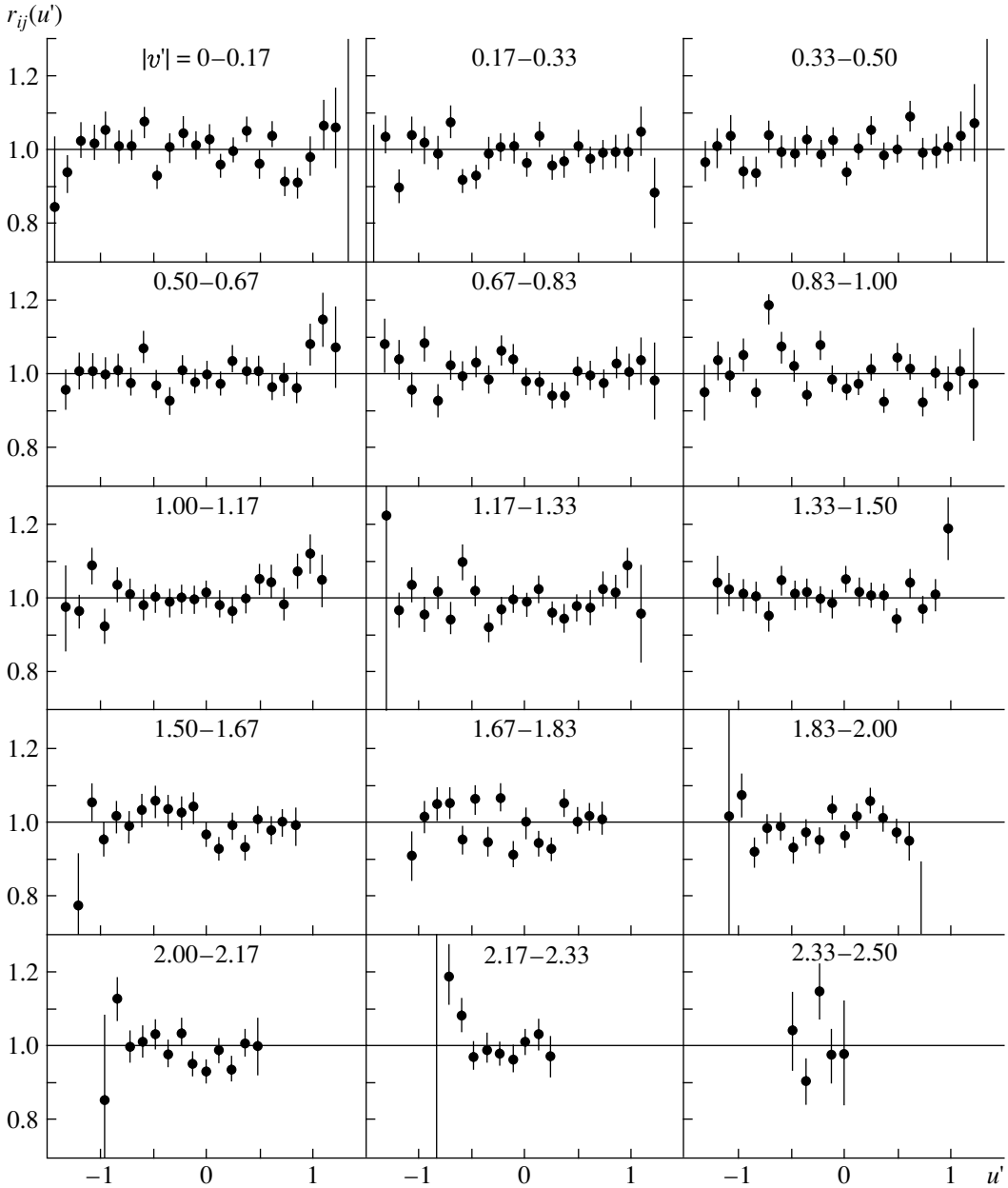

Fig. 15. Ratios of the normalized event distributions for the $K^{\pm} \to \pi^{\pm}\pi^0\pi^0$ decays vs. u' for various $|v'|$ intervals.

Using the data from [4], we obtain

$$\frac{\delta(\Delta g)}{\Delta g} = 0.014, \qquad \frac{\delta(\Delta h)}{\Delta h} = 0.024,$$

$$\frac{\delta(\Delta k)}{\Delta k} = 0.019.$$

Other possible sources of the systematic uncertainties were also analyzed. These are the time instability of the electromagnetic calorimeter calibration and of the scintillation hodoscope efficiency, the effect of the Earth's magnetic field on the particle beams of different charge signs, the difference between the cross sections for the interactions of π^+ and π^- with matter, and the difference in the composition and intensity between the beams of positive and negative hadrons. The total contribution of these factors to the systematic uncertainty does not exceed 1×10^{-4}.

It has been shown that the results are stable with varying event selection criteria: the minimum photon energy, the minimum and maximum energies of a charged π meson, the χ^2 C.L. in kinematic fit, and the number of reconstructed tracks. The results also remain unchanged if the events in the bins that are located at the boundary of the Dalitz plot are rejected. We also found Δg, Δh, and Δk by minimizing the

functional for the differences between the Dalitz plots for $K^\pm \to \pi^\pm\pi^0\pi^0$ decays. The results are in agreement with estimates (3) and (4).

Thus, the estimates of the systematic uncertainties are

$$\delta(\Delta g) = 7 \times 10^{-4}, \qquad \delta(\Delta h) = 5 \times 10^{-4}, \quad (5)$$
$$\delta(\Delta k) = 1.4 \times 10^{-4}.$$

They are approximately an order of magnitude less than the corresponding statistical uncertainties given by Eqs. (3).

CONCLUSIONS

The differences Δg, Δh, and Δk between the Dalitz plot parameters have been measured for $K^\pm \to \pi^\pm\pi^0\pi^0$ decays at the TNF-IHEP setup. The experiment was performed in the 35-GeV/c beams of positive and negative kaons at the IHEP accelerator. Frequent changes in the beam charge sign enabled us to minimize the systematic uncertainties of the experiment. The data analysis demonstrates that the event distributions over the Dalitz variables u and v are indistinguishable for the decays of K^+ and K^- mesons and that the Δg, Δh, and Δk values are consistent with zero within the uncertainty given by Eqs. (3) and (5). Supposing that $\Delta h = \Delta k = 0$, the difference between the Dalitz plot slopes Δg was estimated as

$$\Delta g = 0.0002 \pm 0.0024(\text{stat.}) \pm 0.0007(\text{syst.}).$$

Using $g^+ \approx g^- = 0.652$ [4], we obtain the charge asymmetry

$$A_g = \Delta g/(g^+ + g^-) = 0.0002 \pm 0.0018(\text{stat.})$$
$$\pm 0.0005(\text{syst.}).$$

This is the most accurate estimate of A_g for the $K^\pm \to \pi^\pm\pi^0\pi^0$ decays.

ACKNOWLEDGMENTS

We are grateful to A.A. Logunov, N.E. Tyurin, and A.M. Zaitzev for their support of the experiment; to V.N. Mikhailin for his assistance in the construction and operation of the setup; and to Yu.V. Mikhailov, A.N. Sytin, and V.A. Sen'ko for their help in manufacturing the electronics. We thank the staff of the Accelerator Department and the Beam Division who provided high-quality operation of the accelerator complex, beam extraction system, and the beam channels nos. 8 and 23. We appreciate the assistance of I.N. Belyakov, Yu.G. Nazarov, A.N. Romadanov, and I.V. Shvabovich in the detector construction.

This study is supported in part by the Russian Foundation for Basic Research (project nos. 02-02-17018 and 02-02-17019) and the Council of the President of the Russian Federation for Support of Young Russian Scientists and Leading Scientific Schools (project no. 1305.2003.2).

APPENDIX

CALCULATION OF THE DIFFERENCE BETWEEN THE DALITZ PLOT PARAMETERS

In accordance with formula (1), the probability density function of the Dalitz variables has the form

$$f(u', v') = \frac{\int\limits_D G(1 + gu + hu^2 + kv^2)dudv}{\int\limits_D \int\limits_{D'} G(1 + gu + hu^2 + kv^2)dudvdu'dv'},$$

where u, v and u', v' are the true and measured Dalitz variables, respectively, and $G \equiv G(u, v, u', v')$ is the function that represents the imperfection of the detector and the system of data processing. Integration is performed within the kinematic boundary of the Dalitz plot. This relation can be rewritten as

$$f(u', v') = \frac{a + gb + hc + kd}{1 + g\bar{u} + h\overline{u^2} + k\overline{v^2}},$$

where $a \equiv a(u', v') = \frac{1}{\varepsilon}\int_D G dudv$; $b \equiv b(u', v') = \frac{1}{\varepsilon}\int_D uG dudv$; $c \equiv c(u', v') = \frac{1}{\varepsilon}\int_D u^2 G dudv$;

$$d \equiv d(u', v') = \frac{1}{\varepsilon}\int\limits_D v^2 G dudv;$$

$$\bar{u} = \frac{1}{\varepsilon}\int\limits_D \int\limits_{D'} uG dudvdu'dv';$$

$$\overline{u^2} = \frac{1}{\varepsilon}\int\limits_D \int\limits_{D'} u^2 G dudvdu'dv';$$

$$\overline{v^2} = \frac{1}{\varepsilon}\int\limits_D \int\limits_{D'} v^2 G dudvdu'dv';$$

$$\varepsilon = \int\limits_D \int\limits_{D'} G dudvdu'dv';$$

$\bar{u}$, $\overline{u^2}$, and $\overline{v^2}$ are the mean values of the Dalitz variables and their squares; and ε is the total efficiency of the experiment (including the efficiency of the reconstruction and selection of events) if the matrix element is equal to unity.

Let us introduce the notation

$$g = (g^+ + g^-)/2, \qquad h = (h^+ + h^-)/2,$$
$$k = (k^+ + k^-)/2,$$

$$\Delta g = g^+ - g^-, \qquad \Delta h = h^+ - h^-,$$
$$\Delta k = k^+ - k^-.$$

Expanding the $f^+(u', v')/f^-(u', v')$ ratio of the normalized Dalitz plots in series in Δg, Δh, and Δk and neglecting their quadratic terms, we obtain

$$r(u', v') = \frac{f^+(u', v')}{f^-(u', v')} \tag{A.1}$$
$$\approx 1 + \alpha(u', v')\Delta g + \beta(u', v')\Delta h + \gamma(u', v')\Delta k,$$

where

$$\alpha(u', v') = [b - a\overline{u} + h(b\overline{u^2} - c\overline{u}) \tag{A.2}$$
$$+ k(b\overline{v^2} - d\overline{u})]/D(u', v'),$$
$$\beta(u', v') = [c - a\overline{u^2} + g(c\overline{u} - b\overline{u^2})$$
$$+ k(c\overline{v^2} - d\overline{u^2})]/D(u', v'),$$
$$\gamma(u', v') = [d - a\overline{v^2} + g(d\overline{u} - b\overline{v^2})$$
$$+ h(d\overline{u^2} - c\overline{v^2})]/D(u', v'),$$

$$D(u', v') = (1 + g\bar{u} + h\overline{u^2} + k\overline{v^2})(a + gb$$
$$+ hc + kd).$$

In the case of $u' = u$ and $v' = v$ ("ideal" resolution), formulas (A.1) and (A.2) have the form

$$r_0(u, v) = 1 \tag{A.3}$$
$$+ \frac{A_0(u, v)\Delta g + B_0(u, v)\Delta h + C_0(u, v)\Delta k}{(1 + g\bar{u} + h\overline{u^2} + k\overline{v^2})(1 + gu + hu^2 + kv^2)},$$

where

$$A_0(u, v) = u - \overline{u} + h(u\overline{u^2} - u^2\overline{u}) \tag{A.4}$$
$$+ k(u\overline{v^2} - v^2\overline{u}),$$
$$B_0(u, v) = u^2 - \overline{u^2} + g(u^2\overline{u} - u\overline{u^2})$$
$$+ k(u^2\overline{v^2} - v^2\overline{u^2}),$$
$$C_0(u, v) = v^2 - \overline{v^2} + g(v^2\overline{u} - u\overline{v^2})$$
$$+ h(v^2\overline{u^2} - u^2\overline{v^2}).$$

REFERENCES

1. A. J. Bevan *et al.*, Phys. Lett. B **465**, 355 (1999).
2. A. Lai *et al.*, Eur. Phys. J. C **22**, 231 (2001).
3. A. Alavi-Harati *et al.*, Phys. Rev. Lett. **83**, 22 (1999).
4. K. Hagiwara *et al.*, Phys. Rev. D **66**, 010001 (2002).
5. A. A. Belkov *et al.*, Czech. J. Phys. B **55**, 193 (2004); hep-ph/0311209.
6. G. D'Ambrosio *et al.*, Phys. Lett. B **273**, 497 (1991).
7. G. Isidori *et al.*, Nucl. Phys. B **381**, 522 (1992).
8. E. Gamiz, J. Prades, and I. Scimemi, J. High Energy Phys., No. 09, 042 (2003); hep-ph/0401236.
9. I. V. Ajinenko *et al.*, Phys. Lett. B **567**, 159 (2003).
10. W. T. Ford *et al.*, Phys. Rev. Lett. **25**, 1370 (1970).
11. K. M. Smith *et al.*, Nucl. Phys. B **91**, 45 (1975).
12. G. A. Akopdzhanov *et al.*, in *Proceedings of the First International Workshop on Frontier Science—Charm, Beauty, and CP, Frascati, 2002*, Ed. by L. Benussi *et al.* (LNF, Frascati, 2002), p. 229.
13. V. V. Ammosov *et al.*, Preprint No. 98-2, IFVÉ (Institute of High Energy Physics, Protvino, 1998).
14. A. V. Vasil'ev *et al.*, Prib. Tekh. Éksp., No. 2, 50 (1993).
15. Yu. V. Gilitsky *et al.*, Preprint No. 93-10, IFVÉ (Institute of High Energy Physics, Protvino, 1993).

Translated by E. Kozlovsky

Physics of Atomic Nuclei, Vol. 68, No. 6, 2005, pp. 960–973. Translated from Yadernaya Fizika, Vol. 68, No. 6, 2005, pp. 998–1011.
Original Russian Text Copyright © 2005 by Binon, Blik, Donskov, Inaba, Kolosov, Lednev, Lishin, Mikhailov, Peigneux, Polyakov, Sadovsky, Samoilenko, Sobol, Stroot, Sugonyaev, Takamatsu, Tsuru, Fujii, Khaustov, Shimizu, Yasu.

ELEMENTARY PARTICLES AND FIELDS
Experiment

Investigation of the $\eta\eta$ System in $\pi^- p$ Interactions at a Momentum of 32.5 GeV/c at the GAMS-4π Spectrometer

F. Binon[1], A. M. Blik[2], S. V. Donskov[2], S. Inaba[3], V. N. Kolosov[2]*, A. A. Lednev[2], V. A. Lishin[2], Yu. V. Mikhailov[2], J. P. Peigneux[4], V. A. Polyakov[2], S. A. Sadovsky[2], V. D. Samoilenko[2], A. E. Sobol[2], J. P. Stroot[1], V. P. Sugonyaev[2], K. Takamatsu[5], T. Tsuru[3], I. Fujii[3], G. V. Khaustov[2], H. Shimizu[6], and Y. Yasu[3]

Received May 25, 2004; in final form, October 11, 2004

Abstract—The $\eta\eta$ system produced in charge-exchange $\pi^- p$ interaction at a momentum of 32.5 GeV/c is studied in an experiment performed with the GAMS-4π spectrometer at the 70-GeV accelerator of the Institute for High-Energy Physics (IHEP, Protvino). A partial-wave analysis is performed in the mass range between 1.1 and 3.9 GeV for $-t < 0.2$ (GeV/c)^2, S, D, G, and J waves being taken into account in this analysis. The S wave has a complicated structure, displaying peaks at about 1.5 and 1.7 GeV. These peaks are associated with the $f_0(1500)$ and $f_0(1710)$ mesons. One of the solutions (preferable one) involves the $f_0(2200)$ and $f_2(1950)$ resonances. The mass region above 2.4 GeV is dominated by the G wave. A broad state of mass about 3 GeV and width 0.7 GeV is found in the J wave. The parameters of the resonances in question and their production cross sections are measured.
© 2005 Pleiades Publishing, Inc.

1. INTRODUCTION

The $\eta\eta$ system has been studied in number of experiments with the aim of searches for exotic states. Interest in this system was motivated by the fact that, according to theoretical ideas, gluon states have an intense mode of decay to $\eta\eta$ [1]. The presence of only even waves in the $\eta\eta$ system simplifies the procedure of a partial-wave analysis significantly.

More than 20 years ago, a candidate for scalar glueballs, $G/f_0(1590)$ meson [2, 3], was discovered in studying the $\eta\eta$ system in charge-exchange $\pi^- p$ interaction. The observation of a G meson in the $\eta\eta$ system in the central-production reaction [4, 5] confirmed the hypothesis that this state may involve a significant gluon component. Later on, this state, denoted as the $f_0(1500)$ meson [6], was discovered in some other reactions (proton–antiproton annihilation, radiative decay of J/ψ) where it is natural to expect an enhanced production of gluon-rich mesons. All of this gives sufficient grounds to believe that the $f_0(1500)$ meson is a serious candidate for glueballs.

In the $\eta\eta$ system, there is yet another state, the $f_0(1710)$ meson, which is likely to have an exotic character. This resonance was observed in many experiments, but its spin had been ambiguous for a long time (two possible values of $J = 0$ and 2 had been considered). The observation of $f_0(1710)$ as a scalar state in the radiative decays of J/ψ [7], as well as data from the WA102 experiment for $\pi^+\pi^-$ and K^+K^- systems, made it possible to establish the scalar nature of the $f_J(1710)$ meson unambiguously [8, 9]. The first observation of the $f_J(1710)$ meson in the $\eta\eta$ system, together with the determination of its spin of $J = 0$, was reported by the WA102 Collaboration [10]. A reliable observation of two scalar states, $f_0(1500)$ and $f_0(1710)$, in the central production of the $\eta\eta$ system and an insignificant contribution to the mass spectrum of the signal from the $f_2(1525)$ meson remove any arguments against the splitting of the signal from $G/f_0(1590)$ into two states. Indeed, the main argument against this splitting [11] was based on the assumption that the reliable peak observed in the mass spectrum of the $K\bar{K}$ system in the WA76 experiment [12] was associated with the $f_2(1525)$ meson. However, this assumption contradicts data

[1]Université Libre de Bruxelles, Institut Interuniversitaire des Science Nucléaires, Be-1050 Bruxelles, Belgium.
[2]Institute for High-Energy Physics, Protvino, Moscow oblast, 142284 Russia.
[3]KEK (National Laboratory for High Energy Physics) 1-1 Oho, Tsukuba-shi, Ibaraki-ken 305, Japan.
[4]LAPP (Laboratoire d'Annecy-le-Vieux de Physique des Particules), BP 110, F-7491 Annecy-le-Vieux CEDEX, France.
[5]Engineering Faculty, Miyazaki University, Miyazaki, Japan.
[6]Research Center for Nuclear Physics, Osaka University, Mihogaoka 10-1 Ibaraki, Osaka 567, Japan.
*e-mail: Vladimir.Kolosov@ihep.ru

of the WA102 experiment. The presence of two narrow scalar states whose parameters agree with the results of lattice calculations for the glueball mass in the region around 1.6 GeV calls for pursuing further investigations of the $\eta\eta$ system.

The tensor sector is also of interest. In the $\eta\eta$ system, a $f_2(2175)$ meson, which is the candidate for tensor glueballs [4, 5, 10], was discovered in central production. According to lattice calculations, the mass of the lightest tensor glueball must fall within the range 2200–2300 MeV [13, 14]. One of the solutions [3] contains yet another state, $f_2(1810)$. This state can be associated with the signal seen in the $4\pi^0$ system in charge-exchange interaction [15] and in the central-production reaction [16].

Investigations of high-spin states is yet another realm in meson spectroscopy. The GAMS Collaboration discovered and studied three such states: the $a_4(2020)$, $\rho_5(2230)$, and $f_6(2520)$ mesons [6]. So far, there has been no experimental information about the $\eta\eta$ system in the high-mass region. Investigation of this region is one of the main objectives of the present study.

We have explored the $\eta\eta$ system in charge-exchange $\pi^- p$ interaction. The reaction

$$\begin{array}{c}\pi^- p \to M^0 n, \\ \quad\quad \lfloor\!\to \eta\eta \to 4\gamma\end{array} \qquad (1)$$

was studied at a momentum of 32.5 GeV/c, both η mesons being recorded by using the mode of decay to two photons. Our experiment was performed with the GAMS-4π spectrometer at the 70-GeV proton accelerator of the Institute for High-Energy Physics (IHEP, Protvino). A partial-wave analysis was performed in the mass range between 1.1 and 3.9 GeV for low values of the momentum transfer squared, $-t < 0.2\,(\mathrm{GeV}/c)^2$.

2. DESCRIPTION OF THE EXPERIMENTAL FACILITY

The GAMS-4π spectrometer is a further development of the GAMS-2000 facility [17]. The layout of the equipment used in our apparatus is shown in Fig. 1. The multiphoton GAMS-2000 spectrometer, a wide-aperture detector (WAD) of photons, a veto system, and a hadron calorimeter (GDA-100) are the main elements of the apparatus. Owing to the presence of the wide-aperture detector, the GAMS-4π facility makes it possible to attain simultaneously a high efficiency of the detection of low-energy photons emitted at large angles, a good separation of photons, and a high resolution in the effective mass of two photons in the forward direction. This is due to a relatively large distance (6.8 m) between the hydrogen target used and the GAMS-2000 spectrometer. The central part of the GAMS spectrometer is supplemented with an 8×8 matrix of PWO crystals, the cell dimensions being $19 \times 19 \times 200$ mm [18]. The wide-aperture detector is a projection electromagnetic calorimeter shaped as a lead–scintillator sandwich [19]. The detector has a sensitive area of 248×248 cm and a central hole whose dimensions are 36×36 cm and covers the angular range between 0.15 and 1 rad. The wide-aperture detector consists of four independent blocks of area 124×124 cm in each quadrant partitioned in depth into two modules. Each module involves 14 converter plates and 5-mm layers of scintillator plates. A converter plate is formed by a lead sheet 2 mm thick and two steel sheets 0.8 mm thick, all three being glued together. A scintillator layer consists of 48 scintillation "sticks" of width 25.8 mm and length 124 cm each. Each quadrant has seven layers of sticks arranged horizontally and seven layers of sticks arranged vertically. All seven horizontal layers are combined together to form a horizontal element. Accordingly, a vertical element is formed by the vertical layers. Thus, each quadrant of the wide-aperture detector has 96 (48×2) horizontal and 96 (48×2) vertical scintillation elements. Photomultiplier tubes (FEU-84-3) are used to record light. The total radiation length of the wide-aperture detector is $12.5X_0$. The energy resolution is $13\%/\sqrt{E(\mathrm{GeV})}$ [20]. The distance between the target and the front plane of the wide-aperture detector was slightly different in different data-acquisition runs, being about 1.2 m. All of the particles that passed through the central hole in the wide-aperture detector were recorded in the GAMS spectrometer.

A liquid-hydrogen target (LHT) was surrounded by a scintillation veto system and a lead-glass veto system, which recorded charged particles and photons emitted from the target. These particles originated predominantly from the decays of isobars formed in hadron interactions. The veto system (VS) has a high detection efficiency with respect to charged particles and photons, but it is weakly sensitive to recoil neutrons from reaction (1).

The trigger and the calibration procedure here are virtually identical to those described in [17]. The GAMS-4π spectrometer possesses a high detection efficiency with respect to reaction (1) in the region of $\eta\eta$ masses that extends up to 4.5 GeV.

Our experimental data were collected within five runs of accelerator operation. The total flux of π^- mesons transmitted through the target was about 1.1×10^{12} particles. The sensitivity of our measurements was about 1.5 pb^{-1}.

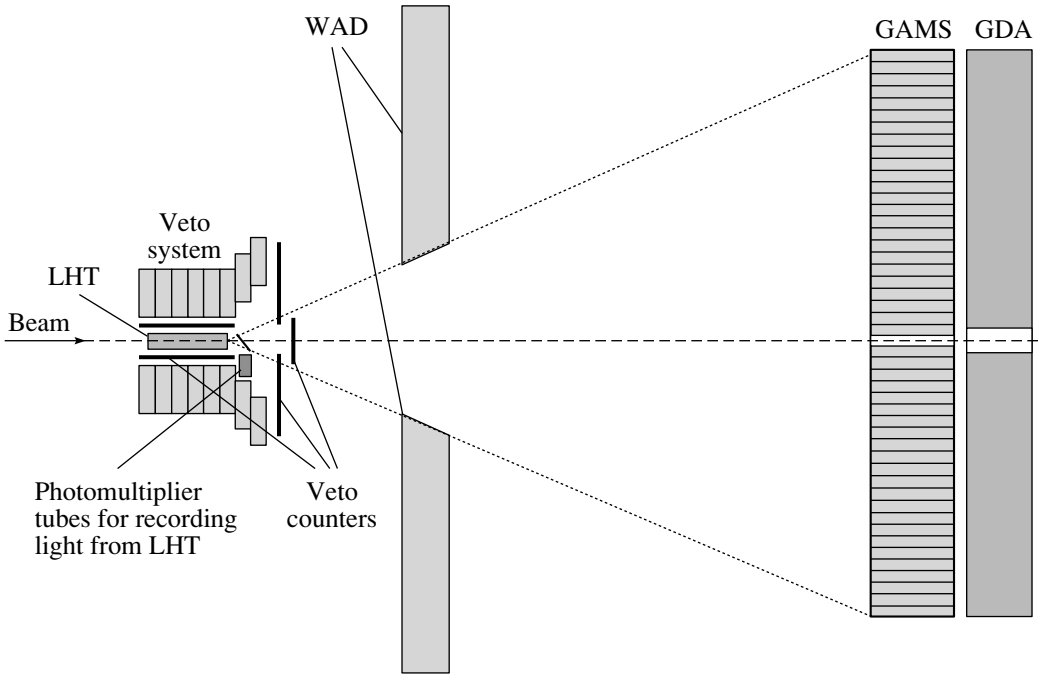

Fig. 1. Layout of the GAMS-4π spectrometer.

3. EVENT SELECTION

In order separate reaction (1) from reconstructed events that involve four photons in the final state, we applied the following selection criteria:

(i) The total energy of four photons must lie in the range 28.5–35.5 GeV.

(ii) The photon energy must exceed 0.6 GeV in the GAMS and 0.15 GeV in the wide-aperture detector.

(iii) Two photons that find their way to the GAMS are considered as one photon if the effective mass of this pair is less than 25 MeV and if the distance between the photons is smaller than 35 mm.

(iv) The distance between the beam axis and the point at which any photon hits the detector exceeds 30 mm.

(v) The invariant mass of a photon pair identified as an η meson must lie in the range $480 < m_{\gamma\gamma} < 620$ MeV.

(vi) The confidence level of a $2C$ fit (the masses of two η mesons were fixed) must be 92%.

In order to suppress the background from more intense $\pi^0\pi^0$ and $\pi^0\eta$ channels of the reaction, we rejected events if, at least in one of the combinations,

(a) the invariant mass of any photon pair was less than 200 MeV;

(b) the invariant mass of both photon pairs was less 260 MeV;

(c) the invariant mass of one photon pair was less than 260 MeV, while that of the other pair fell in the interval 420–680 MeV.

Figure 2 shows the momentum-transfer-squared distributions of events for $\eta\eta$ invariant masses ranging between 1.1 and 1.5, 1.5 and 1.9, 1.9 and 2.3, 2.3 and 2.8, 2.8 and 3.3, and 3.3 and 3.9 GeV. These distributions were approximated by the exponential dependence $Ae^{-b|t|}$ at low values of the momentum transfer, $-t < 0.2$ $(\mathrm{GeV}/c)^2$. For these mass intervals, we obtained the following values of the slope parameter b: 11.0 ± 0.15, 9.67 ± 0.15, 9.85 ± 0.15, 9.43 ± 0.17, 7.35 ± 0.17, and 4.23 ± 0.17 $(\mathrm{GeV}/c)^{-2}$. We note that the slope parameter changes significantly at mass values above 3 GeV. In order to enhance the contribution of single-pion exchange, only events characterized by $-t < 0.2$ $(\mathrm{GeV}/c)^2$ were selected for the ensuing analysis.

4. DETECTION EFFICIENCY AND INSTRUMENTAL RESOLUTION

The efficiency and the instrumental resolution were determined by the Monte Carlo method with allowance for spectrometer geometry and the resolution of the detectors, the selection procedures and the procedures for a kinematical analysis of events also being taken into account in doing this. The efficiency was represented in the form of an expansion in spherical functions $Y_L^M(\Omega_{\mathrm{GJ}})$ as

$$\varepsilon(\Omega_{\mathrm{GJ}}, M_{\eta\eta}, t) = \sum_{L,M} \varepsilon_{LM}(M_{\eta\eta}, t)\mathrm{Re}\{Y_L^M(\Omega_{\mathrm{GJ}})\}, \quad (2)$$

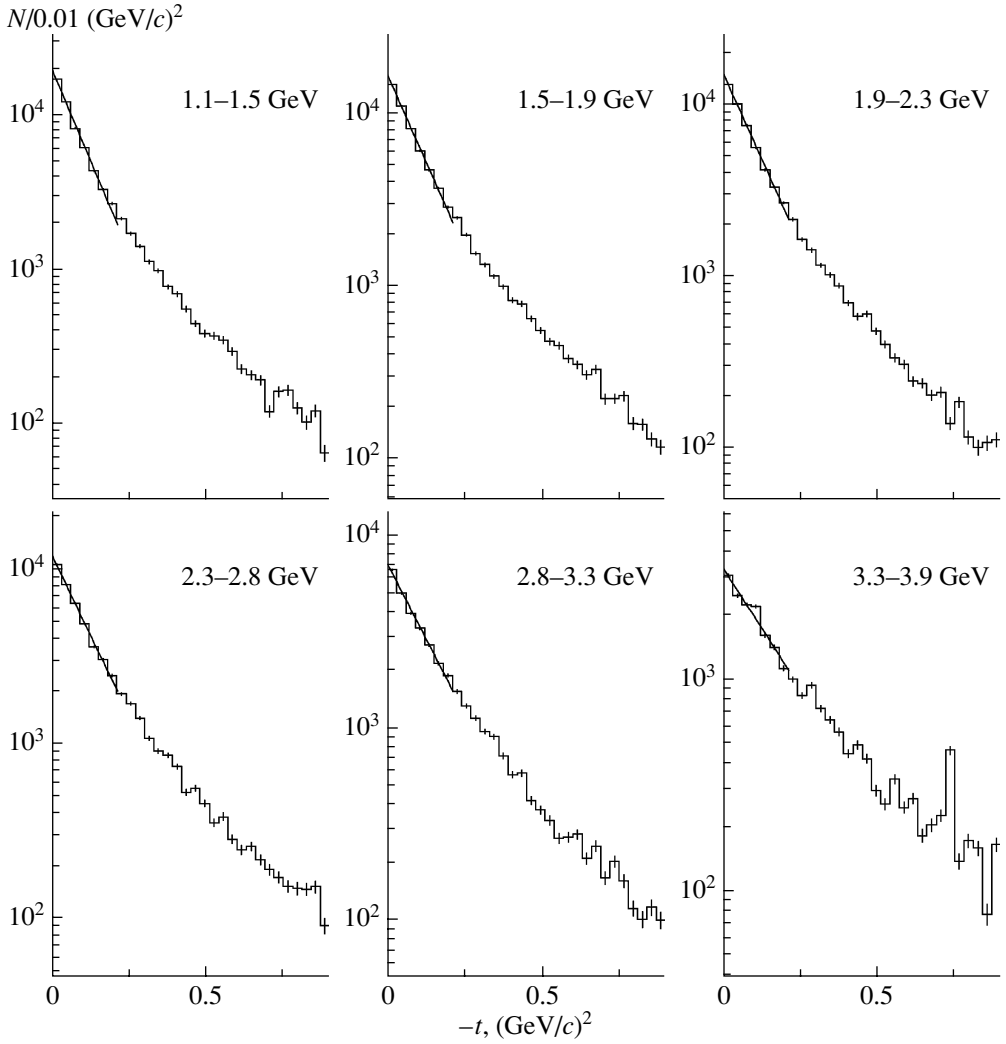

Fig. 2. Distribution of the squares of momentum transfers for various intervals of the $\eta\eta$ mass.

where $\Omega_{\mathrm{GJ}} \equiv [\cos\theta_{\mathrm{GJ}}, \phi_{\mathrm{TY}}]$ is the spatial angle in the Gottfried–Jackson frame.

The efficiency changes smoothly as a function of the effective mass of the $\eta\eta$ system up to 4.5 GeV, the dependence of the efficiency on t also being very weak for $-t < 0.8$ $(\mathrm{GeV}/c)^2$. In Fig. 3, the dashed curve represents the leading term ε_{00} of the expansion in (2) versus the invariant mass of the $\eta\eta$ system. This curve corresponds to the detection efficiency for events uniformly distributed over the phase space. At the $\eta\eta$ masses of 1.5, 2, 3, and 4 GeV, the instrumental mass resolution is 17, 35, about 80, and about 160 MeV, respectively.

5. EFFECTIVE-MASS SPECTRUM AND ANGULAR DISTRIBUTIONS

The mass spectrum of selected events is displayed in Fig. 3. This spectrum includes 101 700 events that passed the selection criterion $-t < 0.2$ $(\mathrm{GeV}/c)^2$. The spectrum in question exhibits a concentration of events in the region around 1.3 GeV and a narrow peak at 1.5 GeV. Some kinds of peaks can also be seen in the vicinities of 1.7 and 2.2 GeV. As will be shown below, a partial-wave analysis suggests that a peak at 1.5 GeV is most likely to be associated with the $f_0(1500)$ meson.

The angular distributions of η mesons in the Gottfried–Jackson frame can be expressed in the form of an expansion in spherical harmonics $Y_L^M(\Omega_{\mathrm{GJ}})$ as

$$I(\Omega_{\mathrm{GJ}}) = \sum_{L=0}^{8}\left[t_L^0 Y_L^0(\Omega_{\mathrm{GJ}}) + 2\sum_{M=1}^{2} t_L^M \mathrm{Re}\left\{Y_L^M(\Omega_{\mathrm{GJ}})\right\}\right]. \quad (3)$$

Figures 4 and 5 show the most significant coefficients t_L^M in the series expansion (3), which are further re-

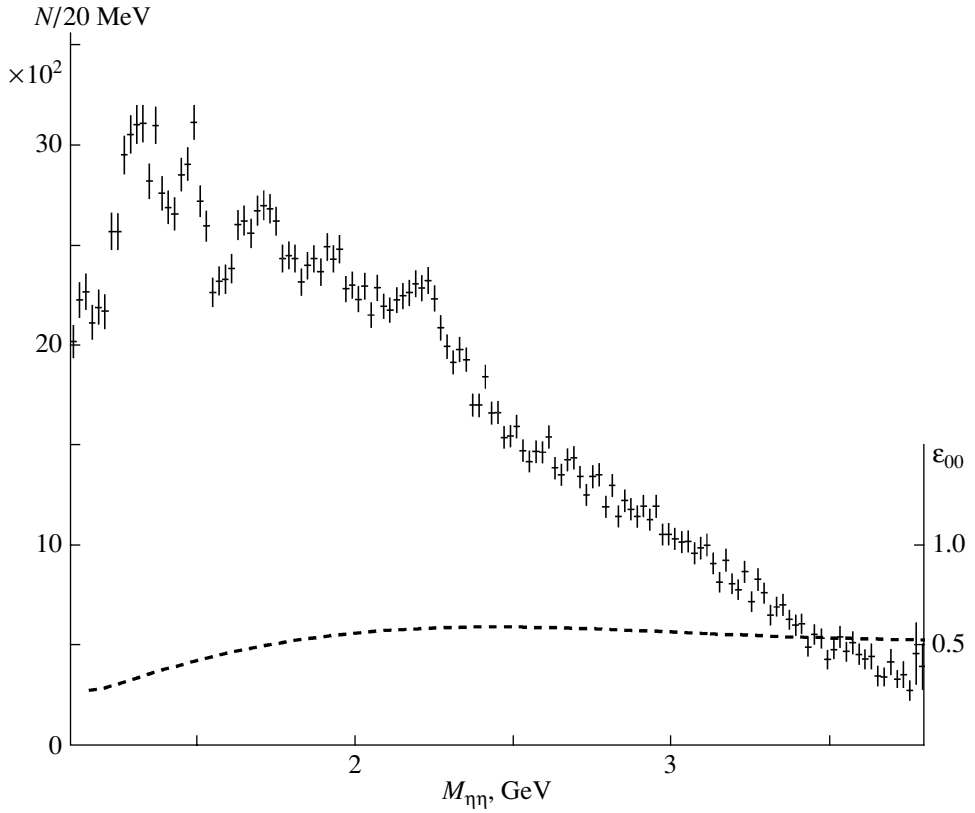

Fig. 3. Invariant-mass spectrum of the $\eta\eta$ system in reaction (1) for $-t < 0.2$ (GeV/c)^2. The dashed curve represents the leading term ε_{00} in the expansion (2) of the spectrometer efficiency.

ferred to as "moments" for the sake of brevity. Under the assumption of spin coherence, these moments can be expressed in terms of partial-wave amplitudes. Table 1 gives expressions for the moments in terms of the amplitudes of the S, D and G waves for $|m| \leq 1$. From the form of these expressions and the data in Figs. 4 and 5 alone, one can draw some conclusions on the relative contributions of partial waves. All $M > 2$ moments do not show significant deviations from zero, and this gives sufficient grounds to assume that the effect of $|m| \geq 2$ waves can be disregarded in analyzing the $\eta\eta$-mass range being studied. Moreover, the $M = 2$ moments do not differ significantly from zero either. We note in this connection that the moments in question can be expressed in terms of the D_-, D_+, G_-, and G_+ waves in the form of linear combinations—$(D_-^2 - D_+^2)$, $(G_-^2 - G_+^2)$, and $(D_-G_- + D_+G_+)$—this indicating that, in the reaction being studied, the amplitudes of the D_- and D_+ waves are approximately equal to the amplitudes of the G_- and G_+ waves, respectively. This is also so for higher waves and is well consistent with the Ochs–Wagner model [21].

The $M = 0$ moments are an order of magnitude greater than the corresponding $M = 1$ models, this being indicative of a dominant role of the $m = 0$ waves. In this case, the weak D_-- and G_--wave amplitudes can be observed in the interference with the more intense S and D_0 waves. For the D_+- and G_+-wave amplitudes, the situation is different; since they appear in the expressions for the moments defined by Eq. (3) in the form of their squares or in the form of the products of these amplitudes, their contribution is strongly suppressed. Thus, we see that, in the case where the D_-, D_+, G_-, and G_+ waves are strong, the $M = 2$ moments can be small if the amplitudes of the D_- and D_+ waves are equal to the amplitudes of the G_- and G_+ waves, respectively. There is yet another scenario in which the amplitudes of the D_-, D_+, G_-, and G_+ waves are merely small. As will be shown in the next section, the second scenario is preferable. Finally, we would like to highlight nonzero values of the moment t_{10}^0 for mass values in excess of 2.5 GeV, this suggesting the manifestation of spin-6 waves and waves of higher spin in this mass interval.

6. MASS-INDEPENDENT PARTIAL-WAVE ANALYSIS

The procedure of a mass-independent partial-wave analysis within the spin-coherence model was

Table 1. Angular momenta (3) in reaction (1) that are expressed in terms of partial-wave amplitudes (use is made here of the following condensed notation: $L^2 \equiv |L|^2$, $LL' \equiv \mathrm{Re}(LL'^*)$)

$$\sqrt{4\pi}t_0^0 = S^2 + D_0^2 + D_-^2 + D_+^2 + G_0^2 + G_-^2 + G_+^2$$
$$\sqrt{4\pi}t_2^0 = 2SD_0 + \frac{2\sqrt{5}}{7}D_0^2 + \frac{\sqrt{5}}{7}(D_-^2 + D_+^2) + \frac{12}{7}D_0G_0 + \frac{2\sqrt{30}}{7}(D_-G_- + D_+G_+) + \frac{20\sqrt{5}}{77}G_0^2 + \frac{17\sqrt{5}}{77}(G_-^2 + G_+^2)$$
$$\sqrt{4\pi}t_2^1 = \sqrt{2}SD_- + \frac{\sqrt{10}}{7}D_0D_- + \frac{2\sqrt{15}}{7}D_0G_- - \frac{4\sqrt{2}}{7}G_0D_- + \frac{10\sqrt{3}}{77}G_0G_-$$
$$\sqrt{4\pi}t_2^2 = \frac{\sqrt{15}}{7\sqrt{2}}(D_-^2 - D_+^2) - \frac{2\sqrt{5}}{14}(D_-G_- - D_+G_+) + \frac{5\sqrt{30}}{77}(G_-^2 - G_+^2)$$
$$\sqrt{4\pi}t_4^0 = 2SG_0 + \frac{6}{7}D_0^2 - \frac{4}{7}(D_-^2 + D_+^2) + \frac{40\sqrt{5}}{77}D_0G_0 + \frac{10\sqrt{6}}{77}(D_-G_- + D_+G_+) + \frac{486}{1001}G_0^2 + \frac{243}{1001}(G_-^2 + G_+^2)$$
$$\sqrt{4\pi}t_4^1 = \sqrt{2}SG_- + \frac{2\sqrt{15}}{7}D_0D_- + \frac{17\sqrt{10}}{77}D_0G_- + \frac{10\sqrt{3}}{77}G_0D_- + \frac{243\sqrt{2}}{1001}G_0G_-$$
$$\sqrt{4\pi}t_4^2 = \frac{\sqrt{10}}{7}(D_-^2 - D_+^2) + \frac{9\sqrt{15}}{77}(D_-G_- - D_+G_+) + \frac{81\sqrt{10}}{1001}(G_-^2 - G_+^2)$$
$$\sqrt{4\pi}t_6^0 = \frac{30\sqrt{65}}{143}D_0G_0 - \frac{20\sqrt{78}}{143}(D_-G_- + D_+G_+) + \frac{20\sqrt{13}}{143}G_0^2 - \frac{\sqrt{13}}{143}(G_-^2 + G_+^2)$$
$$\sqrt{4\pi}t_6^1 = \frac{10\sqrt{273}}{143}D_0G_- + \frac{5\sqrt{910}}{143}G_0D_- + \frac{2\sqrt{1365}}{143}G_0G_-$$
$$\sqrt{4\pi}t_6^2 = \frac{4\sqrt{910}}{143}(D_-G_- - D_+G_+) + \frac{\sqrt{1365}}{143}(G_-^2 - G_+^2)$$
$$\sqrt{4\pi}t_8^0 = \frac{490\sqrt{17}}{2431}G_0^2 - \frac{392\sqrt{17}}{2431}(G_-^2 + G_+^2)$$
$$\sqrt{4\pi}t_8^1 = \frac{294\sqrt{85}}{2431}G_0G_-$$
$$\sqrt{4\pi}t_8^2 = \frac{42\sqrt{595}}{2431}(G_-^2 - G_+^2)$$

described in detail elsewhere (see, for example, [22]). In order to fit angular distributions, the maximum-likelihood method is used in each mass interval. This reduces to minimizing, in terms of partial-wave amplitudes, the functional (see Table 1)

$$F = -\sum_{i=1}^{N} \ln I(\Omega_{\mathrm{GJ}}^i) + \sum_{L,M} t_L^M \varepsilon_L^M, \qquad (4)$$

where N is the number of events in the chosen mass bin, ε_L^M are moments in the expansion of the detection efficiency, and t_L^M are moments of angular distributions in terms of partial waves.

In order to analyze data in the range extending up to 1.7 GeV, the bin width was chosen to be 20 MeV. Only the $J = 0$ and 2 waves are significant in this mass range. Therefore, we have considered the S, D_0, D_-, and D_+ waves. Two possible solutions are illustrated in Fig. 6. The procedure for matching solutions in neighboring mass intervals is described in [23]. Because of a large intensity of the D wave at the reaction threshold in the second solution, we consider it as an unphysical solution. In the physical solution, the contribution of $m = 0$ waves is everywhere much greater than the contribution of $|m| = 1$ waves. The phase coherence of the D_0 and D_- waves (in our notation, the phase difference between these waves is π) is yet another special feature of the data, which was already observed in previous experiments devoted to studying the production of $\eta\eta$ and $K\bar{K}$ systems in charge-exchange reactions and which is in good agreement with the predictions of the Ochs–Wagner model. In the mass range extending up to 1.7 GeV, the contribution of the G wave is negligible, with the result that the chosen solution is unambiguous. At the last stage of the analysis, the amplitude of the G_0 wave was fixed, in the mass region bounded from above by 1.7 GeV, on the basis of the mass-dependent solution obtained earlier (see next section).

For a partial-wave analysis in the range of $\eta\eta$ masses between 1.7 and 2.5 GeV, the bin width was chosen to be 40 MeV. The contribution of $J \geq 4$ waves is sizable in the moments t_6^0 and t_8^0. Our analysis revealed that the contribution of higher waves is negligible in this interval. Only the S, D_0, and G_0 waves (which corresponds to $J = 0$, 2, and 4 at $m = 0$) were taken into account at the initial stage of our partial-wave analysis. Within this simplified model of a partial-wave analysis, there are two nontrivial solutions. At the next stage, the solutions obtained

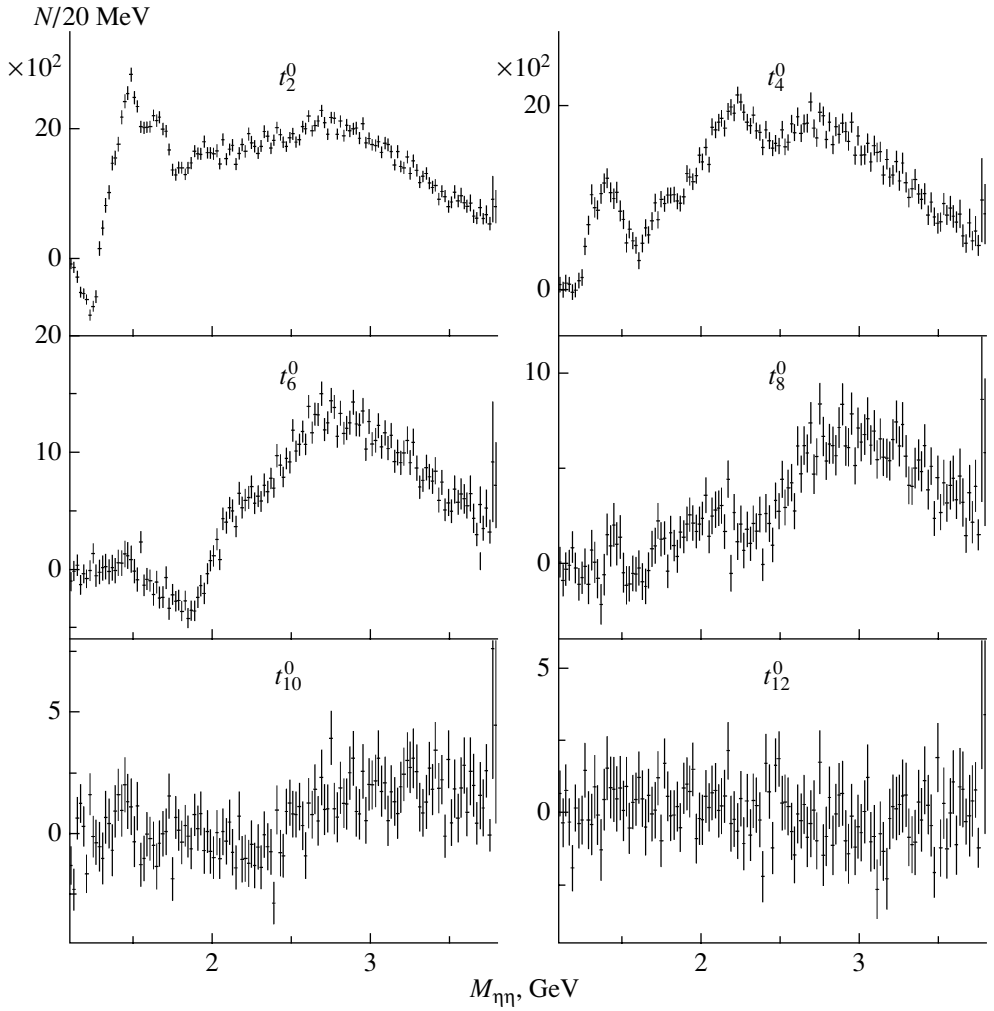

Fig. 4. Spherical-harmonic moments t_L^M at $M = 0$ versus the invariant mass of the $\eta\eta$ system for $L = 2, 4, 6, 8, 10$, and 12.

in this way were supplemented with $|m| = 1$ waves—namely, with D_-, D_+, G_-, and G_+—and the analysis was repeated. As a result, we found solutions where the contribution of the D_-, D_+, G_-, and G_+ waves is small. Since the $M = 0$ moments are everywhere much greater than the $M = 1$ moments, only these solutions are considered in the ensuing analysis. Thus, two different solutions were found in each mass interval.

One of the two possible solutions is shown in Fig. 7. In the S wave, one can observe three relatively broad peaks at 1.3, 1.6, and 2.2 GeV. In the S-wave spectrum, there is a narrow spectrum corresponding to the $f_0(1500)$ meson. Only one peak in the region around 1.6 GeV [$G(1590)$ meson] was observed in previous experiments of the GAMS Collaboration. The parameters of this resonance differed from the parameters of the scalar resonance observed in other experiments [24, 25]. In the present experiment, we have obtained an order of magnitude vaster data sample, and this made it possible to separate the signal in the vicinity of $G(1590)$ into two resonances, $f_0(1500)$ and $f_0(1710)$. This result is in agreement with data from the WA102 experiment, where a signal from the scalar meson $f_0(1710)$ was observed in the $\pi^+\pi^-$ and K^+K^- channels [8, 9]. A peak in the region around 2.2 GeV—it is observed only in this solution—is also noteworthy. In the D_0 wave, one can see three peaks occurring in the regions around 1.4, 1.9, and 2.4 GeV. Finally, the G_0 wave exhibits a signal from the $f_4(2050)$ meson. All of this taken together favors the interpretation of this solution as a physical one.

The second solution is displayed in Fig. 8. In the region around 2 GeV, the D wave exhibits a peak of potentially complicated structure.

In the mass region above 2.5 GeV, two solutions were found with the aid of a similar procedure. The mass-bin width was chosen to be 80 MeV. Since the $L = 10$ moment shows the presence of higher spin states, amplitudes corresponding to spin values of up

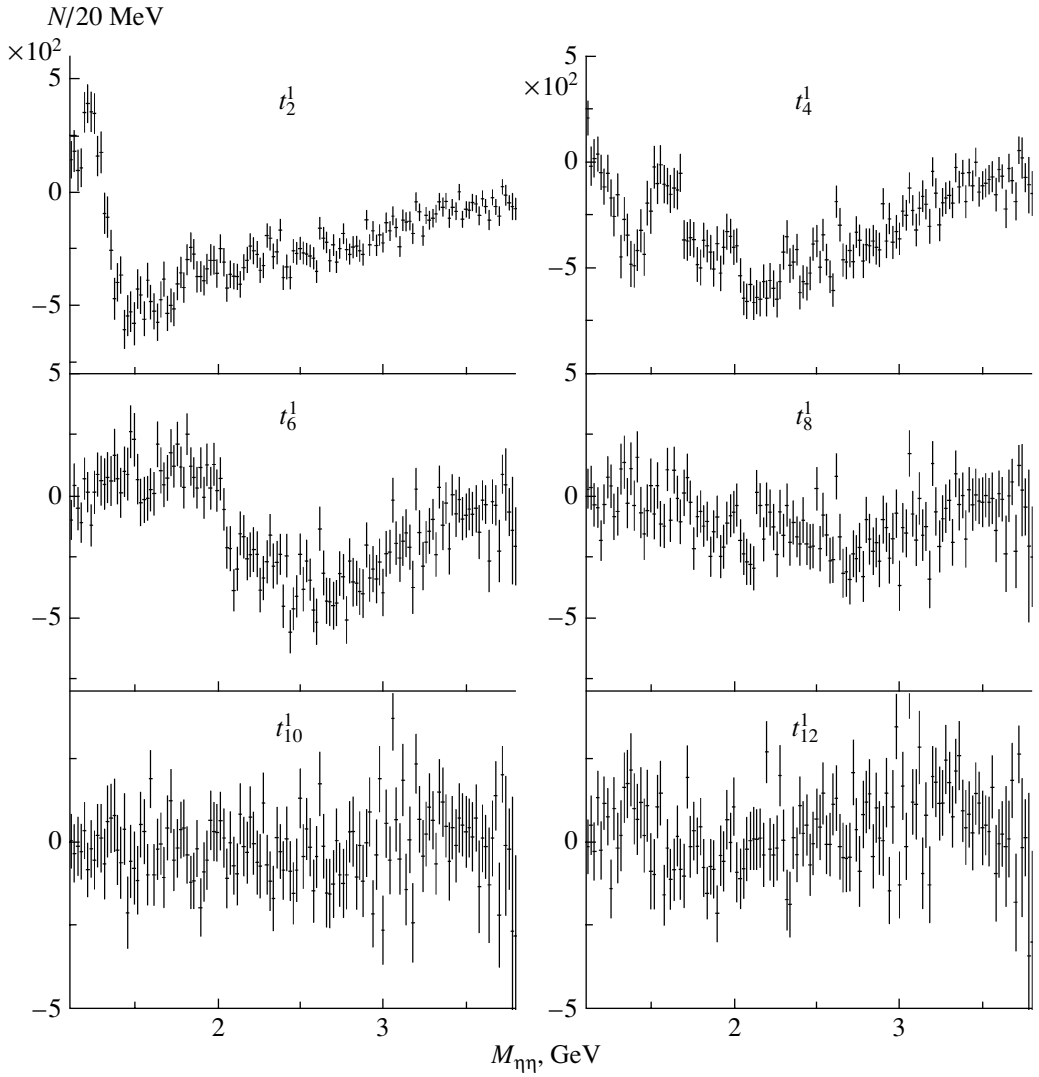

Fig. 5. Spherical-harmonic moments t_L^M at $M = 1$ versus the invariant mass of the $\eta\eta$ system for $L = 2, 4, 6, 8, 10$, and 12.

to six were included in the fit. A sharp change in the slope parameter of the t dependence in the vicinity of 3 GeV is indicative of the possible contribution from waves involving exchange of natural spin–parity. For amplitudes of unnatural spin–parity alone, the number of nontrivial solutions increases to 32 in this case. In a simplified version of the analysis, we found only two solutions, which correspond to two solutions in the region below 2.5 GeV. In the solutions obtained in this way, the J wave in Fig. 9 exhibits a broad peak in the vicinity of 3 GeV.

7. MASS-DEPENDENT PARTIAL-WAVE ANALYSIS

In order to determine the parameters of the resonances that are formed in the $\eta\eta$ system, the experimental moments corrected for the efficiency were approximated by the moments calculated on the basis of a model partial-wave analysis. The expression for the lm partial-wave amplitude has the form

$$A^{lm}(M_{\eta\eta}) = \sum_{k=1}^{N_{\rm res}} a_k^{lm} e^{i\theta_k} \mathrm{BW}_k(M_{\eta\eta}), \qquad (5)$$

where $N_{\rm res}$ is the number of resonances in each partial wave; a_k and θ_k are, respectively, the amplitude and the phase of the kth resonance; and BW_k are the relativistic Breit–Wigner amplitudes involving the relevant Blatt–Weisskopf barrier factors [26]. In order to describe a relatively narrow peak in the D wave in the region around 1.4 GeV, use was previously made of two close resonances $f_2(1270)$ and $f_2(1525)$ [3, 27]. In our fit, the parameters of these resonances were fixed at their values given by the Particle Data Group. For $f_2(1270)$, we assumed that the $\pi\pi$ mode saturates its total width.

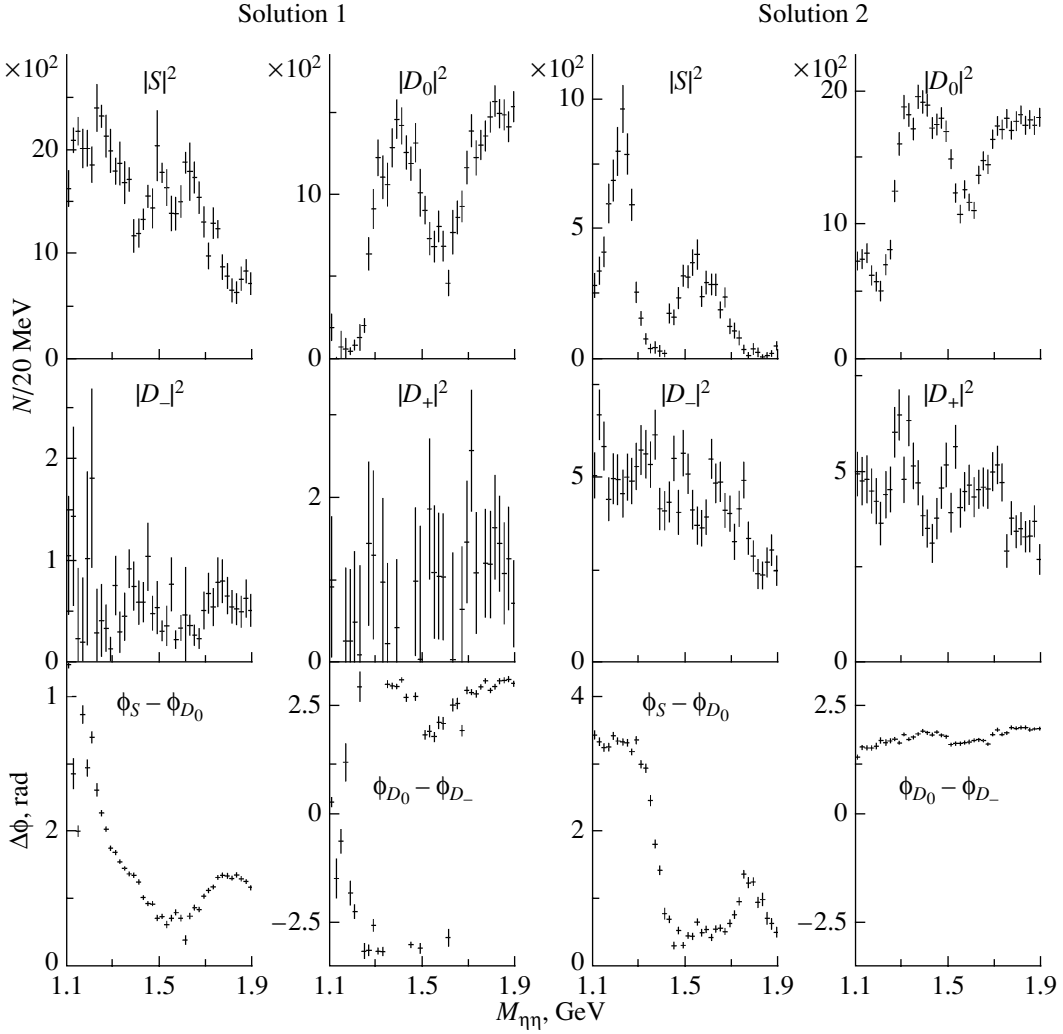

Fig. 6. Results of a mass-independent partial-wave analysis of the $\eta\eta$ system for $-t < 0.2$ (GeV/c)^2 in the mass interval 1.1–1.7 GeV with allowance for S, D_0, D_-, and D_+ waves. Two possible solutions are displayed. The second solution is considered as an unphysical one.

The χ^2/ndf values obtained for the first and second solutions were 1.19 and 1.32, respectively. The number of degrees of freedom (ndf) at the bin width of 20 MeV was about 3500. In Tables 2 and 3, we present the parameter values both for the resonances that clearly manifest themselves in the mass-independent partial-wave analysis and for the resonances that we presently consider only as background resonances. In these tables, the background resonances are labeled with an asterisk. Two asterisks there label background resonances that are discarded in some versions of the fit. The errors quoted in Tables 2 and 3 are predominantly systematic ones—they stem from the scatter of the parameters in different versions of the fit. There is a rather large systematic uncertainty in the parameters of the background resonances. By way of example, we indicate that, in order to describe a broad structure in the D wave in the region around 2 GeV in the second solution (Table 3), we had to introduce four Breit–Wigner resonances. At the same time, neither the mass spectrum nor the behavior of the phase of the D wave shows clear-cut indications of these objects. Moreover, the resonances in question do not have unambiguous analogs in the elementary-particle table of the Particle Data Group. In view of all this, we are inclined to believe that the second solution, which exhibits these resonances, is unphysical.

Tables 2 and 3 also give the cross sections for the coherent sum in each partial wave. Because of interference, these cross sections do not reduce to the sum of the cross sections for all resonances in a given wave. The relative systematic error in the sum is much less than the error in individual cross sections for each resonance. In some versions, a spin-8 background resonance was included in the fit. Probably,

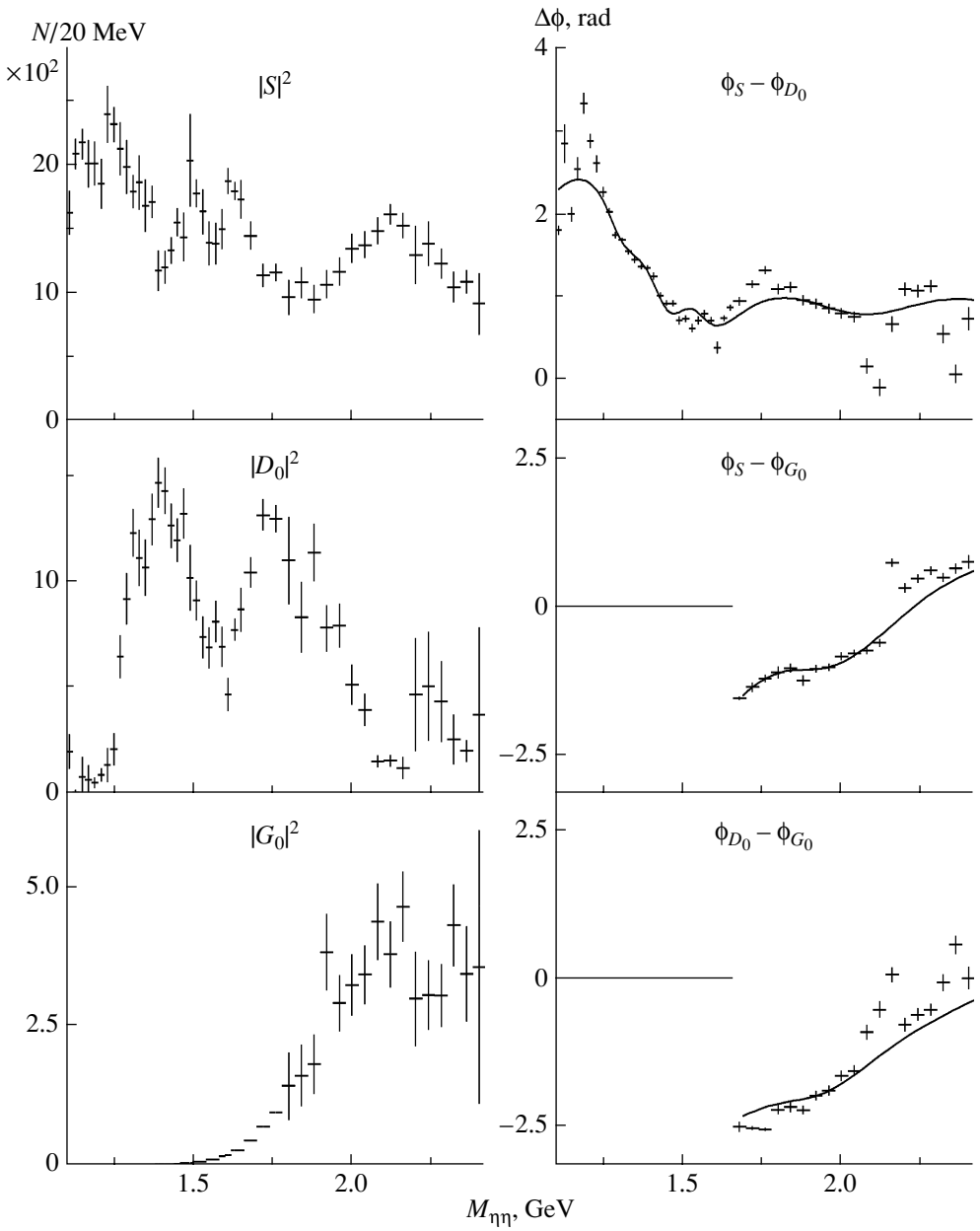

Fig. 7. First (preferable) mass-independent partial-wave analysis of the $\eta\eta$ system for $-t < 0.2\,(\mathrm{GeV}/c)^2$ in the mass interval 1.1–2.5 GeV with allowance for all waves up to spin-4 ones inclusive. Waves of "+" and "−" projections are not shown as insignificant ones. The solid curves represent the results of a mass-dependent partial-wave analysis.

the presence of this wave is responsible a slight discrepancy between the results of the mass-dependent and the mass-independent (without allowing for the spin-8 term) fit for the J in the region around 3.4 GeV and above (see Fig. 9).

By and large, we were able to attain an acceptable quality of data description with a finite set of resonances that manifest themselves in the physical (in our opinion) solution of the partial-wave analysis. At the same time, the method in question has some obvious limitations. First, other resonance-production and resonance-decay processes were disregarded in the analysis. Second, it is well known that the parametrization of amplitudes in the Breit–Wigner form is very accurate far off reaction thresholds and in the absence of a strong overlap of resonances. On the contrary, the presence of many overlapping resonances in each partial wave is characteristic of the $\eta\eta$ system in reaction (1), two resonances of considerable importance, $f_0(1370)$ and $f_2(1270)$, being produced near the threshold. In view of this, we consider our present results as a starting point for a

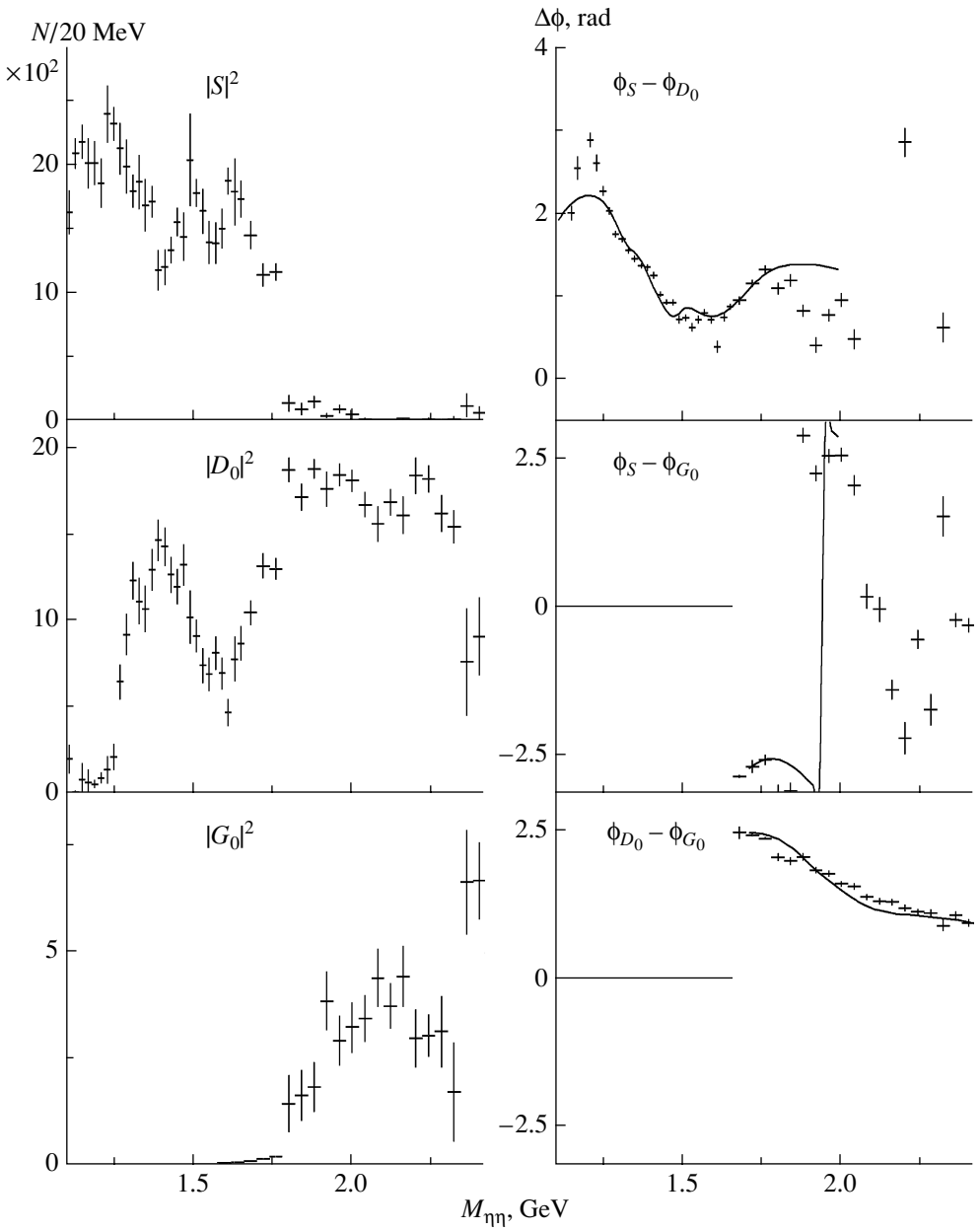

Fig. 8. As in Fig. 7, but for the second solution of a mass-independent partial-wave analysis.

global analysis that must also include our data on the $\pi^0\pi^0$ and K_SK_S systems.

8. DISCUSSION OF THE RESULTS

In the first (physical) solution, the S wave shows a series of peaks, this being indicative of the presence of a few scalar resonances. This behavior of the S wave is characteristic of the $\pi^0\pi^0$ system as well [23] and therefore seems quite natural.

In the mass-independent data analysis, a narrow peak corresponding to the $f_0(1500)$ meson is clearly seen in the S wave. This peak is also quite distinct in the effective-mass spectrum of the $\eta\eta$ system, the signal-to-background ratio there being about 1/6. Therefore, it comes as no surprise that this peak, which was also noticeable in the mass spectra in previous experiments characterized by poorer statistics [2, 3], was not mentioned by the authors of the respective articles. We note that, in the analysis of the $\eta\eta\pi$ system at the VES facility [28], the peak associated with the $f_0(1500)$ meson is also clearly seen in the $\eta\eta$ mass spectrum.

The resonance position $M = 1495 \pm 15$ MeV is in good agreement with the Particle Data Group value for the $f_0(1500)$ meson; however, the value obtained

Table 2. Parameters of the resonances obtained from a mass-dependent partial-wave analysis of the $\eta\eta$ system for the first solution [background resonances (see main body of the text) are labeled with an asterisk; background resonances that are discarded in some versions of the fit are labeled with two asterisks]

J^{PC}	Resonance	M, MeV	Γ, MeV	Cross section, nb
0^{++}	$f_0(1370)$	1350 ± 100	300 ± 50	70 ± 25
	$f_0(1500)$	1493 ± 7	90 ± 15	3.0 ± 0.8
	$f_0(1710)$	1670 ± 20	260 ± 50	48 ± 12
	$f_0(2200)$	2210 ± 50	380 ± 90	180 ± 35
	Total cross section in the S wave			240 ± 25
2^{++}	$f_2(1270)$	1275.4	185.1	30 ± 8
	$f_2(1525)$	1524.5	76	1.8 ± 0.9
	$f_2(1950)$	1930 ± 25	450 ± 50	90 ± 30
	*	2700 ± 90	850 ± 100	70 ± 25
	**	$\sim$1590	$\sim$400	$\sim$20
	Total cross section in the D wave			154 ± 12
4^{++}	$f_4(2050)$	2005 ± 10	340 ± 80	11 ± 3
	*	$\sim$2800	$\sim$700	$\sim$60
	*	$\sim$3500	$\sim$800	$\sim$20
	**	1710 ± 7	130 ± 30	$\sim$0.5
	Total cross section in the G wave			70 ± 14
6^{++}	f_6	3100 ± 100	700 ± 130	13 ± 4
8^{++}	**	$\sim$3600	$\sim$800	$\sim$5

for its width, $\Gamma = 90 \pm 20$ MeV, is somewhat smaller than its counterpart given in the Particle Data Group tables.

We interpret the peak in the S wave around 1.7 GeV as the $f_0(1710)$ meson. For its mass and width, we obtained the values

$$M = 1680 \pm 20 \text{ MeV} \quad \text{and} \quad \Gamma = 260 \pm 50 \text{ MeV}.$$

The $f_0(2200)$ resonance can be seen in only the physical solution. We note that this state manifests itself only upon including the G wave in the analysis.

The physical solution also shows evidence for the production of a $f_2(1950)$ meson, which was previously observed in the $\eta\eta$ system in proton–antiproton annihilation [29]. On the other hand, this solution does not exhibit a $f_2(2150)$ meson, which was previously observed in the central-production process in the WA102 experiment [9, 10].

In either solution, the $f_0(1370)$ resonance is observed in the low-mass region. However, one can see that, while the masses and widths of the other resonances in the S wave remain more or less stable in different versions of the fit, the mass and the width of $f_0(1370)$ change within rather broad intervals. The physical background in the S wave was described as the subthreshold-resonance tail. It turned out that the parameters of this background term correlate very strongly with the parameters of the $f_0(1370)$ resonance. In view of this, the parameters of this reso-

Table 3. Parameters of the resonances obtained from a mass-dependent partial-wave analysis of the $\eta\eta$ system for the second solution (the meaning of the asterisks here is identical to that in Table 2)

J^{PC}	Resonance	M, MeV	Γ, MeV	Cross section, nb
0^{++}	$f_0(1370)$	1300 ± 80	250 ± 100	85 ± 10
	$f_0(1500)$	1500 ± 15	85 ± 20	2.6 ± 0.9
	$f_0(1710)$	1690 ± 25	260 ± 60	44 ± 12
	Total cross section in the S wave			120 ± 12
2^{++}	$f_2(1270)$	1275.4	185.1	40 ± 9
	$f_2(1525)$	1524.5	76	1.6 ± 0.7
	*	~1900	~250	
	*	~2000	~350	
	*	~2000	~550	
	*	~3500	~900	
	Total cross section in the D wave			290 ± 25
4^{++}	$f_4(2050)$	1960 ± 20	380 ± 40	19 ± 3.5
	*	~2800	~750	~70
	Total cross section in the G wave			75 ± 14
6^{++}	f_6	3230 ± 120	700 ± 140	11 ± 4
8^{++}	**	~3600	~900	~5

nance have yet to be established precisely. The situation in other experiments was similar [6].

In either solution of the partial-wave analysis, there is also a broad state of spin 6. For its mass and width, we obtained the following estimates:

$$M = 3150 \pm 150\ \text{MeV} \quad \text{and} \quad \Gamma = 700 \pm 150\ \text{MeV}.$$

Further, we use the cross section 2.6 ± 0.2 μb measured at 38 GeV/c for the production of a $f_2(1270)$ meson in the charge-exchange reaction and introduce the correction for the energy dependence of this cross section [23] in order to estimate the branching ratio for the decay $f_2(1270) \to \eta\eta$. This yields

$$\text{Br}(f_2(1270) \to \eta\eta) = (2.7 \pm 0.7) \times 10^{-3},$$

which is in agreement with the Particle Data Group value of this quantity and which indicates that the data of the present experiment are by and large consistent with earlier data.

9. CONCLUSIONS

We have performed a partial-wave analysis of the $\eta\eta$ system in charge-exchange $\pi^- p$ interaction at 32.5 GeV/c. The analysis covers the mass range between 1.1 and 3.9 GeV for $-t < 0.2\,(\text{GeV}/c)^2$ and takes into account S, D, G, and J waves. The most probable physical solution has been determined.

In the mass range below 2 GeV, our partial-wave analysis has revealed the presence of a few overlapping resonances of various spins. In particular, the S wave exhibits three distinct states: $f_0(1370)$, $f_0(1500)$, and $f_0(1710)$, two partly overlapping states $f_0(1500)$ and $f_0(1710)$ being separated in the region of the $G(1590)$ meson owing to vast statistics of the experiment.

At high masses of the $\eta\eta$ system, preference in the partial-wave analysis has been given to the solution that shows the $f_2(1950)$ and $f_0(2200)$ resonances.

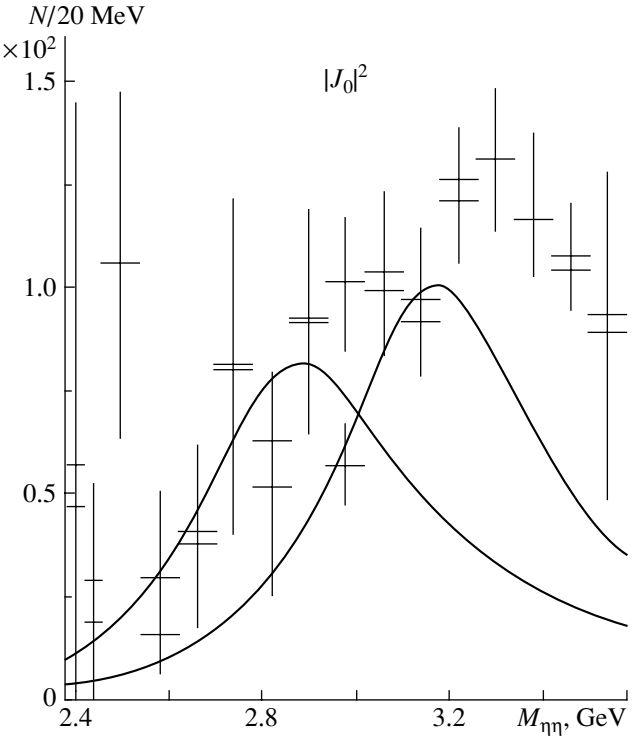

Fig. 9. J_0 wave obtained from a mass-independent partial-wave analysis of the $\eta\eta$ system for $-t < 0.2\ (\mathrm{GeV}/c)^2$ in the mass interval 2.4–3.6 GeV. Shown are the results for two mass-independent solutions. The solid curves represent the results of a mass-dependent partial-wave analysis for two solutions. A slight discrepancy between the results of the mass-independent and mass-dependent partial-wave analyses at masses of about 3.4 GeV and higher mass values is likely to be due the spin-8 effect (see main body of the text).

The mass range above 2.4 GeV is dominated by the G wave. A broad state of mass 3150 ± 150 MeV and width 700 ± 150 MeV has been discovered in the J wave.

ACKNOWLEDGMENTS

We are grateful to the directorate of IHEP for support of our experiments at the GAMS-4π spectrometer and to V.F. Obraztsov, V.I. Romanovsky, and Yu.P. Gouz for stimulating discussions.

This work was supported in part by the Russian Foundation for Basic Research (project no. 04-02-17450).

REFERENCES

1. S. S. Gershteĭn, A. K. Likhoded, and Yu. D. Prokoshkin, Yad. Fiz. **39**, 251 (1984) [Sov. J. Nucl. Phys. **39**, 156 (1984)].
2. F. Binon *et al.*, Nuovo Cimento A **78**, 313 (1983).
3. D. Alde *et al.*, Yad. Fiz. **44**, 120 (1986) [Sov. J. Nucl. Phys. **44**, 75 (1986)].
4. D. Alde *et al.*, Phys. Lett. B **201**, 160 (1988).
5. A. V. Singovski, Nuovo Cimento A **107**, 1911 (1994).
6. K. Hagiwara *et al.*, Phys. Rev. D **66**, 010001 (2002).
7. BES Collab. (J. Z. Bai *et al.*), Phys. Lett. B **472**, 207 (2000); Phys. Rev. Lett. **81**, 1179 (1998).
8. D. Barberis *et al.*, Phys. Lett. B **453**, 316 (1999).
9. D. Barberis *et al.*, Phys. Lett. B **453**, 305 (1999).
10. D. Barberis *et al.*, Phys. Lett. B **479**, 59 (2000).
11. Yu. D. Prokoshkin, Dokl. Akad. Nauk SSSR **316**, 900 (1991) [Sov. Phys. Dokl. **36**, 155 (1991)].
12. T. A. Armstrong *et al.*, Phys. Lett. B **227**, 186 (1989).
13. G. Bali *et al.*, Phys. Lett. B **309**, 378 (1993).
14. J. Sexton *et al.*, Phys. Rev. Lett. **75**, 4563 (1995).
15. D. Alde *et al.*, Phys. Lett. B **198**, 286 (1987).
16. D. Alde *et al.*, Yad. Fiz. **47**, 1273 (1988) [Sov. J. Nucl. Phys. **47**, 810 (1988)].
17. F. Binon *et al.*, Nucl. Instrum. Methods Phys. Res. A **248**, 86 (1986).
18. A. M. Blick *et al.*, Preprint No. 96-57, IFVÉ (Inst. High Energy Phys., Protvino, 1996); F. G. Binon *et al.*, Preprint No. 97-4, IFVÉ (Inst. High Energy Phys., Protvino, 1997); Nucl. Instrum. Methods Phys. Res. A **428**, 291 (1999).
19. Yu. D. Prokoshkin, Preprint No. 87-99, IFVÉ (Inst. High Energy Phys., Serpukhov, 1987).
20. S. A. Akimenko *et al.*, Preprint No. 88-16, IFVÉ (Inst. High Energy Phys., Serpukhov, 1988).
21. W. Ochs and F. Wagner, Phys. Lett. B **44B**, 271 (1973).
22. S. U. Chung, Phys. Rev. D **56**, 7299 (1997).
23. D. Alde *et al.*, Eur. Phys. J. A **3**, 361 (1998).
24. C. Amsler *et al.*, Phys. Lett. B **340**, 259 (1994).
25. D. Barberis *et al.*, Phys. Lett. B **413**, 217 (1997).
26. M. Svec, Phys. Rev. D **53**, 2343 (1996); J. Blatt and W. Weisskopf, *Theoretical Nuclear Physics* (Wiley, New York, 1952; Inostrannaya Literatura, Moscow, 1954), p. 359.
27. R. S. Longacre *et al.*, Phys. Lett. B **177**, 223 (1986).
28. D. V. Amelin *et al.*, Preprint No. 95-112, IFVÉ (Inst. High Energy Phys., Protvino, 1995).
29. A. V. Anisovich *et al.*, Phys. Lett. B **449**, 145 (1999).

Translated by A. Isaakyan

Physics of Atomic Nuclei, Vol. 68, No. 6, 2005, pp. 974–981. Translated from Yadernaya Fizika, Vol. 68, No. 6, 2005, pp. 1012–1019.
Original Russian Text Copyright © 2005 by Aleev, Amaglobeli, Ardashev, Balandin, Basiladze, Berezhnev, Bogdanova, Boguslavsky, Vasiliev, Vischnevskaya, Volkov, Vorobiev, Voronin, Golovnya, Golubkov, Gorokhov, Gorkov, Gramenitsky, Grishin, Grishkevich, Egorov, Ezhov, Ermakov, Ermolov, Zhidkov, Zakamsky, Zapolsky, Zverev, Zmushko, D. Zotkin, S. Zotkin, Karmanov, Kiryakov, V. Kozlov, Yu. Kozlov, Kokoulina, Korotkov, Kosarev, Kramarenko, Kubarovsky, Kuznetsov, N. Kuzmin, V. Kuzmin, Kurchaninov, Lanshikov, Larichev, Levitsky, Leflat, Lyutov, Maiorov, Merkin, Minaenko, Mitrofanov, Moiseev, Murzin, Nikitin, Nomokonov, Oleinik, Orfanitsky, Parakhin, Petrov, Pilavova, Pleskach, Popov, Rudenko, Rufanov, Riadovikov, Senko, Sidorov, Soldatov, Tikhonova, Topuria, Furmanec, Kholodenko, Tsyupa, Shalanda, Shafranov, Yukaev, Yakimchuk.

ELEMENTARY PARTICLES AND FIELDS
Experiment

Observation of a Narrow Baryon Resonance Decaying to pK_S^0 in Proton–Nucleus Interactions at 70 GeV/c with the SVD-2 Setup

A. N. Aleev[1)], N. S. Amaglobeli[†1)], E. N. Ardashev[2)], V. P. Balandin[1)], S. G. Basiladze[3)], S. F. Berezhnev[3)], G. A. Bogdanova[3)], I. V. Boguslavsky[1)], M. V. Vasiliev[2)], A. M. Vischnevskaya[3)], V. Yu. Volkov[3)], A. P. Vorobiev[2)], A. G. Voronin[3)], S. N. Golovnya[2)], S. A. Golubkov[4)], S. A. Gorokhov[2)], A. V. Gorkov[5)], I. M. Gramenitsky[1)], N. I. Grishin[3)], Ya. V. Grishkevich[3)], N. N. Egorov[4)], V. B. Ezhov[3)], G. G. Ermakov[3)], P. F. Ermolov[3)], N. K. Zhidkov[1)], L. L. Zakamsky[2)], V. N. Zapolsky[2)], E. G. Zverev[3)], V. V. Zmushko[2)], D. S. Zotkin[3)], S. A. Zotkin[3)], D. E. Karmanov[3)], A. A. Kiryakov[2)], V. V. Kozlov[3)], Yu. F. Kozlov[4)], E. S. Kokoulina[1)], N. V. Korotkov[3)], I. G. Kosarev[1)], V. A. Kramarenko[3)], A. V. Kubarovsky[3)*], E. N. Kuznetsov[3)], N. A. Kuzmin[1)], V. A. Kuzmin[3)], L. L. Kurchaninov[2)], G. I. Lanshikov[1)], A. N. Larichev[3)], M. S. Levitsky[2)], A. K. Leflat[3)], S. I. Lyutov[3)], S. V. Maiorov[3)], M. M. Merkin[3)], A. A. Minaenko[2)], G. Ya. Mitrofanov[2)], A. M. Moiseev[†2)], V. S. Murzin[3)], V. A. Nikitin[1)], P. P. Nomokonov[3)], A. A. Oleinik[1)], S. V. Orfanitsky[3)], V. V. Parakhin[2)], V. S. Petrov[2)], L. V. Pilavova[5)], A. V. Pleskach[2)], V. V. Popov[3)], R. E. Rudenko[2)], I. A. Rufanov[1)], V. N. Riadovikov[2)], V. A. Senko[2)], A. I. Sidorov[4)], M. M. Soldatov[2)], L. A. Tikhonova[3)], T. P. Topuria[1)], N. F. Furmanec[1)], A. G. Kholodenko[2)], Yu. P. Tsyupa[2)], N. A. Shalanda[2)], M. D. Shafranov[†1)], A. I. Yukaev[1)], and V. I. Yakimchuk[2)]**

The SVD Collaboration

Received July 6, 2004; in final form, November 23, 2004

Abstract—Data from the SVD-2 experiment that were obtained at the IHEP accelerator in 70-GeV/c proton–nucleus interactions are analyzed with the aim of searches for an exotic Θ^+ baryon that decays through the pK_S^0 channel. The reaction $pN \to pK_S^0 + X$ characterized by a bounded multiplicity of charged secondaries is used for this analysis. A resonance of mass $M = 1526 \pm 3(\text{stat.}) \pm 3(\text{syst.})$ MeV/c^2 and width $\Gamma < 24$ MeV/c^2 is observed in the invariant-mass spectrum of the pK_S^0 system at a statistical significance of 5.6σ. The mass and the width of this resonance correspond to the recently found positive-strangeness Θ^+ baryon, which was predicted to be an exotic baryon consisting of five quarks (pentaquark), $uudd\bar{s}$. The total cross section for the production of a Θ^+ baryon in pA interactions is estimated at a value within the range 30–120 μb for $x_F \geq 0$. An analysis of the A dependence of the cross section for Θ^+-baryon production does not reveal a significant deviation from the A dependence for inelastic events ($\sim A^{0.7}$). © *2005 Pleiades Publishing, Inc.*

1. INTRODUCTION

Exotic baryons consisting of five quarks (pentaquarks) and their properties were predicted by Diakonov, Petrov, and Polyakov on the basis of the chiral soliton model in 1997 [1], although the first theories

[†]Deceased.
[1)]Joint Institute for Nuclear Research, Dubna, Moscow oblast, 141980 Russia.
[2)]Institute for High Energy Physics, Protvino, Moscow oblast, 142284 Russia.
[3)]Institute of Nuclear Physics, Moscow State University, Vorob'evy gory, Moscow, 119992 Russia.
[4)]Research Institute of Material Science and Technology, Zelenograd, Moscow, 103460 Russia.
[5)]NIITAL Research and Production Association, Zelenograd, Moscow, 103460 Russia.
[*]e-mail: alex_k@hep.sinp.msu.ru
[**]e-mail: larisa@sinp.msu.ru

describing pentaquark hadrons were proposed a few decades ago [2–6]. In [1], the Θ^+ baryon, which is the lightest member of the antidecouplet of pentaquarks, had a mass of 1530 MeV/c^2, a width of $\Gamma \leq 15$ MeV/c^2, a spin of 1/2, and a positive parity. Later on, Stancu and Risca [7] proposed describing a stable $uudd\bar{s}$ pentaquark within the constituent quark model. Capstick *et al.* [8] put forth the idea of an isotensor pentaquark, while Karliner and Lipkin [9] developed a cluster model, considering the Θ^+ baryon as a bound diquark–triquark state. Jaffe and Wilczek [10] proposed a model where the Θ^+ baryon consists of two diquarks (ud) and a strange antiquark. Simultaneously, attempts were made to predict pentaquarks of negative and positive parity by using lattice QCD models [11, 12]. The model of chiral solitons was described in more detail in the review article of Kopeliovich [13].

The predictions of Diakonov, Petrov, and Polyakov [1] gave impetus to experimental searches for pentaquarks; as a result, corroborations that the Θ^+ baryon exists recently came from several laboratories (LEPS [14], DIANA [15], CLAS(d) [16, 17], SAPHIR [18], ITEP [19], CLAS(p) [20]). In those experiments, the Θ^+ baryon was observed as a narrow resonance peak in the nK^+ or pK^0_S invariant-mass spectra, its mass being about 1540 MeV/c^2. More recently, the HERMES Collaboration reported the observation of a narrow baryon state of mass 1528 MeV/c^2 in quasireal photoproduction [21], while the ZEUS Collaboration recorded a peak at 1522 MeV/c^2 in the pK^0_S channel [22].

In the present study, we report on the results of our searches for the Θ^+ baryon in the proton–nucleus interactions (in silicon, carbon, and lead targets) induced by a 70-GeV/c proton beam from the accelerator of the Institute for High Energy Physics (IHEP, Protvino). Specifically, we study the reactions

$$pN \to \Theta^+ + X, \quad \Theta^+ \to pK^0_S, \quad K^0_S \to \pi^+\pi^-$$

by using the SVD-2 setup.

The data obtained in this way were analyzed for the inclusive reaction of bounded charged-particle multiplicity in the region of projectile-proton fragmentation ($x_F(pK^0_S) > 0$) [23].

2. SVD-2 SETUP

The main objective of the SVD-2 experiment is studying charmed-particle production in hadron-nucleus interactions at threshold energies [24–30].

The layout of the SVD-2 setup is shown in Fig. 1. The basic elements of the setup are the following:

(1) a high-precision microstrip vertex detector (MSVD) including

(a) a microstrip beam telescope (MBT) [it consists of three pairs of XY silicon microstrip detectors (MSD 1–6) having 128 strips spaced by 50 μm],

(b) an active target (AT) [it consists of five microstrip silicon detectors of thickness 300 μm, a lead foil 220 μm thick, and a carbon target 500 μm thick (the distance between all targets is 4 mm)],

(c) a microstrip silicon detector (MSD) {it consists of three pairs of XY microstrip silicon detectors (MSD 7 and 8 have 640 strips spaced by 25 μm, MSD 9 and 10 have 640 strips spaced by 50 μm, and MSD 11 and 12 have 1024 strips spaced by 50 μm) and a $UYVX$ quadruplet (MSD 13–16) having 1024 strips spaced by 50 μm [27]};

(2) a large-aperture magnetic spectrometer (LAMS) including

(a) and electromagnet MC-7A characterized by an aperture of 1.8×1.3 m^2 and a distance of 3 m between the magnetic poles (it creates a uniform magnetic field of strength 1.18 T),

(b) two sets of wire proportional chambers (WPC) (the first set is formed by one UYV triplet characterized by a sensitive area of 1.0×1.0 m^2 and a distance of 2 mm between the wires and is placed in front of the magnet in the scattered magnetic field; the second set consists of five triplets UYV of sensitive area 1.0×1.5 m^2; some chambers of this set are placed in front of the magnet, while the remaining ones (13 chambers) are positioned between the magnetic poles in a uniform magnetic field [28]);

(3) a multicell threshold Cherenkov counter (TCC) (the counter was constructed for identifying charged particles; it has an entrance aperture of 177×130 cm^2 and consists of 32 spherical mirrors arranged in four rows of eight; the threshold momenta of charged particles are 4 and 21 GeV/c for π mesons and protons, respectively; the counter is filled with Freon and is operated at a temperature of 20°C and atmospheric pressure; in the momentum range from 4 to 21 GeV/c, the detection efficiency for charged pions is 70% in the data-acquisition run);

(4) a gamma detector (DEGA) (it consists of 1536 full-absorption lead glass Cherenkov counters; each counter has an area of 38×38 mm^2 and a length of 505 mm; the total sensitive area of the detector is 1.8×1.2 m^2; the gamma detector ensures the detection of photons in the energy range from 50 MeV to 20 GeV at a coordinate resolution of 2 to 3 mm).

The SVD-2 trigger system generated a trigger signal that was based on data obtained with the beam scintillation detectors placed in front of the active target, data obtained with the scintillation hodoscope

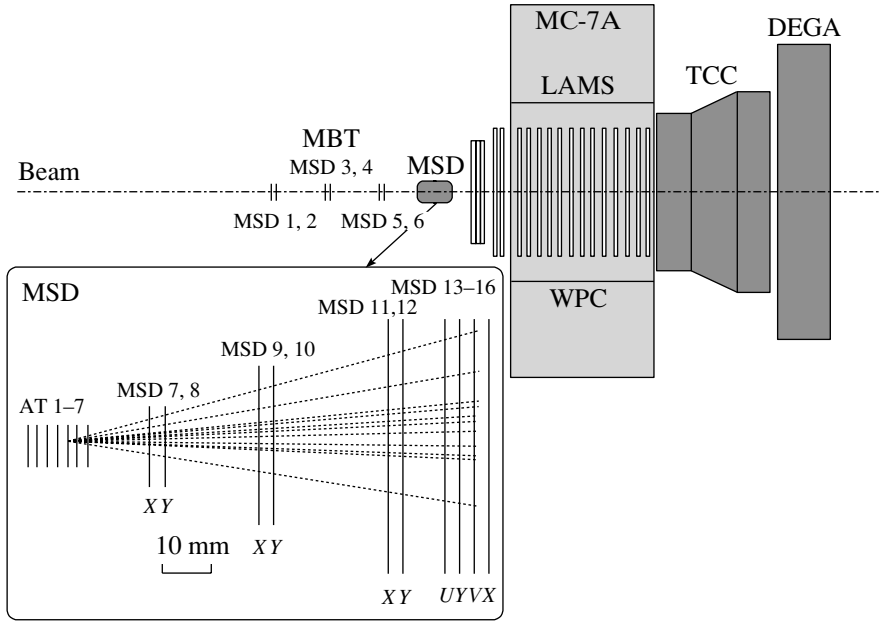

Fig. 1. Layout of SVD-2 setup.

situated behind the threshold Cherenkov counter, and data on ionization losses in the silicon detectors of the active target.

Each of the five planes of the active target was segmented into eight strips. The signal from each strip was transferred to the input of a three-level comparator. Coded data from the output of the comparators were fed to the input of a two-level RAM, where the trigger signal was developed by using lookup-table modules. This method made it possible to extract events in which the primary vertex was in any of the active-target planes [29].

The SVD-2 setup was irradiated with a proton beam of momentum $P_p = 70$ GeV/c and intensity $I \approx (5{-}6) \times 10^5$ protons per accelerator spill. The total statistics of the experiment were 5×10^7 inelastic events. With allowance for the trigger efficiency, the total sensitivity of the experiment was 1600 events/μb for inelastic pA interactions.

3. PROCEDURE FOR DATA PROCESSING AND RESOLUTION OF THE SVD-2 SETUP

The algorithm for reconstructing the position of the primary interaction vertex is based on the so-called tear-down procedure [31, 32]. At first, straight lines are drawn through the X and Y counts in the microstrip tracker by the least squares method. We then apply quality criteria to the reconstructed tracks in order to remove fake and badly reconstructed tracks. The surviving tracks are included in a vertex fit for which the quantity $\chi^2(N_{\rm tr})$ is calculated. Further, each track is excluded separately from the fit, and the new quantity $\chi^2(N_{\rm tr}-1)$ is computed for the remaining tracks. We then select those tracks whose elimination leads to the maximum value of the difference $\chi^2(N_{\rm tr}) - \chi^2(N_{\rm tr}-1)$ under the condition that this difference exceeds a threshold $\Delta_{\rm max}$ that was chosen to be three. Such tracks have an increased impact parameter with respect to the primary vertex and, because of this, are excluded from it. In the present analysis, the minimum impact parameter for the secondary tracks was 40 to 60 μm, depending on the target used. The above procedure is repeated as long as there remain tracks that can be excluded. For a further analysis, we select events involving a well-reconstructed primary vertex and two or more tracks having increased impact parameters with respect to the primary vertex. These events are tested for the presence of a secondary vertex ($V0$ decay) in both the X and the Y projection. The application of different clustering methods [33] makes it possible to improve the accuracy in determining the primary vertex. This accuracy (resolution) was estimated at 70 to 120 μm for the Z coordinate and at 8 to 12 μm for the X and Y coordinates. For secondary vertices, these resolutions are 250 and 15 μm, respectively. The impact-parameter resolution for tracks characterized by momenta in the range 3–5 GeV/c is 12 μm, while the average angular acceptance of the vertex detector is $\pm$250 mrad.

In order to reconstruct charged-particle tracks in the magnetic spectrometer, a novel method (variable-momentum method) was developed for the SVD setup. In the procedure for track recognition and

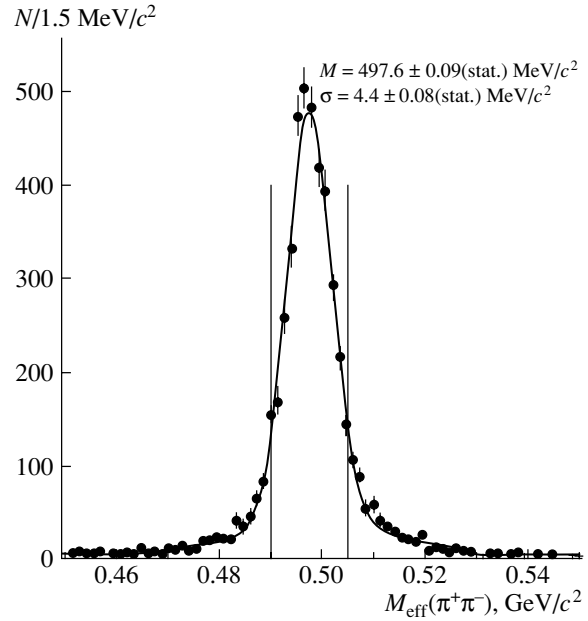

Fig. 2. Effective-mass spectrum of the $\pi^+\pi^-$ system. The $\pm 1.7\sigma$ region is bounded by the vertical lines.

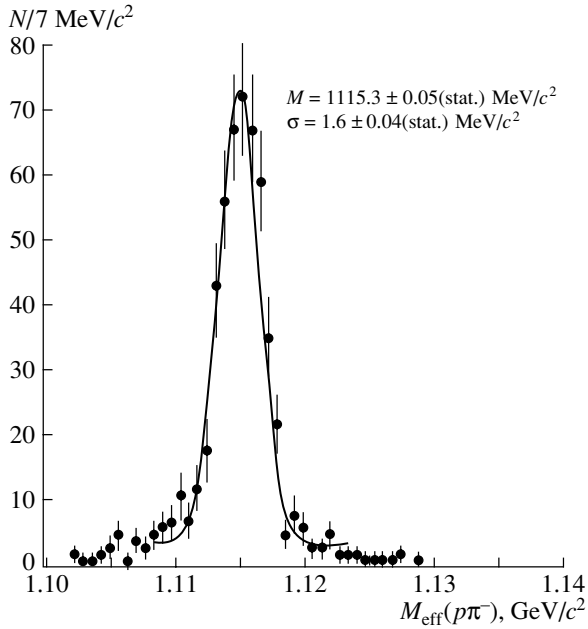

Fig. 3. Effective-mass spectrum of the $p\pi^-$ system.

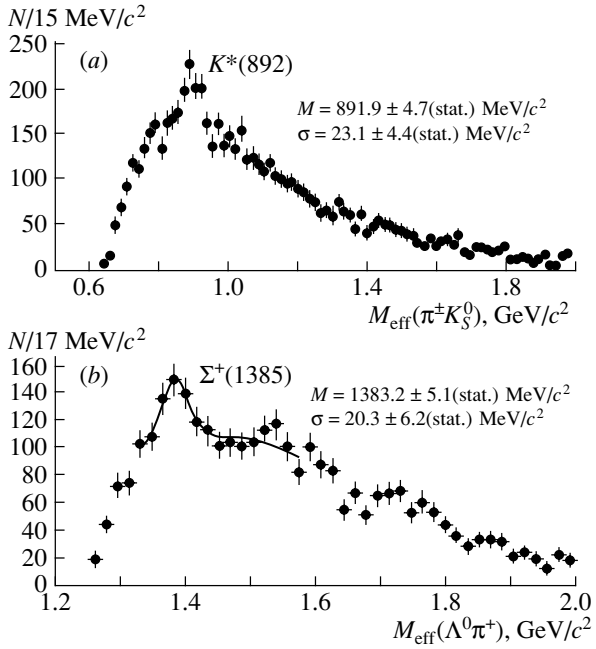

Fig. 4. (a) Total effective-mass spectrum of the $\pi^+K_S^0$ and $\pi^-K_S^0$ systems and (b) effective-mass spectrum of the $\Lambda^0\pi^+$ system.

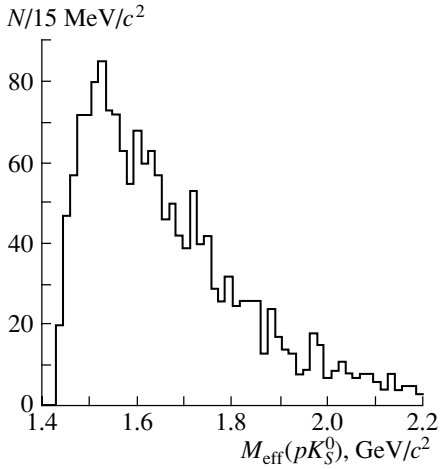

Fig. 5. Effective-mass spectrum of the pK_S^0 system in the reaction $pN \to pK_S^0 + X$.

reconstruction, use is made in this method of the a priori knowledge of the angular features of the tracks and of interaction-point coordinates in the vertex detector [34]. For an analysis of data of the SVD-2 experiment, the method was improved by using precalculated tables including the coordinates of the points of intersection of possible tracks with the planes of the proportional chambers. This enables one to increase the speed of the algorithm by two orders of magnitude. A spectrometer that involves a vertex detector makes it possible to attain high resolutions in the effective masses of strange particles—for example, the standard deviations in the effective-mass distributions for K_S^0 mesons and Λ^0 hyperons are, respectively, 4.4 and 1.6 MeV/c^2 (see Figs. 2 and 3). The momentum resolution for a track involving 15 hits measured in the proportional chambers is 0.5–1.0% for the momentum range

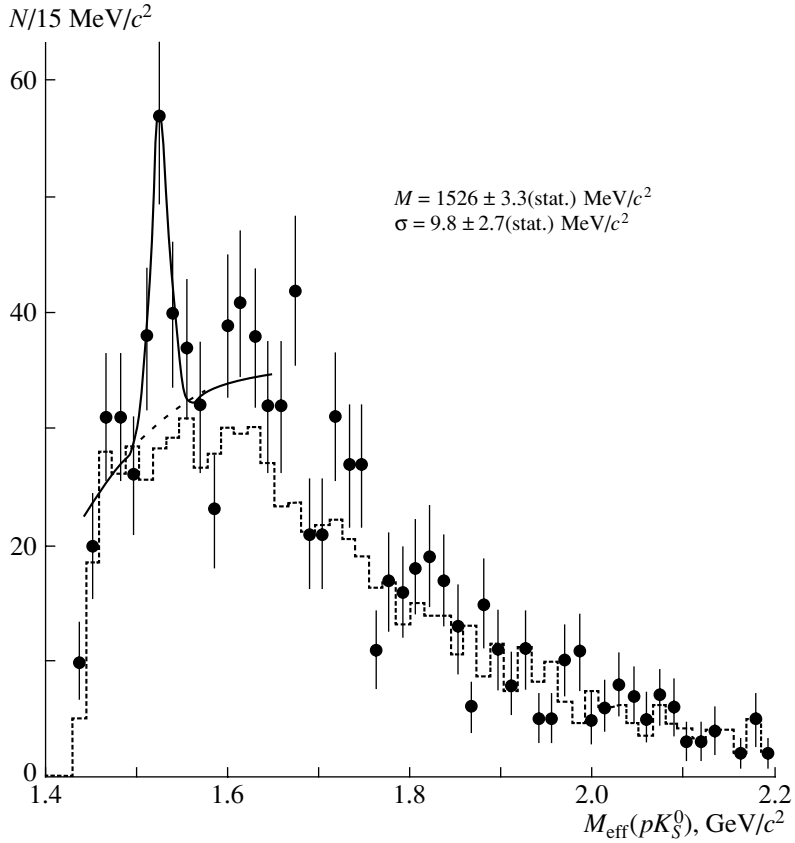

Fig. 6. Effective-mass spectrum of the pK_S^0 system in the reaction $pN \to pK_S^0 + X$ with allowance for the selection criteria (i) and (ii) (see main body of the text). The dotted histogram shows the background obtained upon a simulation based on the FRITIOF code.

4–20 GeV/c. The errors in measuring angles are determined by the coordinate resolution of the vertex detector and by the effect of multiple Coulomb scattering in target materials and in silicon plates and are estimated at 0.2 to 0.3 mrad. The average angular acceptance of the magnetic spectrometer is $\pm$200 and $\pm$150 mrad for, respectively, the horizontal and the vertical coordinate.

Figure 4*a* shows the total effective-mass spectrum for the $\pi^+K_S^0$ and $\pi^-K_S^0$ combinations. In this spectrum, the $K^*(892)$-meson peak is quite distinct. In Fig. 4*b*, one can observe the $\Sigma^+(1385)$-hyperon peak in the effective-mass spectrum of the $\Lambda^0\pi^+$ system. The masses and widths of these peaks and the masses of K_S^0 and Λ^0 are in good agreement with the values presented by the Particle Data Group [35].

4. ANALYSIS OF THE EFFECTIVE-MASS SPECTRUM OF THE pK_S^0 SYSTEM

Events for which the multiplicity of charged particles in the primary vertex was not greater than five were selected for analyzing the effective-mass spectrum of the pK_S^0 system. This selection pursued, first of all, the goal of suppressing the combinatorial background and the goal of reducing the probability of the emergence of events involving rescattering on nuclei and the background from K_S^0 mesons produced in the central rapidity region. About 34% of all inelastic events and about 15% of all detected K_S^0 mesons satisfy this selection criterion. For the selected events, the mean multiplicity of particles, including π^0 mesons and neutral strange particles, is eight.

K_S^0 mesons were identified by their decay to two charged π mesons ($K_S^0 \to \pi^+\pi^-$), where two unlikely charged tracks intersected at the common secondary vertex. Candidates of mass $M(p\pi^-)$ less than 1.12 GeV were rejected in order to eliminate the background of Λ^0-hyperon decays. The final effective-mass spectrum of the $\pi^+\pi^-$ system is shown in Fig. 2. For the ensuing analysis, we selected about 3800 K_S^0 mesons that decayed before the first plate of the vertex detector (decay length not larger than 35 mm). The average decay length of K_S^0 mesons is $\leq$20 mm.

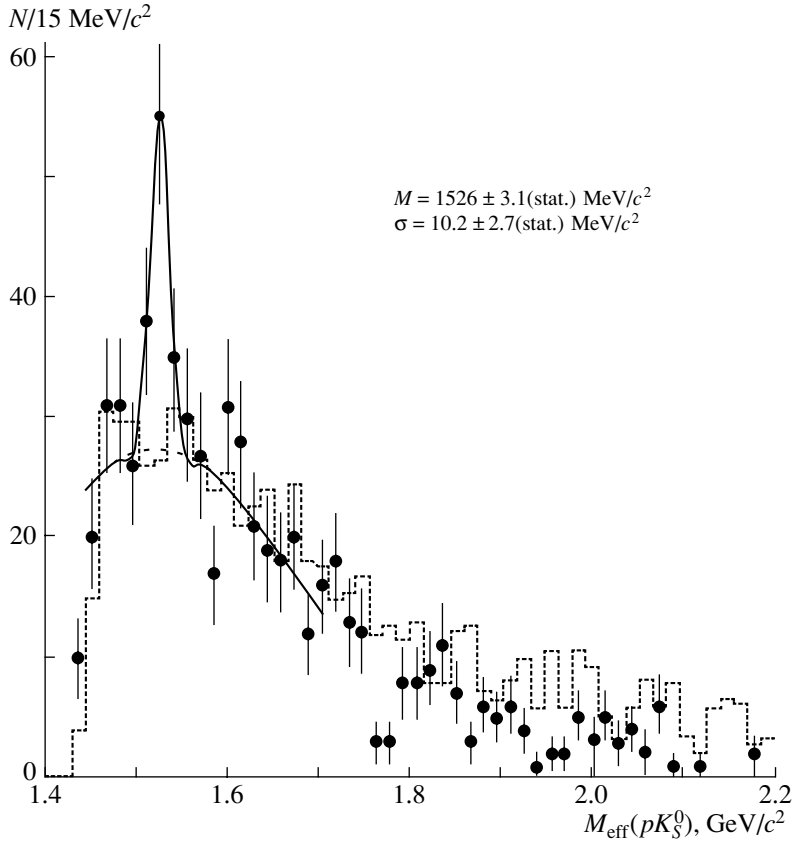

Fig. 7. As in Fig. 6, but upon the application of the selection criterion $P_{K_S^0} \leq P_p$ [38].

Protons were selected as positively charged particles for the case where the number of recorded counts in the magnetic spectrometer was not less than ≥ 15 and where the momentum was within the interval $4 \leq P_p \leq 21$ GeV/c. In this momentum range, π mesons must be recorded by the the Cherenkov counter; therefore, the absence of hits in the threshold Cherenkov counter was also required.

The effective-mass spectrum of the pK_S^0 system is shown in Fig. 5. This spectrum does not show any noticeable peaks, apart from some excess of events in the vicinity of 1530 MeV/c^2.

In the ensuing analysis of the spectrum, we applied the cuts

(i) $490 \leq M(\pi^+\pi^-) \leq 505$ MeV/c^2

and

(ii) $\cos\alpha \geq 0$, where α is the pK_S^0 emission angle in the c.m.s. of the projectile proton and the target nucleon involved.

The first of these cuts improves the resolution in the effective mass of the pK_S^0 system, while the second corresponds to the spectrometer aperture and suppresses the background of π mesons misidentified as protons.

Figure 6 shows the effective-mass spectrum of the pK_S^0 system that was obtained upon the application of these cuts. The spectrum exhibits a narrow peak at a mass value around 1526 MeV/c^2, the half-width being $\sigma \simeq 10 \pm 3$ MeV/c^2. In order to estimate the background shape, we simulated the background of inelastic pSi events on the basis of the FRITIOF code [36]. In the simulation, we took into account the trigger efficiency, the setup acceptance, the errors in the track parameters, and the conditions of K_S^0-meson decays. From Fig. 6, one can see that, in the mass region above 1550 MeV/c^2, the resulting curve does not fully describe the actual background, and this may be due to the presence of excited Σ^{*+} resonances in this region that decay to pK_S^0 with a sizable partial cross section [35]. For the KN system, the presence of broad peaks in this mass region may be a consequence of the Deck mechanism [37]. In order to suppress these peaks, it was proposed to apply the kinematical cut $P_{K_S^0} \leq P_p$ [38], which, in the mass region above 1550 MeV/c^2, leaves around 90% of all Θ^+-baryon decays and efficiently suppresses the decays of Σ^{*+} resonances.

The final effective-mass distribution of the pK_S^0

system is shown in Fig. 7. In order to describe the spectrum in the region $1.3 < M(pK_S^0) < 1.7$ GeV/c^2, we employed a Gaussian distribution for the signal and a fourth-degree polynomial for the background. The dotted-line histogram represents the background obtained in the simulation according to the FRITIOF code. One can observe 50 events in the peak above the background of 78 events. The statistical significance of the peak within the mass window $\Delta M_{\text{eff}} = 45$ MeV/c^2 was estimated on the basis of the ratio $N_P/\sqrt{N_B}$, where N_B is the number of background events and N_P is the number of events in the peak above the background and was found to be 5.6σ. By using data on the above inclusive reaction alone, it is impossible to determine the strangeness of the observed resonance; however, we interpret the observed state as the recently discovered Θ^+ baryon of positive strangeness, since, in the mass range 1500–1550 MeV/c^2, we did not observe Σ^{*+} resonances.

It was verified that the observed peak is not a reflection of other known resonances (such as $K^{*\pm}(892)$ or Δ^0) or an artificially generated peak. Also, no significant peaks were found in the effective-mass spectra of the pK_S^0 system for events in which the proton mass was assigned to a π^+ meson that was detected by the threshold Cherenkov counter. In the selected events, the admixture of π^+ mesons was estimated at a level of 10% (upon taking into account the above selection criteria). The admixture of K^+ mesons was found to be negligible (less than 5%), since K^+ mesons of momentum in excess of 10 GeV/c must be recorded by the Cherenkov detector.

Since neither the mechanism responsible for the production of Θ^+ baryons nor the dependence of the cross section on the multiplicity of charged particles is known, one can only roughly estimate the total cross section for the production of Θ^+ baryons in the proton–nucleus interactions. The detection efficiency for Θ^+ baryons was estimated on the basis of a simple Monte Carlo model involving variations in the energy spectrum of the pK_S^0 resonance. In estimating the cross section, we took into account the contributions of the decays $\Theta^+ \to pK_S^0$ (25%) and $K_S^0 \to \pi^+\pi^-$ (68.6%), the probability of K_S^0-meson detection in the vertex detector, and the acceptance of the setup. The detection efficiency for K_S^0 mesons was refined on the basis of a comparison of the observed number of events with that expected for the inclusive production of K_S^0 mesons in the reaction $pN \to K_S^0 + X$, the respective production cross section being well known [39]. The resulting detection efficiency for Θ^+ baryons is 0.07%. The total cross section for the production of Θ^+ baryons in proton–nucleus interactions was estimated at 30 to 120 μb (in the region $x_F \geq 0$). So large a scatter is explained by the uncertainties in the dependence of the cross section on the multiplicity of charged particles, the different numbers of events for different background models, and the uncertainties in the detection efficiency.

An analysis of the A dependence in the vicinity of the observed peak did not reveal any significant distinction from the analogous dependence for inelastic events ($\sim A^{0.7}$). This result contradicts the conclusions drawn in [19], where it was stated that the cross section for Θ^+-baryon production in νA interactions depends strongly on A.

5. CONCLUSIONS

The inclusive reaction $pN \to pK_S^0 + X$ has been studied at the IHEP 70-GeV/c proton accelerator with the aid of the SVD-2 setup. Upon the application of some cuts, a narrow resonance of mass $M = 1526 \pm 3(\text{stat.}) \pm 3(\text{syst.})$ MeV/c^2 and width $\Gamma < 24$ MeV/c^2 has been observed in the effective-mass spectrum of the pK_S^0 system at a statistical significance of 5.6σ. The mass and the width of the resonance correspond to the recently discovered Θ^+ baryon of positive strangeness, which was predicted in [14–21] to be an exotic baryon consisting of five quarks (pentaquark), $uudd\bar{s}$.

ACKNOWLEDGMENTS

We are grateful to V.P. Kubarovsky (RPI/JLab), B.B. Levchenko (Institute of Nuclear Physics, Moscow State University), and N.P. Zotov (Institute of Nuclear Physics, Moscow State University) for stimulating discussions and comments.

This work was supported in part by the Russian Foundation for Basic Research (project nos. 03.02.16894 and 03.02.16869), the program Universities of Russia (project no. 02.03.030), and the Council of the President of the Russian Federation for Support of Leading Scientific Schools (grant no. 1685.2003.02). Special thanks are due to the Ministry for Industry, Science, and Technology of the Russian Federation for support in developing the vertex detector (contract no. 40.032.11.34).

REFERENCES

1. D. Diakonov, V. Petrov, and M. Polyakov, Z. Phys. A **359**, 305 (1997).
2. R. L. Jaffe, *Talk Presented at The Topical Conference on Baryon Resonances, Oxford, UK, 1976*, SLAC-PUB-1774 (1976).
3. A. V. Manohar, Nucl. Phys. B **248**, 19 (1984).

4. M. Chemtob, Nucl. Phys. B **256**, 600 (1985).
5. M. Praszalowicz, in *Proceedings of the Workshop on Skyrmions and Anomalies, Cracow, Poland, 1987*, Ed. by M. Jezabeck and M. Praszalowicz (World Sci., Singapore, 1987), p. 112.
6. H. Walliser, Nucl. Phys. A **548**, 649 (1992).
7. Fl. Stancu and D. O. Riska, hep-ph/0307010.
8. S. Capstick, P. R. Page, and W. Roberts, hep-ph/0307019.
9. M. Karliner and H. J. Lipkin, Phys. Lett. B **575**, 249 (2003); hep-ph/0307243.
10. R. L. Jaffe and F. Wilczek, hep-ph/0307341.
11. S. Sasaki, hep-lat/0310014.
12. F. Csikor *et al.*, hep-lat/0309090.
13. V. B. Kopeliovich, Usp. Fiz. Nauk **174**, 323 (2004) [Phys. Usp. **47**, 309 (2004)].
14. LEPS Collab. (T. Nakano *et al.*), Phys. Rev. Lett. **91**, 012002 (2003); hep-ex/0301020.
15. DIANA Collab. (V. V. Barmin *et al.*), Yad. Fiz. **66**, 1763 (2003) [Phys. At. Nucl. **66**, 1715 (2003)]; hep-ex/0304040.
16. CLAS Collab. (S. Stepanyan *et al.*), Phys. Rev. Lett. **91**, 252001 (2003).
17. CLAS Collab. (V. Kubarovsky and S. Stepanyan), in *Proceedings of 8th Conference on the Intersections of Particle and Nuclear Physics (CIPANP 2003), New York, NY, USA, 2003*; hep-ex/0307088.
18. SAPHIR Collab. (J. Barth *et al.*), Phys. Lett. B **572**, 127 (2004).
19. A. E. Asratyan, A. G. Dolgolenko, and M. A. Kubantsev, Yad. Fiz. **67**, 704 (2004) [Phys. At. Nucl. **67**, 682 (2004)]; hep-ex/0309042.
20. CLAS Collab. (V. Kubarovsky *et al.*), Phys. Rev. Lett. **92**, 032001 (2004); **92**, 049902(E) (2004).
21. HERMES Collab. (A. Airapetian *et al.*), Phys. Lett. B **585**, 213 (2004).
22. ZEUS Collab. (S. Chekanov *et al.*), hep-ex/0405013.
23. SVD Collab. (A. Aleev *et al.*), Preprint No. 2004-4/743, NIIYaF MGU (Institute of Nuclear Physics, Moscow State University, Moscow, 2004); hep-ex/0401024.
24. N. S. Amaglobeli *et al.*, Yad. Fiz. **64**, 958 (2001) [Phys. At. Nucl. **64**, 891 (2001)].
25. E. N. Ardashev *et al.*, Preprint No. 99-28/586, NIIYaF MGU (Inst. Nucl. Phys., Moscow State Univ., Moscow, 1999).
26. A. Leflat, A. Kubarovsky, *et al.*, Nucl. Phys. A **699**, 352 (2002).
27. P. F. Ermolov *et al.*, in *Universities of Russia—Basic Research. Elementary-Particle and Nuclear Physics* (MIFI, Moscow, 2002), p. 89.
28. A. N. Aleev *et al.*, Prib. Tekh. Éksp., No. 5, 51 (2003) [Instrum. Exp. Tech., No. 5, 624 (2003)].
29. G. A. Bogdanova *et al.*, Prib. Tekh. Éksp., No. 4, 31 (2001) [Instrum. Exp. Tech., No. 4, 449 (2001)].
30. L. A. Tikhonova *et al.*, Frascati Phys. Ser. **XXXI**, 413 (2003).
31. G. Borisov, DELPHI Note 94-125/PROG 208 (1994).
32. M. Narain and F. Stichelbaut, D0 Note 3560 (1999).
33. A. A. Kiryakov, V. N. Ryadovikov, A. V. Kubarovsky, and V. V. Popov, Preprint No. 2003-38, IFVÉ (Inst. High Energy Phys., Protvino, 2003).
34. P. F. Ermolov, A. V. Kubarovsky, and M. S. Levitskiĭ, Prib. Tekh. Éksp., No. 5, 39 (1998) [Instrum. Exp. Tech., No. 5, 626 (1998)].
35. Particle Data Group (K. Hagiwara *et al.*), Phys. Rev. D **66**, 010001 (2002).
36. H. Pi, Comput. Phys. Commun. **71**, 173 (1992).
37. A. M. Endler *et al.*, Z. Phys. C **7**, 137 (1981).
38. B. Levchenko, hep-ph/0401122.
39. V. V. Ammosov *et al.*, Nucl. Phys. B **115**, 269 (1976).

Translated by A. Isaakyan

Physics of Atomic Nuclei, Vol. 68, No. 6, 2005, pp. 982–990. Translated from Yadernaya Fizika, Vol. 68, No. 6, 2005, pp. 1020–1028.
Original Russian Text Copyright © 2005 by Abraamyan, Kozhin, Melkumov, Khachaturian, Khudaverdyan.

ELEMENTARY PARTICLES AND FIELDS
Experiment

Inclusive Neutral-Pion Production in dC and dCu Interactions at a Momentum of 4.5 GeV/c per Nucleon

Kh. U. Abraamyan[1)*], M. A. Kozhin[1)], G. L. Melkumov[1)], M. N. Khachaturian[1)], and A. H. Khudaverdyan[2)]

Received April 14, 2004; in final form, October 7, 2004

Abstract—The cross sections for inclusive neutral-pion production in the reactions $d + \mathrm{C} \to \pi^0 + x$ and $d + \mathrm{Cu} \to \pi^0 + x$ at a momentum of 4.5 GeV/c per nucleon were measured over the kinematical region specified by the inequalities $\theta_\pi \leq 16^\circ$ and $E_\pi \geq 2$ GeV (in the laboratory frame). From the ratio of the cross sections for neutral-pion generation on carbon and copper nuclei, the exponent n in the parametrization $Ed^3\sigma/d^3p \sim A_T^n$ is obtained as a function of the cumulative number X in the range $0.6 \leq X \leq 1.8$ and as a function of the square of the transverse momentum in the range $0.04 \leq P_t^2 \leq 0.40$ (GeV/c)^2. The probabilities of the formation of six-quark configurations in the D, ^{4}He, and ^{12}C nuclei are estimated. The double-differential cross section for the reaction $d + \mathrm{C} \to \pi^0 + x$ is determined for the first time by using a data sample containing more than 40 000 neutral pions. © *2005 Pleiades Publishing, Inc.*

1. INTRODUCTION

The present article reports on the results of measurements of inclusive neutral-pion production in the reactions

$$d + A_T \to \pi^0 + x, \quad A_T = \mathrm{C}, \mathrm{Cu} \qquad (1)$$

at a momentum of 4.5 GeV/c per nucleon. This experiment is a continuation of a series of investigations [1–3] that have been conducted with the 90-channel Cherenkov γ spectrometer of the Laboratory of High Energies at the Joint Institute for Nuclear Research (JINR, Dubna) [4]. The objective of these investigations is to clarify the mechanism of pion production in the vicinity of and beyond the kinematical boundary for nucleon–nucleon collisions [5].

2. DESCRIPTION OF THE EXPERIMENT

The experiment in question was performed by using a deuteron beam of momentum 4.5 GeV/c per nucleon ($\Delta p/p = \pm 2\%$) and intensity 10^5 particles per accelerator spill. The experimental equipment used made it possible to measure not only the energies of photons formed in neutral-pion decay but also their emission directions. The layout of our experimental facility is displayed in Fig. 1. The facility includes 90 total-absorption Cherenkov detectors from lead glass, scintillation counters of dimension 5×5 cm^2 (S_1, S_2, S_3) and 15×15 cm^2 (S_4, S_5), a gas threshold counter, a scintillation counter operating in the anticoincidence mode, and a hodoscope of scintillation counters that consists of 40 units having dimensions of 10×100 cm^2.

The target thickness along the beam was 12.6 g/cm^2 for carbon (0.3 radiation length units) and 5.4 g/cm^2 for copper (0.4 radiation length units). Events of the $n\gamma$ type, where $n = 2, 3, \ldots$, that were generated in a target were recorded by the Cherenkov γ spectrometer. The detectors of the γ spectrometer were independent. They were arranged in a 7×13 matrix of dimension 140×215 cm^2. The features of the spectrometer were quoted elsewhere [2, 4].

In the experiment, the distance from the target center to the γ spectrometer along the beam was 340 cm for the carbon target and 520 cm for the copper target. Under the geometric conditions specified above, the ranges of recorded-neutral-pion emission angles in the laboratory frame were $\pm 16^\circ$ and $\pm 10^\circ$, respectively.

Charged particles were recorded by the hodoscope of 40 scintillation counters having dimensions of $2 \times 10 \times 100$ cm^3 each. The scintillation counters were arranged in front of the γ spectrometer. They ensured the detection of charged particles with an efficiency of about 99%. The detectors of the γ spectrometer were partitioned into 14 groups, each containing six or seven units. A linear combination of signals was taken within a group and was transferred to the inputs of discriminators. In our experiment, the thresholds

[1)]Joint Institute for Nuclear Research, Dubna, Moscow oblast, 141980 Russia.
[2)]Yerevan State University, ul. A. Manukyana 1, Yerevan, 375049 Armenia.
[*]e-mail: abraam@sunhe.jinr.ru

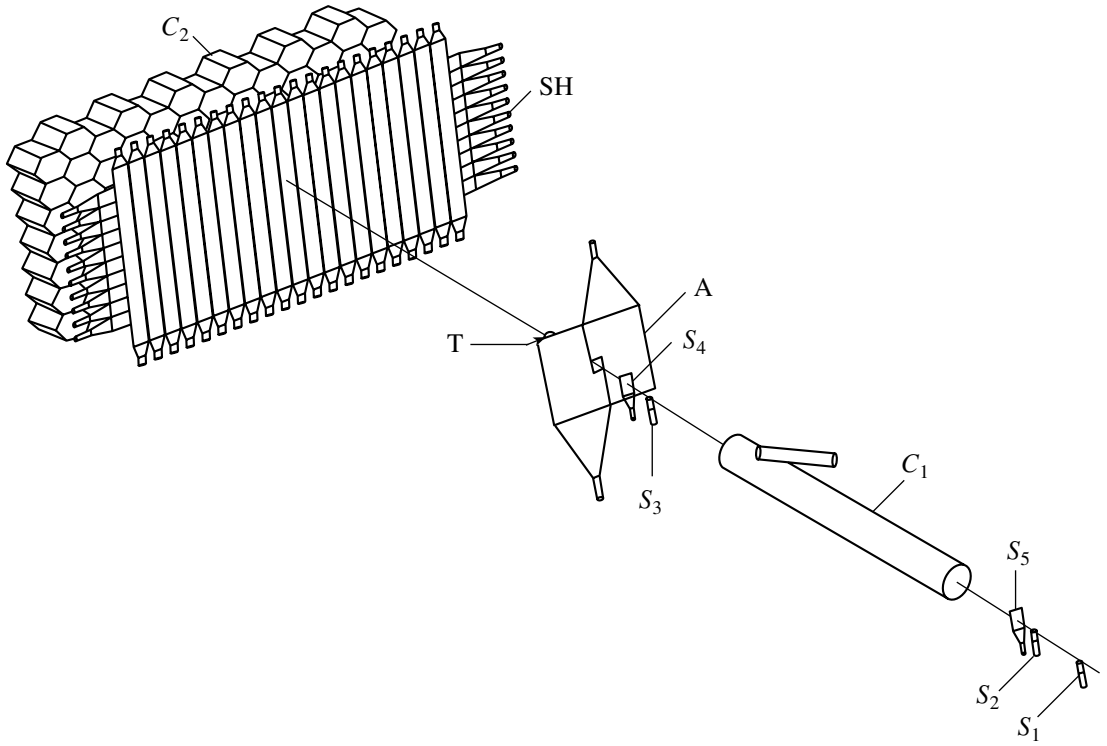

Fig. 1. Layout of the experimental equipment used: (S_1–S_5) scintillation counters, (C_1) gas threshold counter, (A) scintillation counter operating in the anticoincidence mode, (T) target, (SH) hodoscopic scintillation counters, and (C_2) 90-channel lead-glass Cherenkov γ spectrometer.

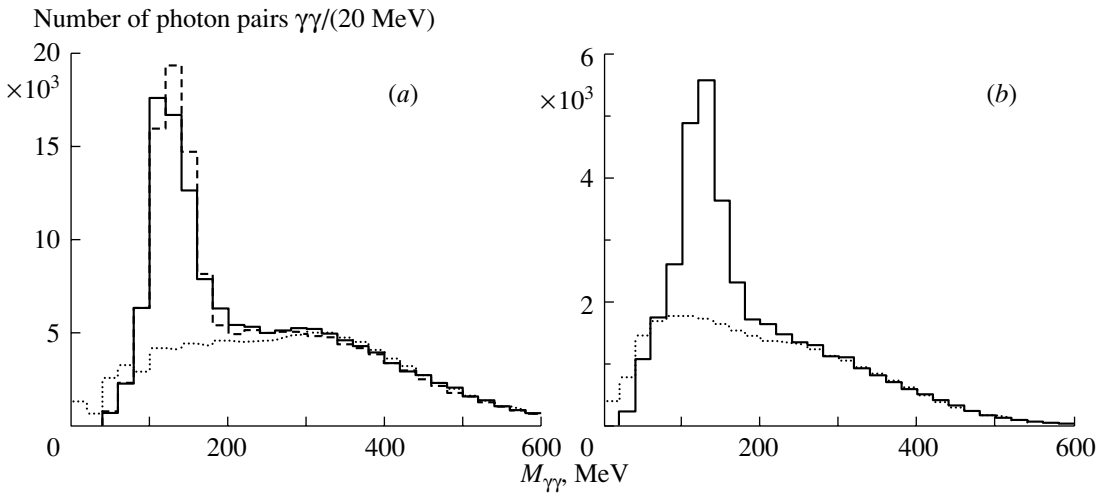

Fig. 2. Effective-mass distributions of photons combined in pairs for the reactions (*a*) $d + \mathrm{C} \to \pi^0 + x$ and (*b*) $d + \mathrm{Cu} \to \pi^0 + x$. The dotted-line histograms represent background distributions obtained by selecting photons at random from different events. The dashed-line histogram in Fig. 2*a* was obtained from a Monte Carlo simulation with allowance for the actual conditions of spectrometer operation and for criteria used in data treatment.

of the discriminators were set to 1.0 GeV. The facility was triggered by the coincidence of signals from beam scintillation counters, halo counters (in the anticoincidence mode), and two or more groups of detectors of the γ spectrometer under the condition that the total energy deposition in these groups exceeded 2 GeV. The average rate of data acquisition was about 10 events per acceleration cycle. In the course of the experiment, 1.51×10^9 and 2.48×10^9 deuterons were transmitted through the carbon and the copper tar-

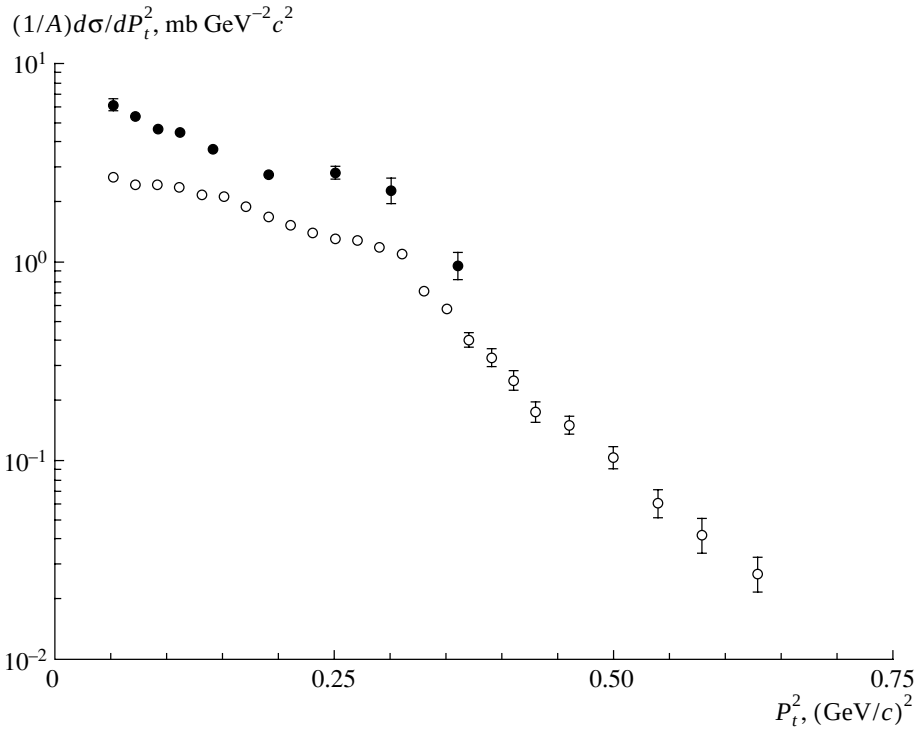

Fig. 3. Differential cross sections for neutral-pion production in the reactions (open circles) $d + \mathrm{C} \to \pi^0 + x$ and (closed circles) $d + \mathrm{Cu} \to \pi^0 + x$ for $\theta_\pi \leq 16^\circ$ and $E_\pi \geq 2$ GeV versus the square of the transverse momentum (in the laboratory frame).

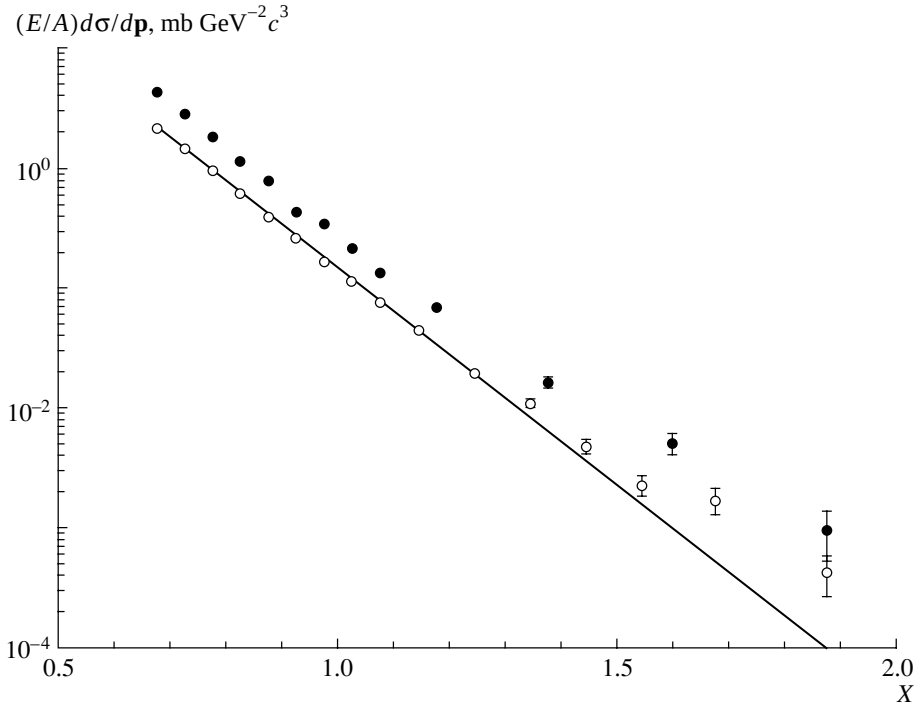

Fig. 4. Invariant inclusive cross sections for neutral-pion production in the reactions (open circles) $d + \mathrm{C} \to \pi^0 + x$ and (closed circles) $d + \mathrm{Cu} \to \pi^0 + x$ versus the cumulative number X. The straight line represents the best approximation of data by formula (2).

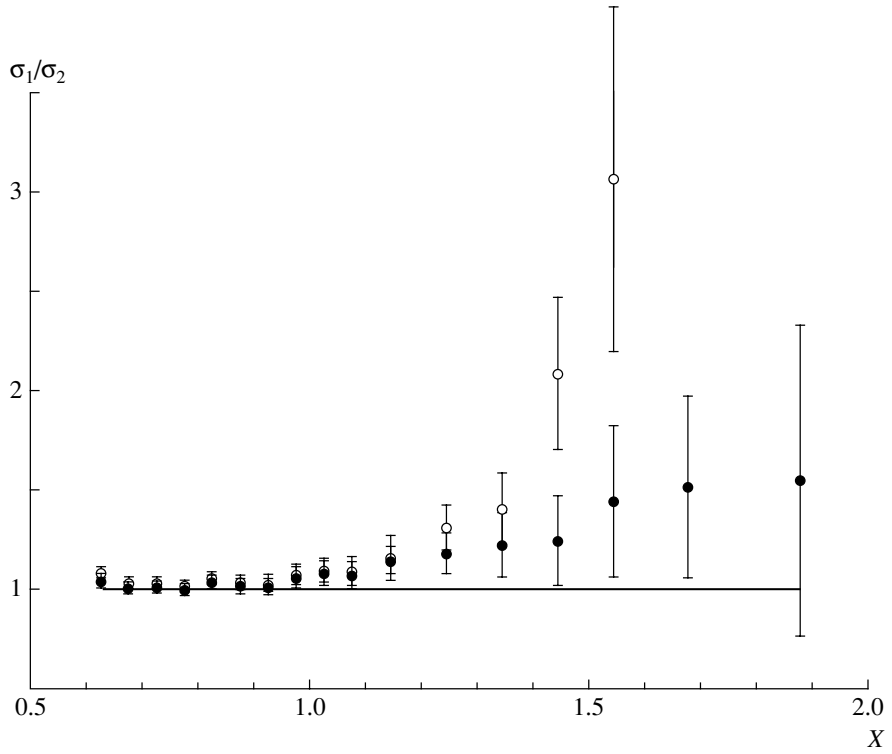

Fig. 5. Ratio of cross sections obtained by using different methods for estimating the background.

get, respectively, and 200 000 triggers for the carbon target and 160 000 triggers for the copper target were logged on magnetic tapes.

3. EVENT SELECTION

Neutral pions were recorded by decays into two photons and were selected from the peak in the invariant-mass distribution (see Fig. 2). In the electromagnetic calorimeter, photons were recognized as clusters (the region of adjacent units in the γ spectrometer where the signal exceeded the detection threshold). The photon energy was calculated on the basis of the energy deposition in the cluster units with allowance for losses that are dependent on the photon-hit location. Under the assumption that photons are generated in the target, the photon-emission direction was determined versus the geometry of a cluster with allowance for the energy deposition in the units.

Primary information was processed by using the code for reconstructing the geometry and energy of events [6]. On the data summary tape, we logged 140 000 events satisfying the following criteria:

(i) $N_\gamma \geq 2$,

(ii) $E_\gamma \geq 500$ MeV,

(iii) $k_\gamma \perp \geq 120$ MeV. Here, N_γ is the number of photons in an event, while E_γ and $k_\gamma \perp$ are the photon energy and transverse momentum respectively.

4. INCLUSIVE SPECTRA OF NEUTRAL PIONS

The effective-mass ($M_{\gamma\gamma}$) distribution of photons combined in pairs such that the total energy satisfies the condition $E_{\gamma 1} + E_{\gamma 2} \geq 2$ GeV is displayed in Fig. 2. The dotted-line histograms there represent the effective-mass distributions for combinations of two photons taken at random from different events.

The reactions $d + \mathrm{C} \to \pi^0 + x$ and $d + \mathrm{Cu} \to \pi^0 + x$ were simulated by using the code formulated in [7] on the basis of the GEANT package [8]. In this simulation, use is made of data on multiparticle neutral-pion production that were obtained in experiments with the two-meter propane chamber of the Laboratory of High Energies at JINR [9]. In simulating events, we verified whether photons hit the facility, generated energy depositions in γ-spectrometer units, and required fulfillment of trigger conditions. The events were recorded on the data summary tape for a subsequent treatment by means of codes for subsequently reconstructing their geometry and energies. The inclusive cross sections for neutral-pion production were calculated for angles in the range $\theta_\pi \leq 16^\circ$ and energies of $E_\pi \geq 2$ GeV (in the laboratory frame).

The P_t^2 distributions obtained experimentally for neutral pions from the reactions $d + \mathrm{C} \to \pi^0 + x$ and

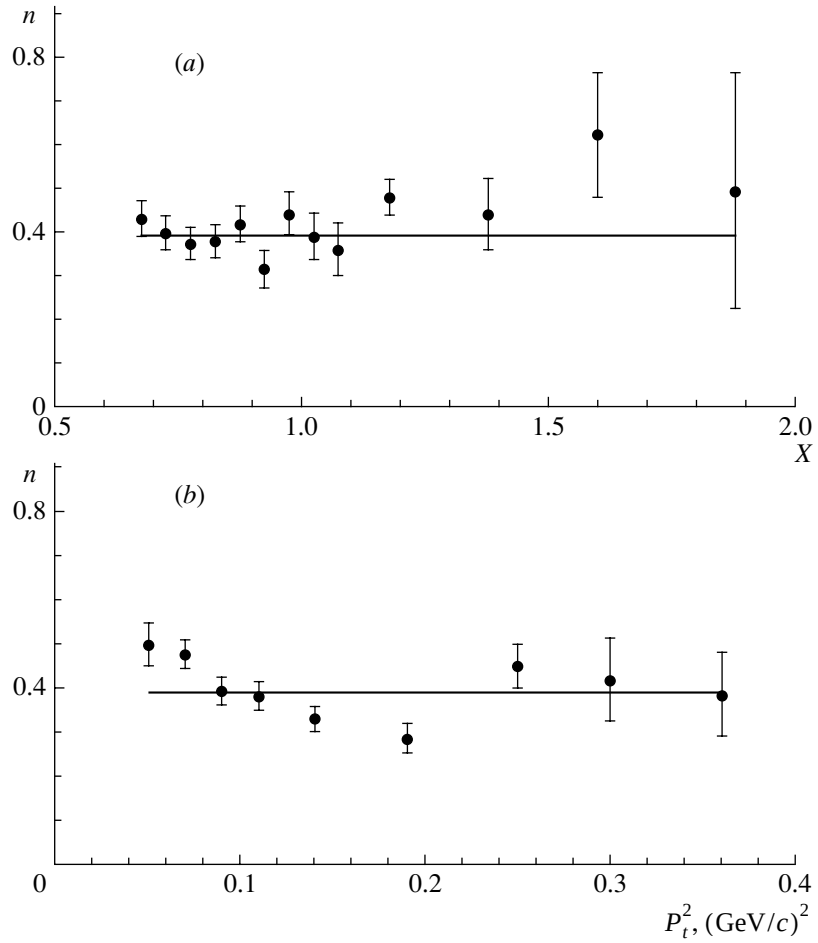

Fig. 6. Exponent n in the parametrization $Ed^3\sigma/d^3p \sim A_T^n$ as a function of (a) the variable X and (b) the square of the neutral-pion transverse momentum for the reactions $d + A_T \to \pi^0 + x$, where A_T = C, Cu.

$d + \mathrm{Cu} \to \pi^0 + x$ and integrated over the aforementioned region of angles and energies are displayed in Fig. 3.

The invariant inclusive cross sections for neutral-pion production in dC and dCu interactions are shown in Fig. 4 versus the cumulative number X. The variable X is determined from the law of energy–momentum conservation for $XN_i + N_t \to (X+1)N_f + \pi^0$ reactions and is given by

$$X = [M_N E_\pi - M_\pi^2/2]/[E_N M_N - E_N E_\pi - M_N^2 + P_N P_\pi \cos\theta_\pi],$$

where M_N, P_N, and E_N are the nucleon mass, momentum, and energy, respectively; M_π, P_π, and E_π are the corresponding quantities for the product pion; θ_π is the pion emission angle in the laboratory frame; and $P_N = 4.5$ GeV/c.

The errors in Figs. 3 and 4 are purely statistical.

5. ESTIMATING SYSTEMATIC ERRORS

Systematic errors may be due an uncontrollable scatter of monitor counts per recorded events and errors in estimating combinatorial background.

Deviations from an average value do not exceed 20% at maximum. The same applies to changes in the number of monitor counts in response to changes in the number of events recorded within an accelerator cycle.

Figure 5 exhibits the ratio of cross sections obtained by two different methods: in estimating the combinatorial background by selecting photons at random from different events (that is, by means of so-called mixing) and in estimating the background on the basis of the results obtained from a Monte Carlo simulation [7] with allowance for the multiparticle production of neutral pions. The estimation of the background by means of mixing was performed by using two methods of selection: without imposing any cuts (open circles) and by imposing the following cuts in selecting events:

Table

E, GeV	π, deg			
	2–4	4–6	6–8	8–10
2.0–2.2	10.4 ± 1.2	4.97 ± 0.33	3.81 ± 0.15	3.23 ± 0.12
2.2–2.4	7.0 ± 0.9	3.04 ± 0.21	2.59 ± 0.09	1.96 ± 0.07
2.4–2.6	4.2 ± 0.6	1.79 ± 0.12	1.54 ± 0.05	1.04 ± 0.04
2.6–2.8	1.68 ± 0.27	1.08 ± 0.08	0.850 ± 0.034	0.525 ± 0.024
2.8–3.0	1.10 ± 0.24	0.649 ± 0.052	0.457 ± 0.021	0.278 ± 0.016
3.0–3.2	0.75 ± 0.21	0.325 ± 0.029	0.256 ± 0.014	0.147 ± 0.010
3.2–3.4	0.56 ± 0.19	0.202 ± 0.020	0.144 ± 0.010	0.075 ± 0.006
3.4–3.6	0.34 ± 0.14	0.099 ± 0.012	0.079 ± 0.006	0.042 ± 0.004
3.6–3.8	0.29 ± 0.18	0.052 ± 0.008	0.042 ± 0.004	0.0191 ± 0.0026
3.8–4.0	0.082 ± 0.052	0.034 ± 0.006	0.0208 ± 0.0028	0.0124 ± 0.0021
4.0–4.2	0.061 ± 0.042	0.0164 ± 0.0041	0.0135 ± 0.0024	0.0064 ± 0.0016
4.2–4.4		0.0094 ± 0.0029	0.0063 ± 0.0015	0.0039 ± 0.0014
	10–12	12–14	14–16	
2.0–2.2	2.39 ± 0.09	1.57 ± 0.08	1.08 ± 0.11	
2.2–2.4	1.453 ± 0.055	0.876 ± 0.044	0.486 ± 0.048	
2.4–2.6	0.735 ± 0.032	0.465 ± 0.028	0.232 ± 0.025	
2.6–2.8	0.365 ± 0.019	0.162 ± 0.012	0.103 ± 0.015	
2.8–3.0	0.186 ± 0.012	0.076 ± 0.007	0.040 ± 0.008	
3.0–3.2	0.099 ± 0.009	0.0414 ± 0.0056	0.0144 ± 0.0035	
3.2–3.4	0.0428 ± 0.0047	0.0191 ± 0.0034	0.0078 ± 0.0029	
3.4–3.6	0.0193 ± 0.0028	0.0065 ± 0.0014	0.0014 ± 0.0008	
3.6–3.8	0.0110 ± 0.0022	0.0033 ± 0.0010	0.0007 ± 0.0005	
3.8–4.0	0.0056 ± 0.0015	0.0033 ± 0.0021		

(i) For the total energy in an event, $E \leq 5.5$ GeV (about 99% of all events).

(ii) For the sum of the energies of photons chosen at random, $E_1 + E_2 \leq 5.5$ GeV.

(iii) For the distance at the spectrometer surface between photons chosen at random, $L \leq 17$ cm (distances that are not observed in a single event).

From Fig. 5, one can see that, after a more adequate selection of photons from different events, the discrepancy between the two results decreases significantly, not exceeding 20% in the region $0.6 \leq X \leq 1.5$.

6. ANALYSIS OF OUR DATA

Our experimental data on the invariant cross section as a function of X were parametrized by an exponential function,

$$(E/A_P)d^3\sigma/d^3p = A_1\exp(-B_1X), \qquad (2)$$

where $A_p = 2$ is the mass number of the projectile nucleus.

For the parameters A_1 (mb GeV^{-2} c^3) and B_1, we obtained the values

$A_1 = 604 \pm 32$, $B_1 = 8.34 \pm 0.06$ for the reaction $d + \mathrm{C} \to \pi^0 + x$

and

$A_1 = 1025 \pm 117$, $B_1 = 8.21 \pm 0.12$ for the reaction $d + \mathrm{Cu} \to \pi^0 + x$.

These values of A_1 and B_1 were obtained by approximating the data in the range $X < 1.6$ (see Fig. 4) without taking into account systematic errors.

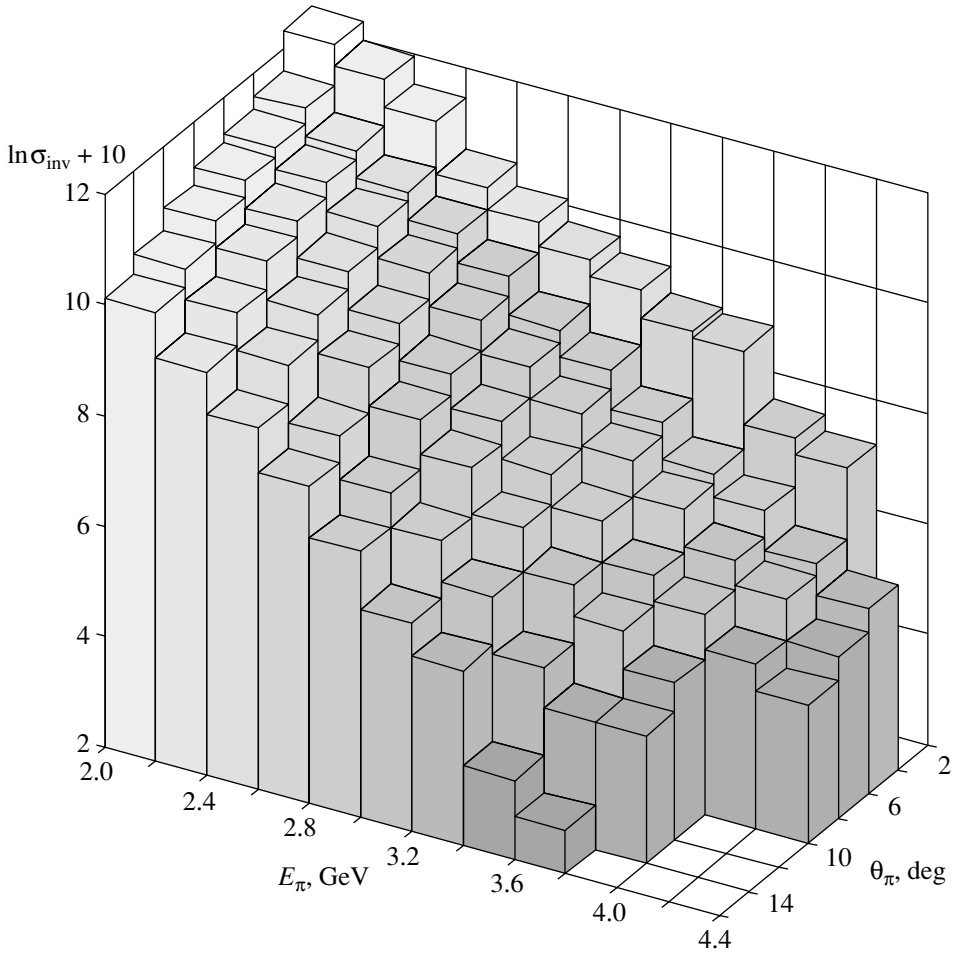

Fig. 7. Invariant cross section $\sigma_{\text{inv}} = (E/2)d^3\sigma/d^3p$ (mb GeV^{-2} c^3) for the reaction $d + \text{C} \to \pi^0 + x$ versus the emission angle of the product pion and its energy (in the laboratory frame).

The ratio of the invariant cross sections for neutral-pion production on C and Cu target nuclei was represented in the form $\sigma_{\text{Cu}}/\sigma_{\text{C}} = (A_{\text{Cu}}/A_{\text{C}})^n = (63.5/12)^n$. The exponent n as a function of the variables X and P_t^2 is displayed in Fig. 6. One can see that, in the region $X > 0.6$, the invariant cross section for neutral-pion production in deuteron–nucleus interactions depends only slightly on the mass number of the target nucleus. The average value of n is 0.39 ± 0.02. Our results indicate that the processes in (1) for $X > 0.6$ involve the peripheral region of the target nucleus.

Figure 6*a* shows that the dependence of the invariant cross section on the target-nucleus mass changes modestly with X, this being in agreement with the result obtained in [2]. In all probability, this behavior of the exponent n is associated with the dominance of the quark-recombination mechanism in meson production [10] (see the respective discussion in [2]).

Denoting by p_i, where $i = 6, 9, \ldots$, the probabilities of the formation of i-quark configurations in a nucleus, we find that, in the region around $X \sim 1$, where the contribution of configurations involving nine or more quarks is insignificant [11], the invariant cross sections for the reactions in (1) admit the representation (we omit here a constant factor)

$$E d^3\sigma/d^3p \sim A\left\{1 - \sum_{i\,=\,6,\,9,\,\ldots} p_i\right\} n_{q/3}(X) \qquad (3)$$
$$+ p_6[(A-2)n_{q/3}(X) + n_{q/6}(X/2)],$$

where

$$X n_{q/i}(X) = [B(\eta_i^{(2)}, \eta_i^{(1)} + 1)]^{-1}(1-X)^{\eta_i^{(1)}} X^{\eta_i^{(2)}}$$

are the quark distributions in an i-quark configuration according to quark-counting rules at $\eta_i^{(1)} = 2(i-1) - 1$, $\eta_6^{(2)} = 0.5$, $\eta_3^{(2)} \approx 0.65$ [12], $B(\ldots, \ldots)$ being an Euler beta function.

Assuming that the probability p_3 of the absence of

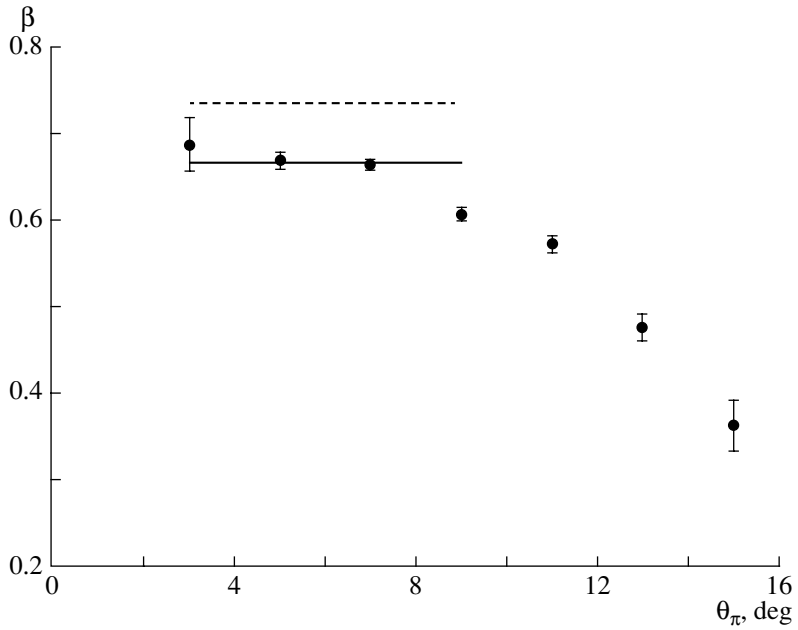

Fig. 8. Dependence of the parameter β in (7) at $T_0 = 160$ MeV on the neutral-pion emission angle. The solid line represents the average value of β in the range $\theta_\pi \leq 8^\circ$. The dashed line corresponds to its counterpart at $T_0 = 140$ MeV.

nucleon correlations in a nucleus is

$$p_3 = 1 - \sum_{i\,=\,6,\,9,\,\ldots} p_i \approx 1 - p_6$$

and employing formula (3) and data obtained in the present study (Fig. 4) and in [2, 3] for the region $0.95 \leq X \leq 1.1$, we deduce the following estimates for the probabilities of the formation of six-quark configurations in the deuteron and in the helium and carbon nuclei:

$$p_6(\mathrm{D}) \approx 2\%, \quad p_6(^4\mathrm{He}) = 5{-}10\%, \qquad (4)$$
$$p_6(^{12}\mathrm{C}) = 20{-}40\%.$$

The lower bounds on p_6 for the helium and carbon nuclei in (4) were obtained without taking into account the effect of nucleon shadowing and six-quark configurations in a nucleus: in (3), it is assumed that $\sigma \sim A_{\mathrm{ir}}^{\alpha}$, where $\alpha = 1$ and A_{ir} is the number of fragmenting centers (nucleons and six-quark configurations). At the minimum possible value of $\alpha = 2/3$, the above values of p_6 increase by a factor of about 2.

7. DOUBLE-DIFFERENTIAL CROSS SECTION

On the basis of a data sample that includes about 45 000 neutral pions, we have determined the double-differential cross section for the reaction $d + \mathrm{C} \to \pi^0 + x$ as a function of the emission angle of the product pion and its energy,

$$(E/A)(d^3\sigma/d^3p) = (E/2)\Delta\sigma/(p^2\Delta p\Delta\Omega) \qquad (5)$$
$$\approx (1/2E)\Delta\sigma/(\sin\theta\cdot\Delta\theta\Delta E\cdot 2\pi).$$

The results (in mb GeV^{-2} c^{-3}) are given in the table and in Fig. 7.

The data obtained in this way make it possible to test the so-called cluster mechanism of pion production. If one assumes the existence of an intermediate object (for example, clusters proposed in [13, 14]), then the invariant cross section for neutral-pion production takes the form

$$Ed^3\sigma/d^3p \sim \exp(-E^*/T_0), \qquad (6)$$

where E^* is the neutral-pion energy in the cluster rest frame and $T_0 \sim m_\pi$ is a universal hadron temperature. In the laboratory frame, we have

$$Ed^3\sigma/d^3p \sim \exp(-E/T), \qquad (7)$$
$$T = T_0(1-\beta^2)^{1/2}/(1-\beta\cos\theta),$$

where β is the cluster speed.

The values of β that were obtained from (7) at $T_0 = 160$ MeV (as was accepted in [13]) for various neutral-pion emission angles are presented in Fig. 8. This figure shows that the character of the dependence $\beta(\theta_\pi)$ in the region $\theta_\pi < 8^\circ$ is compatible with the hypothesis that there exists an intermediate cluster, but the possible cluster speeds appear to be low: $\beta = 0.66$ at $T_0 = 160$ MeV and $\beta = 0.73$ at $T_0 = 140$ MeV. In order to explain such velocities, it is necessary to assume that the reactions in question involve more than two target nucleons, but this is not compatible with the observed A dependence on the target mass number (see Fig. 6).

ACKNOWLEDGMENTS

We are grateful to V.V. Arkhipov, S.G. Reznikov, S.N. Plyashkevich, V.I. Prokhorov, and A.I. Shirokov for assistance in measurements. We are also indebted to E.B. Plekhanov and S.S. Shimansky for enlightening comments.

REFERENCES

1. Kh. U. Abraamyan *et al.*, Yad. Fiz. **59**, 271 (1996) [Phys. At. Nucl. **59**, 252 (1996)].
2. Kh. U. Abraamyan *et al.*, Phys. Lett. B **323**, 1 (1994).
3. Kh. U. Abraamyan *et al.*, Yad. Fiz. **60**, 2014 (1997) [Phys. At. Nucl. **60**, 1843 (1997)].
4. R. G. Astvatsaturov *et al.*, Nucl. Instrum. Methods **163**, 343 (1979).
5. A. M. Baldin, Fiz. Élem. Chastits At. Yadra **8**, 429 (1977) [Sov. J. Part. Nucl. **8**, 175 (1977)]; Preprint No. P7-5808, OIYaI (Joint Institute for Nuclear Research, Dubna, 1971).
6. N. N. Govorun *et al.*, in *Proceedings of Meeting on Programming and Mathematical Methods for Solving Physics Problems* (Joint Institute for Nuclear Research, Dubna, 1973), D10-7707, p. 453.
7. V. M. Iz"yurov and M. N. Khachaturyan, Report No. 1-83-274, OIYaI (Joint Institute for Nuclear Research, Dubna, 1983).
8. R. Brun *et al.*, GEANT, CERN, DD/78/2.
9. G. N. Agakishiev *et al.*, Preprint No. E1-84-321, OIYaI (Joint Institute for Nuclear Research, Dubna, 1984); G. R. Gulkanyan *et al.*, Yad. Fiz. **46**, 826 (1987) [Sov. J. Nucl. Phys. **46**, 469 (1987)].
10. G. Berlad and A. Dar, Phys. Lett. B **102B**, 385 (1981).
11. V. K. Luk'yanov and A. I. Titov, Fiz. Élem. Chastits At. Yadra **10**, 815 (1979) [Sov. J. Part. Nucl. **10**, 321 (1979)].
12. H. J. Pirner and J. P. Vary, Phys. Rev. Lett. **46**, 1376 (1981).
13. M. I. Gorenshteĭn, G. M. Zinov'ev, and V. P. Shelest, Yad. Fiz. **26**, 788 (1977) [Sov. J. Nucl. Phys. **26**, 414 (1977)].
14. I. L. Rozental' and Yu. A. Tarasov, Usp. Fiz. Nauk **163** (7), 29 (1993) [Phys. Usp. **36** (7), 572 (1993)].

Translated by A. Isaakyan

Physics of Atomic Nuclei, Vol. 68, No. 6, 2005, pp. 991–998. From Yadernaya Fizika, Vol. 68, No. 6, 2005, pp. 1029–1036.
Original English Text Copyright © 2005 by Azhgirey, Afanasiev, Isupov, Ivanov, Khrenov, Ladygin, Ladygina, Litvinenko, Peresedov, Yudin, Zhmyrov, Zolin.

ELEMENTARY PARTICLES AND FIELDS
Experiment

Measurement of the Tensor A_{yy} and Vector A_y Analyzing Powers of the Deuteron Inelastic Scattering of Beryllium at 5.0 GeV/c and 178 mrad*

L. S. Azhgirey, S. V. Afanasiev, A. Yu. Isupov, V. I. Ivanov, A. N. Khrenov, V. P. Ladygin, N. B. Ladygina, A. G. Litvinenko, V. F. Peresedov, N. P. Yudin[1)], V. N. Zhmyrov, and L. S. Zolin**

Joint Institute for Nuclear Research, Dubna, Moscow oblast, 141980 Russia

Received April 9, 2004

Abstract—Tensor A_{yy} and vector A_y analyzing powers in the inelastic scattering of deuterons with a momentum of 5.0 GeV/c on beryllium at an angle of 178 mrad in the vicinity of the excitation of baryonic resonances with masses up to ~1.8 GeV/c^2 have been measured. The A_{yy} data are in good agreement with the previous data obtained at 4.5 and 5.5 GeV/c. The results of the experiment are compared with the predictions of the plane-wave impulse approximation and ω-meson-exchange models.
© 2005 Pleiades Publishing, Inc.

1. INTRODUCTION

Deuteron inelastic scattering for hydrogen and nuclei at high energies has been extensively investigated at different laboratories in recent years [1–13]. The interest in this reaction is due mainly to the possibility of studying nucleon–baryon (NN^*) interaction.

Firstly, since the deuteron is an isoscalar probe, inelastic scattering of deuterons, $A(d,d')X$, is selective to the isospin of the unobserved system X, which is bound to be equal to the isospin of the target A. This feature, for instance, was used to search for $\Delta\Delta$ dibaryons with an isospin $T=0$ in the $d(d,d')X$ reaction [6]. Inelastic scattering of deuterons on hydrogen, $H(d,d')X$, in particular, is selective to the isospin 1/2 and can be used to obtain information on the formation of baryonic resonances $N^*(1440)$, $N^*(1520)$, $N^*(1680)$, and others.

Secondly, deuteron inelastic scattering at relativistic energies involves high momentum transfers. Therefore, if the deuteron scattering takes place as a result of NN collisions, one may expect it to be sensitive to the structure of the deuteron and, possibly, to the manifestation of nonnucleonic degrees of freedom, namely, NN^* and N^*N^* components in the deuteron wave function [14, 15]. In this respect, inelastic scattering of deuterons on nuclei at high transferred momenta can be considered as a complementary method to the elastic pd and ed scatterings, deuteron breakup reaction, and electro- and photodisintegration of the deuteron to investigate the deuteron structure at short distances.

Thirdly, deuteron inelastic scattering can be sensitive to the amplitudes of $NN^* \to NN^*$ processes in the kinematical range, where the contribution of double-scattering diagrams [7] is significant.

Lastly, since there is a large momentum transfer, one can hope to get information on the formation of the $6q$ configuration in the deuteron.

Differential cross section measurements of deuteron inelastic scattering have been performed at Saclay at 2.95 GeV/c [1, 4] for hydrogen, at Dubna [3, 5, 7] for different targets at deuteron momenta up to 9 GeV/c, and at Fermilab [2] at higher energies for hydrogen. Calculations performed in the framework of the multiple-scattering formalism [7] have shown that the differential cross section of the $H(d,d')X$ reaction can be satisfactorily described by hadron–hadron double scattering. The amplitudes of the elementary processes $NN \to NN^*$ have been extracted for $N^*(1440)$, $N^*(1520)$, and $N^*(1680)$ resonances [7].

The availability of polarized deuteron beams at high energies allowed one to continue the investigation of the $(d,d')X$ process; however, polarization data on deuteron inelastic scattering are still scarce. Polarized deuterons of high energies have been used to study the tensor analyzing power T_{20} in the vicinity

*This article was submitted by the authors in English.

[1)]Moscow State University, Moscow, Russia.

**e-mail: ladygin@sunhe.jinr.ru

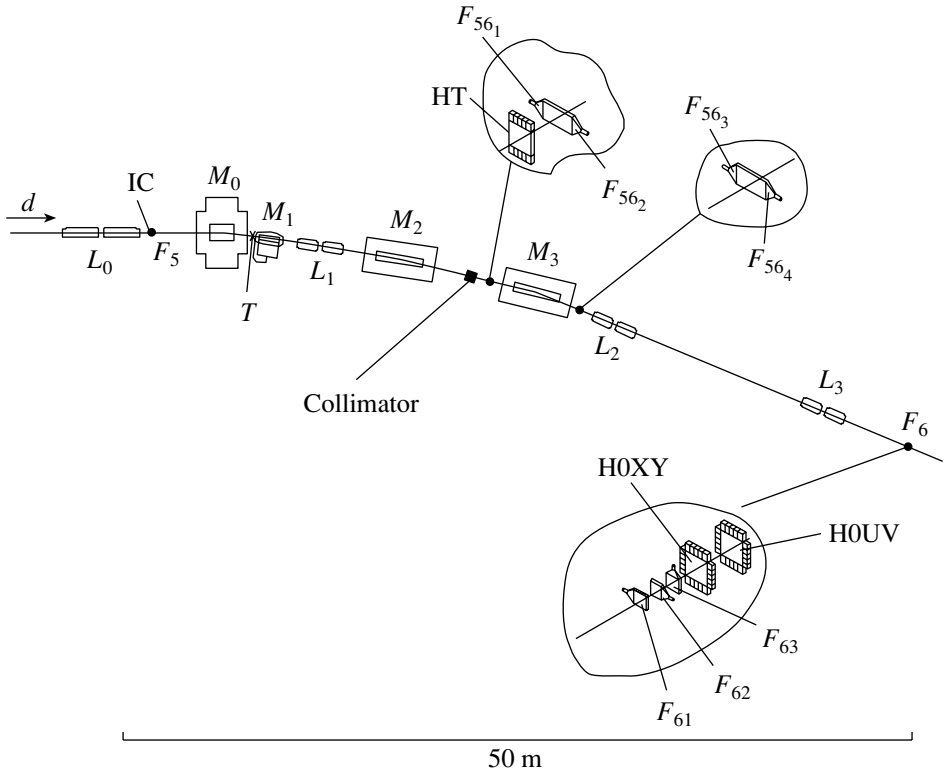

Fig. 1. Layout of the SPHERE setup with beam line VP1. M_i and L_i designate magnets and lenses, respectively; IC is the ionization chamber; T is the target; F_{61}, F_{62}, F_{63} are trigger counters; $F_{56_{1-4}}$ are scintillation counters and HT is a scintillation hodoscope for TOF measurements; H0XY and H0UV are beam profile hodoscopes.

of the Roper resonance ($P_{11}(1440)$) excitation on hydrogen and carbon targets at Dubna [8] and on a hydrogen target at Saclay [9]. Measurements of T_{20} in deuteron scattering at 9 GeV/c on hydrogen and carbon have been performed for missing masses up to $M_X \sim 2.2$ GeV/c^2 [10]. The experiments have shown a large negative value of T_{20} at a momentum transfer of $t \sim -0.3\,(\mathrm{GeV}/c)^2$. Such a behavior of the tensor analyzing power has been interpreted in the framework of the ω-meson-exchange model [16] as due to the longitudinal isoscalar form factor of the Roper resonance excitation [17]. The measurements of the tensor and vector analyzing powers A_{yy} and A_y at 9 GeV/c and 85 mrad of the secondary deuteron emission angle in the vicinity of the undetected system mass of $M_X \sim 2.2$ GeV/c^2 have shown large values. The obtained results are in satisfactory agreement with the plane-wave impulse approximation (PWIA) calculations [18]. It was stated that the spin-dependent part of the $NN \to NN^*(\sim 2.2\ \mathrm{GeV}/c^2)$ process amplitude is significant. The measurements of A_{yy} at 4.5 GeV/c and 80 mrad [12] have also shown a large value of the tensor analyzing power. The exclusive measurements of the polarization observables in the $H(d,d')X$ reaction in the vicinity of the Roper resonance excitation performed recently at Saclay [13] also demonstrated large spin effects.

In this paper, we report new results on the tensor and vector analyzing powers A_{yy} and A_y in deuteron inelastic scattering on a beryllium target at an incident deuteron momentum of 5.0 GeV/c and $\sim$178 mrad of the secondary emission angle. Details of the experiment are described in Section 2. The comparison with the existing data and theoretical predictions is given in Section 3. Conclusions are drawn in Section 4.

2. EXPERIMENT

The experiment was performed using a polarized deuteron beam at the Dubna Synchrophasotron at the Laboratory of High Energies of JINR and the SPHERE setup shown in Fig. 1 and described elsewhere [11, 12]. The polarized deuterons were produced by the ion source POLARIS [19]. The sign of the beam polarization was changed cyclically and spill-by-spill, as "0," "−," "+," where "0" means the absence of the polarization, and "+" and "−" correspond to the sign of p_{zz} with the quantization axis perpendicular to the plane containing the mean beam orbit in the accelerator.

The tensor polarization of the beam was determined during the experiment by the asymmetry of protons from the deuteron breakup on a beryllium target, $d + \mathrm{Be} \to p + X$, at zero emission angle and proton momentum of $p_p \sim \frac{2}{3} p_d$ [20]. It was shown that the deuteron breakup reaction in such kinematic conditions has a very large tensor analyzing power $T_{20} = -0.82 \pm 0.04$, which is independent of the atomic number of the target ($A > 4$) and of the momentum of incident deuterons between 2.5 and 9.0 GeV/c [21]. The tensor polarization averaged over the whole duration of the experiment was $p_{zz}^{+} = 0.716 \pm 0.043(\mathrm{stat.}) \pm 0.035(\mathrm{syst.})$ and $p_{zz}^{-} = -0.756 \pm 0.027(\mathrm{stat.}) \pm 0.037(\mathrm{syst.})$ in the "+" and "−" beam spin states, respectively.

The stability of the vector polarization of the beam was monitored by measuring the asymmetry of quasielastic pp scattering on a thin CH_2 target placed at the F_3 focus of the VP1 beam line. The values of the vector polarization were obtained using the results of the asymmetry measurements at the momenta 2.5 GeV/c per nucleon and 14° of the proton scattering angle with the corresponding value of the effective analyzing power of the polarimeter $A(CH_2)$ taken as 0.234 [22]. The vector polarization of the beam in different spin states was $p_z^{+} = 0.173 \pm 0.008(\mathrm{stat.}) \pm 0.009(\mathrm{syst.})$ and $p_z^{-} = 0.177 \pm 0.008(\mathrm{stat.}) \pm 0.009(\mathrm{syst.})$.

The slowly extracted beam of tensor polarized 5.0-GeV/c deuterons with an intensity of $\sim 5 \times 10^8$ particles per beam spill was incident on a 16-cm-thick beryllium target positioned ~2.4 m downstream of the F_5 focus of the VP1 beam line (see Fig. 1). The intensity of the beam was monitored by an ionization chamber placed in front of the target. The beam positions and profiles at certain points of the beam line were monitored by the control system of the accelerator during each spill. The beam size at the target point was $\sigma_x \sim 0.4$ cm and $\sigma_y \sim 0.9$ cm in the horizontal and vertical directions, respectively.

Data were obtained for four momenta of the secondary particles between 2.7 and 3.6 GeV/c. The secondary particles emitted at ~178 mrad from the target were transported to the focus F_6 by means of two bending magnets (M_0 and M_1 were switched off) and three lense doublets. The acceptance of the setup was determined via Monte Carlo simulation taking into account the parameters of the incident deuteron beam, nuclear interaction and multiple scattering in the target, in the air, windows and detectors, energy losses of the primary and secondary deuterons, etc. The momentum acceptances for four cases of the magnetic element tuning are shown in Fig. 2.

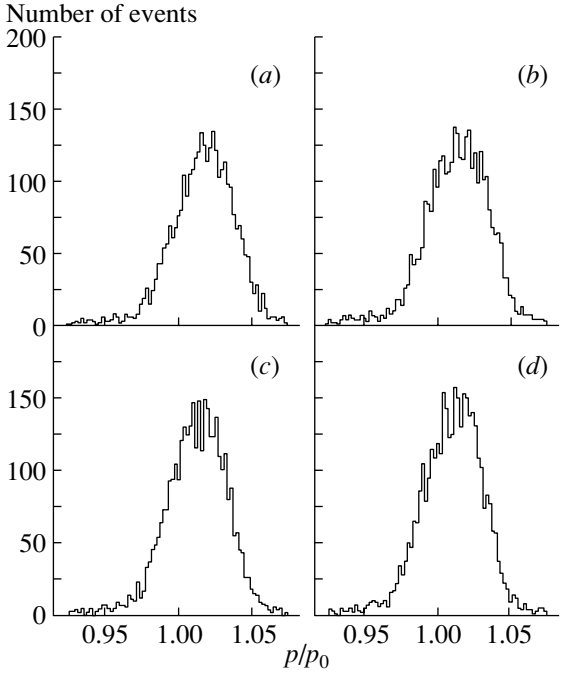

Fig. 2. The momentum acceptances of the setup for deuterons for different magnetic element tuning. Panels *a*, *b*, *c*, and *d* correspond to secondary deuteron momenta of 2.7, 3.0, 3.3, and 3.6 GeV/c, respectively.

The momentum and polar angle acceptances were $\Delta p/p \sim \pm 2\%$ and ± 18 mrad, respectively.

The coincidences of signals from the scintillation counters F_{61}, F_{62}, and F_{63} were used as a trigger. Along with the inelastically scattered deuterons, the apparatus detected the protons originating from deuteron fragmentation. For particle identification, the time-of-flight (TOF) information with a baseline of ~28 m between the start counter F_{61} and the stop counters F_{56_1}, F_{56_2}, and F_{56_4} was used in the off-line analysis. The TOF resolution was better than 0.2 ns (1σ). The TOF spectra obtained for all four cases of magnetic element tuning are shown in Fig. 3. At higher momentum of the detected particles, only deuterons appear in TOF spectra; however, when the momentum decreases, the relative contribution of protons becomes more pronounced. In data processing, useful events were selected as the ones with at least two measured TOF values correlated. This allowed the residual background to be ruled out completely.

The tensor A_{yy} and vector A_y analyzing powers were calculated from the yields of deuterons n^{+}, n^{-}, and n^0 for different states of the beam polarization after correction for dead time of the setup by means of the expressions

$$A_{yy} = 2\frac{p_z^{-}(n^{+}/n^0 - 1) - p_z^{+}(n^{-}/n^0 - 1)}{p_z^{-} p_{zz}^{+} - p_z^{+} p_{zz}^{-}}, \quad (1)$$

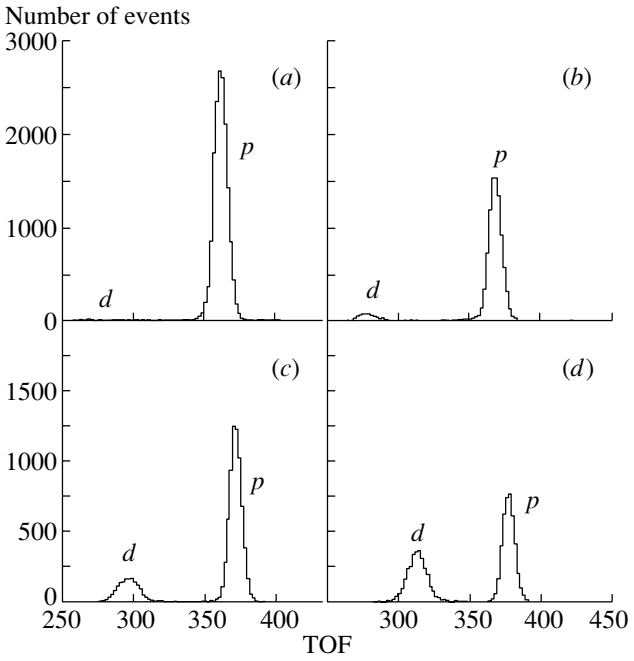

Fig. 3. The TOF spectra obtained for different magnetic element tuning. Panels *a*, *b*, *c*, and *d* correspond to secondary deuteron momenta of 2.7, 3.0, 3.3, and 3.6 GeV/c, respectively.

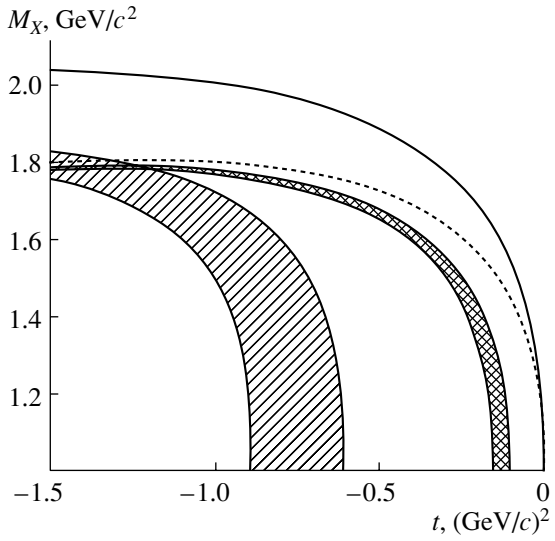

Fig. 4. The kinematical plot of the missing mass M_X vs. 4-momentum t at the initial deuteron momenta between 4.5 and 5.5 GeV/c. The solid and dashed curves correspond to the conditions (middle of the acceptance) of the experiment performed at zero angle and at 5.5 and 4.5 GeV/c, respectively [8]. The dashed area demonstrates the region of 4-momentum t and missing mass M_X covered within the acceptance of the present experiment, while the hatched area shows the conditions of the experiment performed at 4.5 GeV/c and ∼80 mrad [12].

$$A_y = -\frac{2}{3}\frac{p_{zz}^-(n^+/n^0-1)-p_{zz}^+(n^-/n^0-1)}{p_z^-p_{zz}^+-p_z^+p_{zz}^-}.$$

These expressions take into account different values of the polarization in different beam spin states and are simplified significantly when $p_z^+ = p_z^-$ and $p_{zz}^+ = -p_{zz}^-$.

The data on the tensor A_{yy} and vector A_y analyzing powers in the deuteron inelastic scattering obtained in this experiment are given in the table. The reported error bars are statistical only. The systematic errors are ∼5% for the both A_{yy} and A_y.

The values of the secondary-deuteron momentum p, width (RMS) of the momentum acceptance Δp, 4-momentum t, and missing mass M_X given in the table are obtained from Monte Carlo simulation. The averaged momentum of the initial deuteron equals 4.978 GeV/c due to the energy losses in the target.

The values of the missing mass M_X given in the table were calculated under the assumption that the reaction occurs on a target with proton mass. In this case, the 4-momentum transfer t and missing mass M_X are related as follows:

$$M_X^2 = t + m_p^2 + 2m_pQ, \qquad (2)$$

where m_p is the proton mass and Q is the energy difference between the incident and scattered deuterons.

The dashed area on the kinematical plot given in Fig. 4 demonstrates the region of 4-momentum t and missing mass M_X covered by the setup acceptance in the present experiment. The solid and dashed curves correspond to the initial deuteron momenta of 5.5 and 4.5 GeV/c and zero emission angle [8], respectively. The hatched area shows the conditions of the experiment performed at 4.5 GeV/c and ∼80 mrad [12]. One can see that the same missing mass M_X corresponds to different t under conditions of the previous [8, 12] and present experiments. In this respect, the data obtained at 5.0 GeV/c and ∼178 mrad provide new information on the t and M_X dependences of the analyzing powers A_{yy} and A_y.

3. RESULTS AND DISCUSSION

In Fig. 5, the data on the tensor analyzing power A_{yy} in the inelastic scattering of 5.0-GeV/c deuterons on beryllium at an angle of 178 mrad are shown as a function of the transferred 4-momentum t by closed triangles. The A_{yy} has a positive value at $|t| \sim 0.9$ (GeV/c)^2 and crosses zero at larger $|t|$. The data on tensor analyzing power obtained at zero emission angle at 4.5 and 5.5 GeV/c [8] on hydrogen are given by open triangles and squares, respectively (recall that, for these data, $A_{yy} = -T_{20}/\sqrt{2}$). The

The tensor A_{yy} and vector A_y analyzing powers of the inelastic scattering of 5.0-GeV/c deuterons on beryllium at an angle of ∼178 mrad

$p \pm \Delta p$, GeV/c	t, (GeV/c)^2	M_X, GeV/c^2	$A_{yy} \pm dA_{yy}$	$A_y \pm dA_y$
2.747 ± 0.060	-1.461	1.776	0.108 ± 0.120	-0.538 ± 0.168
3.042 ± 0.067	-1.206	1.716	-0.128 ± 0.106	0.101 ± 0.145
3.340 ± 0.070	-1.023	1.627	0.097 ± 0.068	-0.020 ± 0.097
3.638 ± 0.077	-0.901	1.508	0.182 ± 0.054	0.373 ± 0.076

data obtained at 4.5 GeV/c and at an angle of 80 mrad [12] are shown by open circles. As was established earlier [8, 12], there is no significant dependence of A_{yy} on the A value of the target. The observed independence of the tensor analyzing power of the atomic number of the target indicates that the rescattering in the target and medium effects are small. Hence, nuclear targets are also appropriate to obtain information on the baryonic excitations in deuteron inelastic scattering [8, 10–12]. One can see the regular behavior of the A_{yy} data from our experiment and previous data [8, 12] in a wide region of $|t|$. At small $|t|$ (≤ 0.3 (GeV/c)^2), A_{yy} rises linearly up to the value of ∼0.3, and then it smoothly decreases and changes sign at $|t| \sim 1$ (GeV/c)^2.

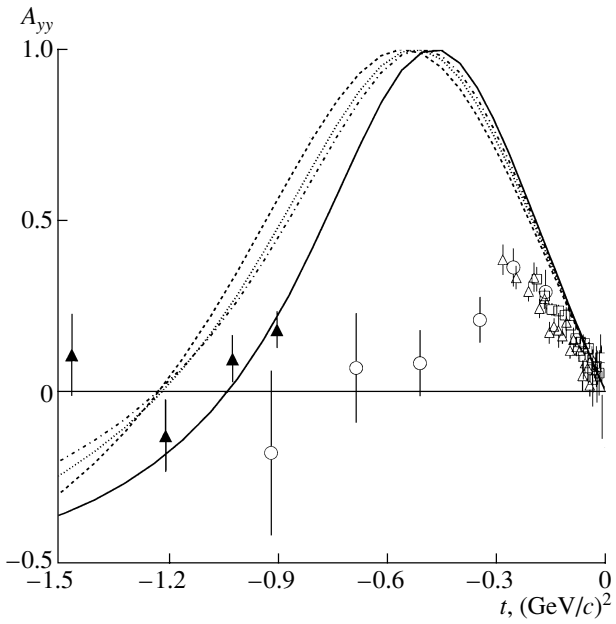

Fig. 5. Tensor analyzing power A_{yy} in deuteron inelastic scattering on beryllium at 5.0 GeV/c and 178 mrad and at 4.5 GeV/c and 80 mrad [12] given by closed triangles and open circles, respectively; on hydrogen at 4.5 and 5.5 GeV/c at zero angle [8] shown by open triangles and squares, respectively, as a function of the 4-momentum t. The solid, dashed, dotted, and dash-dotted curves are predictions in the framework of PWIA [18] using DWFs for the Paris [23] and Bonn A, B, and C [24] potentials, respectively.

The $(d, d')X$ data on A_{yy} and A_y obtained at 9 GeV/c and 85 mrad at large $|t|$ in the vicinity of the baryon excitation with the mass $M_X \sim 2.19$ GeV/c^2 [11] have been satisfactorily explained in the framework of PWIA [12] (see Fig. 6). In this model, the tensor and vector analyzing powers are expressed in terms of three amplitudes (T_{00}, T_{11}, and T_{10}) defined by the deuteron structure and the ratio r of the spin-dependent-to-spin-independent parts of the elementary process $NN \to NN^*$:

$$A_{yy}(q) = \frac{T_{00}^2 - T_{11}^2 + 4r^2T_{10}^2}{T_{00}^2 + 2T_{11}^2 + 4r^2T_{10}^2}, \qquad (3)$$

$$A_y(q) = 2\sqrt{2}r\frac{(T_{11} + T_{00})T_{10}}{T_{00}^2 + 2T_{11}^2 + 4r^2T_{10}^2}. \qquad (4)$$

One can see that the vector analyzing power A_y is proportional to the ratio r, while the tensor analyzing power A_{yy} is sensitive to r very weakly.

The amplitudes T_{00} and T_{11} are expressed in terms of S and D waves of the deuteron as follows:

$$T_{00} = S_0(q/2) + \sqrt{2}S_2(q/2), \qquad (5)$$

$$T_{11} = S_0(q/2) - \frac{1}{\sqrt{2}}S_2(q/2),$$

where S_0 and S_2 are the charge and quadrupole form factors of the deuteron. They are defined in the stan-

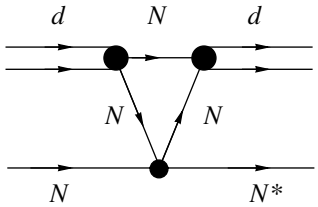

Fig. 6. Diagram of the plane-wave impulse approximation for deuteron inelastic scattering with the baryonic excitation.

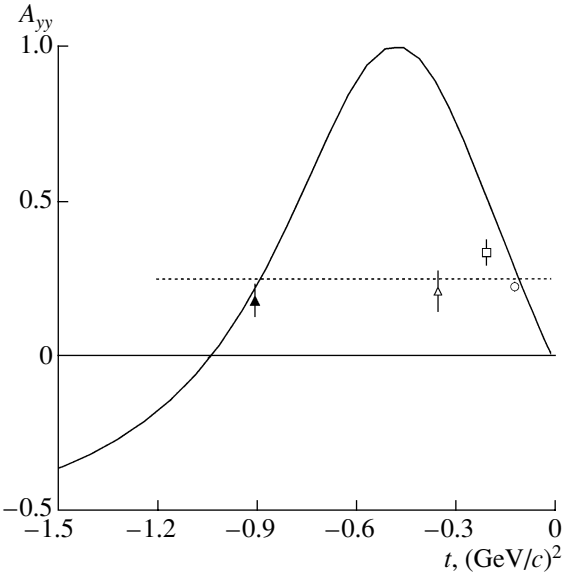

Fig. 7. The A_{yy} data from the present experiment (closed triangle) along with the data obtained with 4.5- and 5.5-GeV/c deuterons at zero angle [8] (open circle and square, respectively) and the data at 4.5 GeV/c at an angle of 80 mrad [12] plotted vs. 4-momentum t for the missing mass $M_X \sim 1550$ MeV/c^2 (open triangle). The solid curve is the calculations in PWIA using DWFs for Paris [23]. The dashed line is the predictions within the ω-meson-exchange model [17].

dard way

$$S_0(q/2) = \int_0^\infty (u^2(r) + w^2(r)) j_0(rq/2) dr, \quad (6)$$

$$S_2(q/2) = \int_0^\infty 2w(r) \left(u(r) - \frac{1}{2\sqrt{2}} w(r) \right) j_2(rq/2) dr,$$

where $u(r)$ and $w(r)$ are S and D waves of the deuteron in the configuration space; $j_0(qr/2)$ and $j_2(qr/2)$ are Bessel functions of the zero and second order, respectively; and $q^2 = -t$.

Amplitude T_{10} is also defined by the S and D waves of the deuteron:

$$T_{10} = \frac{i}{\sqrt{2}} \int_0^\infty \left(u^2(r) - \frac{w^2(r)}{2} \right) j_0(rq/2) dr \quad (7)$$

$$+ \frac{i}{2} \int_0^\infty w(r) \left(u(r) + \frac{w(r)}{\sqrt{2}} \right) j_2(rq/2) dr.$$

The ratio of the spin-dependent-to-spin-independent parts of the elementary amplitude of the $NN \to NN^*$ process r is taken in the simple form [18]

$$r(q) = aq, \quad (8)$$

where a is a constant.

The curves in Fig. 5 are predictions of the A_{yy} behavior in the framework of the PWIA [18]. The solid curve in Fig. 5 is calculated with the deuteron wave function (DWF) for the Paris potential [23], while the dashed, dotted, and dash-dotted curves correspond to the DWFs for the Bonn A, B, and C potentials [24], respectively. One can see good agreement of the A_{yy} data from the present experiment with the PWIA calculations [18] using the Paris DWF.

The deviation of the data obtained in the previous experiments [8, 12] at $|t| \sim 0.3$–0.8 (GeV/c)^2 from the predictions of PWIA, as well as the different behavior of the tensor analyzing power in the $(d, d')X$ process and in ed [25, 26] and pd [27] elastic scattering, indicates the sensitivity of A_{yy} to the baryonic resonance excitation via double-collision interactions [7], where the resonance is formed in the second NN collision or the resonance formed in the first NN interaction elastically scatters on the second nucleon of the deuteron.

The sensitivity of the tensor analyzing power in deuteron inelastic scattering off protons to the excitation of baryonic resonances has been pointed out in [16] in the framework of the t-channel ω-meson-exchange model. The cross section and the polarization observables can be calculated from the known electromagnetic properties of the deuteron and baryonic resonances N^* through the vector dominance model. In this model, the t dependence of the tensor analyzing power in deuteron inelastic scattering is defined by the t dependence of the deuteron form factors and the contribution of the Roper resonance due to its nonzero isoscalar longitudinal form factor [17]. In such an approximation, the tensor analyzing power is a universal function of $|t|$ only, without any dependence on the initial deuteron momentum, if the finite values of the resonance widths are neglected. Since the isoscalar longitudinal amplitudes of $S_{11}(1535)$ and $D_{13}(1520)$ vanish due to spin-flavor symmetry, while both isoscalar and isovector longitudinal couplings of $S_{11}(1650)$ vanish identically, the tensor analyzing power A_{yy} in inelastic deuteron scattering with the excitation of one of these resonances has the value of $+0.25$ independent of t [12].

The t dependence of A_{yy} at $M_X \sim 1550$ and 1650 MeV/c^2 is shown in Figs. 7 and 8, respectively. The closed triangles are the results of the present experiment, while the open squares, circles, and triangles are results obtained earlier at 4.5 and 5.5 GeV/c [8, 12]. The solid curves are the results of the PWIA calculations [18] using the Paris DWF [23]. The dashed lines are the expectations of the ω-meson-exchange model [16, 17]. One can see that the behavior of A_{yy} at $M_X \sim 1550$ MeV/c^2 (Fig. 7)

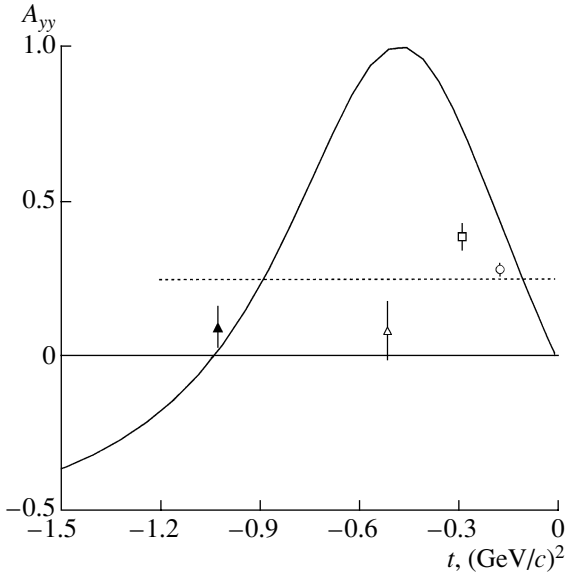

Fig. 8. The same as in Fig. 7, but for the missing mass $M_X \sim 1650$ MeV/c^2.

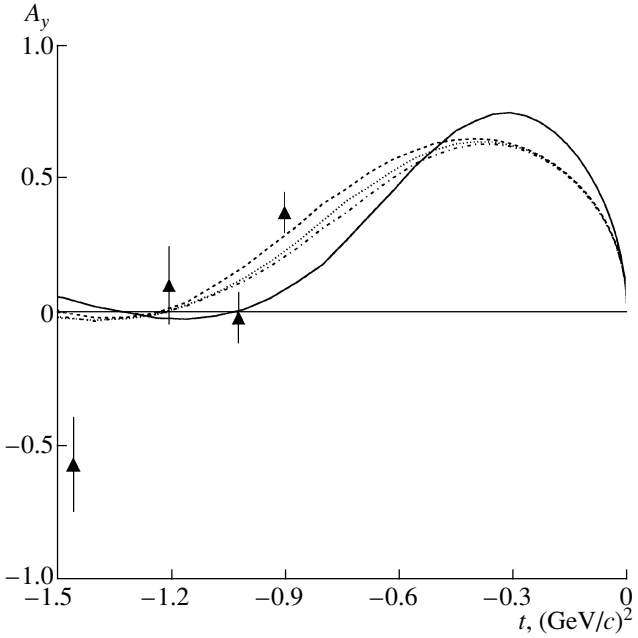

Fig. 9. Vector analyzing power A_y in deuteron inelastic scattering on beryllium at 5.0 GeV/c at an angle of 178 mrad as a function of the 4-momentum t. The solid, dashed, dotted, and dash-dotted curves are predictions in the framework of PWIA [18] using DWFs for the Paris [23] and Bonn A, B, and C [24] potentials, respectively.

is not in contradiction with the ω-meson-exchange-model prediction [17], while at $M_X \sim 1650$ MeV/c^2 (Fig. 8) some deviation from the constant value of $+0.25$ is observed. However, as we mentioned above, at these missing masses it may be necessary to consider additional contributions from the $F_{15}(1680)$ and $P_{13}(1720)$ resonances, which also have nonzero longitudinal isoscalar form factors and, therefore, can significantly affect the t dependence of the tensor analyzing power. Note also that, since we study the inclusive $(d, d')X$ reaction, many resonances contribute at a fixed M_X due to their finite widths, while the theoretical predictions in Figs. 7 and 8 are obtained for separate contributions of the $S_{11}(1535)$, $D_{13}(1520)$, and $S_{11}(1650)$ resonances. In this respect, exclusive (or semiexclusive) measurements with the detection of the resonance decay products could help to distinguish between the contributions of different baryonic resonances.

The values of the vector analyzing power A_y are small except for the first point at $M_X \sim 1500$ MeV/c^2. In the framework of PWIA [18], such a fact can be considered as a significant role of the spin-dependent part of the elementary amplitude of the $NN \to NN^*$ process.

The behavior of the vector analyzing power A_y obtained in the present experiment is plotted in Fig. 9 versus t. The curves are obtained using expression (4) with the ratio r of the spin-dependent-to-spin-independent parts of the $NN \to NN^*$ process taken in the form (8) with the value $a = 1.0$. The solid curve in Fig. 9 is obtained with the DWF for the Paris potential [23], while the dashed, dotted, and dash-dotted lines correspond to the DWFs for the Bonn A, B, and C potentials [24], respectively. The PWIA calculations give approximately the same results at the value $a \sim 0.8-1.2$. It should be noted that a might have different values for different M_X; however, we took a fixed value for simplicity due to the lack of data.

4. CONCLUSIONS

We have presented the data on the tensor and vector analyzing powers A_{yy} and A_y in inelastic scattering $(d, d')X$ of 5.0-GeV/c deuterons on beryllium at an angle of ~178 mrad in the vicinity of the excitations of baryonic masses from 1.5 up to 1.8 GeV/c^2. This corresponds to the range of 4-momentum $|t|$ between 0.9 and 1.5 (GeV/c)^2.

The data on A_{yy} are in good agreement with the data obtained in previous experiments at momenta between 4.5 and 5.5 GeV/c [8, 12] when they are compared versus variable t.

It is observed also that A_{yy} data from the present experiment are in good agreement with PWIA calculations [18] using conventional DWFs [23, 24]. On the other hand, the behavior of the A_{yy} data obtained in the vicinity of the $S_{11}(1535)$ and $D_{13}(1520)$

resonances is not in contradiction with the predictions of the ω-meson-exchange model [17], while at higher excited masses this model may require taking into account the additional baryonic resonances with nonzero longitudinal form factors.

The vector analyzing power A_y has a large value at $M_X \sim 1500$ MeV/c^2, which could be interpreted as a significant role of the spin-dependent part of the elementary amplitude of the $NN \to NN^*$ reaction.

Exclusive polarization experiments [13] with the detection of resonance decay products could significantly advance the understanding of the mechanism of the different baryonic resonance excitation and spin properties of their interactions with nucleons.

ACKNOWLEDGMENTS

We are grateful to the LHE accelerator staff and POLARIS team for providing good conditions for the experiment. We thank I.I. Migulina for the help in the preparation of this manuscript.

This work was supported in part by the Russian Foundation for Basic Research (project no. 03-02-16224).

REFERENCES

1. J. Banaigs *et al.*, Phys. Lett. B **45B**, 535 (1973).
2. Y. Akimov *et al.*, Phys. Rev. Lett. **35**, 763 (1975).
3. L. S. Azhgireĭ *et al.*, Yad. Fiz. **27**, 1027 (1978) [Sov. J. Nucl. Phys. **27**, 544 (1978)]; **30**, 1578 (1979) [**30**, 818 (1979)].
4. R. Baldini Celio *et al.*, Nucl. Phys. A **379**, 477 (1982).
5. V. G. Ableev *et al.*, Yad. Fiz. **37**, 348 (1983) [Sov. J. Nucl. Phys. **37**, 209 (1983)].
6. M. P. Combets *et al.*, Nucl. Phys. A **431**, 703 (1984).
7. L. S. Azhgireĭ *et al.*, Yad. Fiz. **48**, 1758 (1988) [Sov. J. Nucl. Phys. **48**, 1058 (1988)].
8. L. S. Azhgirey *et al.*, Phys. Lett. B **361**, 21 (1995).
9. Experiment LNS-E250 (unpublished).
10. L. S. Azhgirey *et al.*, JINR Rapid Commun., No. 2[88]-98, 17 (1998).
11. L. S. Azhgirey *et al.*, Yad. Fiz. **62**, 1796 (1999) [Phys. At. Nucl. **62**, 1673 (1999)].
12. V. P. Ladygin, L. S. Azhgirey, S. V. Afanasiev, *et al.*, Eur. Phys. J. A **8**, 409 (2000); L. S. Azhgirey, V. V. Arkhipov, S. V. Afanasiev, *et al.*, Yad. Fiz. **64**, 2046 (2001) [Phys. At. Nucl. **64**, 1961 (2001)].
13. L. V. Malinina, G. D. Alkhazov, W. Augustyniak, *et al.*, Phys. Rev. C **64**, 064001 (2001).
14. L. Glozman, Prog. Part. Nucl. Phys. **34**, 123 (1995).
15. L. S. Azhgirey and N. P. Yudin, Yad. Fiz. **63**, 2280 (2000) [Phys. At. Nucl. **63**, 2184 (2000)].
16. M. P. Rekalo and E. Tomasi-Gustafsson, Phys. Rev. C **54**, 3125 (1996).
17. E. Tomasi-Gustafsson, M. P. Rekalo, R. Bijker, *et al.*, Phys. Rev. C **59**, 1526 (1999).
18. V. P. Ladygin and N. B. Ladygina, Yad. Fiz. **65**, 188 (2002) [Phys. At. Nucl. **65**, 182 (2002)].
19. N. G. Anishchenko *et al.*, in *Proceedings of the 5th International Symposium on High-Energy Spin Physics, Brookhaven, 1982*; AIP Conf. Proc. **95**, 445 (1983).
20. L. S. Zolin *et al.*, JINR Rapid Commun., No. 2[88]-98, 27 (1998).
21. C. F. Perdrisat *et al.*, Phys. Rev. Lett. **59**, 2840 (1987); V. Punjabi *et al.*, Phys. Rev. C **39**, 608 (1989); V. G. Ableev *et al.*, Pis'ma Zh. Éksp. Teor. Fiz. **47**, 558 (1988) [JETP Lett. **47**, 649 (1988)]; JINR Rapid Commun., No. 4[43]-90, 5 (1990); T. Aono *et al.*, Phys. Rev. Lett. **74**, 4997 (1995).
22. L. S. Azhgirey *et al.*, Prib. Tekh. Éksp., No. 1, 51 (1997) [Instrum. Exp. Tech. **40**, 43 (1997)]; Nucl. Instrum. Methods Phys. Res. A **497**, 340 (2003).
23. M. Lacombe *et al.*, Phys. Lett. B **101B**, 139 (1981).
24. R. Machleidt *et al.*, Phys. Rep. **149**, 1 (1987).
25. M. Garcon *et al.*, Phys. Rev. C **49**, 2516 (1994), and references therein.
26. D. Abbott *et al.*, Phys. Rev. Lett. **84**, 5053 (2000).
27. V. Ghazikhanian *et al.*, Phys. Rev. C **43**, 1532 (1991).

Physics of Atomic Nuclei, Vol. 68, No. 6, 2005, pp. 999–1006. Translated from Yadernaya Fizika, Vol. 68, No. 6, 2005, pp. 1037–1044.
Original Russian Text Copyright © 2005 by Likhoded, Chalov.

ELEMENTARY PARTICLES AND FIELDS
Theory

Effects of the Mixing of Scalar and Pseudoscalar Higgs Bosons in the Process $e^+e^- \to e^+e^-b\bar{b}$ at a Future Linear Electron–Positron Collider

A. A. Likhoded* **and A. E. Chalov**

Institute for High Energy Physics, Protvino, Moscow oblast, 142284 Russia

Received February 19, 2004; in final form, June 17, 2004

Abstract—The sensitivity of data on the process $e^+e^- \to e^+e^-b\bar{b}$ at a future linear electron–positron collider to the deviation of the coupling of the Higgs boson to b quarks from the Standard Model predictions owing to the presence of a pseudoscalar Higgs boson state is analyzed for a collision energy of $\sqrt{s} = 500$ GeV. The admixture of a new hypothetical pseudoscalar Higgs boson state in the $Hb\bar{b}$ vertex is parametrized in the form $m_b/v(a + i\gamma_5 b)$. On the basis of an analysis of data on the process $e^+e^- \to e^+e^-b\bar{b}$, it is shown that experiments at the future linear collider TESLA will make it possible to constrain the parameters $\Delta a = a - 1$ and b as $-0.056 \le \Delta a \le 0.055$ and $-0.32 \le b \le 0.32$, respectively.
© *2005 Pleiades Publishing, Inc.*

1. INTRODUCTION

Searches for the Higgs boson and a determination of its CP nature are one of the key problems in modern particle physics. Within the Standard Model, the Higgs boson is responsible for electroweak-symmetry breaking, fermion masses being directly related to this symmetry-breaking mechanism. Within the simplest version of the theory, an electroweak scalar doublet characterized by an ad hoc ϕ^4 potential is responsible for symmetry breaking, predicting an observable Higgs boson whose quantum numbers are $J^{PC} = 0^{++}$. Popular extensions of the Standard Model predict, in addition to a light scalar state, the existence of a $J^{PC} = 0^{-+}$ pseudoscalar Higgs boson. The minimal supersymmetric standard model involving two Higgs doublets (2HDM), the three-doublet model proposed by Weinberg [1], and so on are the possible extensions of the Standard Model Higgs sector. Electroweak-symmetry breaking due to new strong interactions is an alternative possibility, and a pseudoscalar Higgs boson can exist in this case inclusive (see the review article of Hill and Simmons [2] and references therein). In this connection, it is of paramount importance to distinguish between these scenarios, and this can be achieved by thoroughly studying the CP properties of the hypothesized scalar (pseudoscalar) particle.

Experimental data obtained at the LEP collider in studying the processes $e^+e^- \to ZH$ rule out, within the Standard Model, the existence of a Higgs boson whose mass is smaller than 114.4 GeV [3]. Within the minimal supersymmetric standard model, the physical spectrum involves five Higgs bosons. These are a light and a heavy neutral scalar one (h^0, H^0), a CP-odd pseudoscalar one (A^0), and two charged scalar ones ($H^\pm$), the mass of the lightest scalar state and the mass of the pseudoscalar state being experimentally constrained from below by, respectively, 91 and 91.9 GeV [4].

A method for analyzing the CP nature of the Higgs boson on the basis of its decays to fermions or gauge bosons was developed in [5] and was applied in [6] to studying Higgs boson production in the reaction $e^+e^- \to ZH$. It should be noted that investigations at a photon–photon collider, where different polarizations of initial photons will make it possible to single out different CP states [7], are likely to provide the most direct means for determining the CP properties of the Higgs boson. Data on the ZHH coupling constant can also be obtained from an analysis of the threshold behavior and angular distributions in the process $e^+e^- \to ZH$. In particular, the CP properties of the Higgs boson can be determined in this way to a fairly high degree of precision [8]. At future hadron colliders, such as LHC, an analysis of the azimuthal-angle distribution of detected final jets in the subprocess of gauge-boson fusion will provide an efficient possibility of studying the CP properties of HWW coupling [9] and special features of scalar (pseudoscalar) Higgs boson production [10]. Experimental data on the coupling of the Higgs boson to the t quark from the processes $pp \to t\bar{t}h$ at

*e-mail: andre@mx.ihep.su

LHC [11] and the process $e^+e^- \to t\bar{t}H$ at the future linear electron–positron collider [12] can also be of use in determining the CP properties of the Higgs boson. The possibilities of studying the CP properties of the Higgs boson were also analyzed for the case of a $\mu^+\mu^-$ collider [13].

In the present study, the possibility of determining the relative contributions of scalar and pseudoscalar Higgs bosons to the $Hb\bar{b}$ interaction vertex is explored for the reaction $e^+e^- \to e^+e^-b\bar{b}$ at the future linear electron–positron collider TESLA of total energy $\sqrt{s} = 500$ GeV and integrated luminosity 1 ab^{-1} [14]. It is assumed that the Higgs boson will have been discovered earlier at LHC, but a detailed determination of its CP nature will become the immediate task of experiments at the linear collider.

In contrast to the earlier studies reported in [15, 16], where the authors investigated only the subprocesses of radiative Higgs boson production—for example, $e^+e^- \to Z^* \to ZH$—we analyze here all possible contributions to the process $e^+e^- \to e^+e^-b\bar{b}$—in particular, we take into account the subprocess of gauge-boson fusion.

In [17, 18], the possibility of singling out a signal from the pseudoscalar Higgs boson in the processes $e^+e^- \to \nu\bar{\nu}\tau^+\tau^-$ and $e^+e^- \to \nu\bar{\nu}b\bar{b}$ was considered, and it was shown there that an analysis of these reactions will make it possible to set quite stringent constraints on the coupling of the scalar (pseudoscalar) Higgs boson to fermions. However, the impossibility of fully reconstructing reaction kinematics is a drawback of these processes that restricts substantially the sensitivity of data to model parameters. The process $e^+e^- \to e^+e^-b\bar{b}$ enables one to reconstruct fully the final state and the c.m. frame of the Higgs boson, this giving reasons to hope for improving attainable constraints.

The ensuing exposition is organized as follows. In Section 2, we consider the interaction of the scalar (pseudoscalar) Higgs boson and fermions within a model-independent approach. In Section 3, we present the results of an analysis of the process $e^+e^- \to e^+e^-b\bar{b}$. The last section contains general conclusions and an outlook.

2. STRUCTURE OF $Hf\bar{f}$ INTERACTION

In Standard Model extensions that involve extra scalar and pseudoscalar bosons, the lightest spinless particle may be a combination of states that are not parity eigenstates [16]. In addition, it is reasonable to assume that the coupling constants characterizing the interaction of this scalar (pseudoscalar) Higgs boson with gauge bosons and fermions are independent parameters. In this case, the strength of $Hf\bar{f}$ interaction can be parametrized as

$$\frac{m_f}{v}(a + i\gamma_5 b), \qquad (1)$$

where $v = 246$ GeV and where, in the Standard Model, $a = 1$ and $b = 0$. Considering the process $e^+e^- \to e^+e^-b\bar{b}$, we will investigate the case where a and b are independent free parameters and the cases where only one of these parameters deviates from the respective value in the Standard Model. It will be shown below that, in the case where a and b are independent, the resulting constraints on the model parameters appear to be insensitivity regions around the circles $\sqrt{a^2 + b^2} = 1$ in the ab plane.

It should be emphasized that not only do data on the process $e^+e^- \to e^+e^-b\bar{b}$ (without allowance for the subsequent decays of b quarks) include a linear dependence on the parameter a, this dependence being specified by the contribution of the interference of diagrams involving Higgs boson exchange and background diagrams, but they also contain a^2 and b^2 dependences, which are determined by the direct contribution of diagrams involving Higgs boson exchange. In view of this, searches for deviations from the predictions of the Standard Model—such as those that may arise in supersymmetric models—are possible even at the level of processes not involving the subsequent dynamics of b jets.

An analysis of the processes involving the subsequent hadronization of b quarks will provide the possibility of studying P-odd correlations, which will make it possible to separate the contributions of the scalar and the pseudoscalar component of Higgs boson coupling to fermions and to determine the sign of the pseudoscalar component.

In simulating the aforementioned processes by the Monte Carlo method, the differential distributions subjected to analysis were represented in the form of expansions in powers of the parameters a and b with coefficients equal to kinematical factors; that is,

$$\frac{d\sigma}{d\mathcal{O}} = A_0 + a \cdot A_1 + a^2 \cdot A_2 + ab \cdot A_3 + b \cdot A_4 + b^2 \cdot A_5 \ldots,$$

where $\mathcal{O}$ is a quantity observed experimentally and A_i are purely kinematical factors that arise upon squaring the amplitudes of the processes and performing integration over the phase space, which involve no dependence on the parameters a and b, and which are the subject of a direct Monte Carlo simulation. It will be shown below that $A_3 = A_4 = 0$ for the process $e^+e^- \to e^+e^-b\bar{b}$.

The data were simulated with allowance for the special features of the TESLA project; the response of the detector was simulated by using the 3.01 version of the SIMDET package [19]. For the process $e^+e^- \to e^+e^-b\bar{b}$, the Higgs boson mass was set to the value of $M_H = 120$ GeV.

3. PROCESS $e^+e^- \to e^+e^-b\bar{b}$

Within the Standard Model, the cross section for the reaction $e^+e^- \to e^+e^-b\bar{b}$ receives contributions from 50 Feynman diagrams; of these, two diagrams (one describes the radiative production of a Higgs boson, $Z^* \to HZ$, while the other describes the production of a Higgs boson via the fusion of vector bosons, $Z^*Z^* \to H$) are signal diagrams, while the remaining 48 are background diagrams. At $M_H = 120$ GeV and $\sqrt{s} = 500$ GeV, the total cross section for the reaction $e^+e^- \to e^+e^-b\bar{b}$ with allowance for the cut $|\cos\theta_{ee}| \leq 0.9962$ on the scattering angle with respect to the initial-beam axis for the electron or the positron produced in the final state and the cut $M_{e^+e^-} \geq 2$ GeV on the invariant electron–positron mass in the final state is about 4.3×10^{-2} pb.

In exploring the question of whether it is possible in principle to set constraints on model parameters, it is interesting above all to analyze the sensitivity of the process under analysis to these parameters. Figure 1 shows the total cross section for the reaction $e^+e^- \to e^+e^-b\bar{b}$ versus the parameters Δa and b ($\Delta a = a - 1$). From this figure, one can see that the dependence on the parameter b has the shape of a parabola that attains a minimum at $b = 0$. This confirms that the expansion of the total cross section features no term linear in b. A different situation is observed for the dependence on the parameter a (Δa). Here, the minimum of the parabola is shifted to the region of negative values of Δa, this indicating the presence of a term linear in a. In addition, the sensitivity of the cross section for the process in question is higher in the region of positive values of Δa; hence, it is natural to expect that the resulting constraints on the parameter a will be more stringent in the region of positive values of this parameter. The presence of terms linear in a is explained by the interference between the diagrams involving a Higgs boson and the background diagrams in the Standard Model. No similar effect occurs for the parameter b since, in the respective vertex, this parameter is multiplied by an imaginary unit, with the result that the first powers of b are canceled in the interference terms

$$M_i M_j^\dagger + M_j M_i^\dagger,$$

where M_i and M_j are the matrix elements of the ith and jth diagrams, respectively. Terms that are linear in the parameter b could arise owing to the emergence of the antisymmetric tensor $i\epsilon^{ijkl}$ upon evaluating the trace $\mathrm{tr}[\gamma_5\gamma_i\gamma_j\gamma_k\gamma_l]$, because this would lead to the cancellation of pure imaginary factors. However, the number of independent momenta is insufficient in the process being considered; in all probability, this effect may emerge only upon taking into account the subsequent hadronization of b jets or their polarization.

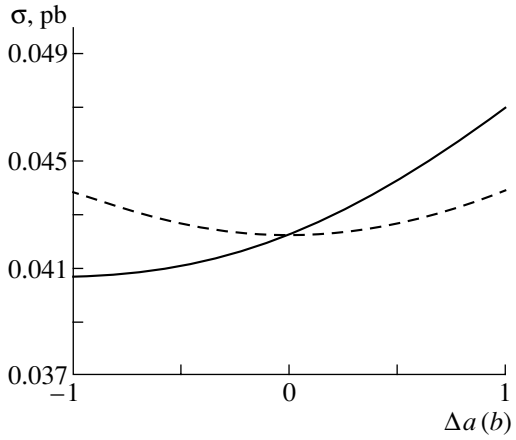

Fig. 1. Total cross section for the reaction $e^+e^- \to e^+e^-b\bar{b}$ as a function of the parameters (solid curve) Δa and (dashed curve) b.

In studying the process $e^+e^- \to e^+e^-b\bar{b}$, we analyze a standard set of experimentally observed distributions—namely, the momentum and scattering-angle distributions of a b jet; the invariant-mass distribution of a pair of b jets; and, in addition, the distribution with respect to the quantity

$$T_{\mathrm{cor}} = \frac{1}{(\sqrt{s}/2)^3}\mathbf{p}_e \cdot [\mathbf{p}_b \times \mathbf{p}_{\bar{b}}],$$

which is highly sensitive to the possible CP-odd effects in the Higgs sector [20].

In Fig. 2, the differential distributions of the cross section for the process $e^+e^- \to e^+e^-b\bar{b}$ with respect to (a) the b-quark momentum, (b) the b-quark scattering angle, (c) the correlation T_{cor}, and (d) the invariant mass of the b jets are presented for the case of the Standard Model, $\Delta a = b = 0$ (closed circles).

In determining the sensitivity of the process to the Higgs boson coupling constants, it is of importance to assess the relative contributions of signal and background diagrams (in the present case, these are diagrams involving a Higgs boson and those that do not involve it, respectively). Figure 2 shows the relative contribution of the diagrams featuring a Higgs boson, which include interference diagrams (crosses circumvented by circles). It can be seen from the figure that, in all distributions, the relative contribution of the diagrams involving the Higgs boson

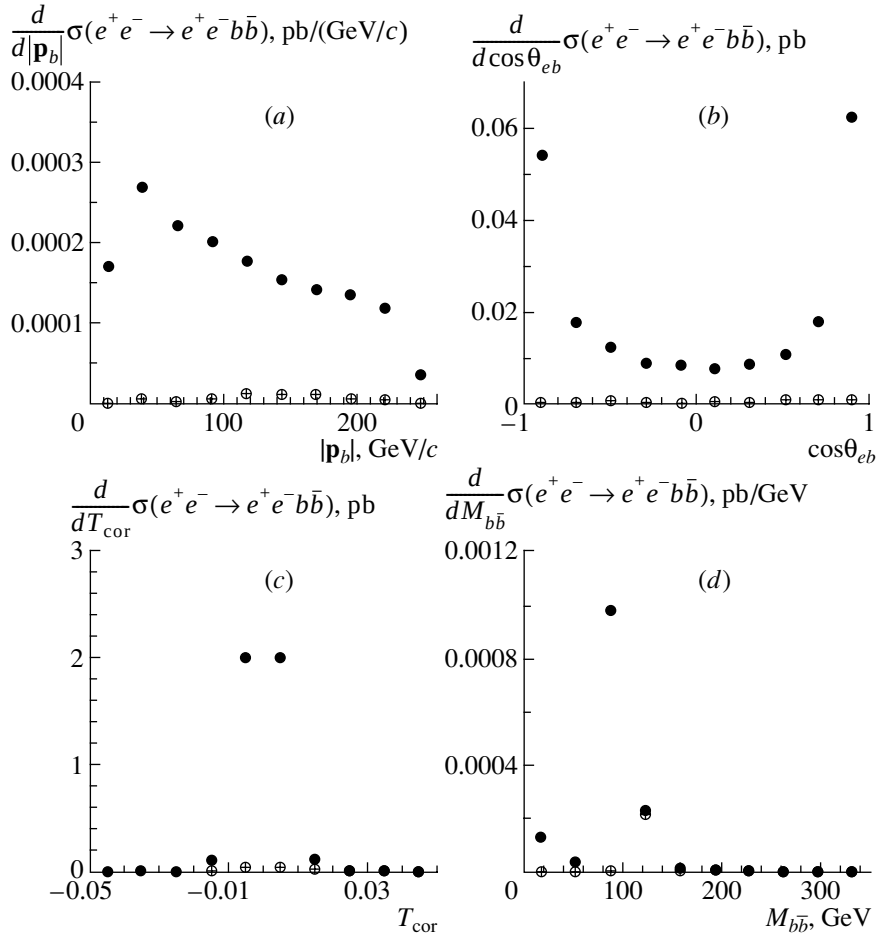

Fig. 2. Differential distributions of the cross section for the process $e^+e^- \to e^+e^-b\bar{b}$ with respect to (a) the b-quark momentum, (b) the b-quark scattering angle with respect to the direction of initial beams, (c) the correlation $T_{\rm cor}$ for the Standard Model at $\sqrt{s} = 500$ GeV and $M_H = 120$ GeV, and (d) the invariant mass of the $b\bar{b}$ pair: (•) contribution of all Standard Model diagrams and ($\oplus$) contributions of the Higgs boson diagrams alone, including the interference diagrams.

is significantly smaller than the contribution of the Standard Model background diagrams. Nevertheless, the possibility of reconstructing the full kinematics of the final state and a high luminosity of the TESLA collider will make it possible to separate the signal associated with the diagrams involving the Higgs boson from the background of the Standard Model diagrams.

The sensitivity of the process in question to variations in the parameters Δa and b can also be illustrated by considering the example of differential distributions. The distribution of the relevant cross section with respect to the scattering angle of a b jet is displayed in Fig. 3 for the case of the contribution from the diagram involving the Higgs boson in the Standard Model ($a = 1,\ b = 0$) and for the case of the contribution from the Higgs boson diagrams with allowance for the pseudoscalar-boson admixture ($a = 1,\ b = 0.5$). From this figure, one can see that a nonvanishing value of the parameter b leads to a general growth of the distribution—this is due to the characteristic b^2 dependence of the contribution from the pseudoscalar Higgs boson.

In setting constraints on the coupling constants a and b, it is also of importance to find experimental observables that are the most sensitive to these parameters. For this, it is reasonable to analyze the so-called sensitivity function

$$S = \frac{\sigma_i^{\rm NEW} - \sigma_i^{\rm SM}}{\Delta\sigma_i^{\rm expt}}, \qquad (2)$$

which is constructed for each bin of the distribution under study. In the definition of the sensitivity function in (2), $\sigma_i^{\rm SM}$ is the value of this distribution within the Standard Model ($a = 1, b = 0$) in the ith bin, $\sigma_i^{\rm NEW}$ is the value of the distribution in the ith bin for the case where one parameter or both of them deviate from their Standard Model values, and $\Delta\sigma_i^{\rm expt}$ is the expected value of the experimental

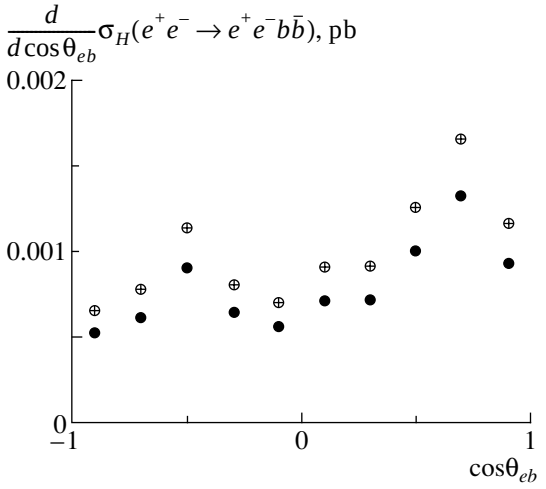

Fig. 3. Differential distribution of the cross section for the process $e^+e^- \to e^+e^-b\bar{b}$ with respect to the scattering angle of a b jet (•) for the case of the Higgs boson contribution within the Standard Model ($a = 1$, $b = 0$) and (⊕) with allowance for the admixture of the pseudoscalar Higgs boson ($a = 1$, $b = 0.5$).

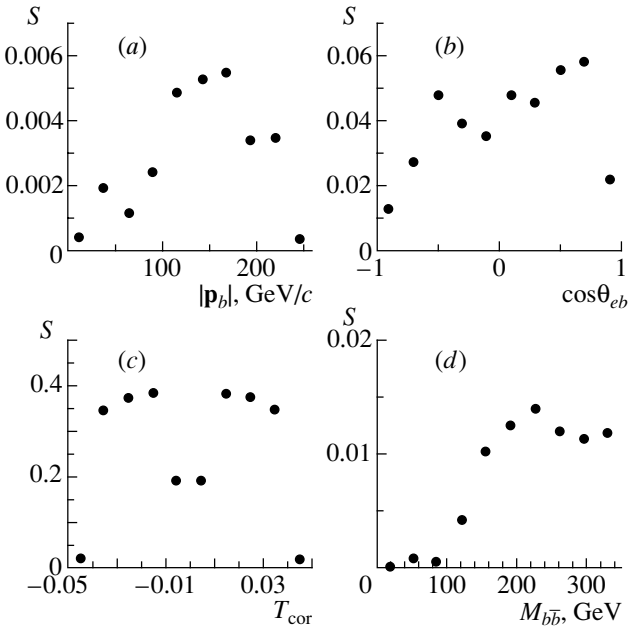

Fig. 4. Sensitivity functions $S(2)$ at $a = 1$ and $b = 0.5$ for the distributions with respect to (a) the b-quark momentum, (b) the b-quark scattering angle, (c) the correlation T_{cor}, and (d) the $b\bar{b}$ invariant mass.

error in the ith bin (an algorithm for calculating this error is given below). For each of the distributions subjected to analysis, Fig. 4 shows the sensitivity function constructed in the way outlined above. For the purposes of illustration, the case of $a = 1$ and $b = 0.5$ is chosen to exemplify new physics. In calculating the experimental error in a bin, use was made of the integrated-luminosity value of $\int \mathcal{L}dt = 1\ \text{ab}^{-1}$. From Fig. 4, one can see that the sensitivity of the process in question to variations in the parameter b is the highest at intermediate values of the b-jet momentum and at high invariant masses of b jets. An analysis of the distributions reveals that the highest sensitivity is observed for the distribution with respect to the scattering angle of a b jet, in which case S varies around a virtually constant high level over the entire kinematical region; for the other observables, either the function S is small, or its maximum is localized in an extremely narrow region of the phase space.

The problem of suppressing the contributions from background processes is an important point in such investigations. For the reaction $e^+e^- \to e^+e^-b\bar{b}$, background processes include $e^+e^- \to e^+e^-ZZ \to e^+e^-b\bar{b}\nu\bar{\nu}$ and $e^+e^- \to ZZZ \to b\bar{b}e^+e^-\nu\bar{\nu}$. As was shown in [21], however, either the cross sections for these processes are extremely small, or their contribution can be suppressed to a level of 0.2 fb.

In order to determine, for the parameters a and b, the regions that can be excluded on the basis of data from experiments at a future linear collider, we use a conventional χ^2 method, where the expected experimental error $\Delta\sigma_i^{\text{expt}}$ is defined as

$$\Delta\sigma_i^{\text{expt}} = \sigma_i^{\text{SM}}\sqrt{\delta_{\text{syst}}^2 + \delta_{\text{stat}}^2}, \qquad (3)$$

where the statistical error in a bin of the distribution being considered is given by

$$\delta_{\text{stat}} = \frac{1}{\sqrt{\sigma_i^{\text{SM}}\varepsilon_{b\bar{b}}\int \mathcal{L}dt}}. \qquad (4)$$

Here, $\varepsilon_{b\bar{b}}$ is the reconstruction efficiency for a pair of b jets. The analysis performed in [21] revealed that the use of the b-trigger algorithm in reconstructing b jets will make it possible to reach an efficiency of $\varepsilon_{b\bar{b}} = 56\%$. The systematic error receives contributions from the detector resolution, the uncertainty in measuring the luminosity (about 0.5%), the errors in separating background processes, and some other effects and is on the order of 1% [14].

From an analysis of various kinematical distributions for the process being studied, it was found that the most stringent constraints on the model parameters can be obtained from data on the differential distribution with respect to the scattering angle of b jets in the case where the kinematical region is broken down into ten bins, this confirming the conclusions drawn from the above analysis of the sensitivity function.

For the parameters a and b, the regions that can be excluded on the basis of data from experiments at the

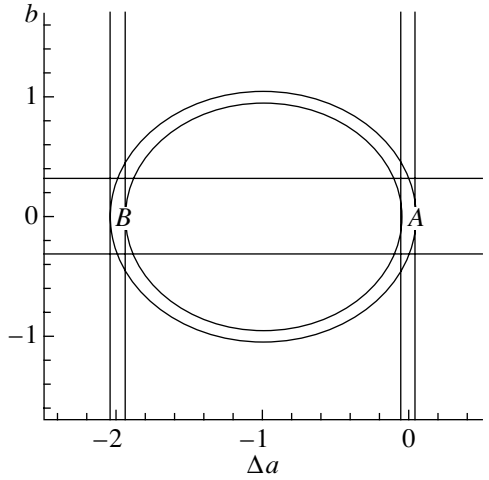

Fig. 5. Allowed regions of the parameters Δa and b at a confidence level of 95% at $\sqrt{s} = 500$ GeV and an integrated luminosity of 1 ab^{-1} for the Higgs boson mass of $M_H = 120$ GeV. In the case where the parameters Δa and b are considered to be independent, the allowed region is enclosed by the elliptic curves. The region between the horizontal straight lines is the region that is allowed for the parameter b at $\Delta a = 0$. The regions between the pairs of vertical straight lines in the left and right parts of the figure are the regions allowed for the parameter Δa at $b = 0$.

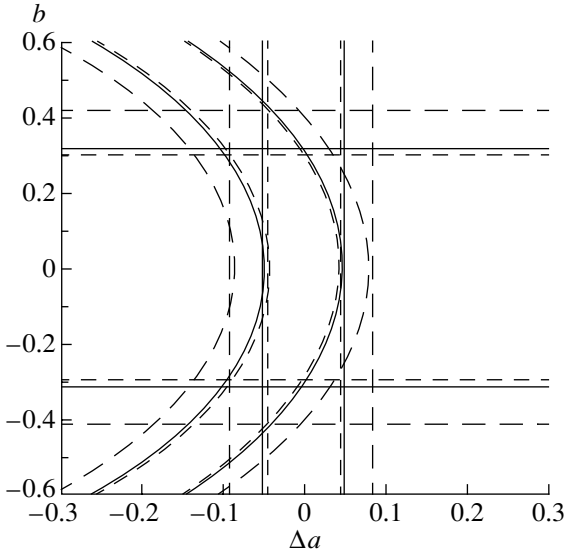

Fig. 6. As in Fig. 5 for region A, but at an integrated luminosity of (regions bounded by the long-dash curves) 100 fb^{-1}, (regions bounded by the solid curves) 1 ab^{-1}, and (regions bounded by the short-dash curves) 10 ab^{-1}.

TESLA collider [14] are shown in Fig. 5 for the total collision energy of $\sqrt{s} = 500$ GeV and an integrated luminosity 1 ab^{-1} at the Higgs boson mass of $M_H = 120$ GeV. For the case where the parameters Δa and b are taken to be independent, the allowed region at a confidence level of 95% is bounded by the elliptic curves. The region between the horizontal straight lines is the region allowed for the parameter b at $\Delta a = 0$. The regions between the pairs of vertical straight lines in the left and right parts of Fig. 5 are those that are allowed for the parameter a at $b = 0$. It can be seen from the figure that, in the case of two independent parameters, the allowed region is the region of insensitivity to the parameters Δa and b; within this region, the individual contributions of these parameters cannot be separated. In successively varying the parameters (allowed regions bounded by vertical and horizontal straight lines), combining the case where $\Delta a = 0$ and b is a free parameter with the case where $b = 0$ and Δa is a free parameter leads to the appearance of two disconnected allowed regions. In Fig. 5, they are labeled with the letters A and B (regions A and B are determined by the intersection of the horizontal band and two vertical bands in the left and right parts of Fig. 5). However, it is quite obvious that, in this case, the allowed region B is nonphysical. On the basis of the assumption that the Standard Model possesses a high predictive power, in which case new-physics effects will manifest themselves only in the form of small deviations from the predictions of the Standard Model, it can easily be shown that, in the case of a perfect experiment, an increase in the luminosity and a decrease in the systematic error will lead to a gradual degeneracy of the region B, with the result that the true allowed region will appear to be localized around the point specified by the coordinates $\Delta a = 0$ and $b = 0$ and predicted by the Standard Model. In determining the regions allowed for the parameter values, we will therefore consider only region A.

The regions allowed for the parameters Δa and b (at a confidence level of 95%) are shown in Fig. 6. In the case where the parameters Δa and b are independent, the allowed region is bounded by the concentric curves; the region bounded by the horizontal region bounded by the horizontal straight lines and that bounded by the vertical straight lines are the regions that are allowed, respectively, for an free parameter b at $\Delta a = 0$ and for a free parameter Δa at $b = 0$. The cases where the integrated luminosity is equal to 100 fb^{-1}, 1 ab^{-1}, and 10 ab^{-1} are represented by the long-dash, solid, and short-dash lines, respectively.

The resulting constraints on the parameters Δa and b can be represented in the form

$$-0.09 \le \Delta a \le 0.08 \text{ for } \int \mathcal{L}dt = 100 \text{ fb}^{-1}, \quad (5)$$

$$-0.056 \le \Delta a \le 0.055 \text{ for } \int \mathcal{L}dt = 1 \text{ ab}^{-1},$$

$$-0.05 \le \Delta a \le 0.05 \text{ for } \int \mathcal{L}dt = 10 \text{ ab}^{-1}$$

in the case of $b = 0$ and free Δa and in the form

$$-0.42 \le b \le 0.42 \text{ for } \int \mathcal{L}dt = 100 \text{ fb}^{-1}, \quad (6)$$

$$-0.32 \le b \le 0.32 \text{ for } \int \mathcal{L}dt = 1 \text{ ab}^{-1},$$

$$-0.3 \le b \le 0.3 \text{ for } \int \mathcal{L}dt = 10 \text{ ab}^{-1}$$

in the case of $\Delta a = 0$ and free b. In the case of Higgs boson masses varied around $M_H = 120$ GeV, the resulting constraints can be approximated to a high precision by multiplying the above constraints by the factor $(M_H/120 \text{ GeV})^2$.

It can be seen that the constraints in (5) and (6) are commensurate with the constraints following from the analysis of data on the processes $e^+e^- \to b\bar{b}\nu\bar{\nu}$ and $e^+e^- \to \tau^+\tau^-\nu\bar{\nu}$ [17, 18] and can be used in a global analysis of data that could be obtained at a future electron–positron collider.

4. CONCLUSIONS AND OUTLOOK

The possibility of detecting a signal from a scalar (pseudoscalar) Higgs boson in studying the process $e^+e^- \to e^+e^-b\bar{b}$ in experiments at a future linear collider has been explored in the present study. It has been shown that data on the reaction $e^+e^- \to e^+e^-b\bar{b}$ will provide the possibility of either discovering the presence of a pseudoscalar Higgs boson state or imposing stringent constraints on the region allowed for the coupling constants.

In particular, data on the process $e^+e^- \to e^+e^-b\bar{b}$ from the future linear collider TESLA of integrated luminosity $\int \mathcal{L}dt = 1$ ab^{-1} and total energy $\sqrt{s} = 500$ GeV would make it possible to obtain constraints on the region of the parameters a and b at a level of a few percent (at free a and fixed b) and at a level of ten percent (at free b and fixed a):

$$-0.056 \le \Delta a \le 0.055,$$
$$-0.32 \le b \le 0.32.$$

These results are commensurate with the results of the analysis performed in [10], where a global fit at $\int \mathcal{L}dt = 500$ fb^{-1} and $\sqrt{s} = 500$ GeV predicted the relative precision in determining the Yukawa coupling constant $g_{Hb\bar{b}}$ at a level of 2.2%.

In conclusion, we would like to make a few comments concerning future experiments. Let us assume that data from a future collider will reveal deviations from Standard Model predictions in processes involving a Higgs boson and that, in addition, there will be data from an independent measurement of the partial Higgs boson width $\Gamma_{H\to b\bar{b}}$ (for example, from data on the resonance production of a Higgs boson at a muon collider). It can be seen that, within the parametrization specified by Eq. (1) and used in this study, the partial Higgs boson widths are $\Gamma_{H\to f\bar{f}} \sim (a^2 + b^2)$, while the observables explored above feature a different dependence,

$$\frac{d\sigma}{d\mathcal{O}} = B_0 + aB_1 + a^2B_2 + b^2B_3.$$

By combining the results obtained by studying the process $e^+e^- \to e^+e^-b\bar{b}$ and data from the measurements of the partial width $\Gamma_{H\to b\bar{b}}$, it will then be possible to separate the contributions of the scalar and pseudoscalar coupling constants a and b and to obtain thereby a direct indication of the CP nature of the Higgs sector.

It should be noted that the absence of the dependence of data available for the process under consideration, as well as for the processes $e^+e^- \to \nu\bar{\nu}b\bar{b}$ and $e^+e^- \to \nu\bar{\nu}\tau^+\tau^-$ (without specific analysis of subsequent decays), on the first power of the parameter b is a significant drawback of these processes. The presumed smallness of the parameter b gives no way to obtain stringent constraints on the parameters of the coupling of the pseudoscalar Higgs boson, which are determined by terms proportional b^2. However, the inclusion of cascade decays—for example, $\tau \to \pi\nu$ and $\tau \to \rho\nu$—makes it possible to deduce additional information about the nature of the Higgs boson. It was shown in [22] that, by analyzing the products of $\rho^+\rho^-$ decay in the process $H \to \tau^+\tau^- \to \rho^+\rho^-\nu_\tau\bar{\nu}_\tau$, one can separate the contributions of the scalar and pseudoscalar Higgs bosons. A more complicated situation is observed for the cases of processes involving the production of b quarks. In principle, the inclusion of b-quark polarization in the final state (for example, on the basis of the cascade decay $b \to c\mu\nu$) would make it possible to observe terms in the distribution that are linear in the parameter b [23]. However, it does not seem possible to observe the weak decays $b \to c\mu\nu$, since a b quark undergoes hadronization into various B-meson states faster than decays via weak-interaction processes. Nevertheless, it was shown in [24] that there exists a tight correlation between the polarization of a b quark and the polarization of the Λ_b baryon produced by this quark. This gives grounds to hope for experimentally determining b-quark polarization and, hence, for separating a signal from terms linear in the parameter b.

ACKNOWLEDGMENTS

We are grateful to A.K. Likhoded and V.V. Kiselev for stimulating discussions on the results of this study and valuable comments.

This work was supported in part by the Russian Foundation for Basic Research (project nos. 01-02-16585, 00-15-96645), the Ministry for Higher Education of the Russian Federation (project no. E00-3.3-62), the Russian Foundation for Basic Research MAC (project no. 03-02-06131), and the Federal Target-Oriented Program Integratsiya (project no. 303233).

REFERENCES

1. S. Weinberg, Phys. Rev. Lett. **37**, 657 (1976).
2. C. T. Hill and E. H. Simmons, hep-ph/0203079.
3. LEP Higgs Working Group, hep-ex/0107029.
4. LEP Higgs Working Group, hep-ex/0107030; U. Schwickerath, hep-ph/0205126.
5. J. R. Dell'Aquila and C. A. Nelson, Nucl. Phys. B **320**, 61, 86 (1989).
6. B. K. Bullock, K. Hagiwara, and A. D. Martin, Phys. Lett. B **273**, 501 (1991); Nucl. Phys. B **395**, 499 (1993).
7. B. Grzadkowski and J. F. Gunion, Phys. Lett. B **294**, 361 (1992); M. Krämer, J. Kühn, M. L. Stong, and P. M. Zerwas, Z. Phys. C **64**, 21 (1994); J. F. Gunion and J. G. Kelly, Phys. Lett. B **333**, 110 (1994).
8. K. Hagiwara and M. L. Stong, Z. Phys. C **62**, 99 (1994); D. J. Miller, S. Y. Choi, B. Eberle, *et al.*, Phys. Lett. B **505**, 149 (2001); V. Barger, K. Cheung, A. Djouadi, *et al.*, Phys. Rev. D **49**, 79 (1994); K. Hagiwara, S. Ishihara, J. Kamoshita, and B. A. Kniehl, Eur. Phys. J. C **14**, 457 (2000); T. Han and J. Jiang, Phys. Rev. D **63**, 096007 (2001).
9. T. Plehn, D. Rainwater, and D. Zeppenfeld, Phys. Rev. Lett. **88**, 051801 (2002).
10. B. Field, S. Dawson, and J. Smith, hep-ph/0311199.
11. J. F. Gunion and J. Pliszka, Phys. Lett. B **444**, 136 (1998).
12. J. F. Gunion, B. Grzadkowski, and X.-G. He, Phys. Rev. Lett. **77**, 5172 (1996).
13. D. Atwood and A. Soni, Phys. Rev. D **52**, 6271 (1995); V. D. Barger, M. S. Berger, J. F. Gunion, and T. Han, Phys. Rep. **286**, 1 (1997); V. D. Barger, T. Han, and C. G. Zhou, Phys. Lett. **480**, 140 (2000); B. Grzadkowski, J. F. Gunion, and J. Pliszka, Nucl. Phys. B **583**, 49 (2000).
14. R.-D. Heuer *et al.*, hep-ph/0106315.
15. G. Bower, *Talk Presented at the Linear Collider Workshop, Chicago, Jan. 7–9, 2002.*
16. B. Grzadkowski and J. F. Gunion, Phys. Lett. B **350**, 218 (1995); B. Grzadkowski, J. F. Gunion, and J. Kalinowski, Phys. Rev. D **60**, 075011 (1999).
17. V. Braguta, A. Chalov, and A. Likhoded, Phys. Rev. D **65**, 054038 (2002).
18. V. Braguta, A. Chalov, A. Likhoded, and R. Rosenfeld, Phys. Rev. Lett. **90**, 241801 (2003).
19. M. Pohl and H. J. Schreiber, Report DESY 99-030.
20. V. Braguta, A. Chalov, and A. Likhoded, Phys. Rev. D **68**, 094008 (2003).
21. K. Desch and N. Meyer, LC Notes, LC-PHSM-2001-025 [http://www.desy.de/lcnotes/2001/025/ww-fus.ps.gz].
22. K. Desch, Z. Was, and M. Worek, hep-ph/0302046.
23. A. Chalov, A. Likhoded, and A. Luchinsky, in press.
24. V. A. Saleev, Phys. Lett. B **426**, 384 (1998); hep-ph/9705256.

Translated by A. Isaakyan